University of California
Santa Barbara

CoNi-base superalloys with improved high temperature properties and 3D printability

A dissertation submitted in partial satisfaction
of the requirements for the degree

Doctor of Philosophy
in
Materials

by

Sean Patrick Murray

Committee in charge:

Professor Tresa Pollock, Chair
Professor Daniel Gianola
Professor Irene Beyerlein
Professor Frédéric Gibou

September 2021

The Dissertation of Sean Patrick Murray is approved.

Professor Daniel Gianola

Professor Irene Beyerlein

Professor Frédéric Gibou

Professor Tresa Pollock, Committee Chair

August 2021

CoNi-base superalloys with improved high temperature properties and 3D printability

by

Sean Patrick Murray

For my family – old, and new

Acknowledgements

Before I began my graduate studies, I had the impression that pursuing a PhD would be a uniquely isolating experience, requiring extended periods of time alone while toiling away in a narrow field of study. I think feelings of isolation are unavoidable for most graduate students at some point in their studies, even without the added stresses of the global COVID-19 pandemic that changed our daily lives. However, looking back on the experience, I can say that these fears were unfounded, since the past five years at UCSB have been the most social, collaborative, and people-filled years I've ever had. The immense outpouring of support from family, friends, and colleagues in the days up to my defense was overwhelming and humbling. None of the work presented in this dissertation was undertaken as a solo effort, and I would like to take some time to profusely thank everyone who encouraged me and sustained me along the way.

First and foremost, I would like to thank my advisor, Tresa Pollock, for her mentoring and guidance. She is by far the hardest working person I know and has inspired me to pursue excellence in my professional career. Tresa is a constant source of insightful research ideas, an understanding and thoughtful mentor, and my biggest cheerleader at conferences and presentations. Despite her numerous students, post-docs, and collaborators, she has always managed to maintain a keen focus on the minute details of my own research, my interests, and my needs as a student. Thank you.

I would next like to thank my mother Donna, my father Jonathan, my older brother Nathan, and my younger sister Jennifer. Their love and support during my doctoral studies has been constant and unconditional. Since the start of the lockdown, we maintained a weekly Sunday video call to chat, share news, and hang out. Oddly enough, I feel like we talk more now than ever...a much appreciated silver lining.

My parents, both being engineers themselves, first gave me the notion that it would be

worthwhile to study engineering at university. I unabashedly followed my brother to the University of Illinois at Urbana-Champaign where we overlapped during my freshman year. While there, I grew as an engineer and a scientist and had my first research experiences working under Profs. Nancy Sottos, Scott White, Paul Braun, and Jessica Krogstad. I was fortunate to work alongside motivated PhD candidates such as Anthony Coppola, Pralav Shetty, Charles Smith, and Megan Emigh. I also need to thank Prof. Pascal Bellon who taught the Metals Processing and Design of Engineering Alloys classes which captivated my attention and made me deeply curious about metallurgy. During my second summer at UIUC, I was able to undertake an internship with GE Aviation at a single crystal turbine blade casting facility in Beavercreek, OH. My mentor, Gary Lynn, deepened my fascination of superalloys for high temperature applications, which I have pursued ever since. My aunt Amy and uncle Ken provided me free housing and meals for the whole summer, for which I will always be grateful. Near the end of my time at UIUC, Prof. Krogstad agreed to a chat over coffee at Grainger Library where I asked her about the prospects of pursuing a PhD. Being a UCSB alumnus herself, I became aware of the program at Santa Barbara and rapidly set my sights on applying. I would also like to thank my friends and roommates that were essential to my happiness and success at UIUC, including Brendan, Nick, Charlie, and especially Will, who joined me on a two-month-long backpacking trip in Europe after graduation.

Despite knowing which topics I wanted to explore once I arrived at UCSB, I was a novice when it came to carrying out experiments, preparing samples, and performing microscopy. The Pollock Group members who were present in those first years were always cheerful, knowledgeable, and willing to lend me a hand, including Marissa Lafata, Jackie Avallone, Emily Levin, Will Lenthe, Brent Goodlet, Marie-Agathe Charpagne, Jean-Charles Stinville, Yolita Eggeler, Alice Cervellon, and McLean Echlin. I would especially like to thank Colin Stewart, Rob Rhein, and Venkata Vamsi Koruprolu who

mentored me on cobalt-base superalloys and have inspired me to always pursue excellence in my research. I would like to thank the other students in the materials department and the current Pollock Group students and post-docs who continue to be excellent colleagues and friends, especially Andrew Polonsky, Kira Pusch, Carolina Frey, and Evan Raeker who have been essential to the studies on additive manufacturing of CoNi-base superalloys. The research support staff at UCSB have been stead-fast partners to any student in need of assistance with sample preparation, mechanical testing, or microscopy, therefore I must give many thanks to Deryck Stave, Kirk Fields, Peter Maxwell, Mark Cornish, Aidan Taylor, Claire Chisholm, Gareth Seward, and especially Chris Torbet. It has always been pleasurable to work with the Materials Department office staff that made life run smoothly, including Jocelyn Guzman, Ali Todhunter, Stefani Juarez, Alexandria Huddleston, and Budd Jamieson.

I have been fortunate to have worked with numerous off-campus collaborators, including Prof. Jonathan Cormier at l'Institut Pprime, Michael Kirka, Peeyush Nandwana, and Ryan Dehoff at Oak Ridge National Laboratory, and the team at Carpenter Technology Corporation including Stéphane Forsik, Ning Zhou, Bill Slye, Austin Dicus, Gian Colombo, and many others. Without your support, this document would be much, much thinner. My doctoral committee members consisting of Profs. Daniel Gianola, Frédéric Gibou, and Irene Beyerlein have always had open doors and were frequent guides on the path to becoming a more thoughtful scientist.

I have been lucky to live with great friends and roommates on-campus in San Clemente and off-campus at the Davenport house over the past five years, including Geoffrey, Usama, Sanjeev, Anudhi, Harsha, Jared, Matt, and Felicity (along with, of course, Ruby, Scooter, Freddy, and Alfred). Our weekly barbecues and frequent board game nights with the nearby Scripps Crescent house consisting of Brian, Wyatt, Naomi, Usama (again!), Audra, and Drew were a constant source of relaxation and joy. After numerous themed

parties, cocktail nights out, and movie nights in, I'd also like to thank the Bouncy Castle that I entered when I became Julija's boyfriend, including Caitlin, Jeff, Emily, Neil, Julia, Ben, Sophia, Madi, Richard, Christian, Emma, Anastasia, and Andrew.

Lastly, none of this would have been possible without Julija. She has always believed in me, and gave me the strength I needed to continue during every difficult moment of my doctoral studies. You are my best friend, and I love you.

Curriculum Vitæ

Sean Patrick Murray

Education

2021	Ph.D. in Materials, University of California, Santa Barbara.
2016	B.S. in Materials Science and Engineering, University of Illinois, Urbana-Champaign.

Publications

14. **S.P. Murray**, E.B. Raeker, K.M. Pusch, C. Frey, C.J. Torbet, N. Zhou, S.A.J. Forsik, A.D. Dicus, G.A. Colombo, M.M. Kirka, and T.M. Pollock. "Microstructure evolution and tensile properties of a selectively laser melted CoNi-base superalloy." In preparation.
13. J. Rossin, P.E. Leser, K.M. Pusch, C. Frey, **S.P. Murray**, C.J. Torbet, S. Smith, S. Daly, and T.M. Pollock. "Bayesian inference of elastic constants and texture coefficients in additively manufactured cobalt-nickel superalloys using resonant ultrasound spectroscopy," *Acta Materialia* **220**, 117287 (2021). [**doi**]
12. **S.P. Murray**, A. Cervellon, J. Cormier, and T.M. Pollock. "Low cycle fatigue of a single crystal CoNi-base superalloy," *Materials Science and Engineering: A* **827**, 142007 (2021). [**doi**]
11. B.R. Goodlet, **S.P. Murray**, B. Bales, J. Rossin, C.J. Torbet, and T.M. Pollock. "Temperature dependence of single crystal elastic constants in a CoNi-Base alloy: A new methodology," *Materials Science and Engineering: A* **803**, 140507 (2020). [**doi**]
10. **S.P. Murray**, K.M. Pusch, A.T. Polonsky, C.J. Torbet, G.G.E. Seward, N. Zhou, S.A.J. Forsik, P. Nandwana, M.M. Kirka, R.R. Dehoff, W.E. Slye, and T.M. Pollock. "A defect-resistant Co–Ni superalloy for 3D printing," *Nature Communications* **11**, 4975 (2020). [**doi**]
9. **S.P. Murray**, K.M. Pusch, A.T. Polonsky, C.J. Torbet, G.G.E. Seward, M.M. Kirka, R.R. Dehoff, N. Zhou, S.A.J. Forsik, P. Nandwana, W. Slye, and T.M. Pollock. "Microstructure and Tensile Properties of a CoNi-Based Superalloy Fabricated by Selective Electron Beam Melting." In S. Tin et al. (Eds.) *Superalloys 2020*. The Minerals, Metals and Materials Series. Springer. [**doi**]
8. K.V. Vamsi, **S.P. Murray**, and T.M. Pollock. "The Yield Strength Anomaly in Co–Ni Design Space." In S. Tin et al. (Eds.) *Superalloys 2020*. The Minerals, Metals & Materials Series. Springer. [**doi**]

7. M.-A. Charpagne, J.-C. Stinville, A.T. Polonsky, M.P. Echlin, **S.P. Murray**, Z. Chen, N. Bozzolo, J. Cormier, V. Valle, and T.M. Pollock. "Tuning Strain Localization in Polycrystalline Nickel-Based Superalloys by Thermomechanical Processing." In S. Tin et al. (Eds.) *Superalloys 2020*. The Minerals, Metals & Materials Series. Springer. [**doi**]
6. M.-A. Charpagne, K.V. Vamsi, Y.M. Eggeler, **S.P. Murray**, C. Frey, S.K. Kolli, and T.M. Pollock. "Design of Nickel-Cobalt-Ruthenium multi-principal element alloys," *Acta Materialia* **194**, 224–235 (2020). [**doi**]
5. C.A. Stewart, **S.P. Murray**, A. Suzuki, T.M. Pollock, and C.G. Levi. "Accelerated discovery of oxidation resistant CoNi-base γ/γ' alloys with high $L1_2$ solvus and low density," *Materials & Design* **189**, 108445 (2020). [**doi**]
4. **S.P. Murray**, J.-C. Stinville, P.G. Callahan, R.K. Rhein, and T.M. Pollock. "Low Cycle Fatigue of Single Crystal γ'-containing Co-based Superalloys at 750 °C," *Metallurgical and Materials Transactions A* **51**, 200–213 (2020). [**doi**]
3. R.K. Rhein, P.G. Callahan, **S.P. Murray**, J.-C. Stinville, M.S. Titus, A. Van der Ven, and T.M. Pollock. "Creep Behavior of Quinary γ'-Strengthened Co-Based Superalloys," *Metallurgical and Materials Transactions A* **49**, 4090–4098 (2018). [**doi**]
2. B.R. Goodlet, L. Mills, B. Bales, M.-A. Charpagne, **S.P. Murray**, W.C. Lenthe, L. Petzold, and T.M. Pollock. "Elastic Properties of Novel Co-and CoNi-Based Superalloys Determined through Bayesian Inference and Resonant Ultrasound Spectroscopy," *Metallurgical and Materials Transactions A* **49**, 2324–2339 (2018). [**doi**]
1. A.M. Coppola, L.G. Warpinski, **S.P. Murray**, N.R. Sottos, and S.R. White. "Survival of actively cooled microvascular polymer matrix composites under sustained thermomechanical loading," *Composites Part A: Applied Science and Manufacturing* **82**, 170–179 (2016). [**doi**]

Patent Applications

1. T.M. Pollock, C.A. Stewart, **S.P. Murray**, and C.G. Levi. "High temperature oxidation resistant Co-based gamma/gamma prime alloys DMREF-Co," US Patent Application 16/375,687 (2020).

Abstract

CoNi-base superalloys with improved high temperature properties and 3D printability

by

Sean Patrick Murray

Ni-base superalloys have been the material of choice for structural components in the hot sections of turbine engines since the 1940s. Superalloy research and development has proceeded with specific turbine applications such as blading, vanes, and disks in mind. For the blade alloys that must withstand the most thermomechanically severe environment downstream from the combustor, an excellent balance of high temperature mechanical properties (strength, ductility, creep, and fatigue), oxidation resistance, processability, coating compatibility, and cost must be achieved. Many of these exceptional properties are conferred by their microstructure that consists of a high volume fraction of sub-micron scale γ' precipitates (Ni_3Al, $L1_2$) that are coherent with a refractory-rich solid-solution strengthened γ matrix (Ni, A1). These alloys are typically cast into single crystals that exhibit further improved high temperature creep performance due to the absence of grain boundaries. While decades of research have sought to discover materials that can perform at temperatures beyond what is capable with the technologically mature Ni-base superalloys, suitable replacements have not yet been found.

The discovery of a γ' phase in the Co-Al-W ternary system by C.S. Lee in 1971, which was rediscovered and described in more detail in 2006 by Sato et al., has enabled the development of novel classes of γ' strengthened Co-base superalloys for high temperature applications. Since the solidus temperatures of these alloys can be over 100 °C greater than their Ni-base counterparts, these alloys may provide a path to higher temperature capability than is currently available. Co-base superalloys form a similar γ-γ' microstruc-

ture where the γ' phase is based on Co_3(Al,W). Creep studies have shown that single crystal Co- and CoNi-base have creep performance greater or equal to 1st-generation Ni-base single crystals. However, early model alloys have also been demonstrated to have low γ' solvus temperatures, poor oxidation resistance, and high mass density. There is also a dearth of data on their response to cyclic loading and fatigue failure. To achieve the balance of properties necessary for high temperature applications, the compositions of Co- and CoNi-base alloys need to be refined through alloying and the resultant mechanical and environmental properties assessed.

In this work, low cycle fatigue tests conducted on single crystal Co-base superalloys demonstrate that these alloys have low strength and poor resistance to oxidation-assisted surface cracking which severely reduces the fatigue life compared to legacy Ni-base alloys. These property shortcomings motivate the development of novel Co-base alloy compositions with improved high temperature properties. An alloy design study using high-throughput alloy synthesis and rapid characterization methods has identified a promising region of CoNi-base composition space with alloys that exhibit improved properties including elevated γ' solvus temperature, favorable oxidation kinetics due to formation of a protective alumina scale, and reduced mass density. Low cycle fatigue tests on a novel alloy from this composition space, SB-CoNi-10+, demonstrate improved fatigue resistance that is similar to 1st-generation Ni-base blade alloys.

Single crystal castings of SB-CoNi-10+ revealed that this alloy exhibits a favorable solidification behavior with mild amounts of as-cast microsegregation. This suggests that these alloys may be amenable to the extreme thermal conditions present in additive manufacturing techniques such as selective laser melting and electron beam melting. High performance Ni-base superalloys are difficult to process with fusion-based processes since large amounts of cracks often form in the as-printed alloy that severely degrade the mechanical properties. The SB-CoNi-10 alloy has been fabricated with multiple additive

manufacturing techniques and has been demonstrated to be resistant to the formation of cracks or significant porosity. Studies on the room temperature and elevated temperature tensile properties are presented along with investigations on the effect of various heat treatment schedules on the alloy microstructure. CoNi-base superalloys are suitable candidates for further development for additive manufacturing since they can produce a high γ' volume fraction microstructure while still being 3D printable with minimal amounts of defects. These alloys could be utilized by engineers to leverage the design flexibility of additive manufacturing for novel high temperature components with complex geometries, innovative cooling channels, and reduced material waste.

Contents

Chapter 1

Introduction and Background

1.1 Single crystal Ni-base superalloys for high temperature applications

Ni-base superalloys are a class of metallic materials that have an exceptional balance of high temperature mechanical properties, environmental resistance, microstructural stability, processability, and cost [1]. These alloys are primarily responsible for significant advancements in the fuel efficiency of electricity producing land-based natural gas turbines [2] and aeroengines for airplane flight [3] and are also widely used in rocket engines, nuclear power generation, and chemical processing [4]. Similar to how the mechanical properties of steels are highly tunable depending on their chemical composition and processing pathway, the Ni-base superalloys can be tuned for specific applications by adjusting the volume fraction of the γ' phase, by rebalancing of various beneficial alloying additions, or by processing through different fabrication methods to control the grain-scale microstructure. The compositional design space for these materials is large and the chemical compositions of individual alloys are complex, often with >10 different chem-

ical species present that each contribute to the desired mechanical, environmental, and thermophysical properties of the alloy [5]. Exploiting this chemical design space through research and development of novel superalloys has continued steadily to the present day since 1929 when small additions of Al and Ti were made to a commonly used "80/20" Nickel-chromium alloy, resulting in an unexpected improvement in creep performance [6].

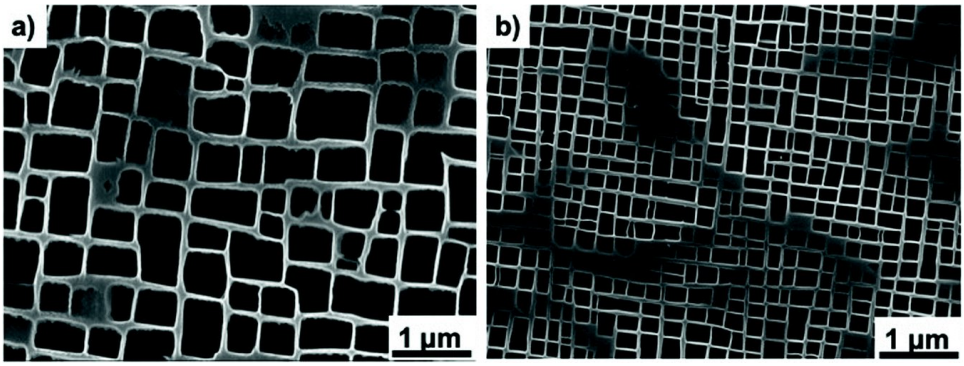

Figure 1.1: Scanning electron micrographs of the γ-γ' scale microstructure in (a) CM-SX-4+ and (b) TMS-238. Adapted from "Tensile, Low Cycle Fatigue, and Very High Cycle Fatigue Characterizations of Advanced Single Crystal Nickel-Based Superalloys" by L.M.B. Ormastroni et al., 2020, in *Superalloys 2020* p. 341-351. Copyright 2020 The Minerals, Metals & Materials Society. Adapted with permission [7].

Ni-base superalloys consist of a solid-solution strengthened matrix based on Ni (γ, A1) that is precipitation strengthened by a coherent, ordered intermetallic based on Ni_3Al (γ', $L1_2$). Alloying additions can be generally classified as either γ-formers or γ'-formers depending on their tendency to partition between the two phases. Elements such as Al, Ti, Nb, Ta, Pt, and the base element Ni partition to the γ' precipitates and elements such as Co, Cr, W, Mo, Re, and Ru partition to the γ matrix [8, 9]. The γ and γ' phases have a small negative misfit parameter, δ, on the order of $\sim 10^{-3}$ defined as:

$$\delta = \frac{2(a_{\gamma'} - a_{\gamma})}{(a_{\gamma'} + a_{\gamma})} \tag{1.1}$$

where a_{γ} and $a_{\gamma'}$ are the lattice parameters of the γ and γ' phase respectively, result-

ing in coherent γ/γ' interfaces that are believed to strongly affect the high temperature mechanical properties and resistance to coarsening [10]. The two-phase γ-γ' microstructure that is formed after appropriate heat treatments confers an excellent combination of strength and ductility to the alloy. Micrographs of typical γ-γ' microstructures are shown in Fig. 1.1. The high γ' volume fraction superalloys, where the γ' phase constitutes a majority of the phase fraction ($> 60\%$) in the form of evenly dispersed, sub-micron, cuboidal precipitates, are employed in applications where the most severe combinations of high temperatures and high stresses are present. The most notable example are the single crystalline blades and vanes in the high-pressure turbines of aeroengines that convert the hot gas path produced by the combustor into work that drives the fan, and thereby provides thrust for the aircraft. These alloys are so intertwined with the development of these components that they are commonly referred to simply as "blade alloys". These components experience a range of temperature and stress conditions where mechanical integrity must be maintained for tens of thousands of hours of operation, with some local hot spots at blade tips experiencing temperature excursions as high as 1200 °C. This is 90% of the temperature where these alloys begin to melt [4]. The composition of the γ' phase has a strong effect on the strength of the alloy by controlling the anti-phase boundary energy of the γ' and the resistance to dislocation shear [11]. The γ phase can contain a high concentration of heavy refractory elements such as Re, W, and Mo which can impede the motion of dislocations that bow around the γ' phase during high temperature creep [12]. Small additions of Re in particular have been shown to provide significant improvements to creep performance, which is commonly referred to as the "Re-effect" [13]. As new generations of single crystal blade alloys have been developed, the Re content has been used for classification, resulting in 0 wt.% Re alloys to be referred to as 1^{st}-generation, 3 wt.% Re alloys as 2^{nd}-generation, and 6 wt.% Re alloys as 3^{rd}-generation. As the refractory alloy content of blade alloys increases, the formation

of deleterious topologically close-packed (TCP) phases after long-time high temperature exposure becomes more prevalent. Additions of Ru have been shown to suppress the formation of these phases, and subsequent Ru-containing 4^{th}-, 5^{th}-, and 6^{th}-generation Ni-base superalloys have since been developed [14].

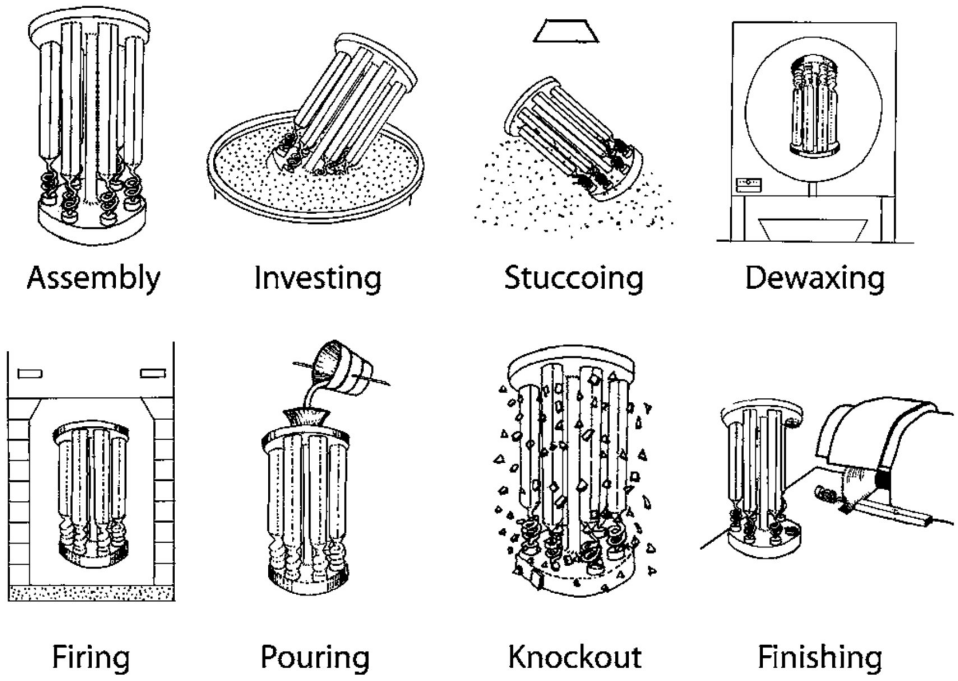

Figure 1.2: A schematic of the investment casting process for single crystal Ni-base superalloys. Reproduced from "The Superalloys: Fundamentals and Applications" by R. Reed, 2006, p. 123. Copyright 2006 by Cambridge University Press. Reproduced with permission [5].

Additional improvements in high temperature capability have been achieved through advancements in superalloy processing and fabrication. The creep properties of superalloy castings can be improved through directional solidification which suppresses the formation of transverse grain boundaries present in equiaxed castings that would be normal to the loading direction of a turbine blade in operation. A further refinement was implemented in the 1960s and 70s through the Bridgman crystal growth process, where the use of a $\langle 001 \rangle$ starter crystal along with a "pigtail" grain selector in the investment

casting process allows for the fabrication of ⟨001⟩-aligned single crystals. This completely eliminates the Coble creep deformation mechanism of mass transfer along grain boundaries at high temperature, eliminates the creep cavitation damage that can occur in power law creep, and reduces the rate of Nabarro-Herring creep through the crystal that is dependent on the inverse of the grain size [15, 16]. Examples of turbine blading after conventional casting, directional solidification, and single crystal growth are shown in Fig. 1.3 and a schematic of the steps required to convert a wax positive assembly of bars into an investment cast single crystal are presented in Fig. 1.2.

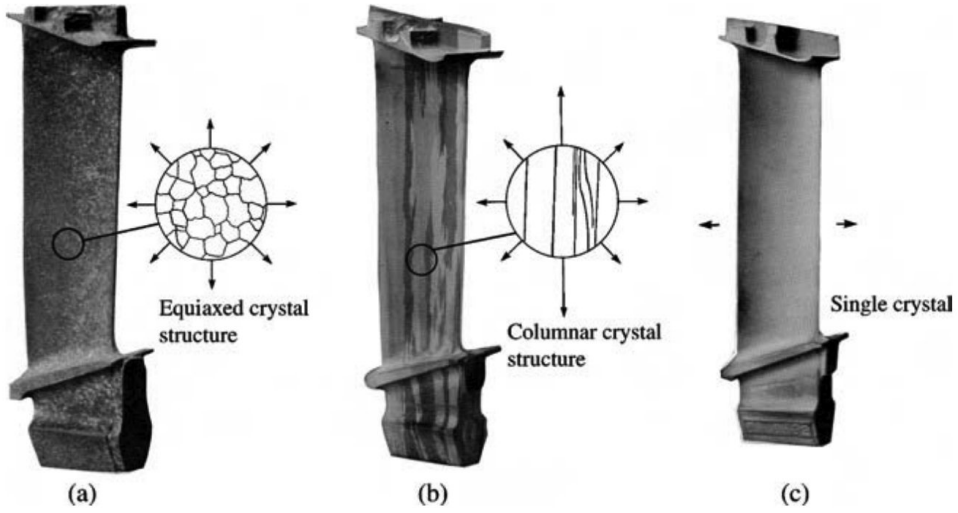

Figure 1.3: Examples of turbine blading in the (a) equiaxed, (b) columnar, (c) and single crystal forms. Reproduced from "The Superalloys: Fundamentals and Applications" by R. Reed, 2006, p. 20. Copyright 2006 by Cambridge University Press. Reproduced with permission [5].

Single crystalline Ni-base superalloy compositions have been adjusted to account for the elimination of grain boundaries, allowing for reductions in grain boundary strengtheners such as C, B, and Zr that also depressed the solidus temperatures of the alloys [6]. However, some C content remains beneficial for unidirectional solidification behavior [17]. Since Hall-petch strengthening can no longer be leveraged to increase the strength of single crystalline blade alloys, special attention has been paid to understanding the

strength of the γ-γ' microstructure through control of the planar fault energies of the γ' precipitates and solid solution strengthening in the γ matrix [18, 19, 20]. As higher temperatures for turbine temperatures were reached, the importance of forming low volatility protective oxide scales upon oxidation became critical. This has motivated the reduction of Cr content and the further additions of Al in blade alloys in order to promote the formation of the highly desirable α-Al_2O_3 scale after exposure to air at high temperatures. These compositional changes also increase the γ' volume fraction and γ' solvus temperature at the cost of some hot corrosion resistance [1].

The relationships between processing, structure, properties,and performance in Ni-base superalloys are well studied, with several textbooks and over 2000 research articles published on the mechanical properties and deformation behavior of Ni-base superalloys alone [1]. There are 14 proceedings of the Superalloys conferences that have taken place every 4 years since 1968 in Seven Springs, Pennsylvania, with the exception of Superalloys 2021 which was delayed in 2020 due to the global COVID-19 pandemic and was held virtually in September 2021 (the contents of Ch. 6 of this thesis were included in these proceedings). For several decades, there have been many important players that have driven superalloy development and understanding such as turbine engine companies, national laboratories, and numerous research universities. This global effort has led to significant improvements in the high temperature performance of Ni-base superalloys, as shown in Fig. 1.4. As the desire for further increases in turbine engine efficiency are desired, requiring increasing turbine entry temperatures (TET), there is a growing concern that Ni-base superalloys have reached a maturity beyond which significant improvements are difficult to realize. This has motivated a dedicated research effort into developing novel material systems for the hot-section components of future turbine engines that can go "beyond" the capabilities of Ni-base superalloys, either through improved thermomechanical performance or by enabling novel processing techniques such as additive

manufacturing to fabricate components for the hot sections of turbine engines.

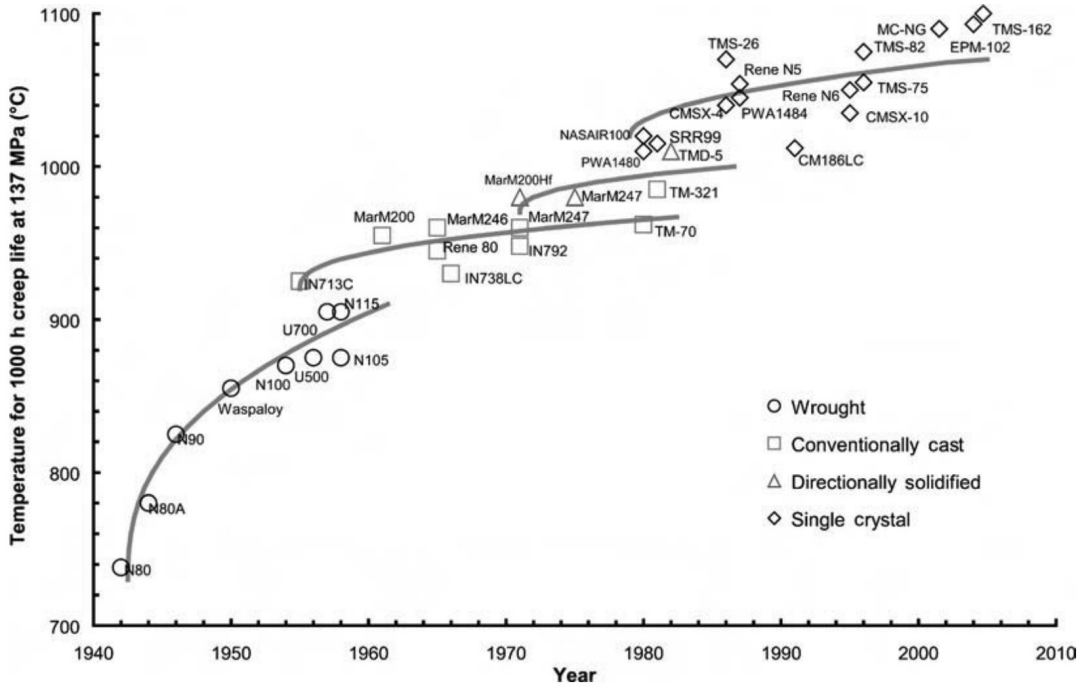

Figure 1.4: Improvement in creep performance of Ni-base superalloys over the decades since their introduction in the 1940s. Reproduced from "The Superalloys: Fundamentals and Applications" by R. Reed, 2006, p. 19. Copyright 2006 by Cambridge University Press. Reproduced with permission [5].

Many candidate materials for high temperature applications are first considered for their higher melting points than Ni-base superalloys ($T_{m,Ni} = 1455$ °C). This has resulted in recent research efforts on ceramic matrix composites (CMCs), MAX phases, refractory alloys, and certain classes of high entropy alloys. Other classes of both Co-base and Fe-base superalloys have also been developed alongside Ni-base alloys in the past century, and while the base elements of these alloys have higher melting points than Ni ($T_{m,Co} = 1495$ °C, $T_{m,Fe} = 1538$ °C), it was only recently that precipitation strengthening similar to the high γ' volume fraction Ni-base superalloys could be realized in these systems.

1.2 γ'-containing Co- and CoNi-base superalloys

The possibility of precipitation strengthening by a coherent, geometrically close-packed phase in Co-base alloy systems was first identified in the PhD thesis of Charles Samuel Lee from the University of Arizona, entitled "Precipitation-Hardening Characteristics of Ternary Cobalt-Aluminum-X Alloys" [21]. Ternary Co-4.25 wt.% Al-X alloys where X was Ti, Nb, Ta, Mo, and W were arc-melted and heat-treated in order to investigate the possibility of precipitation hardening through microstructure evaluation and hardness testing. In total, 17 ternary alloy systems along with 3 promising quaternary systems that included Cr were investigated. Each system was solution heat-treated and subsequently aged at temperatures between 600 and 900 °C for time intervals between 0.1 and 1000 h followed by hardness testing. While a variety of phases were observed, a previously undiscovered cubic phase with a lattice parameter similar to Co was observed in the Co-Al-W systems. These alloys exhibited a continuous hardening behavior upon aging. On pg. 61, C.S. Lee writes, "Perhaps by optimizing the Al and refractory metal content, a coherent cubic precipitate, such as was found in the Co-Al-W system, might be preserved and optimized, thus forming the basis for a useful alloy." This work went largely unnoticed for 45 years, but C.S. Lee had discovered that the Co-Al-W ternary can produce a γ-γ' microstructure identical to Ni-base superalloys where the γ matrix is instead based on Co and the γ' phase is based on $Co_3(Al,W)$. An article published in 1984 by Chester T. Sims on the history of superalloys writes, "γ' now often composes up to 50% of contemporary nickel alloys, but cannot form in cobalt alloys" [6]. Had C.S. Lee's work been more widely noticed and understood, the development of γ'-strengthened Co- and CoNi-base superalloys could have been accelerated by several decades.

This finding was brought to the attention of superalloy researchers in the mid-2000s by the study of Sato et al. which identified the location of the small two-phase γ-γ' phase

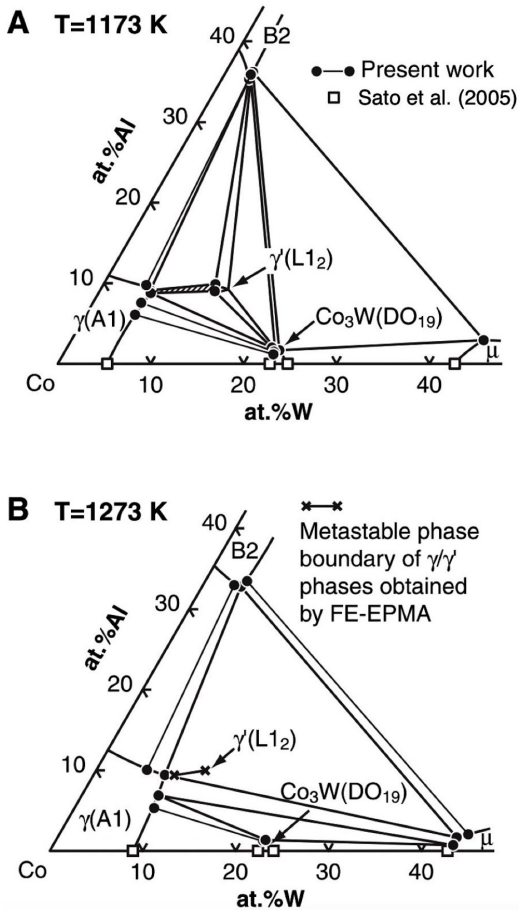

Figure 1.5: Isothermal section diagrams of the Co-Al-W ternary system in the Co-rich portion at (A) 1173 K and (B) 1273 K. Reproduced from "Cobalt-Base High-Temperature Alloys" by J. Sato et al., *Science* **312**, 2006, p. 90-91. Copyright 2006 by AAAS. Reproduced with permission [22].

field in the Co-Al-W ternary that appeared stable at 900 °C but was not present at 1000 °C (Fig. 1.5) [22]. They more thoroughly described the thermophysical properties of γ'-strengthened Co-Al-W alloys, demonstrated that they could be strengthened by additions of Ta, and that the small positive misfit parameter could be tuned to control precipitate morphology (Fig. 1.6). Importantly, these Co-base alloys possessed higher solidus and liquidus temperatures by 50-100 °C compared to their Ni-base counterparts and yet had morphologically identical precipitation strengthened microstructures [23]. The suppressed γ'-solvus temperatures of ternary Co-Al-W alloys near 1000 °C are approxi-

mately 300 °C lower than Ni-base blade alloys resulting in a total loss in high temperature strength above 1000 °C. However, this does provide a wider processing window where the alloy is single phase γ during heat treatment. Compression tests on ternary alloys and Ta-modified alloys at elevated temperatures by Suzuki et al. demonstrated that a yield stress anomaly (YSA) is present above 600 °C in these Co-base alloys, similar to conventional Ni-base alloys [24, 25]. From these seminal works, 15 years of research has sought to rapidly understand and develop Co-base alloy systems for high temperature applications in order to develop new classes of γ'-strengthened superalloys.

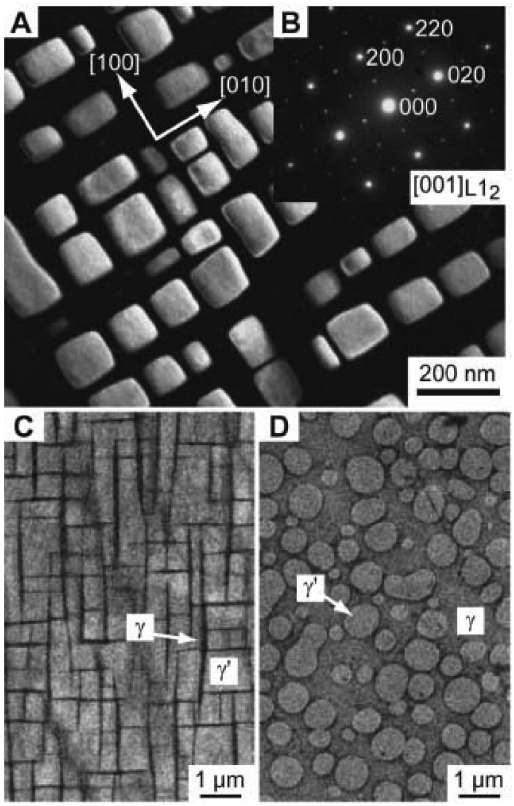

Figure 1.6: Electron micrographs of Co-9Al-7.5W alloy annealed at 1173 K for 72 hours. (A) Darkfield image. (B) Selected area diffraction pattern. (C and D) Field emission scanning electron micrographs of Co-8.8Al-9.8W-2Ta (C) and Co8.8Al-9.8W-2Mo (D) annealed at 1273 K for 1 week. Reproduced from "Cobalt-Base High-Temperature Alloys" by J. Sato et al., *Science* **312**, 2006, p. 90-91. Copyright 2006 by AAAS. Reproduced with permission [22].

However, elevated melting points must be combined with a variety of exceptional properties such as high-temperature strength (consisting of high yield, γ'-solvus temperature, creep rupture, ductility, and fatigue), low density, and environmental resistance to successfully introduce novel alloys as rotating components in the high-pressure turbine. Ternary Co-base alloys fall short on many of these requirements, and therefore alloying is required to elevate the γ'-solvus temperature, reduce the mass density, and promote beneficial oxidation response. Several decades of prior research on Ni-base superalloys combined with modern computational and high-throughput alloy synthesis and characterization techniques has provided an exciting opportunity to rapidly develop the simple ternary alloys into multi-component alloys with balanced properties. However, the small compositional domain of the two-phase γ-γ' phase field in the Co-Al-W ternary results in limited compositional flexibility where excess amounts of Al or W can promote the formation of CoAl (β, B2), Co_3W (χ, $D0_{19}$) or Co_7W_6 (μ, $D8_5$) phases [26]. Additions of Ni into the Co-Al-W system can greatly widen the two-phase field and raise the γ' solvus temperature, allowing for greater amounts of beneficial alloying additions to be added without the formation of deleterious 3^{rd}-phases [27]. For these reasons, CoNi-base alloys that contain 20-40 at.% Ni have been demonstrated to be a promising pathway to develop novel superalloys that have the compositional flexibility needed to achieve balanced properties [28, 29, 30, 31, 32, 33, 34, 35, 36].

The mass density of alloys for rotating components is an important consideration since this is directly linked to the stresses that the blades and turbine disk will experience during operation, along with the necessity for light-weighting of aircraft engines for increased payload [37]. Due the high W content of ternary Co-Al-W alloys of roughly 10 at.% that is necessary to reach the small γ-γ' phase field, these alloys exhibit mass densities near 10 g cm^{-3} which is ~15% greater than comparable 1^{st}-generation Ni-base superalloys such as AM1 or CMSX-2 [5, 38]. This has motivated the development of

W-free Co-base superalloys that would have more attractive specific strengths. Since the removal of W destabilizes the γ' phase, these alloys contain other γ'-formers such as Mo, Nb, and Ta along with significant additions of Ni between 20-30 at.% [38, 39, 40]. This has also led to the development of Co-Ti-Cr ternary alloys with γ-γ' microstructures that have solvus temperatures above 1100 °C, low densities near 8.1 g cm^{-3}, and reasonable positive misfit parameters near 0.5% [41]. This is a significant improvement over binary Co-Ti alloys which possess unacceptably high misfit parameters that results in a loss of coherency between the γ and Co_3Ti γ' phase [42]. In general, the reduction of W content from CoNi-base superalloys has been demonstrated in multiple studies to be an effective strategy to reduce the mass density to levels seen in Ni-base superalloys [34, 35, 36].

The protection of the superalloy surface from corrosion and oxidation is equally important as their elevated strength at high temperatures, especially in the context of thin-walled components with internal cooling passages. While blade alloys are coated with thermal barrier coating systems that provide protection to the alloy surface, the alloy surface must be able to resist significant oxidation in the aggressive turbine environment in the event of coating spallation or foreign object damage. Single crystal Ni-base blade alloys have excellent oxidation resistance due to the rapid formation of a continuous layer of α-Al_2O_3 in service, which is promoted by the high Al content and additional Cr content of the alloy. Co-Al-W ternary alloys do not possess this beneficial behavior and often form α-Al_2O_3 as discrete internal particles, only forming a continuous layer that prevents the further ingress of oxygen after significant amounts of both external and internal oxidation [23, 43, 44, 45]. Preferably, the oxidation reaction is rapid such that the formation of a γ'-denuded zone is largely reduced and mass gain is minimized, as is the case in René N5 where Al_2O_3 forms as an external layer only 1 µm thick without significant overlaying oxides after 1 h exposure in air at 1100 °C [46]. Some amount of overlaying oxides such as monoxides and spinels can be acceptable, as in the

case of CMSX-4, as long as the overall oxide scale thickness remains thin on the order of a couple microns [47].

The PhD thesis research of C. Stewart investigated the oxidation behavior of compositional spaces relevant to CoNi-base alloys using high-throughput combinatorial alloy synthesis through ion plasma deposition (IPD) along with rapid assessment of Al_2O_3-forming behavior through photo stimulated luminescence spectroscopy (PSLS) after oxidation [46, 48, 49, 50]. These techniques allowed for a rapid exploration of a complex multi-component compositional space of Co-Ni-W-Al-Cr-Ta alloys that could both produce a two-phase γ/γ' microstructure with high temperature stability and have suitable oxidation behavior. The selected alloying additions allowed for a tractable search of this compositional space, and is likely the minimum number of elements that could be included to achieve balanced properties in a CoNi-base superalloy. Further additions of solid-solution strengtheners (Mo, Re, Ru), γ'-formers (Ti, Nb, and Hf), and minor elements (B, C, Y, La, Si, Zr) would likely lead to CoNi-alloys with improved properties over what was explored in these studies, but systematically exploring the properties of these compositions is extremely difficult experimentally.

Three CoNi-base alloy libraries were fabricated through IPD, with each library consisting of a triangular array of 78 buttons beneath three cathode alloy sources at each corner. All cathodes consisted of Co-Ni-Al-W-Ta-Cr alloys with varying amounts of each element, and some select cathodes being Ni-free or W-free. Each library was fabricated with a Ni-free cathode and a Ni-containing cathode (labeled as Cathode 1 and 2 in the thesis) along with a third Ni-containing cathode (Cathodes 3, 4, and 5) that either contained (i) elevated Cr, (ii) reduced W, or (iii) elevated Ta. Deposition of roughly 150 µm thick layers of alloy upon the buttons was desired. These samples were subsequently solution heat treated at 1200 °C above the highest expected γ'-solvus for homogeneity and then polished to 50 nm colloidal alumina. A standard oxidation test of 1 h at 1100

°C in dry air was applied to observe whether Al_2O_3 formation would occur and whether the oxide formed rapidly enough to create a continuous layer. Samples from the libraries were investigated by PSLS with a 633 nm wavelength incident laser at multiple locations to measure the presence/absence of a characteristic α-Al_2O_3 flourescence doublet at 14400 cm^{-1} [46]. Overlaying oxides such as NiO and CoO are translucent to the excitation beam and the luminescence signal, allowing for detection of α-Al_2O_3 below these oxides provided that they are sufficiently thin. Interestingly, tilt-polish experiments revealed that CoO has a higher signal absorptivity compared to NiO, allowing only for overlaying oxide scales on the order of 5 µm to transmit signal sufficiently for detection [48]. Therefore, this technique can both identify the presence of α-Al_2O_3 in CoNi-alloys and also indicate which alloys have thin overall scale thicknesses. These non-destructive evaluations were also paired with destructive cross-sectioning through the oxide scales to validate the PSLS technique, measure the oxide scale thickness, characterize the various oxides that may have formed, and observe the possible presence of 3^{rd}-phases in the bulk of the IPD alloys after solutioning and oxidation testing [49], since good oxidation performance must still be paired with a two-phase γ-γ' microstructure for the desired mechanical behavior. Stewart's research on this topic is presented in several research articles, and the work described in Ch. 3 of this thesis builds upon these studies in order to develop a multi-component CoNi-base alloy with balanced high-temperature properties [46, 48, 49, 50].

Despite these initial hurdles, one of the most exciting aspects of Co- and CoNi-base alloys are their favorable solidification behavior compared to Ni-base superalloys [34, 51, 52]. While the increased refractory content of Ni-base superalloys improves their high temperature mechanical performance, this also results in a higher susceptibility to form grain defects during unidirectional solidification such as misoriented grains and freckle chains [17]. The source of these defects is the development of convective instabilities

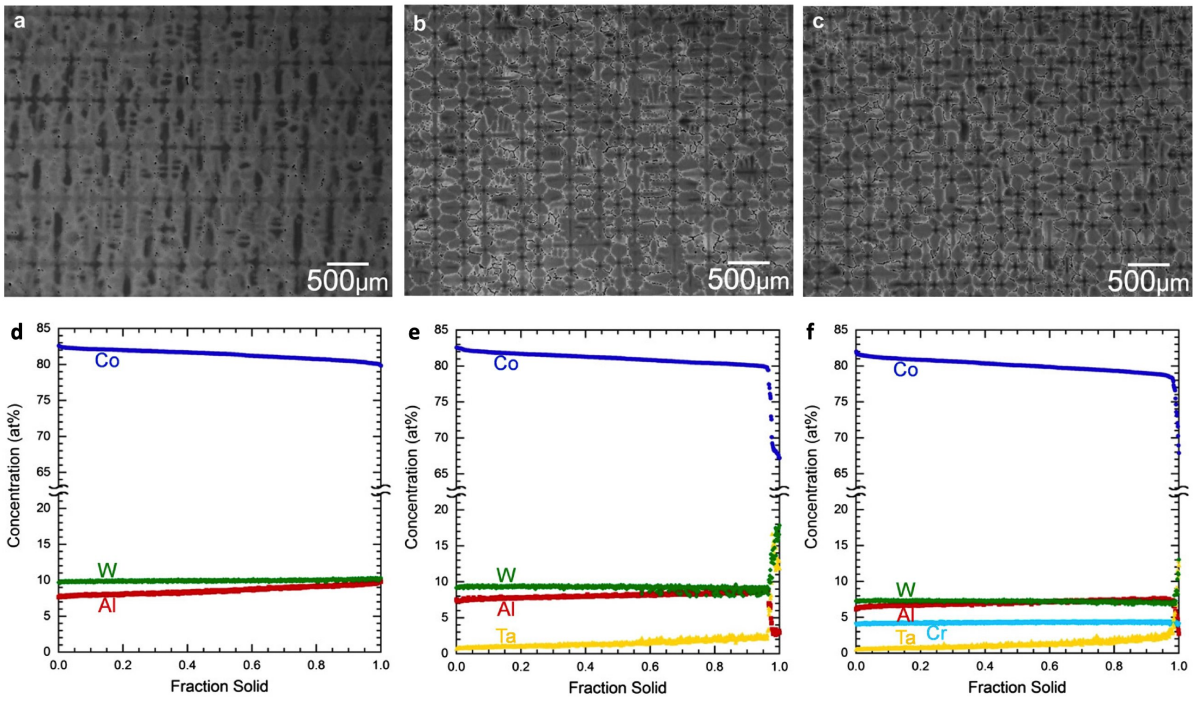

Figure 1.7: Optical micrographs of the as-solidified single-crystals with the composition of (a) 11W, (b) 2Ta and (c) CrTa. Concentration profiles obtained by grid scan of EPMA for single-crystals with the composition of (d) 11W, (e) 2Ta and (f) CrTa. Adapted from "Single-crystal solidification of new Co–Al–W-base alloys" by M. Tsunekane et al., 2011, *Intermetallics* **19**, p. 636-643. Copyright 2011 by Elsevier Ltd. Adapted with permission [51].

near the solid-liquid interface that are driven by solute partitioning between the solid and the liquid. In Ni-base superalloys, the strong partitioning of W, Re, and Mo to the solid offsets the strong partitioning of Ta to the liquid, which reduces the density of the liquid ahead of the solidification front and promotes density inversion with the melt. This can result in the transport of fragmented dendrites into the melt which act as nuclei for misoriented grains [53]. One way to overcome these density inversions is to flip the mold upside-down and to dip and withdraw the mold from a superalloy melt, ensuring that the low density liquid near the solidification front can not invert with the higher density melt due to gravity [54], but this introduces additional complexity to the solidification process.

The intensity of microsegregation during solidification can be described using the Scheil equation [55]. With the assumptions of infinite diffusion in the liquid and no diffusion in the solid, the equation can be expressed as:

$$C_{\mathrm{s}} = kC_{\mathrm{o}}(1 - f_{\mathrm{s}})^{k-1} \tag{1.2}$$

where C_{s} is the concentration of the solid, C_{o} is the starting composition of the melt, f_{s} is the fraction solidified, and the distribution coefficient is defined as $k = C_{\mathrm{s}}/C_{\mathrm{l}}$. Bridgman single crystal casting trials on Co-base superalloys revealed that solute partitioning was much less severe compared to Ni-alloys. For example, Tsunekane et al. used electron probe micro-analysis (EPMA) on as-cast single crystals to measure the distribution coefficient value for W in Co-base alloys to be near $k_W = 1.0$ as opposed to approximately $k_W = 1.5$ in Ni-base alloys [51]. This produces relatively flat compositional profiles, as shown in Fig. 1.7. Ta-containing Co-base alloys were found to still have strong partitioning of Ta to the liquid, resulting in the favorable condition of the liquid ahead of the solidification front increasing in density during solidification, eliminating the possibility of convective instabilities altogether. This is particularly interesting in the case of large castings for industrial gas turbine blades where the reduced cooling rates inherent in the larger casting increases the permeability of the dendritic solidification front, and therefore greatly increases the susceptibility to grain defects compared to smaller turbine blades. Single crystal casting trials on a novel CoNi-base superalloy and quantitative assessment of the as-cast segregation are presented in this thesis in Ch. 3 and compared to the previous literature.

1.3 Creep and fatigue behavior of high γ' volume fraction superalloys

Single crystal Ni-base superalloys experience sustained mechanical loading at a higher fraction of their melting point than any other modern alloy [6]. Their remarkably low creep rates at elevated temperatures allow for tens of thousands of hours of use in service without significant deformation that would require replacement of a part, leading them to be very economically valuable. This is combined with sufficient strength, ductility, low cycle fatigue resistance, high cycle fatigue resistance, environmental resistance, and phase stability at these elevated temperatures. In this section, a brief description of the creep and low cycle fatigue performance of single crystal Ni-, Co-, and CoNi-base superalloys will be presented, along with descriptions of the deformation mechanisms and microstructural degradation that occurs in these loading scenarios. Uniaxial loading along the $\langle 001 \rangle$ crystallographic direction will be considered since this is the the most technologically relevant orientation, however studies have been performed on the fatigue and creep properties of crystals loaded along the $\langle 101 \rangle$ and $\langle 111 \rangle$ orientations as well.

Creep behavior: While Ni-base superalloys exhibit high yield strengths up to temperatures of 700-800 °C due to the YSA [5, 56, 57, 58], it is of practical significance to understand the time-dependent inelastic deformation that can occur at stresses lower than the yield strength. This process is known as creep deformation. Blade tip clearances must satisfy tight tolerances in service, so typically blades must be removed from service if creep strain greater than a few percent are accumulated. While the temperature and stress profiles in service may vary during take-off, cruise, and landing, creep tests are normally performed under isostress and isotemperature conditions at several different stress-temperature combinations to assess creep performance. This data is then normalized using a Larson-Miller Parameter (LMP) approach to combine the effects of

temperature and time on a single axis which is then plotted against the applied stress. Tests are often taken to rupture, although interrupted creep tests allows for observation of the dislocation deformation mechanisms that were active in the various stages of creep and reveal the state of the γ-γ' microstructure.

The excellent resistance to creep deformation of single crystal Ni-base superalloys can be attributed to a variety of factors including (i) the absence of grain boundaries, (ii) optimized γ' volume fraction, (iii) high planar fault energies of the γ' phase, and (iv) the strong partitioning of heavy refractory elements such as Re, Mo, and W to the γ matrix. Creep curves for Mar-M200 processed through conventional casting, directional solidification, and Bridgman casting are shown in Fig. 1.8. In particular, the creep strain rate is reduced and the creep rupture life is significantly increased as the grain boundary content of the alloy is reduced. It's interesting to note that there exists an optimal γ' volume fraction that results in a peak in the creep performance that out-performs the response from pure γ and pure γ' alloys. The creep rupture life as a function of γ' volume fraction is shown in Fig. 1.9 for Ni-base single crystal alloys TMS-75 and TMS-82+, which shows that a monolithic increase in γ' volume fraction does not necessarily result in longer creep life. Note that the creep rupture data is presented on a log scale, with the optimized γ' volume fraction resulting in creep performance over 10^4 times greater than pure γ and over 10 times greater than pure γ'.

To develop an understanding the synergystic improvement of the creep performance due to the two-phase γ-γ' microstructure, observations of the deformation mechanisms active under various creep conditions are required. This is possible through transmission electron microscopy (TEM) studies on interrupted creep specimens, as demonstrated by Pollock et al. on $\langle 001 \rangle$-aligned CMSX-3 single crystals crept between 800-900 °C at stresses up to 552 MPa [12]. TEM observations were performed at each stage of the creep curve, including the brief incubation phase, the primary creep phase, the steady-state

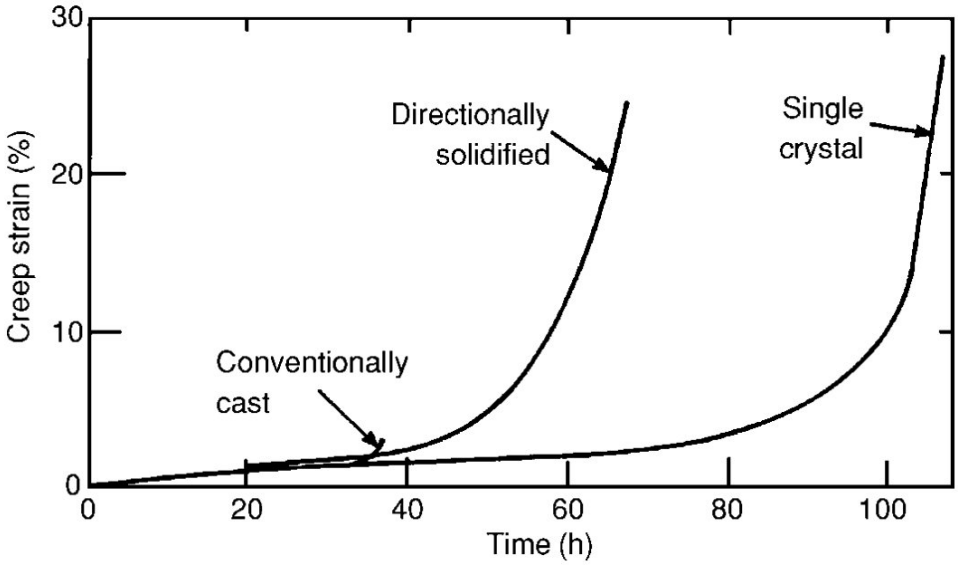

Figure 1.8: Evolution of creep strain with time for Mar-M200 under loading of 206 MPa and 982 °C in the conventionally cast (equiaxed) condition, the directionally solidified (columnar) condition, and the single-crystal form. Reproduced from "The Superalloys: Fundamentals and Applications" by R. Reed, 2006, p. 130. Copyright 2006 by Cambridge University Press. Reproduced with permission [5].

secondary creep phase, and the tertiary phase that leads to rupture. The initial dislocation density is low, with infrequent colonies of "grown-in" dislocation tangles in the γ phase around irregularly shaped γ' precipitates. These dislocation character are a/2$\langle 110 \rangle$ unit dislocations that lie on $\{111\}$ slip planes, typical of other fcc alloys. Dislocations were not observed in the γ' phase in the aged state. In the incubation phase, dislocation loops spread exclusively in the γ from the "grown-in" dislocation regions, but filling of the entire γ matrix has not yet been achieved. The ordered γ' phase can be treated initially as impenetrable at the stress levels for creep testing due to their high APB energy, and therefore dislocations must bow through the narrow γ channels and overcome the local Orowan resistance, τ_{or}, which is defined as

$$\tau_{or} = \frac{\mu b}{l} = \sqrt{\frac{2}{3}}\frac{\mu b}{h} \tag{1.3}$$

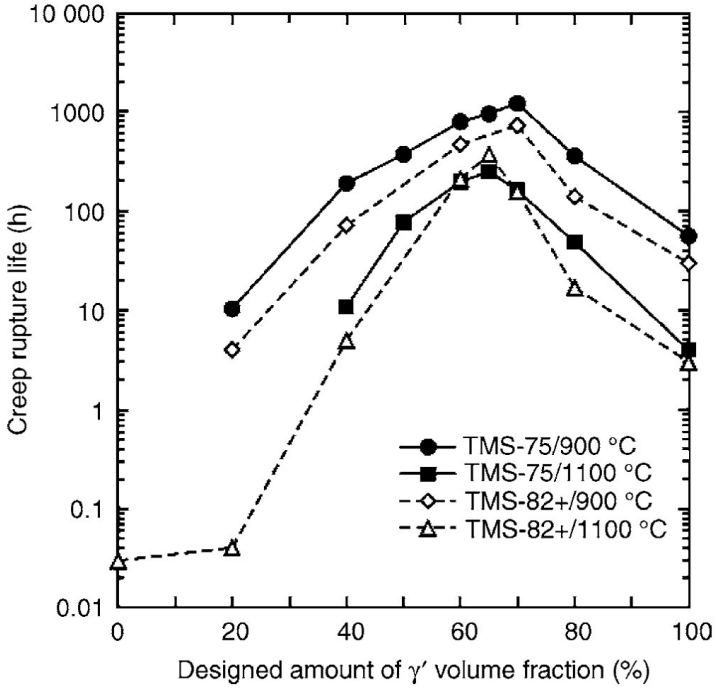

Figure 1.9: Variation of the creep rupture lives of the single crystal superalloys TMS-75 and TMS-82+, as a function of the amount of γ' phase [59]. The creep rupture life is largest when the γ' fraction is about 70%. Reproduced from "The Superalloys: Fundamentals and Applications" by R. Reed, 2006, p. 153. Copyright 2006 by Cambridge University Press. Reproduced with permission [5].

where μ is the shear modulus, b the Burgers vector, and l is the channel dimension along the $\langle 110 \rangle$ direction across a channel of thickness h. Inserting typical values for CMSX-3 (h = 60 nm, l= 73.5 nm, b = 0.254 nm, and μ = 48.2 GPa) produces an Orowan resistance of 166 MPa, which corresponds to an uniaxial applied stress of 408 MPa just to push dislocations through the fine-scale γ channels.

Initially, dislocations with similar Burgers vectors are observed in the incubation period, indicating that these dislocations emanate from single sources. As dislocations from these sources impinge on one another, a three-dimensional nodal dislocation network can from on the γ-γ' interfaces, which relieves the misfit between these two phases. This creates a quasi-stationary dislocation network in time that deforms the γ but leaves the γ' largely undeformed until stresses in the matrix build up to a point that dislocations

can be pushed into the γ'. Shearing of the γ' is normally indicative of the accelerating creep rate during the tertiary creep stage before failure. Due to the high APB energy of the γ', this dislocations pass through the γ' as tight superdislocation pairs that are connected by a narrow APB. Final rupture occurs due to the formation of cavities that results in microvoid coalescence that forms along the fraction surface.

The strong partitioning of heavy refractories elements, most notably Re, to the γ phase is also associated with slower creep strain rates. The addition of 2-3 wt. % Re to the first-generation single crystal alloys resulted in a doubling of the creep life, as shown in Fig. 1.10, with some members of the superalloys community referring to Re as the "magic dust" for this reason [13, 60]. However, The underlying causes of the so-called "Re-effect" on creep performance are still not fully understood and are a topic of scientific debate [61]. Diffusion couple studies have shown that Re is one of the slowest diffusing species in Ni, with a rate that is even an order of magnitude less than W. Re also partitions very strongly to the minority γ phase, where additions of 2 wt. % globally result in a 7 wt. % concentration in the matrix after heat treatment. The slow diffusivity of Re can slow down the coarsening and rafting kinetics of the γ' phase, delaying the onset of accelerating creep rates, but this alone can not account for the dramatic increase in creep life that Re affords the alloy. This has led many to suspect whether fine Re clusters form in the γ matrix that act as barriers to dislocation motion, or if the Re segregates heavily to the γ/γ' interface where dislocations travel through a thermally-activated climb process. This process is depicted schematically in Fig. 1.11. Experimental evidence of these clustering phenomenon are not conclusive, with atom probe tomography (APT) studies paired with state-of-the-art cluster detection algorithms resulting in no cluster detection in Ni-X alloys (where X is 10 wt. % of either Ta, W, Re, Ir or Pt) or in 2^{nd}-generation blade alloy CMSX-4. Therefore, it is likely that Re strongly affects the vacancy diffusion mechanisms that are necessary for the dislocation glide-climb process

to occur, but placing this on a firm quantitative foundation is still needed.

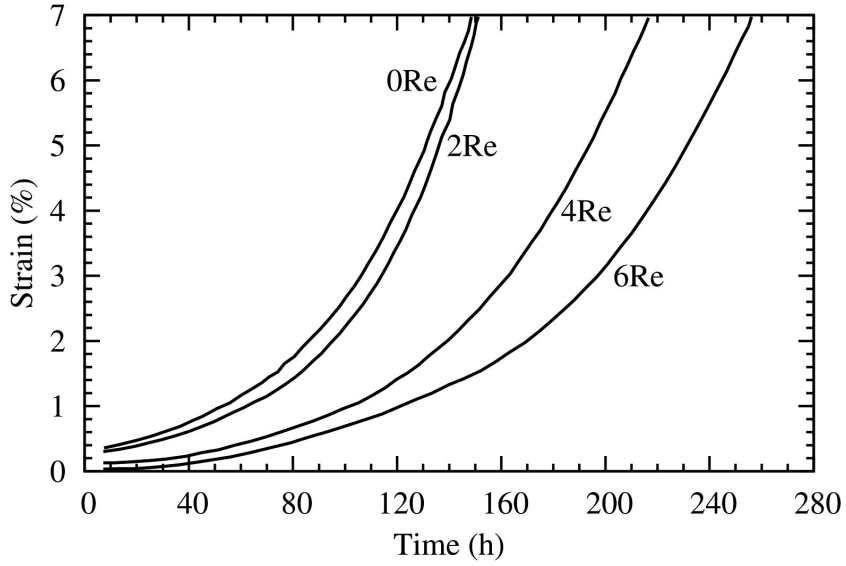

Figure 1.10: Creep curves for alloy 1444 and Re-containing derivatives studied by Giamei et al. at 899 °C under a load of 380 MPa [60]. Reproduced from "What is the role of rhenium in single crystal superalloys?" by A. Mottura and R. Reed, 2014, *MATEC Web of Conferences* **14**, 01001. Copyright 2014 by the authors, published by EDP Sciences [13].

Next, the creep response of single crystal Co- and CoNi-base superalloys will be briefly described. There are key differences compared to the Ni-base superalloys. The first investigations on Co-base single crystals were performed in 2012 by Tanaka et al. in Japan and Titus et al. in the United States [62, 63, 64]. Tanaka et al. prepared single crystals of a ternary Co-Al-W alloy along with alloy variants that contained Ta additions and Ta+Ni additions. The alloyed specimens had similar γ' solvus temperatures near 1100 °C while containing various amounts of γ' volume fraction after heat treatment. They performed all of their creep experiments at 1000 °C with an applied load of 137 MPa. This resulted in the ternary Co-Al-W alloys to be single-phase γ during creep testing due to low γ' solvus in their alloy measured as 977 °C, and therefore these alloys experienced creep lifetimes less than one minute [64]. The alloyed single crystals withstood creep deformation between 29 and 188 h before rupture, with the alloy with the highest γ'

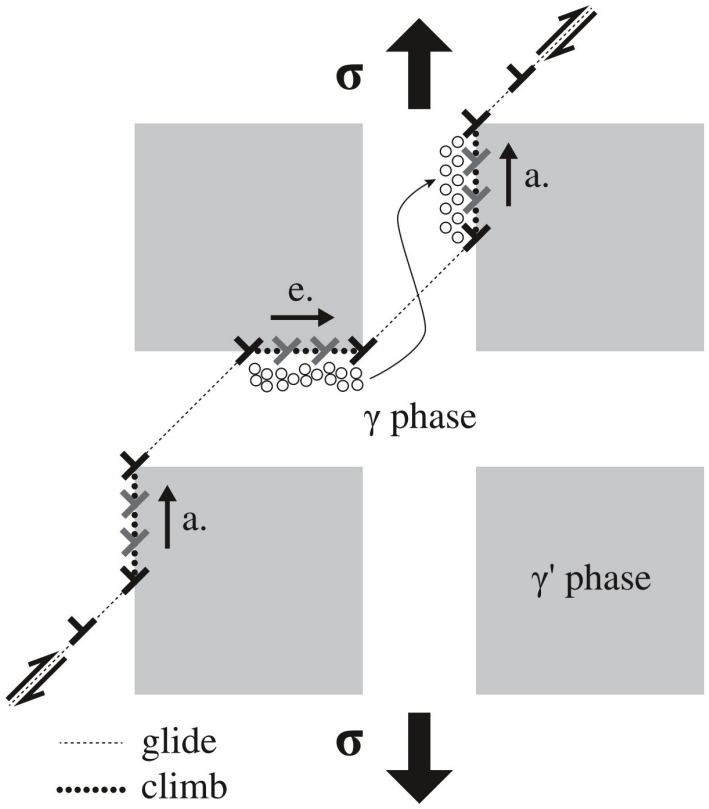

Figure 1.11: A 2D schematic of the climb-assisted glide process occurring in tertiary creep and the resulting vacancy flow from the horizontal to the vertical channels. Reproduced from "What is the role of rhenium in single crystal superalloys?" by A. Mottura and R. Reed, 2014, *MATEC Web of Conferences* **14**, 01001. Copyright 2014 by the authors, published by EDP Sciences [13].

volume fraction (85 %) performing the best. This is in contrast to the Ni-base superalloys, where a monotonic increase in the γ' volume fraction doesn't correspond directly to improved creep performance. This behavior has been observed again recently in the study of Bezold et al. using Co-Al-W-Ta single crystals with varying γ' volume fractions [65]. Titus et al. performed their experiments at 900 °C and at applied stresses between 275 and 379 MPa, allowing for the ternary Co-Al-W alloy specimens to have some γ' present during testing [63]. They also investigated alloys with additions of 2Ta and 6Ti to raise the γ' solvus near 1100 °C. The alloyed specimens performed better than the base ternary alloy and an alloy containing Cr and Ta, indicating that the γ' stability is closely

tied to the creep performance of the alloy. The creep performance of these model alloys was between that of 1st-generation and 2nd-generation Ni-base single crystals, which was promising due to the lack of Re in these Co-base systems. While Re is also a very slowly diffusing element in Co, additions of Re have been demonstrated to not be nearly as effective in Co-base single crystals as they are in Ni-base single crystals [66]. This partly due to the less intense partitioning of Re between the γ and γ' in Co-base single crystals that has been confirmed by APT experiments, which would result in a negligible change to the diffusion behavior of the mildly Re-containing matrix.

Another major difference between the alloy classes are the presence of large, extended planar faults that are frequently observed within the γ' precipitates during the early stages of creep deformation for Co- and CoNi-base superalloys [67, 68, 69, 70, 71]. These include superlattice intrinsic stacking faults (SISFs), superlattice extrinsic stacking faults (SESFs), APBs, and APB-SISF-APB configurations where an SISF loop is embedded within an APB. While some authors estimate that the plastic deformation accommodated by γ' shearing events only accounts for $\approx$10 % of the total creep strain, these observations indicate that the stresses needed to shear the precipitates are likely lower than the local Orowan resistance of the γ channels. Numerous observations have been made of local phase transformations along these planar faults along with the segregation of various elements. While the exact nature of the segregation mechanism is under debate, it is clear that chemical segregation along these planar faults can lower the local planar fault energy which increases the driving force for the dislocation to continue to shear across the precipitate. Interestingly, dislocations on other slip planes that impinge upon these faults often do not shear them, resulting in planar fault interactions that may act as a hardening mechanism [72]. The study of planar fault segregation in Co-, CoNi-, and Ni-base superalloys has led to the development "phase transformation strengthened" superalloys, where control of the amount of η formers and μ formers can promote the

formation of beneficial phases along the planar faults that inhibit additional shearing events into the γ' precipitates [73, 74].

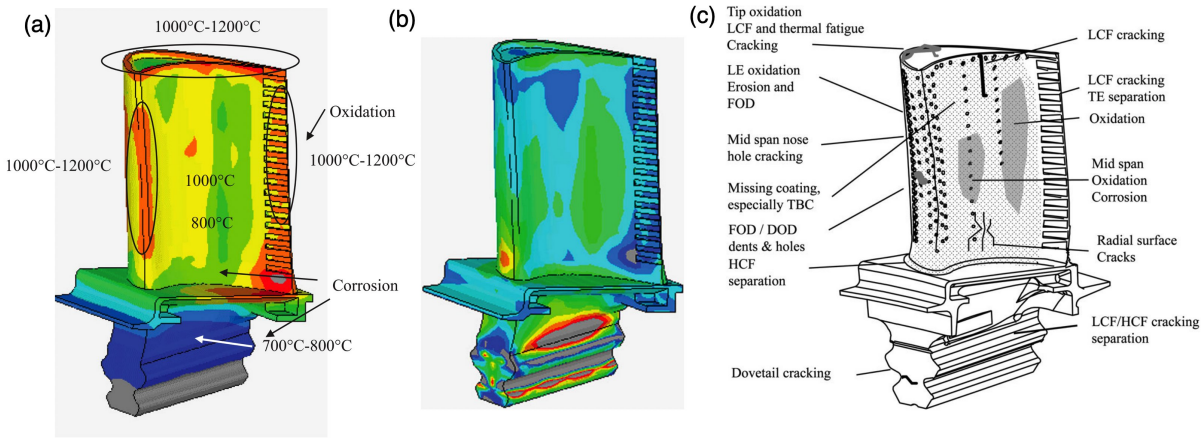

Figure 1.12: (a) Typical range of temperatures on the surface of a stage 1 turbine blade used for commercial aviation. (b) Typical stresses in a turbine blade range from 100 to 500 MPa depending on location. Darker shades near trail edge, leading edge and pressure side areas at 60–90% span are under compression, most other areas are under tension. (c) Typical modes of distress in a high pressure turbine blade. Adapted from "Development of strong, oxidation and corrosion resistant nickel-based superalloys: critical review of challenges, progress and prospects" by R. Darolia, 2019, *Int. Mat. Rev.* **64**, p. 355-380. Copyright 2018 by Institute of Materials, Minerals and Mining and ASM International. Adapted with permission [1].

Low cycle fatigue behavior: Modern aviation gas turbine engines are thought to be exceedingly reliable and safe during operation and failures during flight or during take-off and landing are rare. This is due to stringent inspection regimes that occur before components are in service and at regular intervals during service. The most commonly rejected components are the blades in the compressor and turbine and the turbine vanes [37]. This is mostly due to the extreme environment that these components are placed in which can involve high temperature exposure, foreign object damage (FOD), creep damage, and repeated cyclic loading that results in catastrophic fatigue failure. Inspections normally occur every 2000 h of service with overhauls only every 5000 h, so the components must be able to withstand these conditions for long time frames without

concern [37]. If we consider a turbine rotating at the high speed of 35,000 rpm, any imbalance in the rotor can introduce 2.1×10^6 cycles per hour, resulting in 10^9 cycles in only 500 h which is well before the scheduled inspection. Additional small stress cycles can be introduced by the blades passing the vanes, which can introduce dangerous harmonics with rapid frequencies in the kHz regime [75, 76]. Typical engines will contain prime numbers of blades and vanes (e.g. 59 blades and 19 vanes) in order to reduce the number of available harmonics. While engines are designed to not excite these harmonics during operation, then can still be activated during start-up or shutdown, and can introduce stress cycles at a rate of 12.4×10^7 cycles per hour to the rotating blade and at a rate of 39.9×10^6 cycles per hour to the vanes [37]. Careful construction and balancing of the turbine engine has largely eliminated in service failure from very high cycle fatigue (VHCF) or high cycle fatigue (HCF) which can occur in these applied stress levels and frequency ranges.

Low cycle fatigue (LCF) damage however remains a significant issue. LCF failures are related to the large stress cycles imposed by the start-stop cycle of the turbine engine, and can roughly be approximated as a stress cycle being imposed per flight. While particularly problematic for polycrystalline turbine disks that may contain defects from the fabrication process, LCF is also a concern for turbine blades that experience high stresses and high temperatures. Notches at the attachment point between the blade and disk along with small cooling holes on the blade surface act as stress concentrators that accelerate the fatigue process locally [77]. A schematic of the temperature and stress combinations that a turbine blade experiences in service along with the associated forms of damage that can occur is presented in Fig. 1.12. Cracking is a concern across the entire blade, so research has sought to understand the response of single crystal Ni-base superalloys to cyclic loading at a variety of temperature and stress combinations. While the loading profile of a blade is complex, isotemperature fatigue tests are often

performed with a constant load amplitude or strain amplitude in order to reduce the complexity of the process. Thermomechanical fatigue tests where the temperature and stress vary in-phase or out-of-phase with each other are also performed to assess the fatigue performance and behavior of blade alloys.

Lifetime prediction under fatigue loading conditions is critical. This is normally done by phenomenological expressions such as the Coffin-Manson law. When the strain-range is carefully controlled and the plastic strain range is plotted against the fatigue life on a log-log plot, a straight line is found that can be fit with the following relationship,

$$N_f{}^{\beta}\Delta\epsilon_p = C_D \tag{1.4}$$

where N_f is the cycles to failure, $\Delta\epsilon_p$ is the plastic strain range, and β and C_D are materials constants for curve fitting. Since working with the total strain range, $\Delta\epsilon_t$, is often more convenient for engineering purposes, a correlation similar to the previous equation can be found by recognizing that $\Delta\epsilon_t$ can be rewritten as the sum of the elastic and plastic strain ranges by

$$\Delta\epsilon_t = C_D N_f^{-\beta} + C_E N_f^{-\alpha} \tag{1.5}$$

where the second set of quantities on the right-hand side represents the elastic strain component. Common values for β and α are 0.6 and 0.12 respectively [77]. While these equations indicate that it is the applied strain ranges that determine the fatigue lifetime behavior, these equations are material agnostic and do not provide a mechanism for fatigue damage or provide a deep understanding for the reasons behind the fatigue crack initiation, propagation, and failure processes.

Another useful phenomenological expression for fatigue crack life prediction is to

consider that at some location in the material there is some pre-existing flaw of length a that grows with each stress cycle until the fracture toughness of the alloy is reached. The Paris law describes the steady-state advancement of an initial flaw, da, per unit cycle, dN, as a function of the amplitude of the stress intensity factor around the flaw, ΔK [78]. This is written as

$$\frac{da}{dN} = C\Delta K^m, \text{ when } \Delta K_{th} < \Delta K < K_{Ic} \tag{1.6}$$

where C and m are once again material constants for curve fitting and $\Delta \mathrm{K}_{th}$ and $\Delta \mathrm{K}_{Ic}$ represent the threshold stress intensity range and the stress intensity range at the fracture toughness, respectively. If the initial flaw size, a_i, and final flaw size, a_f, are estimated, the above expression can be integrated from a_i to a_f to determine the cycles to failure that occur during this crack propagation process. Since the detection of cracks within the bulk of large components is difficult, conservative life predictions based on this principle are commonly used to avoid unexpected fatigue failures even though this likely underestimates the total usable fatigue of the component.

In the case of single crystal Ni-base superalloys, it is likely that there is no flaw present within the alloy that is large enough that the threshold stress intensity is exceeded, and therefore these materials spend most of their fatigue lifetimes in the crack initiation and small crack propagation stage as opposed to long-crack propagation that occurs in the steady-state Paris regime [79]. Microstructural inhomogeneities from the casting process such as solidification pores, γ-γ' eutectic regions, and large clusters of carbides are commonly the stress concentrations where damage accumulates and can result in crack initiation. This often results in the formation of a "fish-eye" that emanate from the internal crack initiation site and can be clearly observed on the fracture surface (Fig. 1.13). Precipitation-strengthened alloys can also form persistant slip bands (PSBs)

during cycling that result in extrusions and intrusions on the alloy surface where a stress concentration then develops [80]. PSBs are a result of cyclic slip irreversibility and normally develop in strain-control tests, for example in Waspaloy tested at T = 650 °C presented in Fig. 1.14.

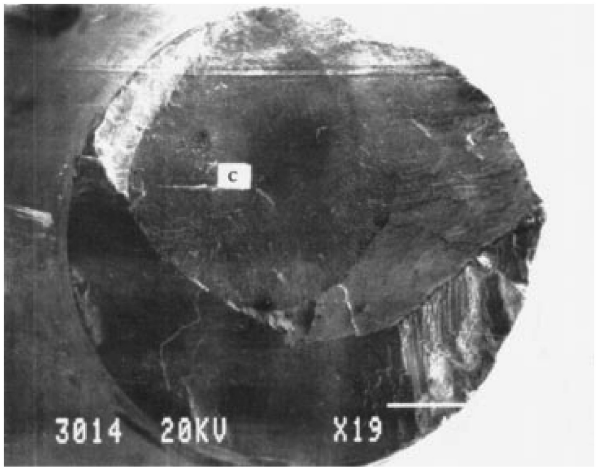

Figure 1.13: Low-frequency fatigue failure fracture surface of a CMSX-4 specimen tested under load control at T = 750 °C and a max stress of 820 MPa with R = 0. Reproduced from "Fatigue behaviour and lifing of two single crystal superalloys" by D. W. MacLachlan and D. M. Knowles, 2001, *Fatigue Fract. Engng. Mater. Struct.* **24**, p. 503-521. Copyright 2001 by John Wiley & Sons Ltd. Reproduced with permission [81].

Since fatigue resistance at elevated temperatures in aggressive environments is relevant to superalloys, the role of environmentally assisted fatigue crack initiation and growth from the alloy surface must be considered [77]. While Ni-base single crystal alloys typically have excellent oxidation behavior, there is normally a transition where fatigue crack initiation transitions from microstructural inhomogenieties (< 850 °C) to oxidation-assisted surface crack initiation (> 850 °C). In general, the formation of oxide-filled surface cracks form which produces a γ' denuded zone due to the depletion of Al to form Al-rich oxides around the crack tip, which weakens the alloy in this region. Subsequent cracking of the oxide scale can expose the underlying base metal to the environment once again, resulting in an accelerating fatigue crack growth behavior. This effect is offset

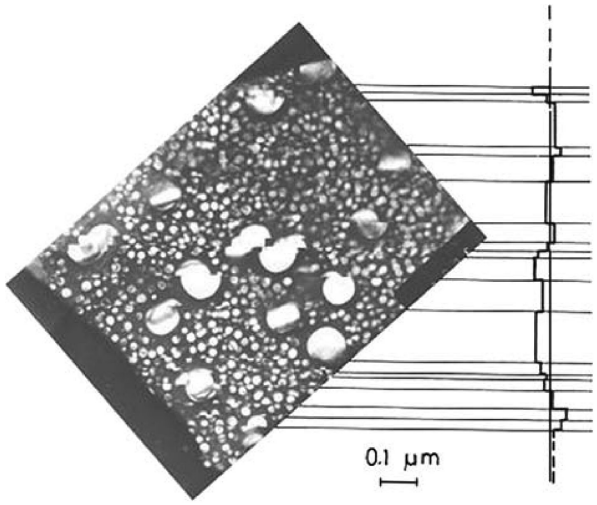

Figure 1.14: Planar-slip PSBs in Waspaloy fatigued until failure at axial plastic strain amplitude $\Delta\epsilon_{pl}/2 = 2 \times 10^{-3}$, $N_f = 550$ cycles, and T= 650 °C. Reproduced from "Cyclic Slip Irreversibilities and the Evolution of Fatigue Damage" by H. Mughrabi, 2009, *Metall. Mater. Trans. B* **40**, p. 431-453. Copyright 2009 by TMS and ASM International. Adapted with permission [80].

somewhat by oxide-induced crack closure where the oxide in the crack prevents perfect mating of the crack faces, effectively blunting the tip of the crack [82]. The effect of the environment is strongly linked to the applied cyclic test frequency and the R-ratio, with low frequencies and $R > 0$ resulting in long periods of time where crack faces are open and exposed to the oxidizing environment. An example of the effect of these test variables on the fatigue life of CMSX-4 tested in air is shown in Fig. 1.15. In particular, for the tests performed at 950 °C the samples loaded with a high cyclic frequency (100 Hz) had significantly longer fatigue lifetimes than those cycled at the lower frequency (0.25 Hz). Sustained peak low cycle fatigue (SPLCF) that includes the addition of compressive holds is also affected by oxidation that results in significant growth strains between the oxidizing crack tip and the surrounding γ' denuded alloy [83, 84].

Understanding the temperature range of the transition between surface crack initiation and internal crack initiation is important for designing processing pathways for single crystal alloys with improved fatigue properties. For example, casting processes

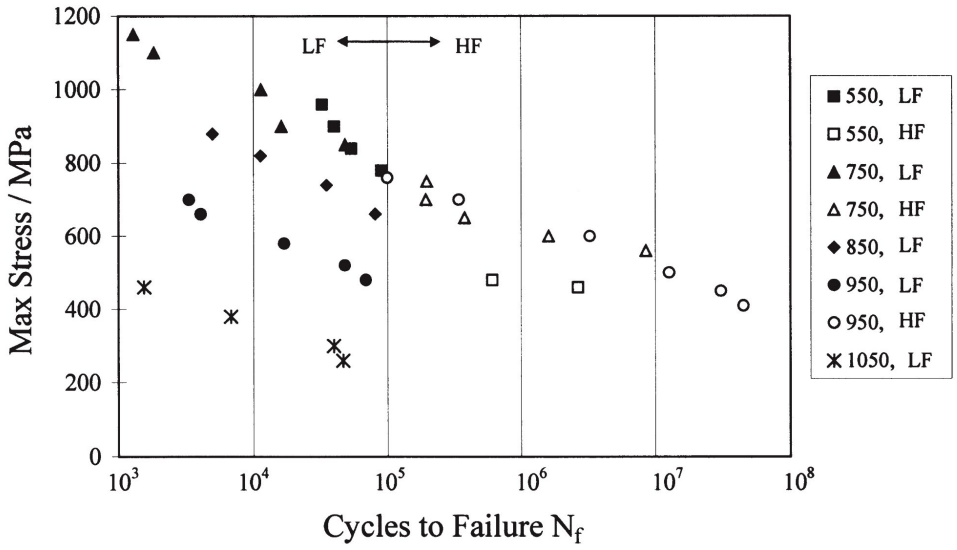

Figure 1.15: Load control, low-frequency and high-frequency data for CMSX-4 at an R-ratio of zero and a range of temperatures. Reproduced from "Fatigue behaviour and lifing of two single crystal superalloys" by D. W. MacLachlan and D. M. Knowles, 2001, *Fatigue Fract. Engng. Mater. Struct.* **24**, p. 503-521. Copyright 2001 by John Wiley & Sons Ltd. Reproduced with permission [81].

with elevated cooling rates such as liquid metal cooling (LMC) can produce fine dendritic structures with reduced solidification pore sizes, which reduces the intensity of the stress concentration around these defects and extends the fatigue lifetime [79]. This benefit to the fatigue life is lost at elevated temperatures when crack initiation from the surface once again becomes dominant. Fatigue testing in high vacuum recovers the improvement the fatigue life performance provided by LMC.

The response of novel γ'-strengthened Co- and CoNi-base single crystals to fatigue was unknown before publication of the data featured in Ch. 2 and 4, respectively. The results and conclusions in these chapters discuss this topic in depth, focusing on low cycle fatigue since this damage mode is a concern in the context of blade applications.

1.4 Additive manufacturing of metals and alloys

Metals-based additive manufacturing (AM), also known as three-dimensional (3D) printing, has grown dramatically over the past 35 years since researchers at the University of Texas at Austin first reported a technique for joining polymer powder in a layer-by-layer fashion with a laser heat source [85, 86]. The technique was soon applied to metals, with the first 3D-printed part, a spur gear, produced by Manriquez-Frayre and Bourell out of powder blends of Cu and 70Pb-30Sn solder [87]. There are now a variety of processes where an initial metallic powder feedstock, wire, or sheet are joined to fabricate a near-net shape component guided by a computer assisted design (CAD) file of the desired component. These techniques include, but are not limited to, powder-bed fusion (PBF) techniques such as selective laser melting (SLM) or electron-beam melting (EBM), direct energy deposition (DED) involving both powder and wire feedstocks, binder jetting, and ultrasonic additive manufacturing. These novel manufacturing techniques have resulted in enhanced design flexibility for engineers who seek to develop components with geometric complexity that would be costly or impossible to produce through conventional techniques such as casting, extrusion, forging, or machining.

AM has begun to experience wide-spread adoption in the aerospace, automotive, energy, consumer products, and medical industries [88]. One particularly strong motivator is that AM could lead to significant greenhouse gas emissions savings by reducing the weight of automobile and aircraft components. It is estimated that every 100 kg reduction in the weight of an airplane can save 13.4-20.0 TJ of jet fuel over the 30-year of an airplane [89]. AM can also lead to simplification of complex components enabling assemblies that used to consist of multiple parts to be reduced into one component, such as the 10-to-1 part reduction of the titanium locking shafts for the doors on the Airbus A350 [90]. AM can also lead to cost savings compared to other manufacturing techniques depending on

the complexity of the part and the part volume required [88]. Material costs can be further saved through powder recycling, which has been demonstrated in some cases to lead to minimal degradation of the final material properties even after 20+ powder reuse cycles in the case of EBM manufactured Ti-6Al-4V [91]. Fusion-based AM techniques such as SLM and EBM are also utilized for aerospace components since microstructural features such as grain structure and texture can be controlled through appropriate process parameter control [92]. Since these two techniques are used throughout this thesis for fabrication of CoNi-alloy specimens, a brief description of each technique is presented below along with key differences between the two techniques.

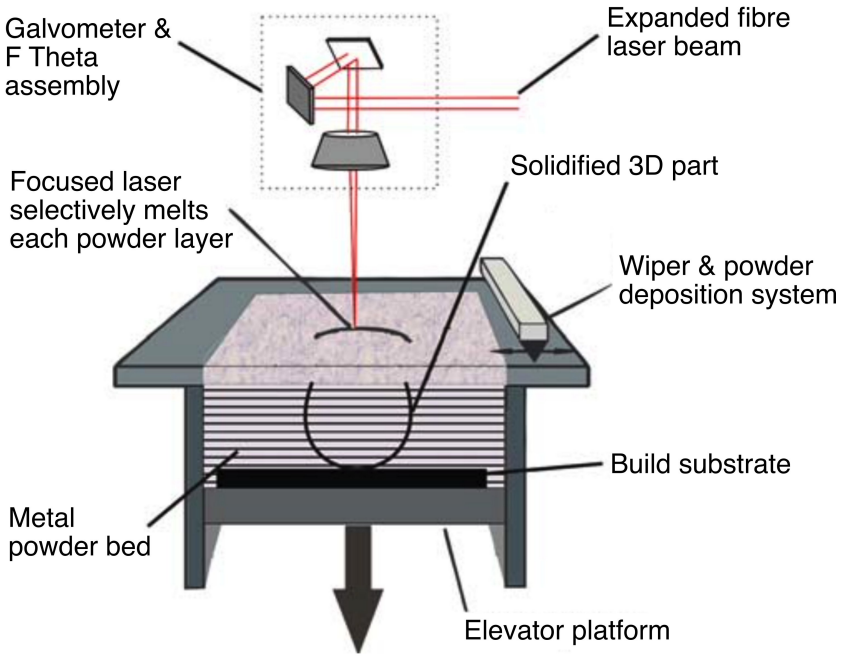

Figure 1.16: A schematic of a typical SLM build chamber. Adapted from "The development of a scanning strategy for the manufacture of porous biomaterials by selective laser melting" by R. Stamp et al., 2009, *J. Mater. Sci.-Mater. M.* **20**, p. 1839-1848. Copyright 2009 by Springer Science and Business Media, LLC. Adapted with permission [93].

The SLM process consists of a series of steps that takes a CAD file through fabrication. A simplified schematic of the SLM process within the build chamber is shown in Fig. 1.16.

Computer software such as Netfabb converts the CAD drawing into a series of layered build instructions which may include additional support structures. A thin layer of metal powder in the range of 20 to 100 µm is applied across a substrate plate in the build chamber by a wiper [94]. A high energy density laser is then used to locally melt and fuse the powder in specific locations according to the the processed data and selected scan settings. While early studies investigated both sintering and melting of metal powders, it is now common to control the laser power and scan speed to achieve complete melting of the metal powder feedstock and portions of the previous layer [95]. This laser is typically either a Nd^{3+}:YAG ($\lambda \approx 1.06$ µm) or Yb^{3+}:YAG ($\lambda \approx 1.03$ µm) fiber laser since metallic powders have high absorptance to radiation in the infrared region [94, 96]. The build platform is then lowered and the process repeated for successive layers until the final component is complete. Process parameter control is required to fabricate fully dense components free from lack-of-fusion defects and keyhole porosity. This can include laser scan speed, laser power, hatch spacing, and layer thickness. The build chamber is usually filled with an inert gas such as nitrogen or argon to minimize oxidation of the alloy powder, especially since pre-heated build platforms that can reduce the thermal stresses of the part are common. A pre-heat temperature of 200 °C is common, although the some systems such as the AconityMINI installed at UC-Santa Barbara have the option of reaching 800 °C for smaller area builds. Loose powder around the built component is removed and often recycled, and samples are removed from the build plate manually or through electric discharge machining (EDM). Some surface finishing may be required depending on the part application and the use of sacrificial support structures.

EBM was first commercialized in 1997 by ARCAM AB Corp. in Sweden, and they are currently the only company that manufactures and sells EBM machines. EBM resembles SLM in many ways except that an electron beam is used to locally melt and join metal powder. This has specific advantages and disadvantages compared to a laser-

based process. The electron beam can be focused and moved by electromagnetic lenses, allowing beam velocities up to 10^5 m/s which effectively allows for instantaneous jumps from point to point [97]. Therefore, innovative heating and melting strategies can be employed. Fig. 1.17 shows how a defocused beam can pre-heat to powder to high temperatures above 1000 °C before melting of each layer. Melting can be performed using conventional raster strategies or through quasi-multi-beam techniques. The application of high pre-heat temperatures promotes an in-situ heat treatment to EBM processed alloys, where different locations along the build height have varying thermal histories. An example of this in-situ heat treatment is shown in Fig. 1.18. This can promote solutioning of as-printed segregation, solid-state transformations between phases, and precipitation and coarsening of precipitates. Charging of the powder layer by the electron beam is a concern, which can result in "smoking" events that disrupt the build process. This restricts EBM to conductive materials such as metals and alloys and requires the use of vacuum (10^{-4}-10^{-5} mbar) and a small pressure of helium (10^{-3} mbar) to prevent electrostatic charging [97].

.

1.5 Considerations for AM of superalloys

Metals-based AM has been applied successfully to several technologically important alloy classes including stainless steels, titanium alloys, CoCrMo alloys, TiAl intermetallics, and Ni-base superalloys such as IN625 and IN718. Many of the alloys that have been found to be compatible with the extreme thermal conditions present in fusion-based AM are also known for their good weldability, which agrees with the concept that AM is effectively a repetitive multi-pass micro-welding process [98]. High γ'-volume fraction superalloys are highly desirable candidates for AM due to their excellent high

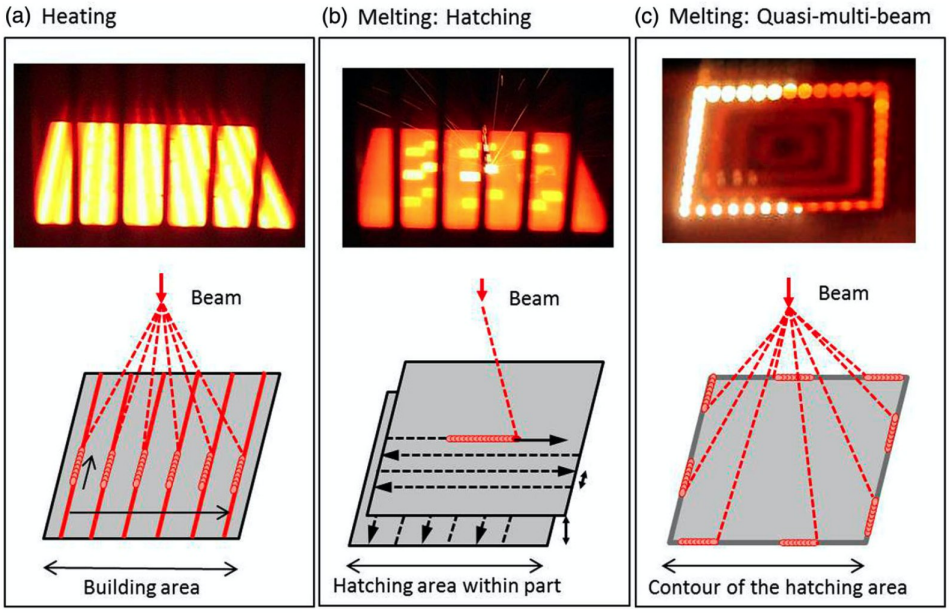

Figure 1.17: Heating and melting during EBM. Top: photographs during the process. Bottom: schematics of the beam movement. (a) Heating by quasi-multi-beam scanning of the total building area with a defocused beam, (b) melting by hatching, and (c) Quasi-multi-beam contour melting by jumping from point to point. Reproduced from "Additive manufacturing of metallic components by selective electron beam melting - A review" by C. Körner, 2016, *Int. Mater. Rev.* **61**, p. 361-377. Copyright 2016 by University Erlangen-Nürnberg [97].

temperature properties, but they unfortunately possess several characteristics that often result in large amounts of defects in the as-printed state, most notably active hot cracking mechanisms such as solidification cracking, liquation cracking, strain-age cracking, and ductility-dip cracking [99]. These phenomena are related to the rapid formation of the γ' rapidly during cooling from the solid-state, which strengthens the solidified material. γ' forming alloying additions also have a strong impact on the partitioning behavior between the solid and the liquid with γ' formers typically partitioning to the liquid and γ formers partioning to the solid. Strong solute enrichment of the liquid during solidification is also observed in precipitation-strengthened alloy classes such as aluminum alloys like AL7075 [100]. Solute partitioning during solidification is often associated with the formation of deep, solute-enriched liquid films that persist to low temperatures between high angle

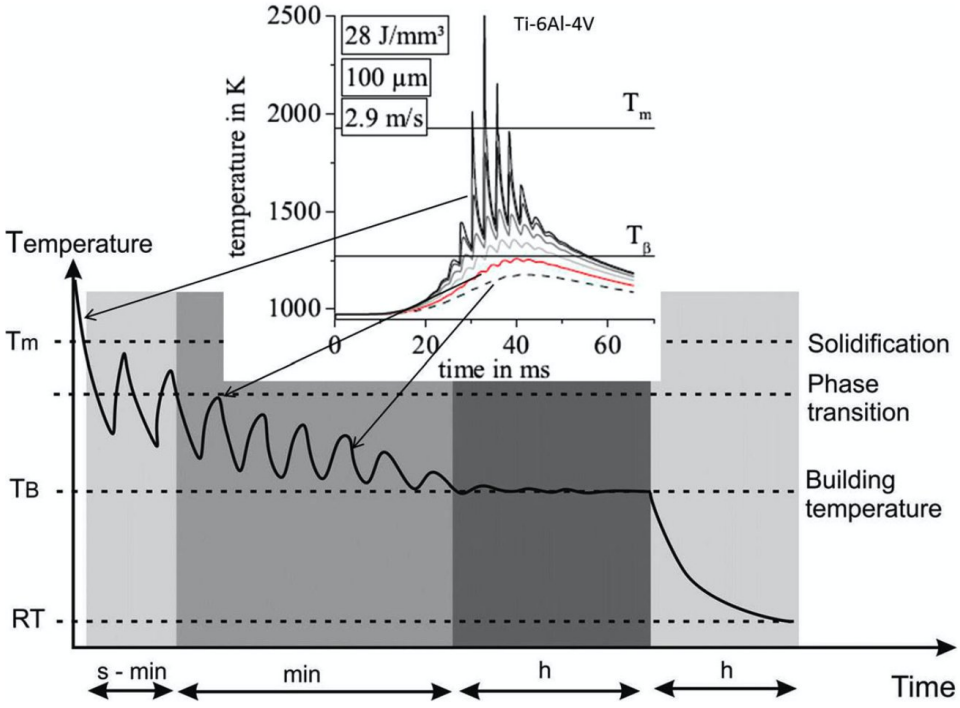

Figure 1.18: In-situ heat treatment during EBM. Schematic of the temperature evolution at a fixed point of the component where the beam passes several times in each layer. A simulated temperature evolution at different depths (in steps of 100 µm) for Ti–6Al–4V is shown to visualise the time scale of temperature variation near the surface during and after melting. Reproduced from "Additive manufacturing of metallic components by selective electron beam melting - A review" by C. Körner, 2016, *Int. Mater. Rev.* **61**, p. 361-377. Copyright 2016 by University Erlangen-Nürnberg [97].

grain boundaries, upon which thermal stresses induced by solidification shrinkage can act to form and propagate cracks [99, 101]. The weldability debit for high γ' volume fraction superalloys can be visualized with the use of Prager-Shira diagrams (Fig. 1.19) from the welding literature which show that Ni-base superalloys with increasing amounts of γ' formers such as Al and Ti experience increasingly worse susceptibility to these hot cracking mechanisms [102].

Several strategies have been employed in high γ' volume fraction Ni-base superalloys to overcome this cracking susceptibility, with several studies producing alloys with significantly reduced crack densities. Careful control of process parameters like scan speed and

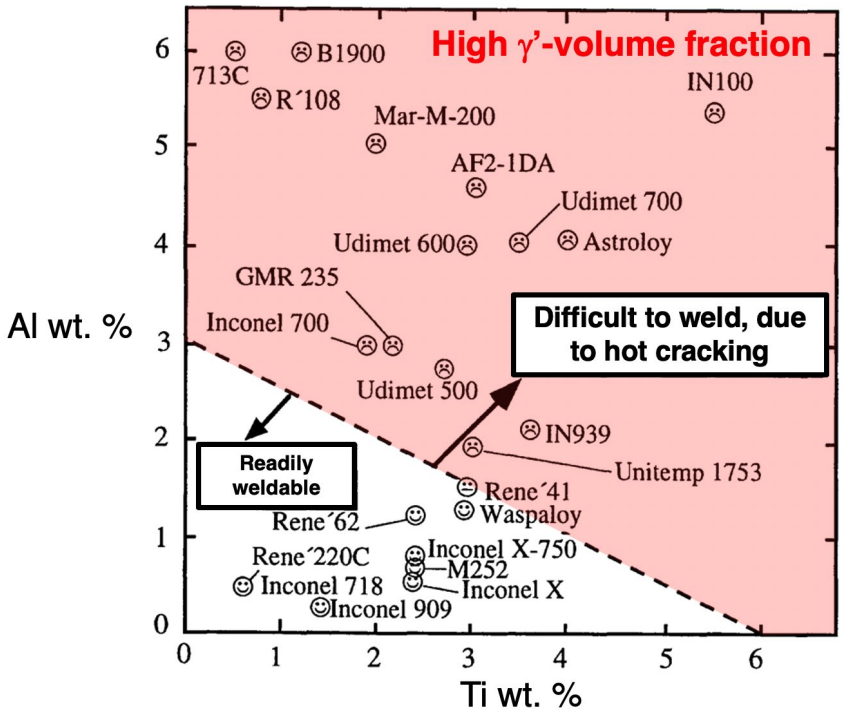

Figure 1.19: Prager-Shira diagram showing weldability as a function of Al vs. Ti content of several Ni-base superalloys. Adapted from "Progress in joining of advanced materials" by G. Çam and M. Koçak, 1998, *Int. Mater. Rev.* **43**, p. 1-44. Copyright 1998 by Taylor and Francis. Adapted with permission [102].

beam power along with high pre-heat temperatures above 1000 °C that are possible in EBM can produce fully-dense samples of 2nd-generation blade alloy CMSX-4 [103]. These alloys have fine columnar grains that grow epitaxially from previous layers with a strong ⟨001⟩ grain texture aligned with the build direction. Extensive design of experiment (DOE) searches are needed to locate the combinations of these three process parameters that produce alloys with the least amount of lack-of-fusion defects, hot cracks, and porosity, often revealing that these superalloys have smaller processing windows compared to more weldable alloys such as IN718 [98]. Similar DOE studies on CMSX-4 using SLM were able to reduce process induced cracking and porosity, but the elimination of hot cracks that formed during printing was not successful [104]. The excellent beam control and preheat in EBM can be tuned to produce specimens with a single crystalline core

that is surrounded by a couple mm thick polycrystalline shell [103, 105, 106, 107]. After appropriate solution and aging heat treatment, creep tests on the extracted single crystalline cores have demonstrated that AM produced CMSX-4 single crystals have excellent creep rupture life [108]. This is likely due to the excellent chemical homogeneity in the alloy after heat treatment due to the fine-scale segregation produced by EBM compared to the Bridgman single crystal growth process [105]. This technique has also been successfully applied to produce single crystals of alloys such as Nimonic 105, Haynes 282, IN738, and MarM-247 (although this alloy exhibited significant cracking, as expected), and these alloys would likely possess good creep properties without the need for traditional single crystal casting [109]. However, single crystals produced by EBM have only been demonstrated to be grown as bars with dimensions less than 1.5 cm $\times$ 1.5 cm in the XY-plane and it is unclear whether these process parameters can produce components with complex thin-walled geometries (such as turbine blades) and sufficiently control the local thermal conditions and meltpool geometry necessary for single crystalline growth.

A mechanism-driven approach through grain-boundary engineering has been suggested by Kontis et al. in 2019 where control of the grain boundary density and grain morphology are leveraged to reducing cracking susceptibility [101]. Modifications of process parameters in EBM can promote either equiaxed grain structures or fine-grained columnar grain structures that more evenly distribute highly segregating elements such as B, Cr, and Mo and distributes the thermal stresses formed during AM over more grain boundary interfaces. When columnar grain widths are widen along the height of the build (>100 µm), cracking begins to appear at sample heights above 12 mm. Interestingly, hot cracks are demonstrated to propagate along high angle grain boundaries aligned with the build direction while low angle grain boundaries appear to be more immune [99].

The bridging and coalescence of dendrite arms can be rationalized by the theoretical models of Rappaz that describe the last stages of solidification and attempt to describe the

temperatures at which a coherent solid forms, i.e. a solid that can sustain tensile stresses [110]. Grain boundaries during solidification can be described as either "attractive" or "repulsive" depending on the magnitudes of the grain boundary energy, γ_{gb}, and the solid-liquid interfacial energy, γ_{sl}. For pure metals, two approaching planar solid-liquid interfaces coalesce into a grain boundary at a critical undercooling, ΔT_b, given by

$$\Delta T_b = \frac{\gamma_{gb} - 2\gamma_{sl}}{\Delta s_f} \left(\frac{1}{\delta}\right) \tag{1.7}$$

where δ is the thickness of the solid-liquid interface and Δs_f is the entropy of fusion [110]. If $\gamma_{gb} < 2\gamma_{sl}$, then $\Delta T_b < 0$ and the liquid film is unstable. Coalescence will occur as soon as the interfaces get close enough (a distance on the order of δ which can be $\approx$1 nm) and is typical of dendrite arms belonging to the same grain. When $\gamma_{gb} > 2\gamma_{sl}$, as is likely the case for high angle grain boundaries with misorientations greater than 15°, liquid films remain stable to lower temperatures and coalescence is delayed. This is further affected by solute-enrichment in the liquid that occurs in highly alloyed Ni-base superalloys. In summation, these processes produce deep, liquid channels between solidifying dendrite arms that are difficult to feed additional liquid into that can offset the shrinkage that occurs during solidification and cooling. Tensile stresses acting upon these regions can produce a void or crack as shown by the hot-tearing criterion of Rappaz, Drezet, and Gremaud (RDG) and by S. Kou in their modified cracking criterions [111, 112].

Due to the incompatibility of commercial high γ' volume fraction Ni-base superalloys with fusion-based additive processes, it is a question whether alloy modification is an appropriate route to develop high temperature materials for AM. As mentioned previously, the compositional designs of blade alloys have historically been adjusted and modified to take advantage of new processing pathways such as directional solidification and Bridgman single crystal casting. One strategy has been to carry out alloying modifications

	Main alloying elements [wt%]												Residual elements [wt%]		
	Ni	Cr[a]	Co[a]	Mo[a]	W[a]	Ta[a]	Al[a]	Ti[a]	Nb	C	B	Zr	Si	Fe	Cu
Min.	Balance	15.7	8.0	1.5	2.4	1.5	3.2	3.2	0.6	0.09	0.007	0.02	–	–	–
Max.		16.3	9.0	2.0	2.8	2.0	3.7	3.7	1.1	0.13	0.012	0.08	0.3	0.05	–
A		15.8	8.6	1.7	2.6	1.7	3.5	3.3	0.80	0.096	0.011	0.060	0.085	0.06	0.011
B		16.1	8.5	1.7	2.6	1.8	3.5	3.4	0.85	0.097	0.010	0.065	0.064	0.08	0.012
C		16.1	8.8	1.8	2.4	2.9	3.5	3.5	0.75	0.130	0.012	0.652	0.105	0.11	0.611
D		15.9	8.4	1.8	2.6	2.0	3.4	3.5	0.80	0.110	0.013	0.041	0.030	0.06	0.164
E		16.2	8.6	1.8	2.7	1.7	3.5	3.3	0.80	0.140	0.015	0.023	0.034	0.82	0.099
F		16.1	8.4	1.7	2.7	1.7	3.5	3.7	0.80	0.140	0.012	0.056	0.212	0.13	0.004
G		16.0	8.6	1.6	2.8	1.8	3.5	3.4	0.90	0.120	0.009	0.011	0.026	0.15	0.001
H		15.9	8.3	1.8	2.6	1.9	3.5	3.3	0.80	0.096	0.014	0.032	0.018	0.09	0.004

[a] values according the suppliers material certificate.

	Trace elements [ppm]													Gas content [ppm]		
	S	Mn	Hf	P	Ag	Bi	Se	Te	Tl	Pb	Ga	Mg	Sn	O_2	N_2	H
A	6	17	50	42	4.5	2.0	32	1.0	4.1	2.4	15.9	26	4.0	300	36	8
B	7	22	53	<3	3.4	1.3	8	2.8	2.6	3.8	15.0	30	3.8	160	8	10
C	46	121	3	<3	7.2	1.1	15	0.7	0.1	7.4	11.9	23	6.2	320	12	8
D	4	18	89	<9	1.4	0.7	25	0.2	2.3	1.9	6.6	40	1.8	290	17	8
E	5	101	4	<9	1.0	0.6	24	0.6	2.6	2.1	12.0	23	85.7	400	19	8
F	6	18	0	<9	1.3	0.5	31	0.8	2.5	22.5	17.1	30	10.1	1000	78	30
G	7	67	331	32	0.4	0.1	30	0.3	1.8	0.9	10.8	13	1.9	190	15	5
H	<4	147	92	<9	10.7	0.2	27	<0.1	2.6	0.2	5.4	34	4.5	360	11	9

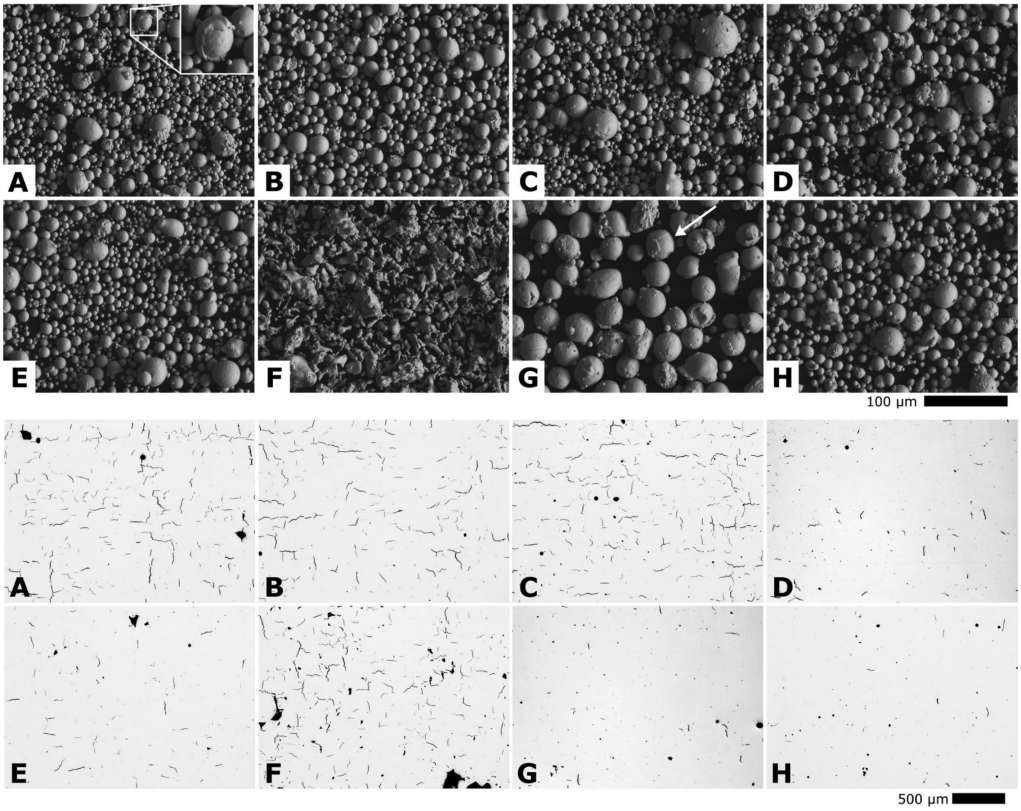

Figure 1.20: An overview of alloy chemistry and microcracking susceptibility of IN738LC with varying minor element contents. Adapted from "Processability of different IN738LC powder batches by selective laser melting" by R. Engeli, T. Etter, S. Hövel, and K. Wegener, 1998, *J. Mater. Process. Tech.* **229**, p. 484-491. Copyright 2016 by ALSTOM Technologie AG. Adapted with permission [113].

that are within the pre-existing alloy specifications such that alloy recertifications are largely avoided. This has been demonstrated to be somewhat successful for Hastelloy X in SLM where reductions of tramp elements such as O, N, Cu, Pd and P combined with increases to solid-solution strengthening elements such as Cr, Mo, and W resulted in a 65% reduction in crack density compared to unmodified Hastelloy X [114]. Control of tramp and minor elements in particular can have a strong impact on printability, which motivates the need for strict powder quality control for AM. Engeli et al. investigated the printability of high γ' volume fraction IN738LC in SLM where multiple alloy powders were acquired from eight different powder suppliers and the print parameters were kept constant [113]. A summary of the alloy chemistries and the printing results are displayed in Fig. 1.20. All of the powders had spherical morphologies, except for powder F which was water atomized. While all of the alloys experience some degree of microcracking, a few of the alloys such as alloys D, G, and H had significantly reduced amounts of microcracking. Regression analysis of the tramp element concentrations and the measured crack densities revealed that several elements such as Si, Ga, and Pb were most correlated with increased crack density. The fourth largest contributing factor was the combined Al+Ti concentration, agreeing well with the previous Prager-Shira diagrams. The powder characteristics also played a role in the amount of residual porosity after printing, with insufficient flow behavior and low apparent density resulted in poor powder recoating in each layer and increased porosity. Engeli et al. claim that through appropriate powder quality and compositional control, it is possible to fabricate crack-free parts of SLM IN738LC [115].

An additional research thrust is to develop novel superalloys for additive that are initially designed with the additive process in mind. Tang et al. presents an "alloys-by-design" approach that consists of combined computational predictions and experimental validations to develop Ni-base superalloys with improved 3D printability [116]. The

search space consisted of Ni-Cr-Co-Al-Ti-Nb-Ta-W-Mo alloys where a 0.1 at.% resolution resulted in over 10^7 trial alloy compositions. For each composition, the freezing range was estimated by a Scheil analysis assuming no back-diffusion (i.e. no diffusion in the solid and infinite diffusion in the liquid), an estimate of the strain-age cracking susceptibility (described as a weighted sum of γ'-forming alloy content in of Al + 0.5Ti + 0.3Nb + 0.15Ta in wt.%), the mole fraction of γ' at 900 °C, and the estimated 1000 h creep life at 137 MPa. By setting limits for the freezing range and strain-age cracking merit index, a Pareto front was developed upon which trial alloys were selected for atomization and fabrication through SLM. Two early alloys named ABD-850AM and a higher γ' forming alloy called ABD-900AM were developed and printed. These alloys possess an excellent resistance to both cracking in the solidfying state and cracking in the solid state, as demonstrated by comparisons to the cracking observed in high γ' volume fraction alloy CM247LC and medium γ' volume fraction alloy IN939. The ABD alloys also show attractive combinations of ductility and strength at high temperatures. However, the compositional tuning that was performed to enhance the printability of these alloys also results in a suppressed γ' solvus temperature of 1025 °C for ABD-850AM (compared to 1250 °C for CM247LC measured in their study) and a reduced γ' volume fraction of 20-30%. Therefore, for the intense temperature and stress combinations experienced by blade alloys, it is likely that these alloys would not be suitable in their creep performance for these conditions. Despite these differences in the final alloy design compared to existing single crystal blade alloys, the consideration of the cracking risks in the solidifying and full-solid state into the design process allowed for the creation of novel alloys that were readily printable and exhibited promising mechanical properties.

In this thesis, we will consider the high γ' volume fraction CoNi-base superalloys described in Ch. 1.2 for processing through AM. Similar to commonly used blade alloys, CoNi-base superalloys can have a two-phase γ-γ' microstructure after appropriate heat

treatments and have been demonstrated to have more favorable solidification characteristics compared to their Ni-base counterparts. This could result in a reduced hot cracking susceptibility by reducing the extent of liquid films between solidifying dendrite arms. Additionally, these alloys tend to have reduced γ' solvus temperatures while maintaining sufficiently high solidus temperatures, which results in a wider processing window between the γ' solvus and the solidus temperature where the alloy is single-phase γ. This may delay the impact of strain-age cracking by reducing the rapid γ' formation at short-times after solidification. Since the yield strengths are often reduced in this class of alloys compared to Ni-base superalloys, this also may allow for greater relaxation of thermal stresses during the printing process if γ' does form. The design of a CoNi-alloy with elevated γ' solvus, promising oxidation response, and low density is presented in Ch. 3. The printability of this CoNi-base superalloy by both SLM and EBM, the two most widely used fusion-based AM techniques, is demonstrated in Ch. 5 and investigations of the microstructure evolution and high temperature tensile behavior is presented in Ch. 6. This demonstrates that CoNi-base alloys are promising candidates for further development and are amenable to fusion-based AM processes.

Chapter 2

Low cycle fatigue of Co-base superalloys[†]

In this chapter, the low cycle fatigue response of model Co-base superalloys coated with a CoNiCrAlY coating are assessed in load-control at 750 °C. Fracture surface imaging and cross-sections of the post-mortem specimens reveal the presence of oxidized surface cracks that are responsible for surface crack initiation, even with the assistance of a coating. TEM investigations near the tip of an oxidized surface crack identify the oxides and metallic phases that formed during fatigue testing. This work demonstrates that improving the oxidation response of this class of alloys will be essential to improve their mechanical properties at elevated temperatures and motivates the alloy design study in the subsequent Ch. 3.

[†]Significant portions of this chapter are reproduced from the following article: S.P. Murray, J.-C. Stinville, P.G. Callahan, R.K. Rhein, and T.M. Pollock, Low Cycle Fatigue of Single Crystal γ'-containing Co-based Superalloys at 750 °C. *Metall. Mater. Trans. A* **51** (2020) 200–213. [**doi**] [117]

2.1 Introduction

Single crystal Ni-based superalloys are designed to have favorable oxidation behavior, enabled by the formation of a passivating layer of α-Al_2O_3 upon high temperature exposure to air. This oxide scale significantly impedes the ingress of oxygen and provides resistance to surface crack initiation during high temperature cyclic loading. The solidification process employed for production of single crystal alloys introduces µm-scale shrinkage pores at the scale of the secondary dendrite arm spacing [118]. Such microstructural inhomogeneities behave as stress concentrations and can promote strain localization and subsequent crack initiation during cyclic loading. Since these features are typically <100 µm in diameter, their associated stress intensity factors are normally below the threshold cyclic stress intensity necessary for crack propagation [82, 118]. For this reason, a significant portion of fatigue life for single crystal superalloys is spent in crack initiation, as opposed to propagation.

Improvements in materials for turbine applications are motivated by increasing turbine engine temperatures, which results in a thermodynamically more efficient engine cycle [2]. However, as the temperatures experienced by Ni-based superalloy components approaches their solidus temperatures, novel materials with elevated melting temperatures are desired for future engine designs. γ'-containing Co-based superalloys have been explored as a promising class of alloys for high temperature load-bearing applications. These alloys possess a morphologically identical microstructure to Ni-based superalloys while exhibiting solidus temperatures up to 100 °C greater [23]. Due to favorable solute partitioning during solidification, these alloys are amenable to single crystal casting by conventional methods [51]. The mechanical properties of these alloys have been studied with respect to high temperature strength [24, 25, 119], creep behavior [62, 64, 120], and elastic response [121]. However, limited studies have been performed to investigate the

response of γ'-containing Co-based superalloys to high temperature cyclic loading.

Strain-controlled low cycle fatigue tests at 750 °C performed by Freund et al. have demonstrated that polycrystalline CoNi-based superalloys have a fatigue response that is comparable to conventional Ni-based polycrystalline cast-and-wrought alloys [122]. This promising result motivates the investigation of other classes of Co-based superalloys. The goal of this study is to evaluate the low cycle fatigue response of single crystal Co-based superalloys at 750 °C in air. By identifying the mechanisms that promote fatigue failures at elevated temperatures, alloying strategies for improved fatigue resistance will be discussed.

2.2 Methods

2.2.1 Materials

The quinary alloys for this study were based upon the ternary Co-Al-W system and were denoted as TiNb and TaNb due to the 1-2 at.% additions of these elements, respectively. The alloy compositions were measured by direct current plasma atomic emission spectroscopy (DCP-AES) and are presented in Table 2.1. Single crystal bars of these alloys were cast using the Bridgman method with an ALD single crystal growth system. The casting molds were preheated to 1575 °C and withdrawn from the hot zone at a rate of 3.4 mm/min. Homogenizing heat treatments at 1340 and 1315 °C for 24 h were performed under vacuum on the TaNb and TiNb alloys, respectively. An aging heat treatment of 900 °C for 24 h was applied to coarsen the γ' precipitates. The γ'-solvus temperatures of the heat-treated alloys were measured with differential thermal analysis (DTA) using a Setaram Setsys 16/18 at a heating rate of 5 K min^{-1} under flowing Ar. The DTA was calibrated with Sn, Ag, Au, Ni, and Pd of at least 99.99% or greater

purity to ensure accurate measurements at elevated temperatures. Additional details on the single crystal alloys used in this study are reported in a previous publication [123].

Table 2.1: Compositions of Alloys and Coating (at.%, DCP-AES for alloys, EPMA for coating)

Alloy	Co	Ni	Al	W	Ti	Ta	Nb	Cr	Y	γ'-solvus	Solidus
TiNb	79.0	-	10.0	8.4	1.4	-	1.2	-	-	1087 °C	1362 °C
TaNb	79.8	-	10.3	7.9	-	1.1	0.9	-	-	1074 °C	1370 °C
Coating	32.7	28.5	20.0	-	-	-	-	18.7	0.1	-	-

Figure 2.1: A CoNiCrAlY coated single crystal Co-base superalloy before low cycle fatigue testing.

Cylindrical dogbone-shaped specimens with a 5 mm wide gauge diameter were machined from the single crystal bars using low stress grinding. A CoNiCrAlY coating was applied to the gauge sections of all specimens through a plasma spray process. An example of a coated dogbone is presented in Fig. 2.1. This coating was applied to inhibit extensive surface oxidation during high temperature testing that could have resulted in significant loss of cross-sectional area in the gauge section. The surface of the specimens were grit-blasted in order to improve the adherence of the protective coating and a 2 h anneal was performed at 1121 °C after the coatings were applied. This annealing temperature was above the γ'-solvus for both alloys considered in this study, and therefore the morphology and size of the γ'-precipitates within the superalloys are a result of cooling from this final heat treatment. A backscattered electron (BSE) micrograph of the two-phase $\gamma + \beta$ coating prior to fatigue testing is shown in Fig. 2.2. The average

thicknesses of the coatings were measured from cross-sections to be 106 ± 6 µm and 157 ± 9 µm for the TiNb and TaNb specimens, respectively. The composition of the coating is presented in Table 2.1 and was assessed by electron probe microanalysis (EPMA) on a Cameca model SX100 containing five wavelength-dispersive spectrometers and a CeB_6 thermionic filament. W-rich and Al-rich interfacial phases between the superalloy substrate and coating were observed before fatigue testing, and likely formed during application and processing of the coating. The pre-fatigue superalloy microstructures are shown in Fig. 2.3. The presence of an Al-rich β-phase in the superalloy substrate on the order of 5 vol.% was observed in both alloy compositions before fatigue testing along with a trace amount of a W-rich phase in the TaNb alloy. The volume fractions of the γ'-precipitates were measured by applying the Yen threshold along with a despeckle filter in Fiji to BSE images taken in regions far from any β-phase precipitates [124, 125]. The γ' volume fractions were measured in these regions to be 79% and 77% for the TiNb and TaNb alloys, respectively.

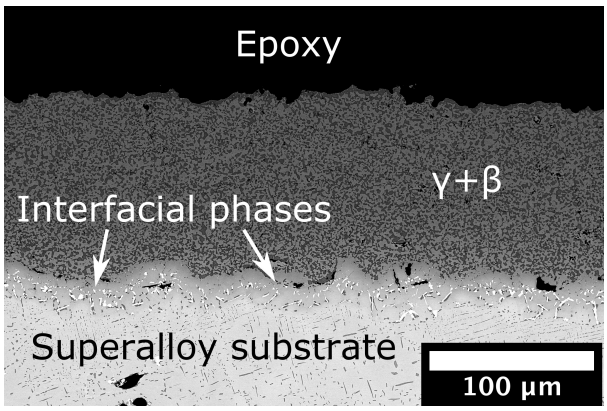

Figure 2.2: BSE micrograph showing the CoNiCrAlY coating applied to a TiNb specimen before fatigue testing. The coating consists of a two-phase $\gamma + \beta$ microstructure and the formation of interfacial phases between the coating and substrate are observed.

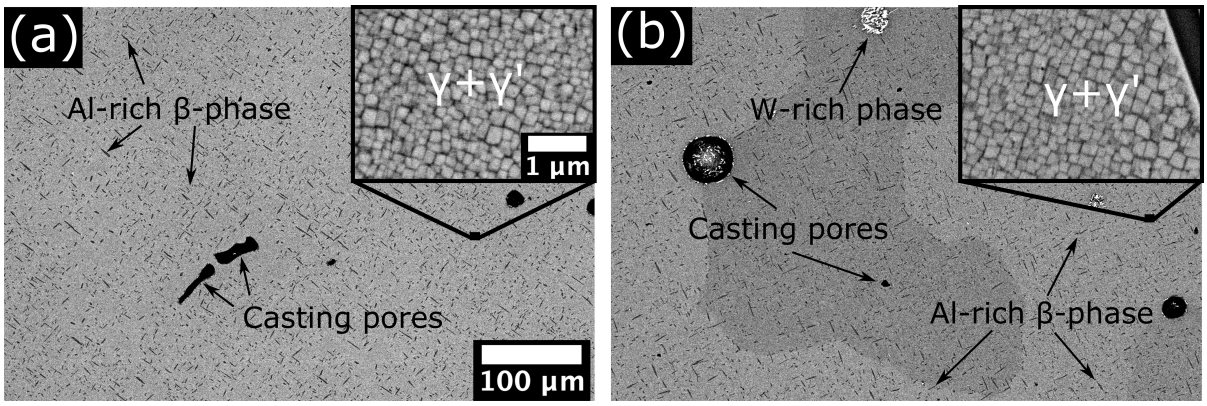

Figure 2.3: BSE micrographs of the starting microstructures for the (a) TiNb and (b) TaNb specimens. Inset micrographs display the fine cuboidal γ-γ' microstructure.

2.2.2 Fatigue testing procedure

Fatigue testing was performed in an MTS hydraulic test frame with a 100 kN load cell. An Ambrell induction heating system with a custom-built water-cooled copper heating coil heated the specimens during testing. The test temperature was maintained by a Eurotherm 2404 Controller combined with a Micro-Epsilon two-color pyrometer that measured the specimen surface temperature in the center of the gauge section. Temperature fluctuations of ± 2 °C were observed during testing. The loading sequence was controlled by an MTS 458.20 MicroConsole. Cyclic strains were measured with a ceramic tipped extensometer centered on the gauge.

Load-controlled fatigue tests were performed isothermally at 750 °C in laboratory air with R = 0.1, (where $R = \sigma_{min}/\sigma_{max}$). The use of a small, non-zero R-ratio prevented sample slippage in the grips during cycling. Loading was applied with a triangular waveform at a frequency of $f = 0.5$ Hz. Maximum stresses in the loading cycle were at or above the elastic limits of the specimens in order to induce failure in the low cycle regime (10^5 to 10^6 load cycles). Samples that survived for more than one week (i.e. ~300,000 cycles) were interrupted and labelled as run-outs. Upon rupture, induction heating was automatically shut-off and the specimens were held in the water-cooled grips

until they returned to room temperature. An interrupted test was also performed at a fraction of the fatigue life in order to investigate the development of fatal cracks. For this test, the loading program was halted followed by shut-down of the induction coil, allowing the sample to cool while remaining in the water-cooled grips under minimal external load.

2.2.3 Characterization

Ruptured specimens had their fracture surfaces investigated and were subsequently cross-sectioned longitudinally by electrical discharge machining (EDM) through locations near the initiation sites. These cross-sections were hot mounted in Epomet, ground down to 1200 grit SiC paper, and then polished to a 0.05 µm finish using a colloidal alumina suspension in a Vibromet polisher. Optical microscopy was performed using a Keyence VHX-5000 digital microscope. 2D-stitching enabled imaging of the entire mounted cross-sections and 3D-stitching was used to create high-resolution images of the entire fracture surface in focus. Scanning electron microscopy (SEM) observations were made using a FEI Nova NanoSEM 650 with a Schottky field emission gun operated between 10-30 kV. Additional microscopy and energy dispersive x-ray spectroscopy (EDX) was performed using a Thermo Scientific Apreo C SEM equipped with a Schottky field emission gun and a Si-drift EDX detector. Secondary electron (SE) images and BSE images were collected during characterization.

For transmission electron microscopy (TEM) observations, specimens were prepared by two methods: (1) 300 µm thick slices of the fatigue specimens were taken perpendicular to the loading direction using EDM, manually ground to a thickness of ~100 µm, and finished with 1200 grit SiC paper. Subsequently, 3 mm diameter discs were punched from these slices and thinned in a Fischione twin-jet electropolisher using a

92.5 vol.% methanol-7.5 vol.% perchloric acid electrolyte. Jet polishing was performed at temperatures between -50 to -40 °C with voltages of 16-28 V and currents of 20-28 mA. (2) Additionally, electron transparent lamella were extracted from cross-sectioned fatigue specimens with the focused ion-beam (FIB) lift-out method using a FEI Helios NanoLab DualBeam. Final thinning was performed with Ga^+ beam settings at 5 kV and 16 pA. The jet-polished foils were observed at 200 kV using transmission electron microscopy (TEM) with an FEI Tecnai G2 Sphera equipped with a LaB_6 thermionic filament. Scanning transmission electron microscopy (STEM) EDX mapping was performed at 200 kV using a Thermo Scientific Talos equipped with a Super-X detector system and an extreme field emission gun. Standardless quantification of the collected EDX spectra was performed using the Cliff-Lorimer ratio method within the Velox software package. STEM-EDX results are presented in terms of at.% where 0 at.% is black and 100 at.% is white. High angle annular dark field (HAADF) images were also collected at the regions used for chemical mapping. Similar to the contrast observed in BSE images, the contrast present in HAADF-STEM micrographs are sensitive to atomic mass (Z), resulting in brighter regions of the images containing heavier elements. This contrast is referred to as Z-contrast throughout the text to distinguish between various regions of the observed oxide scales.

2.3 Results

2.3.1 Fatigue Experiments

A summary of the applied test conditions and fatigue lifetime results for the alloys studied are presented in Table 2.2. These results are compared to similar load-controlled tests performed by MacLachlan and Knowles on the 2^{nd}-generation single crystal Ni-

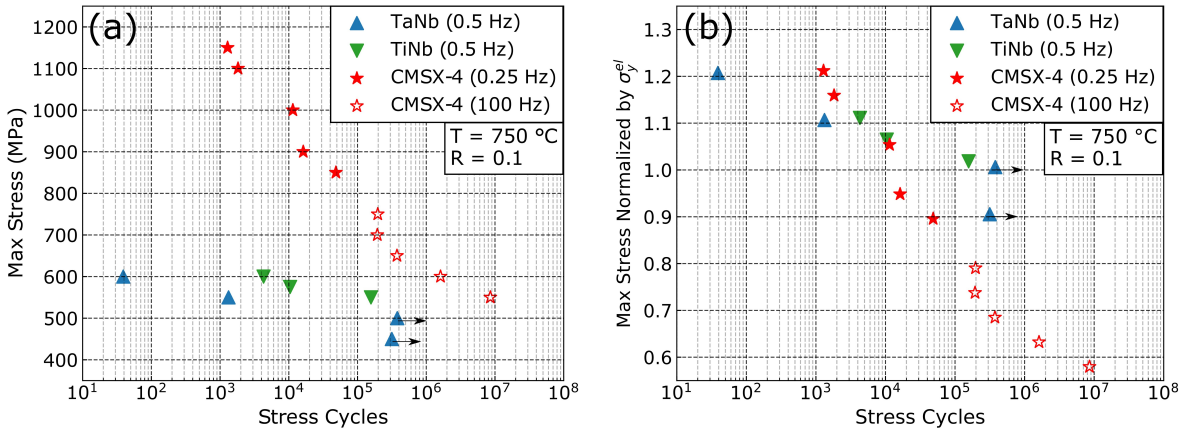

Figure 2.4: (a) A stress-life diagram with σ_{max} vs. cycles to failure for the coated single crystal Co-based superalloys in this study compared to load-controlled, T = 750 °C, R = 0 fatigue tests on uncoated 2nd-generation Ni-based superalloy CMSX-4 using data from the literature [81]. (b) A normalized stress-life diagram with $\sigma_{max}/\sigma_y^{el}$ vs. cycles to failure.

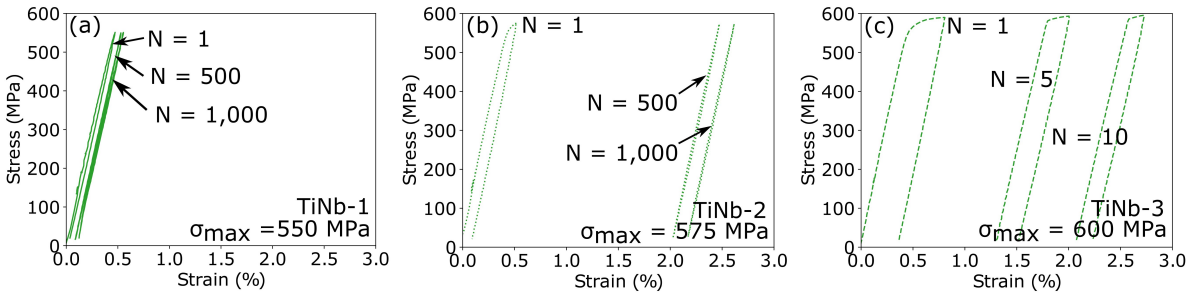

Figure 2.5: Stress-strain plots showing selected stress cycles for (a) TiNb-1, (b) TiNb-2, and (c) TiNb-3.

based superalloy CMSX-4 with R = 0 and T = 750 °C in Fig. 2.4a [81]. The CMSX-4 specimens in their study were uncoated and exposed to the laboratory air environment during testing. MachLachlan and Knowles applied loads using a 0.25 Hz trapezoidal 1s - 1s - 1s - 1s waveform and additionally performed high frequency tests at 100 Hz under load-control with a sinusoidal waveshape for lower stress tests. Fig. 2.4a shows that the Co-based superalloys in this study experienced reduced fatigue lifetimes compared to the Re-containing CMSX-4, particularly at high stresses. For tests performed with a positive R-ratio, inelastic ratcheting strains developed when applied stresses exceeded

the elastic limit of the alloy. This can result in fatigue lifetimes that are shorter than those observed in strain-controlled testing conditions where plastic strains are reversed during compression. An example of ratcheting strains can be observed in Fig. 2.5b and 2.5c, where cyclic stresses applied above the elastic limit resulted in significant amounts of strain accumulated. The ratcheting strains stabilized around 2% strain for TiNb-2 cycled at 575 MPa, whereas the magnitude of the ratcheting strains that were accumulated in TiNb-3 cycled at 600 MPa are not known since the accumulated strain quickly exceeded the 3% strain range of the extensometer. For the TiNb-1 test performed at σ_{max} = 550 MPa, loading is nominally elastic and plastic strains are limited throughout the test, as shown in Fig. 2.5a.

Table 2.2: Summary of test conditions and lifetime results

Alloy Label	Initial σ_{max} (MPa)	Test End	Cycles	Test Length (h)
TiNb-1	550	Rupture	156,860	87.14
TiNb-2	575	Rupture	10,436	5.80
TiNb-3	600	Rupture	4,295	2.39
TiNb-4	550	Int. at 25% life	39,297	21.78
TaNb-1	450	Run-out	315,646	175.36
TaNb-2	500	Run-out	378,734	210.41
TaNb-3	550	Rupture	1,328	0.74
TaNb-4	600	Rupture	39	0.02

Fig. 2.4b displays an additional stress-life plot where the initial maximum stresses have been normalized by the elastic limit, σ_y^{el}, measured during the first cycle of testing. The elastic limits were 497 MPa and 540 MPa for TaNb and TiNb, respectively. For the reference CMSX-4, a value of 949 MPa at T = 750 °C from Hong et al. was chosen for normalization using the same method [126]. After normalization, the results for both Co-based superalloys collapse onto the same line, indicating that the compositional differences in fatigue appear through their influence on plastic yielding. For the tests where loads were applied above the elastic limit of the alloys (i.e. $\sigma_{max} > \sigma_y^{el}$), the

normalized stress-life curves for the Co-based and Ni-based alloys converge. For stresses applied below the elastic limit, the Co-based superalloys resisted failure and were labeled as run-outs.

2.3.2 Fractography

Optical micrographs of the fracture surfaces from ruptured specimens are shown in Fig. 2.6. Surface cracks with almond-shaped crack fronts can be clearly identified due to the oxidation products left in their wake, which is most clearly shown in Fig. 2.6a. At lower applied cyclic loads, cracks were observed to either propagate in a Mode I fashion across most of the gauge width (Fig. 2.6a), or to initially propagate in a Mode I fashion before transitioning into crystallographic cracks on {111}-type planes (Fig. 2.6b and 2.6c). The side-view images in Fig. 2.6 are oriented with the fatal surface crack propagating from left to right, with the angle of the crystallographic crack portions clearly displayed. A focused view of the crystallographic cracking observed in TiNb-3 is displayed in Fig. 2.7a. The initial Mode I portions of each fracture surface were associated with surface oxidation, which indicates that the fatal cracks likely initiated at the surface and that propagation was enhanced by environmental damage.

Near-surface casting pores have been shown in previous studies to be responsible for crack initiation at 750 °C for Ni-based superalloys [118, 79]. These features were not observed to initiate cracks in the investigated Co-based superalloys due to the presence of the coating and the dominance of the surface cracking. Regions of the fracture surface far from the surface-initiation sites showed a tendril-like "cup-cone" surface roughness indicative of ductile fracture (Fig. 2.7d,f) [127]. Regions near the surface-initiation sites were flat and covered in oxidation products (Fig. 2.7c,e). The oxides in these regions had a porous, nodular morphology.

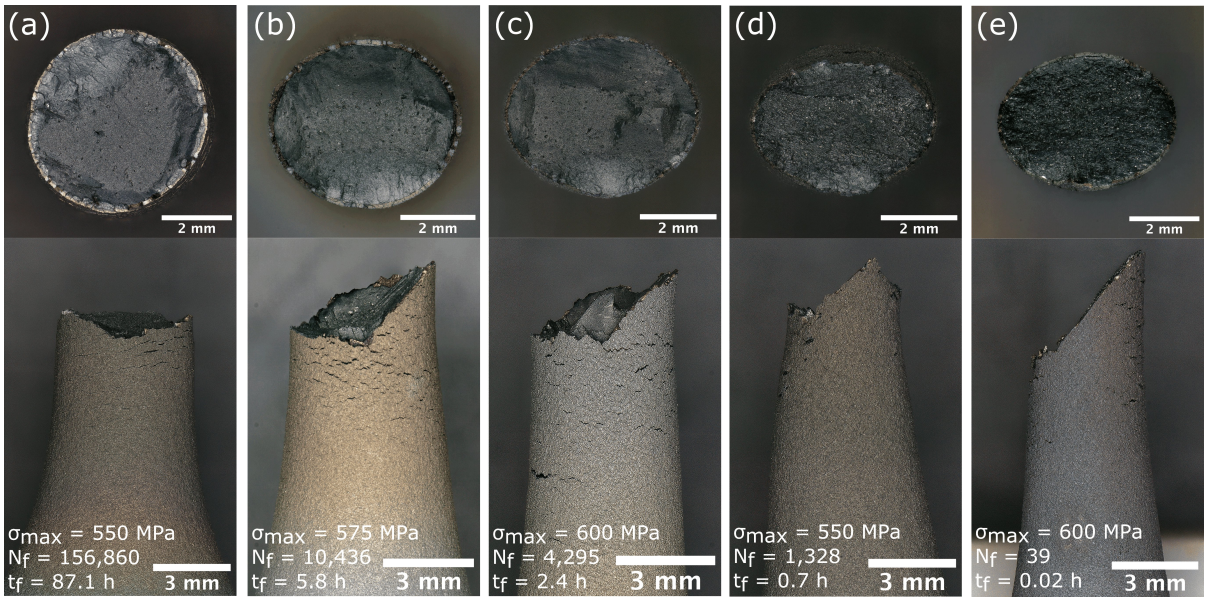

Figure 2.6: Fracture surfaces of the failed specimens taken to failure after fatigue testing at 750 °C in air. The details for each test are (a) TiNb-1, σ_{max} = 550 MPa, $\sigma_{max}/\sigma_y^{el}$ = 1.02 (b) TiNb-2, σ_{max} = 575 MPa, $\sigma_{max}/\sigma_y^{el}$ = 1.06 (c) TiNb-3, σ_{max} = 600 MPa, $\sigma_{max}/\sigma_y^{el}$ = 1.11 (d) TaNb-3, σ_{max} = 550 MPa, $\sigma_{max}/\sigma_y^{el}$ = 1.11 (e) TaNb-4, σ_{max} = 600 MPa, $\sigma_{max}/\sigma_y^{el}$ = 1.21.

Observations of the interrupted and run-out specimens in Fig. 2.8 reveal that the CoNiCrAlY coating was cracked after interrupted fatigue testing. These surface cracks became longer and deeper as the time-length of the fatigue tests increased. Additionally, the exterior of the coating darkened as oxide formed upon the protective coating. Cracking was not observed as an isolated event, and multiple cracks were observed to be spaced evenly across the gauge section.

2.3.3 Surface Cracking

Cross-sections taken near the initiation sites reveal that the periodic secondary cracks along the gauge length propagate through the CoNiCrAlY coating and into the superalloy substrate. An overview of these features is shown in Fig. 2.9. Once a surface crack has reached past the interdiffusion zone between the coating and the superalloy, extensive

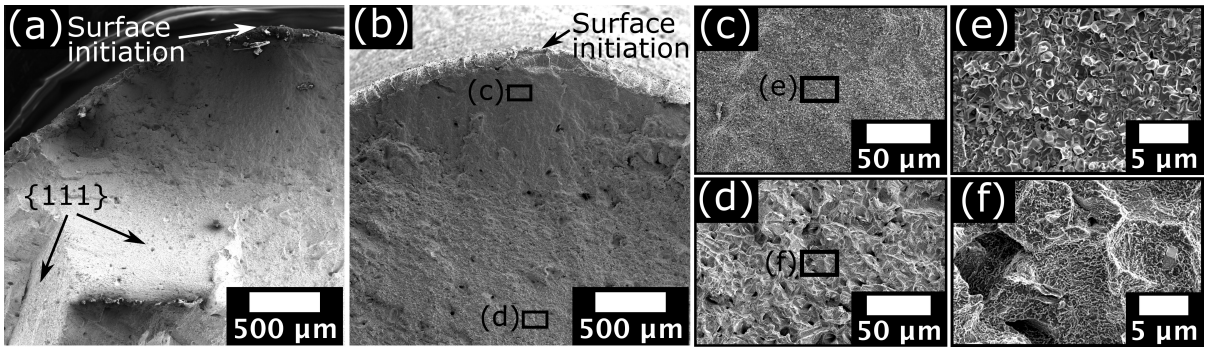

Figure 2.7: SE micrographs of the fracture surfaces of (a) TiNb-3 cycled at σ_{max} = 600 MPa and (b) TiNb-2 cycled at σ_{max} = 575 MPa. Focused views of TiNb-2 near the initiation site of the fatal crack (c,e) and far from the initiation site (d,f) reveal a flat fracture surface covered in oxide transitioning into an oxide-free, dimpled, tendril covered surface typical of ductile fracture.

oxidation occurs along the crack faces and into the superalloy ahead of the crack tip. The fatigue specimens tested at lower stresses such as TiNb-1 or TaNb-1 possessed post-test coatings that appeared to have begun to undergo rumpling compared to their starting microstructure, which is shown in Fig. 2.9 and Fig. 2.10c.

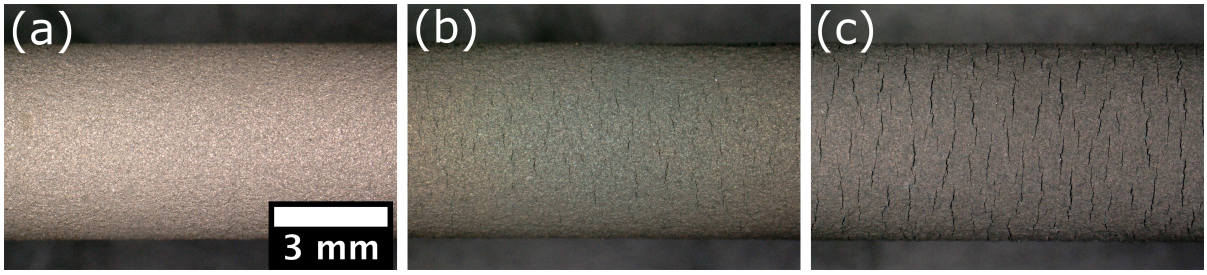

Figure 2.8: Optical micrographs from (a) TiNb-4 before testing (b) TiNb-4 interrupted at 25% of the fatigue life after 21.8 h of cycling (N=39,297), and (c) TaNb-2 interrupted after 210.4 h of cycling (N=378,734)

Fig. 2.10a shows BSE micrographs of the fatal crack for the TiNb-1 alloy tested at σ_{max} = 550 MPa. This image contains the bottom half of an oxidized surface crack. The fatal crack was measured to have grown to a length of 280 µm before crack propagation accelerated. The fracture surface was observed to be oxidized to a depth of 1515 µm along the length of the fatal crack, but the thicknesses of these oxides were significantly lower

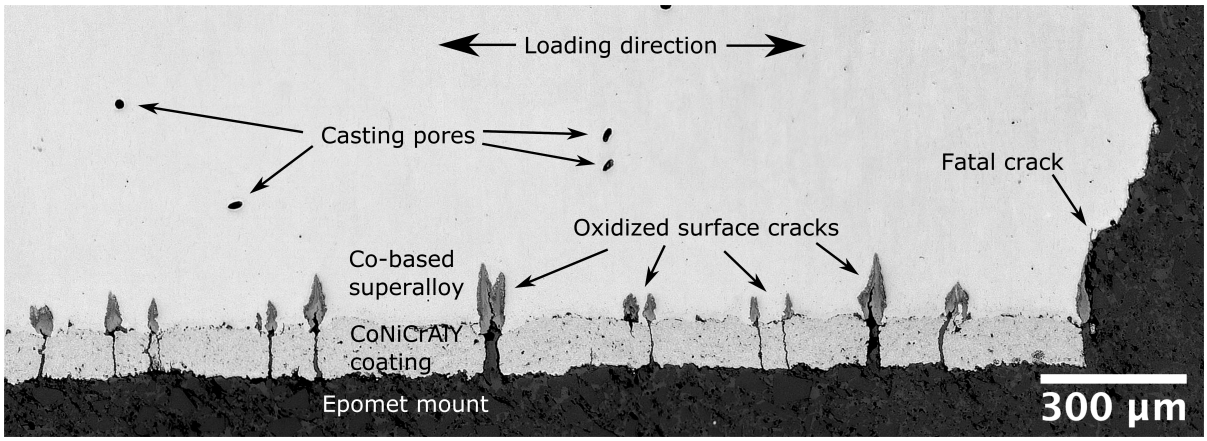

Figure 2.9: A stitched optical micrograph of a cross-section taken through the fatal surface crack of the TiNb-1 specimen after rupture. Secondary surface cracks are observed to be oxidized across the entirety of the gauge section, whereas internal casting pores are not observed to have initiated cracks. Test details: $\sigma_{max} = 550$ MPa, $\sigma_{max}/\sigma_y^{el} = 1.02$, $N_f = 156{,}860$.

than the thicknesses of those that develop during crack initiation, indicating that more of the fatigue life is spent in crack initiation as opposed to crack propagation at these test conditions. Fig. 2.10b shows a typical secondary edge crack for the same sample. The secondary cracks were always observed to be shorter in length than the heavily oxidized region of the fatal crack.

The lengths of the secondary cracks are dependent on the time-length of the fatigue test. Fig. 2.10c and 2.10d show typical edge cracks observed in TaNb-2 and TiNb-2 after cycling at 500 MPa for 210.4 h and 575 MPa for 5.8 h, respectively. For the lower stress test, the oxide scales within the cracks have developed into a layered structure that contains both oxides and intermetallic phases. Since lower stress fatigue tests result in more cycles to failure, this allows more time for oxidation to occur. Additionally, at lower stresses the stress intensity at the crack tip is reduced, resulting in a longer crack length needed to initiate steady-state crack growth. For the higher stress test shown in Fig. 2.10d, the layered oxide scales have not yet fully developed due to the shorter time-length of the fatigue test. However, this cross-section clearly demonstrates the presence

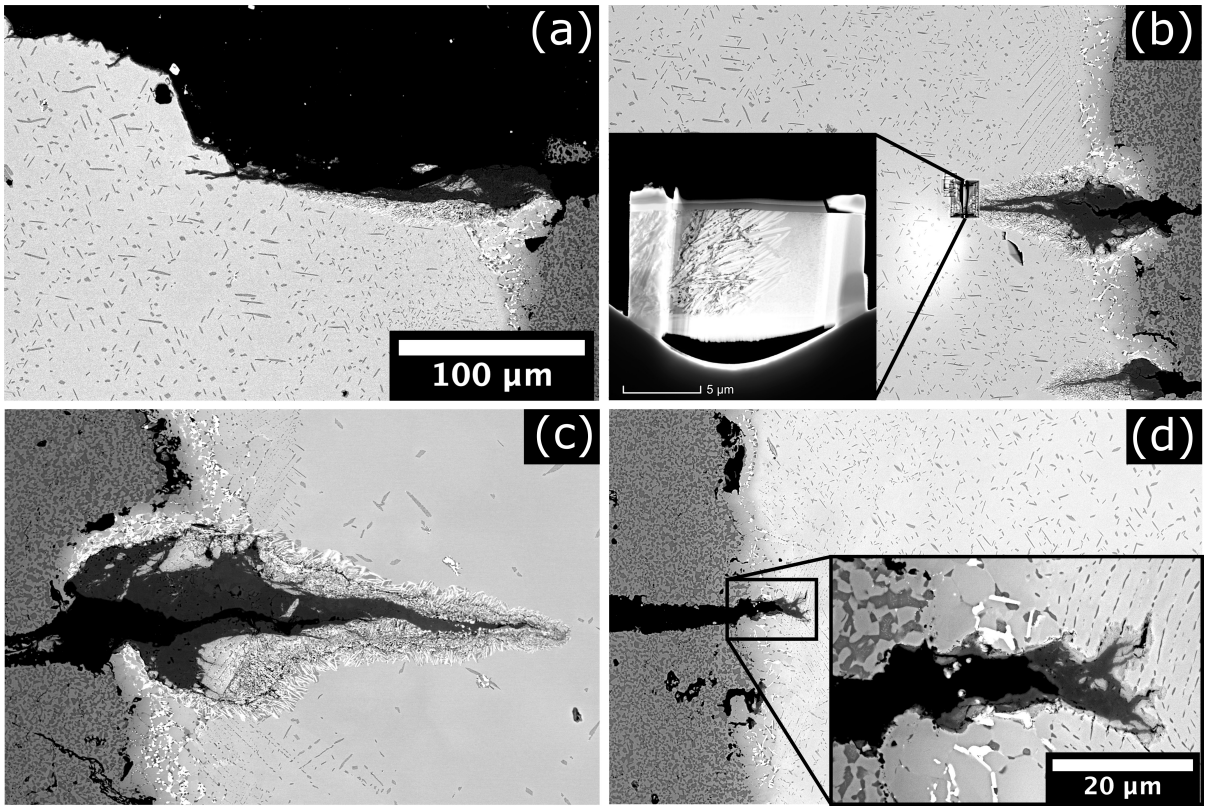

Figure 2.10: BSE micrographs taken from cross-sections of fatigued Co-based superalloys showing (a) the fatal crack and fracture surface of TiNb-1 ($\sigma_{\max}$ = 550 MPa), along with secondary edge cracks far from the fracture surface from (b) TiNb-1, (c) TaNb-2 ($\sigma_{\max}$ = 500 MPa), and (d) TiNb-2 ($\sigma_{\max}$ = 575 MPa)

of a γ'-denuded zone ahead of the oxidized crack tip. This likely weakens the alloy ahead of the crack tip and promotes accelerated crack growth. The extensive formation of a low Z-contrast oxide is observed to develop once cracks have propagated past the interdiffusion zone between the CoNiCrAlY coating and into the Co-based superalloy.

In order to better understand the time necessary for crack penetration through the CoNiCrAlY coating, an interrupted fatigue test was performed on the TiNb-4 specimen at $\sigma_{\max}$ = 550 MPa. Since the previous test on TiNb-1 at $\sigma_{\max}$ = 550 MPa withstood 156,860 cycles before rupture, it is possible to estimate the percentage of fatigue life that has been consumed in the interrupted test. The sample surface was monitored optically during the test every 5% of the fatigue life. The first cracks in the coating

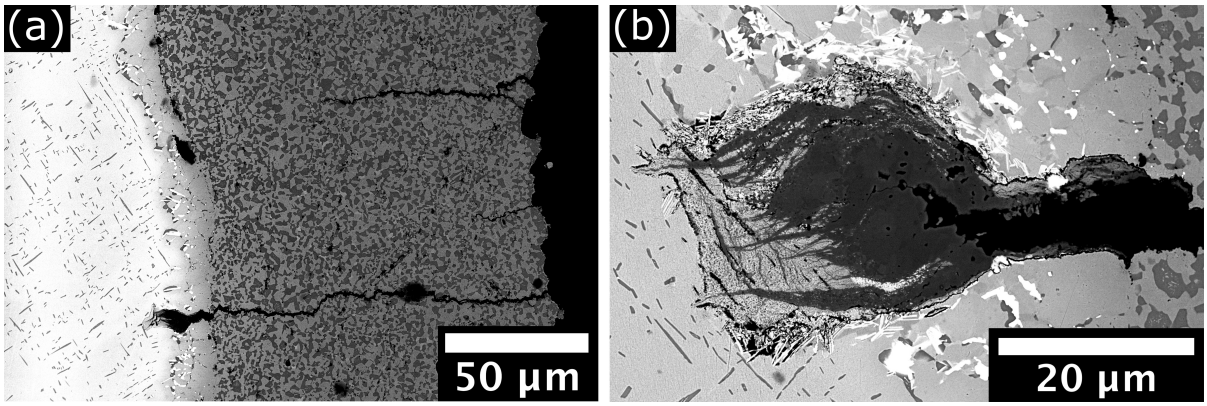

Figure 2.11: BSE micrographs taken from the TiNb-4 cross-section after cyclic loading at $\sigma_{max} = 550$ MPa, interrupted at 25% of the fatigue life. (a) Cracks propagated from the surface of the coating to the superalloy, with not all secondary cracks reaching through the CoNiCrAlY coating. (b) Once cracks reached the superalloy substrate, cracking through the developing outer oxide layer was observed between pores within the oxide scale.

were observed at 20% of the fatigue life, and the test was continued until 25% fatigue life before interruption to allow time for the surface cracks to propagate through the coating. Fig. 2.11 shows a cross-section through the interrupted sample. Surface cracks were observed to still be propagating through the coating with several cracks having already arrived at the superalloy. An enhanced view of an oxidized surface crack that was still developing is shown in Fig. 2.11b. This interrupted test clearly demonstrates that oxidation occurs ahead of the open crack tip. Interestingly, cracking can be observed between pores and flaws that are contained with the porous outer oxide scale.

SEM-EDX mapping was performed to identify the oxides and phases present around the oxidized crack tip in Fig. 2.10b. However, due to the fineness of the features in the oxide scale, it was not possible to locally resolve and identify the phases present using SEM-EDX. For these reasons, TEM investigations were performed on a lamella that was extracted using the FIB lift-out method near the crack tip parallel to the loading direction. As shown in the HAADF-STEM micrograph inset on Fig. 2.10b, the 10 µm-long lamella contained each of the observed oxide layers that formed in the fully developed

oxidized surface cracks.

2.3.4 Phase Identification by STEM-EDX

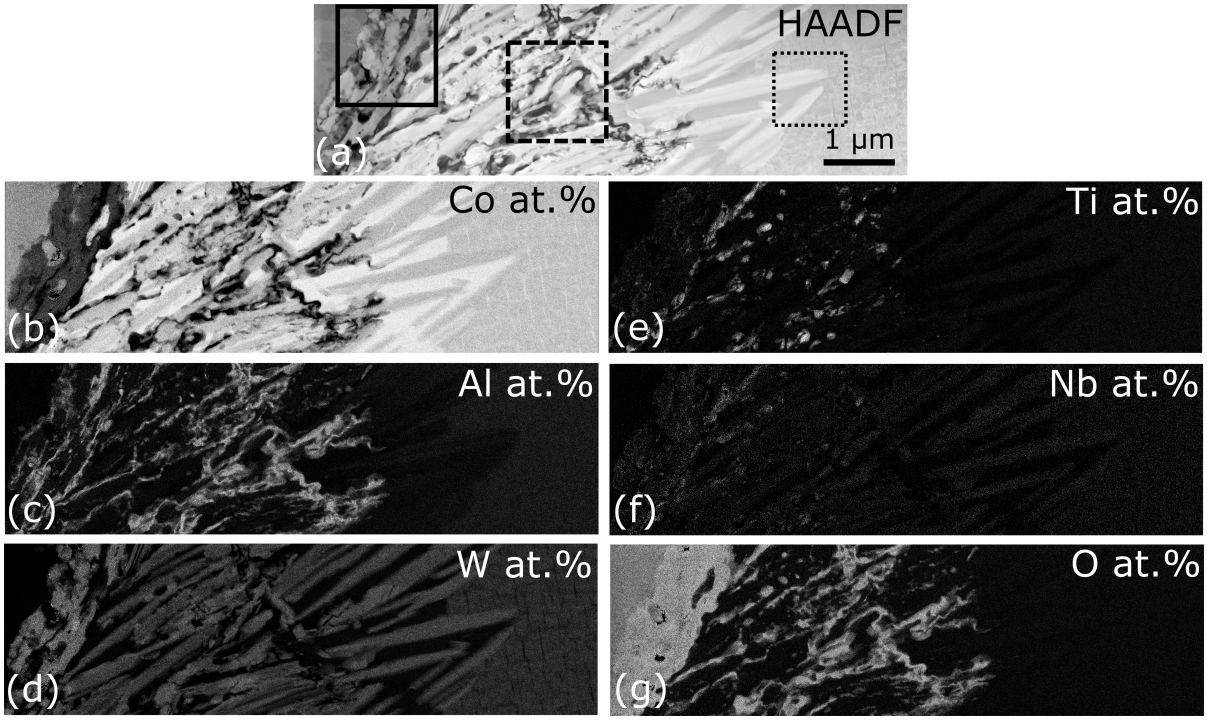

Figure 2.12: STEM-EDX chemical maps in at.% that show the distribution of (b) Co, (c) Al, (d) W, (e) Ti, (f) Nb, and (g) O across the lamella extracted near an oxidized crack tip within TiNb-1. The overlaid boxed regions in (a) the HAADF micrograph of this region were selected for detailed mapping. HAADF-STEM micrographs of these regions are shown in Fig. 2.13.

The use of STEM-EDX allowed for the identification of all phases that formed near an oxidized surface crack in the TiNb-1 sample cycled at 550 MPa for 87.1 h. An overview chemical map was collected using drift-corrected STEM-EDX across the lamella in order to identify the distribution of different elements within the oxide scale. While the Z-contrast in the HAADF-STEM micrograph in Fig. 2.12a provides qualitative information about the phases present, the Co at.% map clearly indicates the presence of a Co-rich outer oxide layer, a Co-depleted inner oxide layer, an internal precipitation region, and

a γ'-denuded zone that contains Co-rich and Co-depleted metallic phases. Interestingly, these compositional maps reveal the presence of small, nodular Ti-rich oxides located near Al-rich oxides distributed through the internal precipitation region. Locating and characterizing these Ti-rich oxides from Z-contrast and point EDX measurements alone would be difficult due to their low contrast and small size.

After identifying the different regions of the oxide scale, local drift-corrected chemical maps were acquired at the three different locations indicated in Fig. 2.12a. HAADF-STEM micrographs from these regions are displayed in Fig. 2.13. The compositions of single phase regions were extracted from the acquired maps at the numbered locations in Fig. 2.13 and a summary of this compositional data is displayed in Table 2.3. By comparing the compositions observed here to phases known to form during oxidation of similar Co-based alloys, each phase was identified [43, 44, 46, 128, 129]. The outer oxide layer was observed to be made of CoO, whereas the inner oxide layer was a mixture of both $CoAl_2O_4$ and $CoWO_4$. The internal precipitation region consists of a tortuous, non-continuous network of Al_2O_3 with nodular TiO_2 particles that form adjacent to the Al_2O_3. This observation is in agreement with oxidation studies on Ti-containing Ni-based and CoNi-based superalloys [129, 130]. Also within this region is the precipitation of the Co_3W χ-phase alongside a Co-rich γ-phase. The formation of χ phase is expected due to the depletion of Al to the oxide scale, which shifts the composition of the alloy locally into a W-rich two-phase field between γ and χ [23]. Deeper into the internal precipitation region, the formation of Al_2O_3 and TiO_2 is no longer observed and there is a region that only contains χ and γ. The original γ-γ' microstructure of the alloy is recovered far from the oxide scale.

Oxidation studies on pure Co have experimentally confirmed that CoO and Co_3O_4 can form within the outer oxide layer, with CoO formation becoming dominant at temperatures above 900 °C [131]. Further examination of the BSE micrographs of the oxide

spikes in Fig. 2.10b and 2.10c indicate two different regions of contrast within the outer Co-rich oxide layer. The Z-contrast of the outermost Co-rich oxide is observed to be darker than the adjacent Co-rich oxide layer, so it is concluded that both Co_3O_4 and CoO are present within the crack after fatigue testing at 750 °C. The lamella used for STEM-EDX in this study was found to only contain CoO in the outer oxide scale, and this is expected since CoO has been observed to form below Co_3O_4 during isothermal oxidation tests on ternary Co-Al-W alloys at 800 °C [132]. This observation of CoO within the lamella is further supported by the observation of the $CoAl_2O_4$ spinel in the inner oxide scale, since this spinel can be synthesized in solid-state reactions between CoO and Al_2O_3 [133].

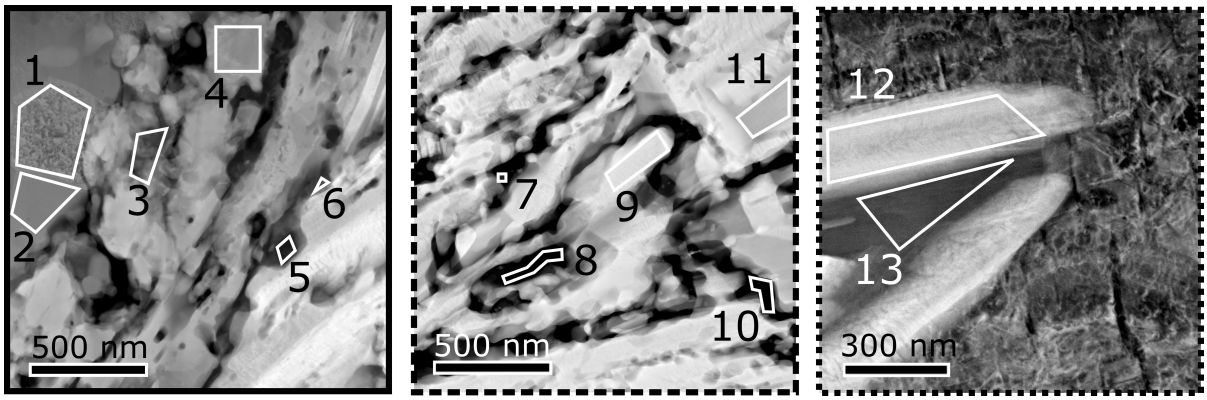

Figure 2.13: HAADF-STEM micrographs from the three regions of interest outlined in Fig. 2.12a with overlaid graphics showing where compositional data was extracted. Compositional measurements and phase identification are summarized in Table 2.3.

2.3.5 TEM observations of planar faults near stress concentrations

Fig. 2.14 shows a summary of representative micrographs from TEM investigations on the microstructure within the bulk of the TiNb-4 sample that was interrupted near 25% fatigue life. The features shown in Fig. 2.14 are located near the center of the

Table 2.3: Compositions (in at.%) acquired by STEM-EDX maps of each region in Fig. 2.13

Region	Co	Al	W	Ti	Nb	O	Oxide / Phase
1	54.82	0.46	0.01	0.06	0.05	44.59	CoO
2	57.15	0.33	0.01	0.05	0.03	42.43	CoO
3	16.52	24.31	1.70	1.77	1.97	53.75	$CoAl_2O_4$
4	20.82	2.66	15.37	0.92	2.40	57.83	$CoWO_4$
5	0.49	36.19	0.04	5.48	0.64	57.16	Al_2O_3
6	4.93	5.79	1.04	21.93	9.54	56.77	TiO_2
7	1.98	8.07	0.34	28.88	6.05	54.69	TiO_2
8	1.04	44.51	0.17	0.33	0.09	53.86	Al_2O_3
9	77.09	2.79	13.41	1.00	2.02	3.69	χ (Co_3W)
10	1.06	41.82	0.03	0.79	0.07	56.22	Al_2O_3
11	95.36	0.97	0.82	0.07	0.09	2.68	γ (Co)
12	78.71	3.63	11.59	1.15	1.56	3.37	χ (Co_3W)
13	92.44	2.91	1.47	0.22	0.10	2.87	γ (Co)

gauge section, far from any oxidized surface cracks that had begun to progress through the coating. Fig. 2.14a and 2.14b display the region surrounding a β-phase precipitate. A focused view on the interface between one of these β-phase precipitates and the γ-γ' microstructure is shown in Fig. 2.14c and 2.14d, with the γ-γ' microstructure far from any β-phase precipitates shown in Fig. 2.14e and 2.14f.

The observed β-phase precipitates are surrounded by envelopes of the γ'-phase. These γ'-envelopes have been shown to form upon cooling after high temperature solutionizing in β-containing Ni-based alloys, with thicker γ'-envelopes forming upon slower cooling [134]. The bright field, dark field, and weak-beam dark field images in Fig. 2.14a-d show a high density of stacking faults within the γ'-precipitates surrounding the β-phase along with dislocation debris that fills the γ channels. It is likely that these faults and dislocations formed during cyclic loading, with the β-phases acting as stress concentrations that promote high stresses resulting in shear of the γ'-phase. It may be inferred that the stress concentrations associated with cracks propagating through the material would result in similar shearing events. The lower applied stresses during this fatigue test

($\sigma_{\max}/\sigma_{\mathrm{y}}^{\mathrm{el}} = 1.02$) can explain the mostly undisturbed γ-γ' microstructure far from the β-phase precipitates, which is shown by the bright field images in Fig. 2.14e and 2.14f using (200) and (220) **g**-vectors, respectively. The additional contrast that appears to be within the γ'-precipitates is likely due to the small scale of the γ'-precipitates, resulting in multiple γ'-precipitates through the thickness of the foil. However, large precipitates such as the one near the center of Fig. 2.14e and 2.14f demonstrate that the γ'-phase remains largely un-sheared after interruption at 25% fatigue life.

2.4 Discussion

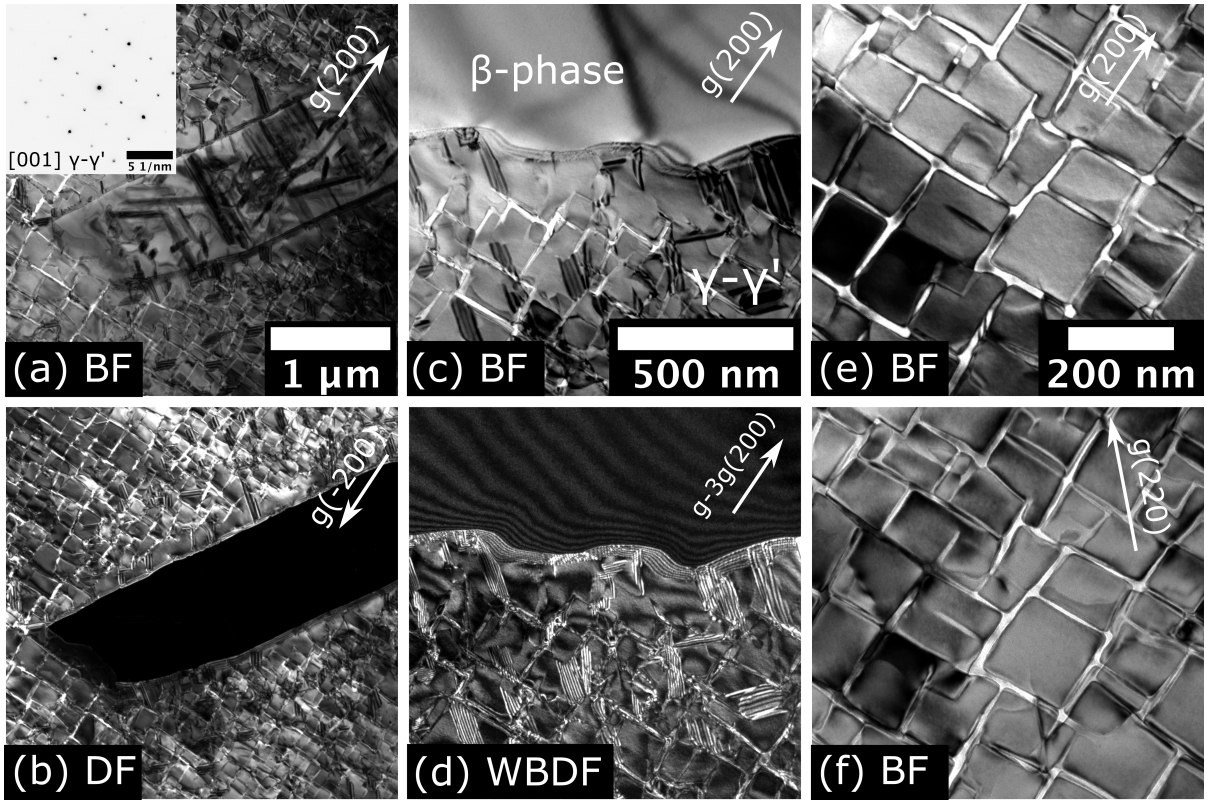

Figure 2.14: TEM micrographs from the bulk of the interrupted TiNb sample, showing (a,b) stacking faults surrounding a β-phase precipitate, (c,d) a focused view of the interface between a β-phase precipitate and the γ-γ' microstructure, (e,f) a region of undisturbed γ-γ' far from any β-phase precipitates.

The present study demonstrates the important role of oxidation in the fatigue response of γ'-containing Co-based superalloys, in spite of the presence of a CoNiCrAlY coating. Surface cracks are observed to propagate through the coating as early as 25% of the fatigue life. Upon extension of these cracks into the base Co-based superalloy, oxidation of the base metal ahead of the crack tip occurs. This likely promotes accelerated crack propagation through the oxide scale between flaws that develop in the oxide scale, such as pores and cracks.

The cracking of the coating occurred early during the fatigue tests despite the testing temperature of 750 °C being above the ductile-to-brittle transition of the applied CoNiCrAlY coating [135]. This cracking may be due to a variety of factors. MCrAlY coatings (M = Ni,Co) typically have coefficients of thermal expansion (CTE) that are greater than Ni-based superalloys [136, 137], but form oxides with lower CTEs that can periodically spall due to the large compressive stresses present [138]. Due to the multiphase character of the coating, oxidation-assisted intrusions that eventually form cracks have been observed [138]. While the formation of interfacial phases between the coating and Co-based superalloy substrate are observed in this study, these phases do not continue to develop during testing at 750 °C and delamination cracking along the coating-substrate interface was not observed. Therefore it is likely that cracking occurred due to an oxidation-assisted fatigue crack growth process through the relatively soft $\gamma + \beta$ coating. This is supported by cross-section observations of the interrupted fatigue test on TiNb-4 (Fig. 2.11a) where cracks within the coating initiated at the surface and propagated along the grain boundaries of the coating where the diffusivity of oxygen is enhanced. This oxidation-assisted process is slower through the coating than through the superalloy substrate due to the high Al and Cr content of the coating providing oxidation resistance.

Cracking through the oxide scale at the crack tip has been previously considered in fatigue crack initiation and propagation modeling on single crystal Ni-based superalloys

by Martinez-Esnaola et al. [139]. This can occur due to local stresses around flaws that develop within the oxide scale near the crack tip. These stresses eventually exceed the fracture toughness of the oxide, and the crack propagates. The fracture toughness of NiO in tension has been assessed at room temperature and 900 °C to be 0.41 and ~1.61 MPa$\sqrt{\text{m}}$, respectively. The fracture toughness of cobalt oxides such as CoO and Co_3O_4 have not yet been experimentally investigated [140]. Theoretical modeling of ideal fracture toughness at room temperature for CoO and NiO provides fracture toughness values of 1.19 and 1.52 MPa$\sqrt{\text{m}}$ respectively, which indicates that Co-rich oxides may be slightly more susceptible to cracking during fatigue crack propagation [141].

In order to assess what length the cracks must become in order to initiate steady-state crack growth in the Paris regime, the stress intensity factor at the crack tip can be considered. For an edge crack in a round bar under tension, the stress intensity can be expressed as:

$$\Delta K = F\Delta\sigma\sqrt{\pi a}. \tag{2.1}$$

where ΔK is the stress intensity range, F is a shape factor, $\Delta\sigma$ is the cyclic stress range, and a is the length of the crack measured from the surface to the farthest crack front [142]. As an example, we shall consider the TiNb-1 sample cycled at 550 MPa. Optical micrographs of the fracture surface in Fig. 2.6a and cross-sections through the fatal crack in Fig. 2.10a show that the fatal surface crack reached a length of approximately 280 µm before the crack growth rate accelerated. Once the crack growth rate accelerates, the oxide observed on the fracture surface is thin due to less time allowed for oxide formation, which provides clear evidence of the transition from crack initiation to crack propagation. The shape factor in Eq. 1, F, depends on the ratio between the crack length and the diameter of the round bar, resulting in a value of $F = 0.74$ [142]. Inserting these values

into Eq. 1 yields:

$$\Delta K = 0.74 * 500 \text{ MPa} * \sqrt{\pi * 280 \ \mu\text{m}} = \Delta K_{Th} = \sim 11 \text{ MPa}\sqrt{\text{m}}. \tag{2.2}$$

where ΔK_{Th} now represents the threshold stress intensity factor. This estimate for the threshold stress intensity factor can be used in comparison to threshold stress intensity factors for Ni-based superalloys that have been measured using compact tension fatigue crack growth experiments. For René N5, a 2$^{\text{nd}}$-generation single crystal Ni-based superalloy, the threshold stress intensity factor under similar loading conditions (T = 750 °C, R = 0.1, f = 0.5 Hz, in air) has been measured as $\Delta K_{Th}^{eff} = 12.25$ MPa$\sqrt{\text{m}}$ after considering the effect of oxide-induced crack closure. These values agree well with the estimate made for the Co-based superalloys studied in this work, indicating that oxide-induced crack closure may affect crack growth while cycling under near-threshold conditions. In this case, it is worth considering the Pilling-Bedworth Ratio where PBR = V_{oxide}/V_{metal} [143]. All of the transition metal oxides have a PBR >1 [144], and the PBR of native oxides on metals of interest are $PBR_{Al_2O_3/Al} = 1.28$, $PBR_{NiO/Ni} = 1.65$, $PBR_{CoO/Co} = 1.76$, and $PBR_{Co_3O_4/Co} = 1.98$. PBR values >1 result in compressive stresses in the oxide scale during growth, which can promote oxide spallation and cracking [145], whereas metals with a PBR of <1 form non-protective oxide scales that are not able to sufficiently cover the metal surface. Since the molar volumes of Co and Ni are similar, the higher PBR for CoO and Co_3O_4 likely promotes oxide-induced crack closure in Co-based superalloys more significantly than NiO in Ni-based superalloys.

Once the cyclic stress intensity factor is above the threshold stress intensity factor within the Paris regime, the change in length of the crack per cycle, da/dN, can be

related to the cyclic stress intensity factor, ΔK, through the Paris Law [146]:

$$da/dN = C(\Delta K)^m \tag{2.3}$$

where C and m are materials dependent constants. Given an initial flaw size, a_o, and a final flaw size, a_f, that depends on the fracture toughness, Eq. 3 can be integrated to obtain an expression for the estimated cycles to failure:

$$N_f = \frac{1}{C(F\Delta\sigma\sqrt{\pi})^m}\Big(\frac{1}{\frac{m}{2}-1}\Big)\Big[\frac{1}{a_o^{\frac{m}{2}-1}} - \frac{1}{a_f^{\frac{m}{2}-1}}\Big]. \tag{2.4}$$

where $m \neq 2$. Reviewing the crack growth data on René N5 under similar loading conditions of T = 750 °C, R = 0.1, f = 0.5 Hz, in air, the constants C and m are determined to be $2.95 * 10^{-12}$ MPa$^{-1.69}$ m$^{-.845}$ and 1.69, respectively [82]. Once again, we can consider the TiNb-1 sample cycled at 550 MPa. If we assume that (1) steady-state crack growth behavior began when a_o = 280 µm and rupture occurred slightly after a_f = 1515 µm, (2) that the shape factor, F, remains constant at $F = 0.96$ during crack growth, and (3) if the values of C and m for René N5 apply to the Co-based superalloys tested in this study, we would expect N_f = 2,058,896 cycles to rupture. Since rupture occurred much earlier for TiNb-1 (N_f = 156,860 cycles) under these test conditions, we can infer that the crack growth rates in this alloy are significantly higher than those observed in Ni-based superalloys. Accelerated fatigue crack growth within the Paris regime is an additional explanation for the short fatigue lifetimes observed, and is likely exacerbated by the non-protective oxidation response that results in the formation of large oxidized surface cracks and γ'-denuded zones.

Fatigue crack initiation in coated single crystal Co-based superalloys has exclusively been observed to occur at the surface at the test temperature of 750 °C. In the case of

fully-reversed strain-controlled low cycle fatigue tests on single crystal Ni-based superalloy AM1, failure due to oxidized surface cracks is not observed until temperatures of 950 °C and above [147]. A competition exists between internal crack initiation, which can be thought of as "in-vacuum", and surface crack initiation that is promoted by environmental effects. Low cycle fatigue tests within vacuum chambers at 950 °C have demonstrated that when the influence of the environment is significantly reduced, fatigue failures once again initiate at internal inhomogeneities in single crystal Ni-based superalloys [79]. Oxidation-assisted fatigue crack initiation and propagation appears to be the dominant failure mechanism under the test conditions presented above. This finding motivates the design of Co-based superalloys with improved oxidation response at high temperatures.

Co-Al-W ternary alloys do not intrinsically form protective Al_2O_3 scales upon oxidation, although the presence of internal Al_2O_3 particles develop in the early stages of oxidation [148]. While previous studies have shown that the formation of Al_2O_3 is achievable in Co-based superalloys upon alloying with Cr additions, the scale formation is sluggish and results in thick layers of over-laying inner and outer oxides during the oxidation process [23, 46]. These overlaying oxides are susceptible to spallation, leading to mass loss at elevated temperatures [45]. Additions of 10 at.% Cr can promote the formation of Cr_2O_3 and Al_2O_3 that can passivate Co-based superalloys from the ingress of oxygen [44]. However, it has been established that Cr_2O_3 is non-protective at high temperatures due to significant volatilization of Cr_2O_3(s) into $CrO_2(OH)_2$(g) by water vapor and oxygen above 1000 °C [149, 150]. Since the combustion environments that Co-based superalloys are being considered for can have temperatures that exceed 1000 °C and contain water vapor, it is beneficial to focus on alloy compositions that promote protective Al_2O_3 oxide scales. Additionally, the role of Cr as a γ-former has been established in Co-Al-W-based superalloys, which is associated with reduced γ'-solvus temperatures

along with the promotion of 3rd-phase formation upon additions of only 2 at.% Cr [151]. Therefore, it is desirable to only include sufficient amounts of Cr to promote protective oxide scale formation without destabilizing the microstructure.

Due to the limited solubility of alloying additions in the Co-Al-W ternary system, alloying strategies that rely on large additions of Cr for oxidation resistance and large additions of γ'-formers such as Ta, Ti, and Nb for high temperature strength are difficult to achieve without the formation of 3rd-phases that may be deleterious to the mechanical properties of the alloy. However, additions of Ni into the Co-Al-W ternary greatly widen the size of the γ/γ' two-phase field leading to a flexible design space [27]. This has led to the development of multinary CoNi-based superalloys that have promising high temperature mechanical properties alongside promising oxidation resistance [152, 153]. As a result of a combinatorial study performed by Stewart et al., CoNi-based superalloys with promising oxidation behavior and high temperature stability are currently under development [46, 48, 49]. The low cycle fatigue response of these single crystal CoNi-based superalloys is currently under investigation and may be greatly enhanced compared to Co-based superalloys due to their improved oxidation resistance and elevated high temperature strength.

2.5 Conclusions

This study has investigated the load-controlled fatigue response of coated single crystal Co-based superalloys at 750 °C in air with an applied R-ratio of R = 0.1. The findings of this study are:

1. CoNiCrAlY-coated single crystal Co-based superalloys have reduced fatigue lifetimes compared to uncoated single crystal Ni-based superalloys in the low cycle regime.

2. Fatal fatigue cracks are observed to initiate at the surfaces of the coated specimens. These cracks propagate by an oxidation-assisted crack growth mechanism. This is in contrast to uncoated single crystal Ni-based superalloys which do not exhibit surface-induced failures until temperatures above 950 °C.

3. Load-controlled fatigue tests performed near the elastic limit of the Co-based superalloys resulted in the formation of oxide-filled cracks. In the superalloy substrate, the cracks consisted of (1) an outer oxide layer, (2) an inner oxide layer, (3) an internal precipitation region, and (4) a γ'-denuded zone. The oxides and phases present in these regions are (1) Co_3O_4 and CoO, (2) $CoAl_2O_4$, $CoWO_4$, TiO_2 (3) TiO_2, Al_2O_3, γ, and χ, and (4) γ and χ.

4. An interrupted fatigue test shows that cracking of the coating occurs around N = $0.2N_f$ for the lower stress condition, which subsequently exposes the Co-based superalloy substrate to the environment.

5. When stresses do not exceed the elastic limit of the material during cyclic loading, the γ-γ' microstructure remains primarily undeformed while extensive stacking fault formation and dislocation debris are observed around stress concentrators within the alloy.

6. Modified alloy compositions and heat treatments providing improved oxidation resistance and higher strength appear necessary to advance the fatigue properties of Co-based and CoNi-based superalloys.

Chapter 3

Design of a CoNi-base superalloy[†]

In this chapter, a systematic and accelerated methodology for alloy design is demonstrated by combining combinatorial synthesis, high-throughput oxide scale characterization, computational density functional theory, and CALPHAD database calculations. By applying this strategy to the senary Co-Ni-W-Al-Cr-Ta alloy system, a novel γ/γ' alloy exhibiting a superior combination of high temperature properties has been identified. Properties include a γ' solvus near 1200 °C, continuous α-Al_2O_3 scale formation after 1 h in air at 1100 °C, and comparable density to 2nd-generation commercial Ni-base superalloys. This novel alloy, SB-CoNi-10, has a nominal composition of 39.8Co – 36.5Ni – 13.2Al – 1.0W – 6.0Cr – 3.5Ta at.%, and is compared with other recently studied Co-, CoNi-, and Ni-base γ/γ' alloys.

[†]Significant portions of this chapter are reproduced from the following article: C.A. Stewart, S.P. Murray, A. Suzuki, T.M. Pollock, and C.G. Levi, Accelerated discovery of oxidation resistant CoNi-base γ/γ' alloys with high $L1_2$ solvus and low density. *Mater. Design* **189** (2020) 108445. [**doi**] [34]

3.1 Introduction

Superalloys are exceptional in their ability resist mechanical and chemical degradation at high temperatures relative to their melting point (i.e. high homologous temperatures). This makes them unique candidates for turbine engine components, where oxidation resistance must be combined with high temperature load-bearing ability. Achieving new materials with higher temperature capabilities can lead to billions of dollars in fuel savings and reduced carbon emissions by increasing the turbine engine combustion temperature, and thus engine efficiency. The drive for higher-temperature materials has pushed the metallurgical development of superalloys for decades. While a scientific understanding of the physical metallurgy involved has developed significantly over this time-frame, Ni-base γ/γ' alloys have largely been developed incrementally with experimentally-intensive approaches [6, 154]. With the discovery of the γ/γ' microstructure in the Co-Al-W ternary system by Sato et al. in 2006 [22], the potential for a new class of Co-base superalloys with superior properties to those of Ni-base alloys was realized. To rapidly explore this compositional space for promising alloys, a new suite of modern design tools have been deployed, including: (i) a high-throughput combinatorial alloy synthesis technique [49, 155], (ii) a rapid photostimulated luminescence spectroscopy (PSLS) oxide screening technique [48], (iii) a CALPHAD thermodynamic database [156], and (iv) first principles density functional theory calculations [157]. With this approach, the effects of various alloying additions on oxidation behavior and stabilization of the strengthening γ' ($L1_2$) phase have been identified, principally within the senary Co-Ni-Al-W-Cr-Ta space.

The six principal elements of interest were selected with the goal of creating a base alloy that achieves both a high γ' solvus temperature, as well as some measure of intrinsic oxidation resistance via the formation of a continuous α-Al_2O_3 layer in air at 1100 °C. Co-Al-W forms the basis of the γ' structure [22], and Ni stabilizes the γ' phase and expands

the two-phase field of interest [27, 151, 158], which is important for incorporating alloying additions without precipitating phases beyond the desired γ/γ'. Cr was added for its strongly beneficial effect on α-Al_2O_3 formation [159], though it has also been observed to depress the γ' solvus [63, 157]. First principles density functional calculations show that Ta is very effective for stabilizing the γ' phase in the Co-Al-W system [157, 160], thus it can balance the detrimental effect of Cr on the solvus temperature. While commercial alloys such as 2^{nd}-generation Ni-base superalloys René N5 or CMSX-4 can have over 9 components [5], the present composition space was anticipated to have the requisite alloying additions to achieve both γ' stability and oxidation resistance in the same alloy (not achievable in the ternary Co-Al-W system), while also having a reduced number of components to allow for greater understanding of the effects of individual alloying elements on alloy behavior. The present study builds on a prior combinatorial study that used ion plasma deposition (IPD) to deposit thick films across three Co-base alloy libraries, reported in more detail elsewhere [49]. This study revealed that increased concentrations of Ni, Al, W, and Cr all reduce the total scale thickness formed in air at 1100 °C after an hour. Furthermore, Al and Cr additions are most effective in promoting the formation of a continuous α-Al_2O_3 scale without other undesirable oxide phases dominating the oxidation response. The general compositional domain of promising oxidation resistance in the IPD alloy libraries was identified as Ni $\geq$ 26 at.%, Al $\geq$ 11 at.%, W between ~7-10 at.%, and Cr $\geq$ 4 at.%. In this compositional range, the formation of Al- and W- rich intermetallic phases was also observed, nominally identified as β-(Ni,Co)Al, and μ-Co_7W_6. These phases were typically present at higher Cr and Al contents, while reduced W content appeared to prevent their formation. Precipitation of the μ and β phases has been reported to deleteriously affect alloy toughness and creep stress-rupture, respectively [161, 162]. While future designs may intentionally include a small amount of these phases for processing purposes [163, 164], the present effort focuses

on achieving a two-phase γ/γ' alloy as a design strategy.

This study investigates the Co-Ni-Al-W-Cr-Ta space to arrive at an alloy composition that possesses both a high γ' solvus and alumina scale forming behavior at 1100 °C in air. Once a base senary composition is identified, higher order additions are explored. Specifically the possibility for reactive elements (RE) to improve oxidation resistance, especially scale adhesion [165] has been preliminarily investigated. It will be shown that the resultant alloy design achieves an unprecedented combination of γ' phase stability and oxidation resistance compared to other Co- and CoNi-base γ/γ' alloys in literature to date. Additionally, solidification distribution coefficients, the chemical partitioning behavior between the γ and γ' phases, thermal expansion behavior, room temperature elastic constants, and single crystal creep properties have been investigated and compared to other Co- and CoNi-base γ/γ' alloys. In doing so, the effectiveness of the suite of design tools used to arrive at a single-crystal composition without the need for a large number of prohibitively expensive single crystal growth trials is demonstrated.

3.2 Methods

3.2.1 Design Approach

A series of CoNi-base γ/γ' alloy compositions, designated SB-CoNi alloys after the University of California Santa Barbara, were designed based on the findings of previous high-throughput combinatorial synthesis studies [49, 48, 46]. The investigations on the behavior of these samples yielded three critical observations utilized in the present research: (i) Compositional regions of promising oxidation behavior were identified; these were nominally alloys that formed a continuous α-Al_2O_3 scale with lesser amounts of overlying oxides after 1 h in air at 1100 °C. (ii) The influence of constituent alloying ad-

ditions on the formation of the thermally grown oxide (TGO) scale was elucidated. (iii) The compositional domains over which the $\gamma + \gamma'$ phases were nominally stable without additional deleterious phases were also identified.

These insights were combined with calculations from a 2011 version of the commercial PANDAT PanCobalt thermodynamic database (CompuTherm LLC, Middleton, WI) of the Co-Ni-Al-W-Cr-Ta system to further refine compositions [156]. Isothermal isoconcentrate (ITIC) sections were calculated at 1100 °C to assess composition regions of more promising oxidation behavior and phase equilibria. The calculated γ/γ' alloy two-phase field of interest was then overlaid with the results of the rapid PSLS screening of oxidation behavior. From this, compositions predicted to have both promising oxidation scales and a γ/γ' microstructure were highlighted. The calculated presence of γ' and lack of any additional undesirable phases was confirmed experimentally via electron microscopy observations from a previous study [49].

From these initially identified regions, a potential design space was outlined by moving compositionally along directions known to benefit oxidation, and towards the corners of the calculated γ/γ' field. The edges of this design space were selected as the initial domain of SB-CoNi alloys. After synthesis and experimental characterization of these alloys, further refinements were made to the composition domain to target improvements in oxidation and γ' stability, while remaining within the two-phase field. Finally, single crystals of the final composition were grown by the Bridgman technique for characterization of high temperature creep properties.

3.2.2 Experimental Approach

Alloy compositions designed by the above approach were synthesized via arc melting of high purity elemental components in a Centorr 5-Series Bell Jar single arc furnace

(Centorr, Nashua, NH) under gettered Ar ($X_o \leq 10^{-11}$). Lenticular buttons 11 mm tall by 28 mm diameter with masses of ~40 g were melted and inverted three times to improve bulk homogeneity, and then solution heat treated at 1245 °C for 12 h, followed by an aging treatment at 1000 °C for 50 h, both under vacuum. Alloy compositions were analyzed using electron probe microanalysis (EPMA) on a Cameca (Ametek Inc, Berwyn, PA) model SX100 with five wavelength dispersive spectrometers, a Thermo NSS energy dispersive spectrometer, and a CeB6 thermionic emission electron source. EPMA quantification was conducted in reference to an alloy sample, Co–6.7W–8.9Al–3.3Cr–1.5Ta at.%, that had itself been characterized via inductively coupled plasma (ICP) analysis (Northern Analytical Laboratory Inc., Londonderry, NH).

Samples for oxidation were polished to a 0.05 µm finish on one test face by VibroMet™ polisher with colloidal alumina suspension. Isothermally oxidized samples were injected into the hot zone of a controlled-atmosphere furnace preheated to the temperature of interest, namely 1100 °C. Samples were held at temperature for 1 h, and then extracted from the hot zone over the course of 5 minutes. A nondestructive technique, PSLS, which has previously proven effective in assessing the formation of α-Al_2O_3 scale and the relative amount of overlying oxides [48, 166], was used for initial screening of the thermally grown oxide. Samples were then prepared for sectioning by sealing the surface with adhesive M-bond 610 (Allied High Tech Products Inc., Rancho Dominguez, CA) and curing for 1 h at 175 °C to preserve the oxide layers. Sealed samples were embedded in epoxy and cross-sectioned, followed by mounting again in epoxy to infiltrate any exposed fractures or pores. The exposed cross-section surface was then polished to a finish of 0.05 µm by a VibroMet™ polisher with diamond suspension. The latter was used in preference to an alumina suspension to preclude any embedded particles of the polishing media from interfering with chemical analysis of the oxide microstructure.

Oxide morphology was examined via backscatter electron (BSE) microscopy in an FEI

NovaNano 650 FEG SEM as well as in an FEI XL30 Sirion FEG SEM (ThermoFisher Scientific Inc., Waltham, MA) with energy dispersive X-ray spectroscopy (EDS) at 15 kV (unless otherwise noted). Transmission electron microscopy (TEM) was performed at 200 kV with an FEI Tecnai G2 Sphera on a lamella of the grown oxide, extracted from the exposed cross-section surface via focused ion beam (FIB) milling using an FEI Helios Dualbeam Nanolab 650 down to 5 kV. Scanning transmission electron microscopy (STEM) was performed on 3 mm discs that were thinned to electron transparency using a Fischione twin-jet electropolisher (E.A. Fischione Instruments Inc., Export, PA). Jet polishing was performed with a 92.5 vol.% methanol-7.5 vol.% perchloric acid electrolyte at temperatures between -45 to -40 °C, a voltage of 16 V, and currents between 30-34 mA. ChemiSTEM chemical mapping was performed at 200 kV using a Thermo Scientific Talos equipped with a Super-X detector system. Quantification of the collected EDS spectra was performed within the Velox software package. Differential thermal analysis (DTA) was performed on a Setaram Setsys 16/18 (Setaram, Caluire, France) with ~350 mg of material in alumina crucibles at a heating rate of 5 °C min^{-1} under flowing argon. X-ray diffraction (XRD) goniometry was conducted of select unoxidized alloys using a Panalytical Empyrean Powder Diffractometer (Malvern PANalytical, Royston, UK). Density measurements were performed on unoxidized alloy samples using the Archimedes method of comparing sample weights in air vs. submerged in deionized water.

In order to fabricate large single crystals for mechanical testing, an alloy ingot was melted by Sophisticated Alloys Inc. (Butler, PA). Single crystal bars approximately 15 mm diameter by 175 mm long were fabricated through the Bridgman growth process with a five-bar investment mold. The mold was pre-heated to 1575 °C before extraction from the furnace hot zone at a rate of 3.4 mm min^{-1}. After removal from the mold, the bars were etched with a solution (vol.%) of 86% HCl–2% HNO_3–12% H_2O+160g $FeCl_3$. ⟨001⟩-oriented specimens were extracted from above the pigtail (bottom of the bar) and the top

of the bar for as-cast segregation measurements by EPMA. Line scans from the dendrite cores to the interdendritic regions confirmed the enrichment and depletion of each major alloying addition from the liquid during solidification. Additional compositional data was collected in a 20 x 20 pt. grid over a 1 mm^2 area across both specimens, sorted using information from the line scans, and subsequently fit with the Scheil equation

$$C_s = kC_o(1 - f_s)^{k-1} \tag{3.1}$$

where C_s is the concentration of an element in the solid at a given fraction solidified value (f_s, which ranges from 0 to 1), C_o is the initial concentration in the melt, and k is the distribution coefficient defined as C_s/C_l where C_l is the concentration of the liquid at a given fraction solidified. By sorting the collected compositional data from the 20 x 20 pt. grid from highest to lowest (or lowest to highest if k <1 for an alloying addition), one can assign an apparent fraction solidified to each data point. Regression fits were applied to data points with apparent f_s values ranging from 0.1 to 0.9 in order to determine statistically significant measurements of the distribution coefficients, k, for each major alloying addition.

The single crystal bars were heat treated under vacuum with a solutionizing treatment at 1245 °C for 12 h followed by aging at 1000 °C for 50 h, in order to produce a regular γ/γ' microstructure. Button-head creep specimens with a 3 mm gauge width were machined from the single crystal bars and finished with a low-surface stress grinding technique. High temperature tensile creep rupture tests were performed under vacuum on a 3:1 lever-arm creep frame integrated with an Oxy-Gon (Epsom, NH) vacuum furnace. An R-type thermocouple was placed onto the gauge section of the creep specimens before testing for temperature monitoring and creep displacements were measured with a pair of linear variable differential transformers. Thermal expansion measurements were performed up

to 1250 °C in air on 25.4 mm long cylinders of alloy with a Model 2016 HU Orton (Westerville, OH) push-rod dilatometer that was calibrated with a 25.4 mm long Al_2O_3 standard prior to testing. Room temperature elastic modulus measurements were made using resonant ultrasound spectroscopy, whereby a Bayesian-inference framework was applied to determine the C_{11}, C_{12}, and C_{44} elastic constants from the acquired resonance frequencies with high accuracy [121].

3.3 Results

Isothermal isoconcentrate (ITIC) sections were calculated for compositions shown previously to yield promising oxidation behavior [49]. The γ/γ' two-phase field was predicted to be absent at 1100 °C at constant 25.0 at.% Ni, 2.0 at.% Cr, 3.5 at.% Ta, a baseline point for the promising region identified earlier, so an additional ITIC section was calculated at an increased Ni content of 35 at.% to stabilize the γ' phase [27]. The desired γ/γ' field was present in this higher-Ni ITIC section, and the results from PSLS screening of oxidized samples were overlaid on this plot (Fig. 3.1). By comparing the domain of promising oxidation behavior (green circles) with the γ/γ' field, an alloy composition that lies within both domains, and thus attains balanced properties i.e. a two-phase γ/γ' alloy with promising oxidation behavior, was identified and labeled button 2-6G (asterisk in Fig. 3.1). This 2-6G alloy composition arrived at from the combinatorial approach would serve as a starting point for the design of the SB-CoNi alloy series. The starting composition was measured by EPMA as Co–32.4Ni–4.4W–11.7Al–3.3Cr–1.5Ta at.%.

From the composition of starting alloy 2-6G measured by EPMA, the Ta was increased to 3.5 at.% to promote stability of the γ' phase. Subsequently, the design space of the SB-CoNi alloys was outlined by moving towards the corners of the calculated γ/γ' phase field in directions favorable for oxidation behavior (Fig. 3.2). In this manner, the

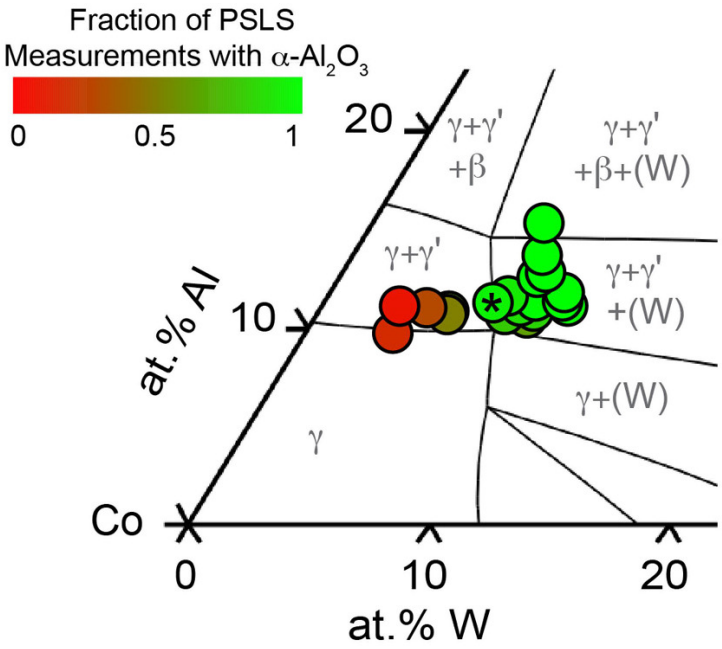

Figure 3.1: Calculated ITIC section at 1100 °C through Co-Al-W at a constant 2.0 Cr–3.5 Ta–35.0 Ni at.% with overlaid PSLS assessment of oxidation behavior. The composition of button 2-6G (SEM EDS) is marked (*), and lies within regions of both more desirable oxidation behavior (green) and the calculated γ/γ' two-phase field.

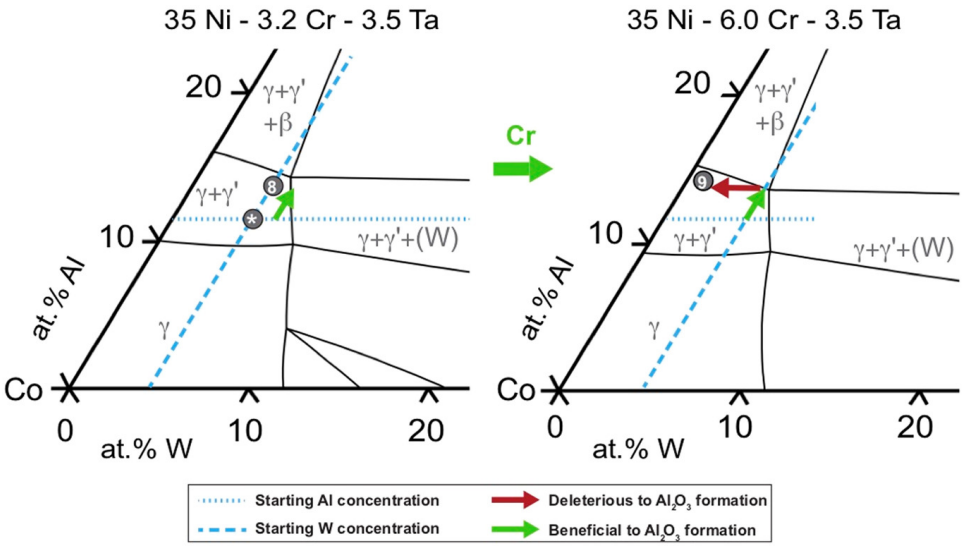

Figure 3.2: Calculated ITIC sections at 1100°C through Co-Al-W at constant 3.2 (left) or 6.0 (right) Cr–3.5 Ta–35.0 Ni at.%, 1100 °C with the compositions of button 2-6G (*), SB-CoNi-8, and SB-CoNi-9 plotted, as measured by EPMA. Compositional effects on oxidation behavior are marked with red arrows if deleterious, and green if beneficial, based on prior studies in this composition space [49].

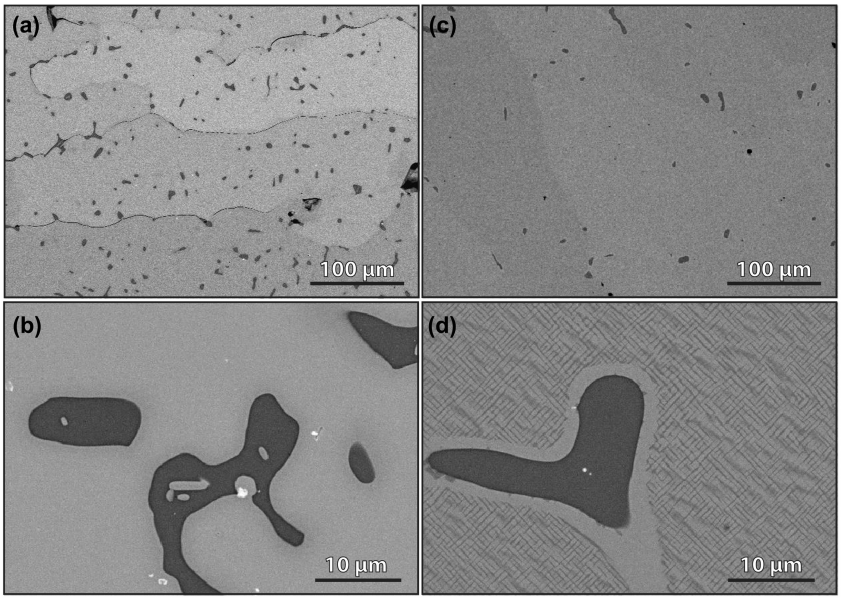

Figure 3.3: BSE micrographs of the alloy microstructures after heat treatment of SB-CoNi-8 (a,b) and SB-CoNi-9 (c,d). An Al-rich third phase is frequently observed (dark grey), and the cuboidal γ/γ' is seen in SB-CoNi-9 at high magnification, with a layer of γ' surrounding the Al-rich particles (d).

compositions of alloys SB-CoNi-8 and SB-CoNi-9 were realized. SB-CoNi-8 has increased Al content from the starting composition 2-6G, which is known to benefit Al_2O_3 formation. SB-CoNi-9 has both increased Al and Cr contents compared to 2-6G, and decreased W content to stay within the calculated γ/γ' phase field. While reduced W content is expected to undesirably increase oxide thickness based on previous experiments in this senary alloy space [49], Al and Cr additions were observed to strongly benefit alumina formation, and would be expected to outweigh the effect of reduced W content on oxidation behavior.

The mechanisms by which alloying elements affect oxidation behavior are discussed in the previous publication [4], but briefly: increased Al will promote its own oxide as the chemical potential of Al is increased and outward diffusivity accelerated, the beneficial effects of Cr on oxidation are attributed to the "third element effect" [159], where an increased Ni:Co ratio is observed to increase Al diffusivity in the bulk alloy [167], and

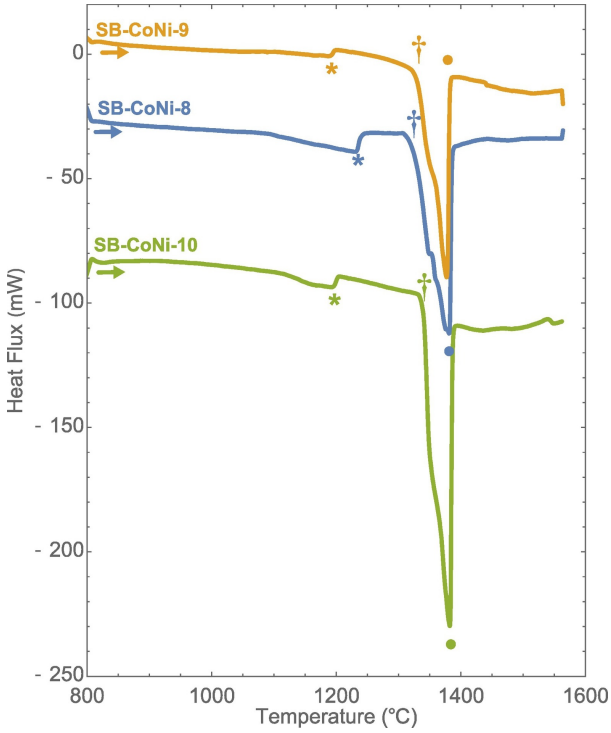

Figure 3.4: DTA heating curves of SB-CoNi-8, 9, and 10 (vertically offset for clarity). Features marked are the γ' solvus (*), solidus (†), and liquidus (•).

increased W is hypothesized to concomitantly increase the Al chemical potential in the senary system [49]. The microstructures of SB-CoNi-8 and -9 after solidification and heat treatment, shown in Fig. 3.3, include a small volume fraction of an Al-rich, likely β-(Ni,Co)Al phase, presumably in a γ/γ' matrix. The latter is difficult to observe in the SEM images for SB-CoNi-8, but its presence in the unoxidized alloy is confirmed by both DTA (Fig. 3.4) and XRD (Fig. 3.5). The cuboidal γ/γ' microstructure was clearly evident for SB-CoNi-9 in BSE/SEM, Fig. 3.3(d), which contains a high fraction of γ' (>50 vol.%).

The γ' solvi of SB-CoNi-8 and 9 alloys were 1233°C and 1191°C, respectively (Table 3.2). After isothermal oxidation in air at 1100 °C for 1 h, both SB-CoNi-8 and -9 exhibited a well-defined α-Al_2O_3 signal by PSLS. After sectioning (Fig. 3.6c-f), both alloys indeed contained a continuous α-Al_2O_3 scale, with SB-CoNi-8 having some portions

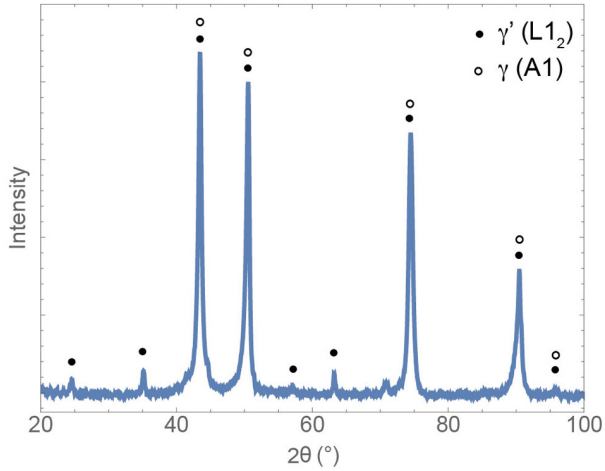

Figure 3.5: XRD scan of SB-CoNi-8, exhibiting reflections from both the γ and γ' phases similar to those seen in Co-Ni-W-Al alloys [27].

Table 3.1: Target and measured alloy compositions. Composition changes for each iteration are in bold.

Alloy	Ni:Co	Co	Ni	Al	W	Cr	Ta
2-6G (EPMA)	0.70	46.6	32.5	11.7	4.4	3.3	1.5
SB-CoNi-8 (Nominal)	**0.88**	39.6	35.0	**14.2**	4.4	3.3	**3.5**
SB-CoNi-8 (EPMA)	0.87	40.0	34.8	14.0	4.4	3.3	3.5
SB-CoNi-9 (Nominal)	0.87	40.3	35.0	14.2	**1.0**	**6.0**	3.5
SB-CoNi-9 (EPMA)	0.87	40.4	35.2	14.3	1.0	5.9	3.2
SB-CoNi-10 (Nominal)	**0.92**	39.8	36.5	**13.2**	1.0	6.0	3.5
SB-CoNi-10 (ICP)	0.93	39.8	37.1	13.1	1.0	5.5	3.5

of oxide ~4.5µm in thickness, and other regions of ~2 µm, for an average oxide thickness of 3.2 µm (Fig. 3.6c,d). These oxide features were similar, though thinner overall, to the oxides observed in starting composition 2-6G (Fig. 3.6a,b). On the other hand, SB-CoNi-9 had a more consistent average thickness of ~1.9 µm (Fig. 3.6e,f). The ~2 µm thick portions of oxide scale in both samples appeared to be primarily Al_2O_3 overlaid by a layer of spinel, while those portions of SB-CoNi-8 that were thicker additionally consisted of outer (Co,Ni)O, and an internal oxidation zone (IOZ) of internally formed Al_2O_3 embedded within tungstate, above the continuous Al_2O_3 (Fig. 3.6d). This unusual scale microstructure has been observed in previous samples, and is discussed at length

Table 3.2: Calculated and experimentally measured solidi and solvi temperatures. All temperature measurements are in °C. P = PANDAT, E = Experimental.

Alloy	Solvus (P)	Solidus (P)	Solvus (E)	Solidus (E)
2-6G (EPMA)	1111	1370	-	-
SB-CoNi-8 (Nominal)	1218	1274	-	-
SB-CoNi-8 (EPMA)	1216	1277	1233	1324
SB-CoNi-9 (Nominal)	1244	1254	-	-
SB-CoNi-9 (EPMA)	1244	1262	1191	1331
SB-CoNi-10 (Nominal)	1236	1275	-	-
SB-CoNi-10 (ICP)	1238	1280	1196	1340

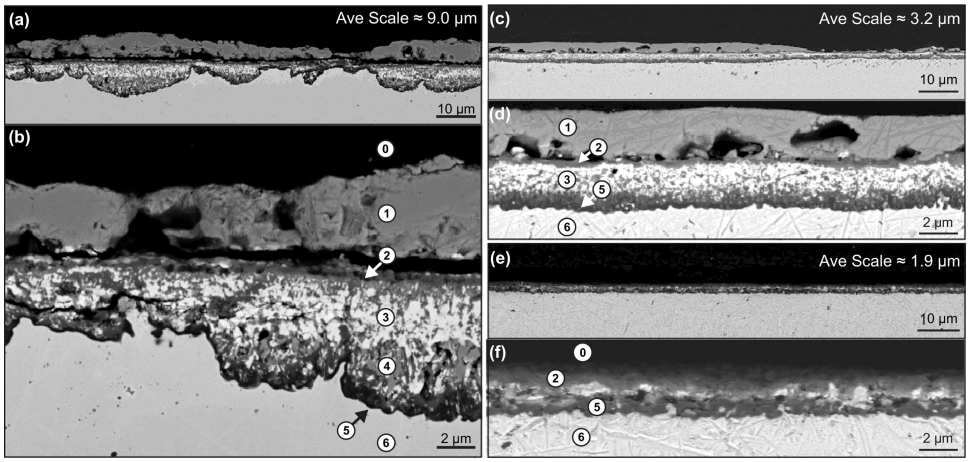

Figure 3.6: BSE micrographs of cross-sectioned (a,b) 2-6G, (c,d) SB-CoNi-8, and (e,f) SB-CoNi-9 after oxidation for 1 h at 1100 °C. Phases in (b,d,f) are labeled based on SEM EDS information: (0) epoxy mount, (1) (Co,Ni)O, (2) (Co,Ni)Al_2O_4, (3) (Co,Ni)(W,Ta)O_4, (4) Ni-rich (Co,Ni)O, (5) Al_2O_3, (6) unoxidized alloy.

in a prior publication [49]. Occasionally, high aspect ratio particles were observed underneath the continuous Al_2O_3 layer (not shown), nominally identified as AlN based on SEM EDS.

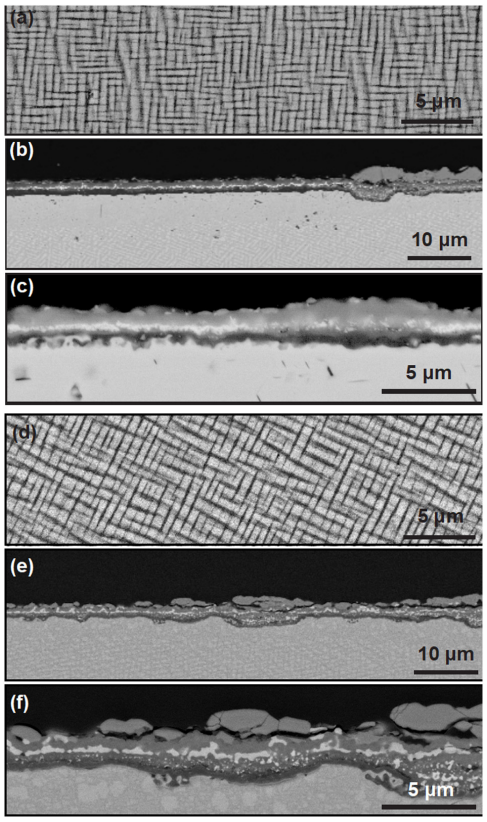

Figure 3.7: BSE micrographs of the SB-CoNi-10 (a) microstructure and (b,c) oxide scale after 1 h at 1100 °C, and the polycrystalline casting of SB-CoNi-10+ (d) microstructure and (d,e) oxide scale after 1 h at 1100 °C. TEM analysis of the scale on SB-CoNi-10 is given in Fig. 3.8.

Based on the alloys that outline the general design space for oxidation resistant γ/γ' Co-Ni-Al-W-Cr-Ta compositions, SB-CoNi-9 was chosen for further refinement based on its superior oxidation resistance in spite of its reduced γ' solvus over SB-CoNi-8. To remove the undesirable Al-rich phase observed in SB-CoNi-9, the Al content of the alloy was slightly lowered, and the Ni content was raised to increase the solubility i.e. expand the size of the γ/γ' two-phase field. The result was SB-CoNi-10 (Table 3.1, Fig. 3.7a-c), which had a high γ' phase fraction (>50 vol.%) and a cuboidal γ/γ' microstructure with no additional alloy phases after heat treatment. Oxidation for 1 h in air at 1100 °C revealed alumina formation, with a total oxide scale thickness ~2 µm. More in-

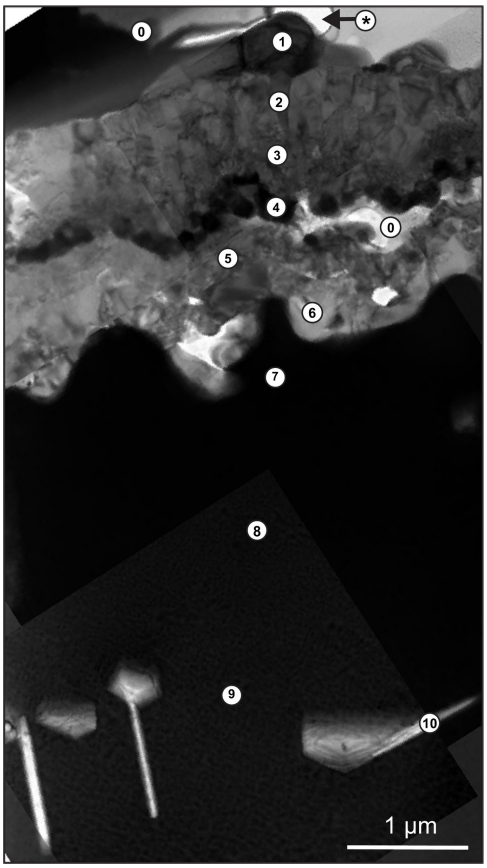

Figure 3.8: Stitched bright-field TEM micrographs of SB-CoNi-10 oxidized for 1 h in air at 1100 °C. Labeled points correspond to TEM EDS measurements (Table 3.3), and are nominally identified as (*) voids, (0) epoxy, (1) (Co,Ni)O, (2) $CoAl_2O_4$, (3) $Co(Al,Cr)_2O_4$, (4) $(Co,Ni)Ta_2O_6$, (5) mixed oxides, (6) Al_2O_3, (7-9) metal within the alloy depletion region, and (10) AlN.

depth analysis by TEM (Fig. 3.8, Table 3.3) showed the scale after 1 h consisted of occasional outer (Co,Ni)O monoxides, layers of spinel $Co(Al,Cr)_2O_4$, particles of tantalate $(Co,Ni)Ta_2O_6$, mixed oxides, and finally continuous Al_2O_3 scale. Underneath theses oxides was an alloy depletion region lean in Al, followed by high aspect-ratio particles that were identified as aluminum nitrides based on TEM EDS measurements (Table 3.3 point 10). The density of the unoxidized SB-CoNi-10 alloy was measured to be 8.65 g/cm^3, which is comparable to the 2nd-generation Ni-base superalloys currently used in aero-engines and lower than other Co-Al-W base alloys (Fig. 3.9).

Table 3.3: TEM EDS measurements of the features observed in SB-CoNi-10 after 1 h in air at 1100 °C (Fig. 3.8), in at.%.

Point	**Phase**	**Ni:Co**	**Co**	**Ni**	**Al**	**W**	**Cr**	**Ta**	**O**	**N**
1	(Co,Ni)O	0.89	27	24	-	-	-	-	50	-
2	$CoAl_2O_4$	0.41	13	5	42	-	1	-	38	-
3	$Co(Al,Cr)_2O_4$	0.25	14	4	26	-	13	-	43	-
4	$(Co,Ni)Ta_2O_6$	0.49	9	4	4	2	2	25	54	-
5	Mixed	0.68	6	4	34	-	3	1	53	-
6	Al_2O_3	-	-	-	39	-	-	-	61	-
7	Sub-scale Alloy	0.84	46	38	4	1	7	5	-	-
8	Sub-scale Alloy	0.91	44	39	5	1	6	4	-	-
9	Sub-scale Alloy	0.95	42	40	7	1	6	4	-	-
10	AlN	0.94	3	3	54	-	-	-	1	38

The SB-CoNi-10 alloy composition was further modified with minor alloying additions of the reactive elements Hf and Y that are known to be beneficial for Al_2O_3 adhesion [165]; B which is observed to reduce oxide scale thickness and promote adhesion [43]; and C which is demonstrated to decrease the incidence of freckle chain defects during single crystal solidification in Ni-base superalloys by reducing the solidification segregation of refractory elements like Ta and W [53]. This alloy was denoted as SB-CoNi-10+ and an ingot of this alloy was acquired for casting using the Bridgman method. An ICP chemical analysis of this ingot prior to casting is given in Table 3.4. Prior to single crystal casting, alloy SB-CoNi-10+ consisted of the same cuboidal γ/γ' microstructure as SB-CoNi-10 when aged similarly (Fig. 3.7d), and formed an oxide scale of a similar morphology after 1 h in air at 1100 °C (Fig. 3.7e,f). After single crystal casting, a macro-etch revealed that the bars did not possess freckle chains or any significant stray grains, as shown in Fig. 3.10. This amenability to single crystal casting is likely aided by favorable partitioning of alloying additions between the solid and liquid during the solidification process. Fig. 2.12 shows a summary of the distribution coefficients for the six major elements within SB-CoNi-10+ and compares them to other Co-base and Ni-base single

Table 3.4: Properties of Co-, CoNi-, and Ni-base γ/γ' alloys from literature (at.%). †Measured by ICP-OES. Sulfur content was < 0.7 parts per million by weight as measured by glow discharge mass spectroscopy.

Alloy	$\mathbf{T}_{\gamma'}$ **(°C)**	$\mathbf{T}_S$ **(°C)**	**Co**	**Ni**	**Al**	**W**	**Ta**	**Cr**	**Ti**	**Other**
CMSX-4 [14, 47]	1291	1337	9.6	Bal.	5.6	6.4	6.5	6.4	1.0	3Re, 0.6Mo, 0.1Hf
FC-2.0 [128]	1113	-	Bal.	30	10	10	-	-	-	2Si
CS-4 [128]	998	-	Bal.	30	10	5	-	-	-	2Si
Unnamed [32]	1269	1298	Bal.	30	10.5	7	2.5	-	4	-
L19 [33]	1126	1317	Bal.	30	7	2	1	-	4	1Nb, 3Mo
ERBOCo-1 [153]	1174	1318	Bal.	32	8	5	1.5	6	2.5	0.4Si, 0.1Hf
SB-CoNi-10+ [34]	1204	1329	Bal.	36.8	13.3	1.0	3.5	5.8	-	0.06C, 0.08B, 0.026Hf, 0.004Y

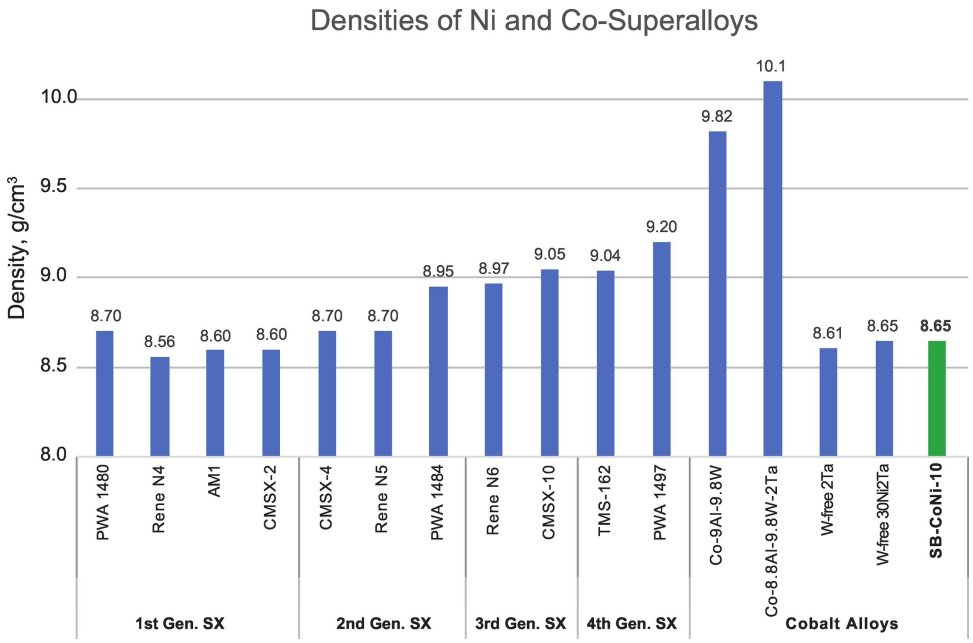

Figure 3.9: Density of SB-CoNi-10 as measured by Archimedes method, compared with commercial Ni-base superalloys and Co-base alloys (g/cm^3) [5, 38, 39].

crystal alloys. Interestingly, the distribution coefficients for Co, W, Ta, and Cr for SB-CoNi-10+ lie between the values observed for Co- and Ni-base alloys, and the value for Al is near unity. Due to this favorable partitioning behavior, it is argued that CoNi-base alloys should be much less susceptible to convective instabilities during casting, which result in casting defects in high-refractory containing Ni-base compositions [168].

The mean coefficient of thermal expansion (CTE) and the instantaneous CTE determined by push-rod dilatometry are shown in Fig. 3.12 compared to 2^{nd}-generation Ni-base superalloy René N5. The mean CTE increases smoothly with temperature, with the exception of reversible anomalies observed near 600 °C and a sharp discontinuity near the γ' solvus temperature, which is related to the dissolution and re-precipitation of the γ' precipitates. The behavior observed at 600 °C has been observed in previous studies of the thermal expansion behavior of CoNi-base alloys, and has interestingly only been observed in Cr containing alloys [153, 169]. Across the entire temperature range investi-

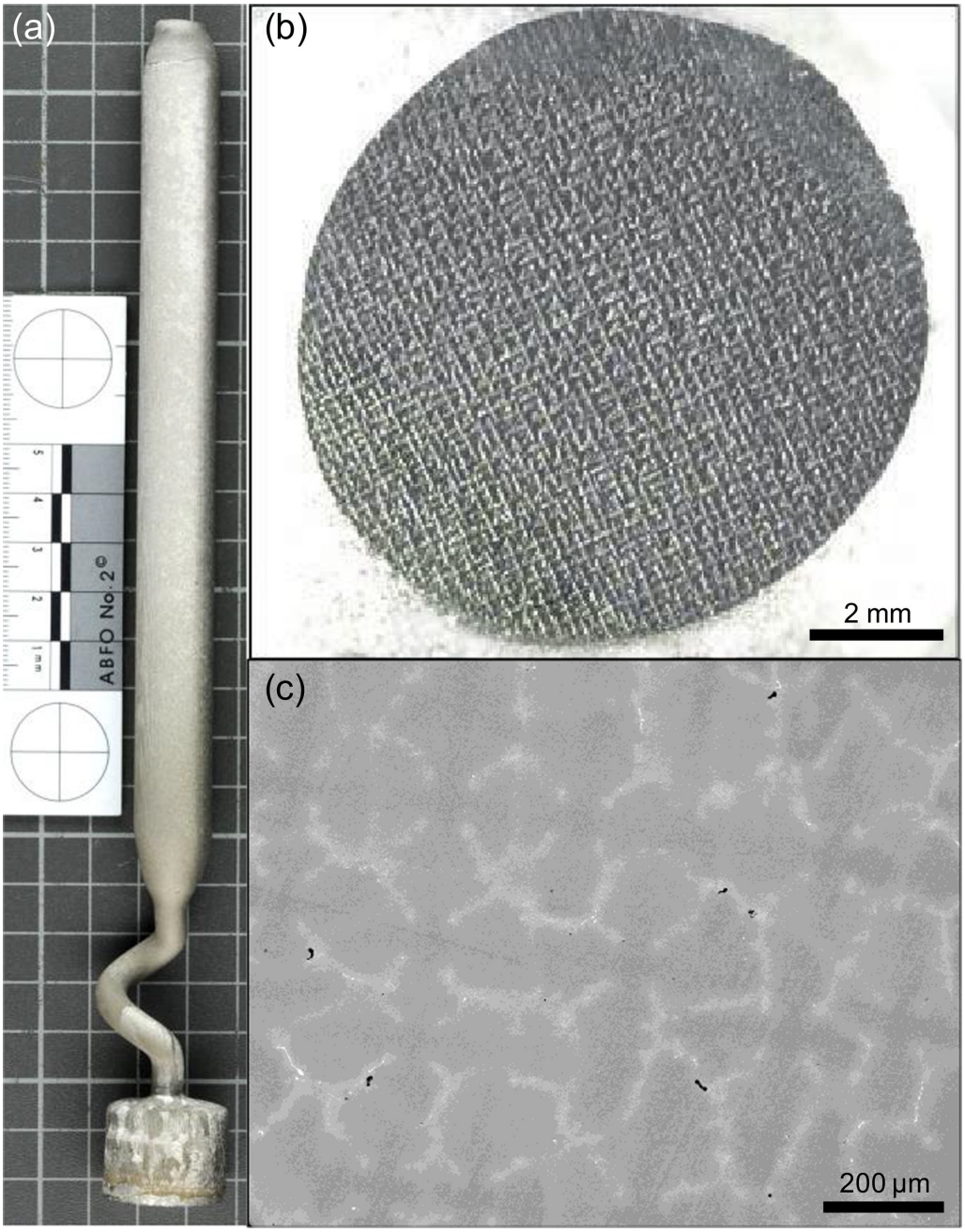

Figure 3.10: Single crystal casting of SB-CoNi-10+ alloy prior to homogenization showing (a) an optical image of an etched single crystal bar, (b) an optical image of an etched section of the bar revealing the dendritic structure along the [001] growth direction with no stray grains, and (c) an SEM BSE micrograph of the dendrites with changing contrast as a result of solute segregation, as quantified in Fig. 3.11. The grid background of (a) has 1 cm spacing.

Table 3.5: Room temperature elastic properties and directional Young's Modulus determined by resonant ultrasound spectroscopy.

	SB-CoNi10+	Co-2Ta[121]	CoNi-A[121]	ERBOCo-1[153]	CMSX-4[121]
C_{11} (GPa)	**236.4**	258.8	256.7	261.8	249.0
C_{12} (GPa)	**150.9**	164.5	157.6	162.9	157.0
C_{44} (GPa)	**133.9**	147.7	142.1	140.1	129.2
Zener Anisotropy	**3.133**	3.133	2.868	2.833	2.809
S_{11} (TPa^{-1})	**8.419**	7.637	7.310	7.308	7.838
S_{12} (TPa^{-1})	**-3.281**	-2.968	-2.781	-2.803	-3.031
S_{44} (TPa^{-1})	**7.470**	6.770	7.037	7.138	7.740
$E_{\langle 100 \rangle}$ (GPa)	**118.8**	130.9	136.8	136.8	127.6
$E_{\langle 110 \rangle}$ (GPa)	**225.4**	248.3	248.5	247.7	230.5
$E_{\langle 111 \rangle}$ (GPa)	**321.7**	354.1	341.5	339.4	315.3

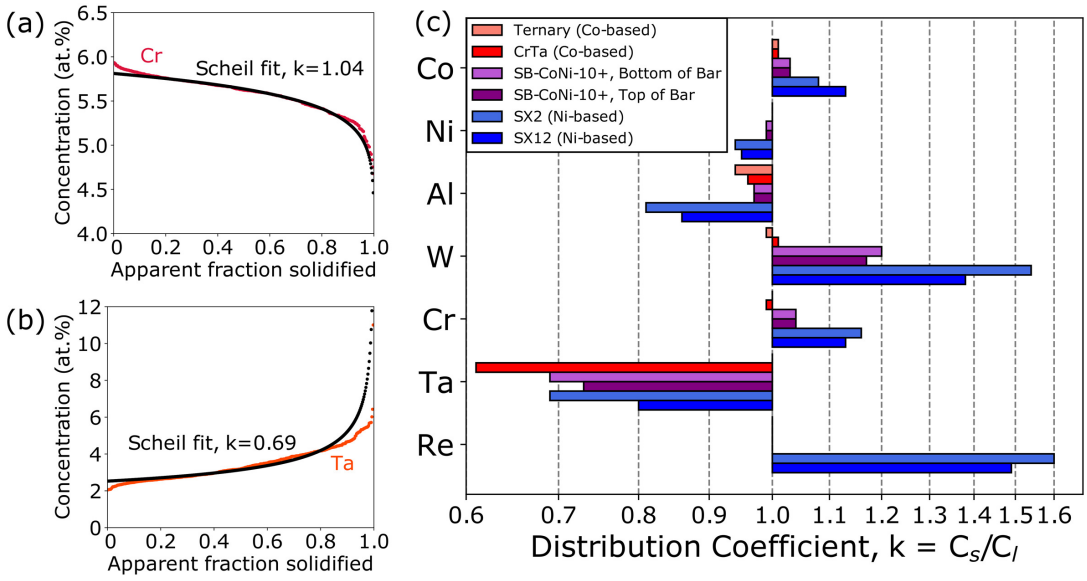

Figure 3.11: Results of EPMA compositional mapping on as-cast SX SB-CoNi-10+. The compositional data and Scheil curve fit for (a) Cr and (b) Ta are presented, along with (c) a summary of the distribution coefficients for SB-CoNi-10+ compared to Co- and Ni-base alloys [51, 53].

gated, SB-CoNi-10+ displays a higher CTE than René N5, which could have detrimental implications for the strain tolerance and durability of thermal barrier coatings used in higher temperature applications [169]. Additionally, the room temperature elastic constants C_{ij} determined by resonant ultrasound spectroscopy (RUS) are displayed in Table 3.5. While the C_{11}, C_{12}, and C_{44} values are lower than other reported Co-base alloys, the Zener Anisotropy ratio ($A = 2C_{44}/(C_{11}\text{-}C_{12})$) has a value >3, similar to Co-base alloys without any Ni content [121]. The magnitude of the elastic anisotropy is an important term in the Yoo torque expression [170] that describes the propensity for superlattice screw dislocations to cross-slip, which is a necessary mechanism for the anomalous effect of temperature on yield strength observed in modern superalloys. Since there is less pronounced anisotropy in the antiphase boundary energies between the cube and octahedral planes for γ'-$Co_3(Al,W)$, alloys with increased elastic anisotropy may provide improved elevated temperature strength due to the higher driving force for cross-slip [171].

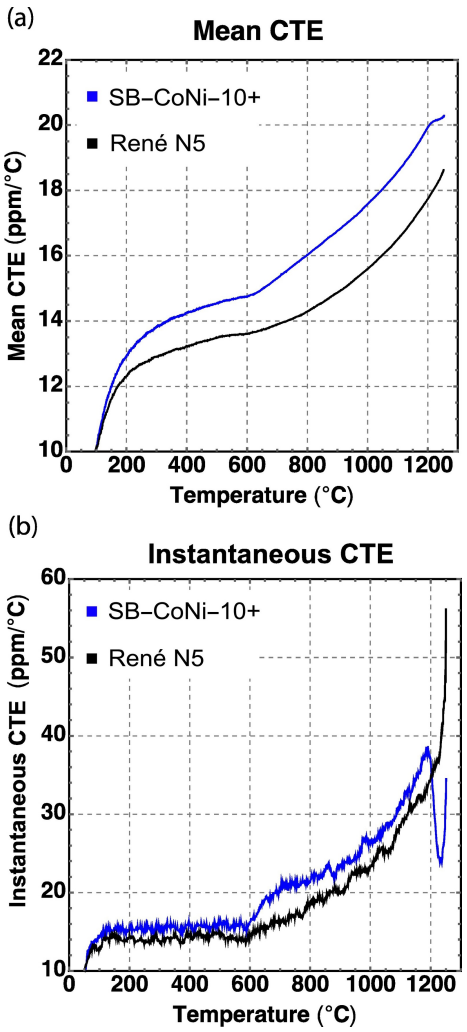

Figure 3.12: Dilatometry data the mean coefficient of thermal expansion and the instantaneous CTE of SB-CoNi-10+ compared to 2nd-gen. Ni-base superalloy René N5.

The elemental partitioning between the γ channels and the γ' precipitates within SB-CoNi-10+ was investigated by STEM. Fig. 3.13(a) shows a high angle annular dark field image of the two-phase γ/γ' microstructure, revealing the high γ' volume fraction along with the presence of small tertiary γ' precipitates within the γ channels. The chemical maps displayed in Fig. 3.13(b-g) show how the major alloying elements are partitioned between the precipitates and the matrix. By taking the ratio between the compositions of these two regions, partition coefficients ($k_{\gamma'/\gamma}$) were found for all major alloying additions

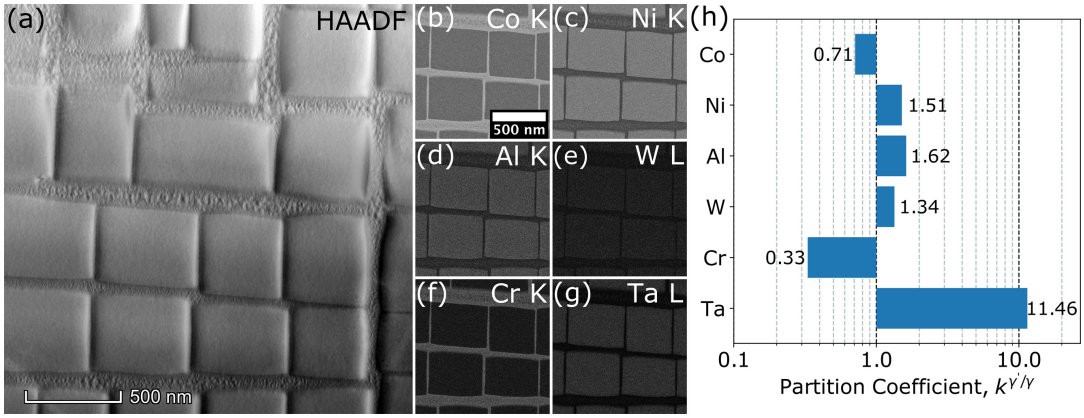

Figure 3.13: (a) High angle annular dark field STEM micrograph of SB-CoNi-10+ after heat treatment. Chemical maps for the six major elements within SB-CoNi-10+ are displayed in (b-g), along with (h) the partition coefficient $k_{\gamma'/\gamma}$ for the major elements in SB-CoNi-10+ extracted from (b-g).

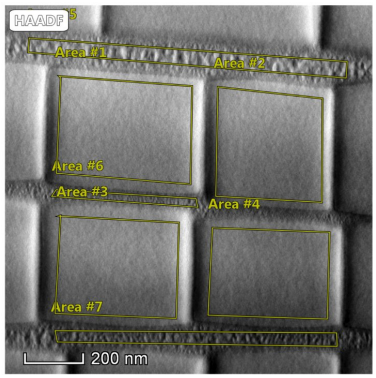

Compositions acquired by STEM-EDS mapping (at.%)

Area	Co	Ni	Al	W	Ta	Cr	
#1	37.58	40.00	13.99	1.37	3.55	3.51	γ'
#2	37.39	40.07	14.14	1.33	3.59	3.49	
#3	37.39	39.81	14.29	1.40	3.59	3.51	
#4	37.58	40.00	13.99	1.37	3.55	3.51	
#5	51.87	27.54	8.88	1.04	0.42	10.25	γ
#6	55.55	23.99	7.81	1.02	0.12	11.51	
#7	53.69	25.49	8.55	1.00	0.21	11.07	

Figure 3.14: Compositions of the γ and γ' phases in SB-CoNi-10+ measured by STEM-EDS.

and displayed in Fig. 3.13(h). The compositions of several γ channels and multiple γ' precipitates in a focused region measured by STEM-EDS are presented in Fig. 3.14.

The results of two creep tests performed in vacuum on single crystals taken to rupture are shown in comparison to other Co-, CoNi-, and Ni-base superalloys from the literature in Fig. 3.15. SB-CoNi-10+ is shown to have a behavior similar to 1st-generation Ni-base single crystal alloys and performs more favorably than most other Co- and CoNi-base alloys by having a longer time to rupture under similar temperature and stress conditions

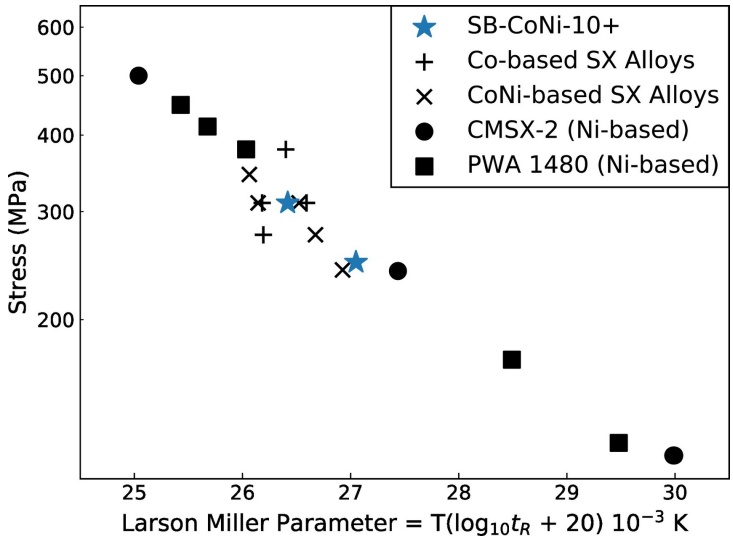

Figure 3.15: A Larson-Miller plot comparing SB-CoNi-10+ to Co-, CoNi-, and Ni-base γ/γ' alloys from the literature. The creep rupture life SB-CoNi-10+ performs similarly to 1^{st}-gen. Ni-base superalloys such as CMSX-2 and PWA 1480 [63, 62, 172, 173].

3.4 Discussion

Using a suite of new alloy design tools, a single crystal alloy with a balanced set of properties has been identified and designated as SB-CoNi-10+. In contrast to the previously investigated $L1_2$-containing Co- and CoNi-base alloys, SB-CoNi-10+ possesses a high solvus and the ability to form a continuous alumina layer with only small amounts of overlying scale during oxidation at 1100 $^\circ$C.

3.4.1 First iteration designs (SB-CoNi-8 and 9): Alloy Microstructure

Comparing the starting composition (2-6G), with the first iteration in alloy design, an appreciable volume fraction of the γ' phase is achieved in SB-CoNi-8 and -9, (Fig. 3.3). However, while all three compositions are predicted by the PANDAT database to fall within the γ/γ' two-phase field, SB-CoNi-8 and 9 both exhibit small amounts of an Al-

rich phase after heat treatment, approximately 4 vol.% and 1 vol.% respectively. This phase is likely β-(Ni,Co)Al as inferred from SEM EDS measurements and the ITIC section showing the three-phase $\gamma/\gamma'/\beta$ field lying close to these alloy compositions (Fig. 3.2). Thus, it is reasonable to ascribe this underprediction of small fractions of the β phase to small inaccuracies in the database, which is still under development. It should also be noted that increasing the Cr content between SB-CoNi-8 and -9 does indeed begin to destabilize the γ' phase and lower the solvus (Table 3.2), as expected [157, 63], though not to an unacceptable level. This Cr content of ~6 at.%, however, is arguably the upper desirable bound in the present senary composition space, as further additions would likely bring the solvus temperature towards that of the oxidation temperature, resulting in the substantial reduction of strengthening γ' phase under the prospective service conditions.

3.4.2 First iteration designs (SB-CoNi-8 and 9): Oxidation Behavior

The oxide microstructure observed in the starting alloy button 2-6G (Fig. 3.6a,b) is unusual, containing a continuous Al_2O_3 layer beneath a IOZ embedded in various other oxides and residual alloy. This microstructure has been discussed at length in a previous publication [49], and is thought to be due to the initial internal oxidation of Al_2O_3, followed by the initiation of patches of continuous Al_2O_3 scale which then grow laterally to undercut the IOZ. Eventually the Al_2O_3 will become continuous and prevent continued oxidation of the underlying metal. If portions of the IOZ embedded in metal are undercut by continuous Al_2O_3 scale before the matrix has oxidized into tungstate, the continued growth of overlying Co-rich oxides may leave behind pockets of IOZ within Ni-rich material at the bottom of the scale layer, above the continuous Al_2O_3, such as seen in Fig. 3.6 point 4. SB-CoNi-8 exhibits a similar scale microstructure to that in

2-6G, with a few notable exceptions. These include the fact that the oxide layers in SB-CoNi-8 are much thinner than their counterparts in 2-6G and that the continuous Al_2O_3 layer is much less tortuous in SB-CoNi-8 (Fig. 3.6d). Furthermore, the entire undercut IOZ in SB-CoNi-8 is embedded in tungstates, with no lower pockets embedded in Ni-rich material.

These changes may be attributed to the fact that SB-CoNi-8 has increased Al content over 2-6G, as well as the fact that the grain size of the arc-melted SB-CoNi-8 (~100-500 µm) is substantially larger than that of the 2-6G sample created by ion plasma deposition (~7 µm). It was previously proposed that the initiation of continuous Al_2O_3 patches after internal oxidation of Al has begun is aided by increased solute diffusion along grain boundaries [49]. In the case of 2-6G, it is posited that the lateral growth of Al_2O_3 scale occurs at a rate not extraordinarily faster than the advancement of the internal oxidation front (IOF). Thus, as the continuous undercutting scale grows, regions of the IOF away from the initiated Al_2O_3 patch have time to progress further down into the alloy substrate. As IOZ undercutting continues, this process would lead to the convoluted final Al_2O_3 scale structure observed in Fig. 3.6a. In the case of SB-CoNi-8, fewer grain boundaries would likely lead to Al_2O_3 patch initiation events occurring much less frequently. Once they do occur, however, the higher Al content could lead to more widespread patch formation. This would yield the observed flatter Al_2O_3 scale, reduced overall scale thickness, and lack of Ni-rich pockets.

In contrast, SB-CoNi-9 appears to exhibit continuous Al_2O_3 scale with no overlying IOZ. This implies that the increased Cr content in SB-CoNi-9 allows formation of continuous Al_2O_3 initially upon oxidation, instead of starting as internal oxidation and later transitioning to continuous behavior. This type of oxidation response is thought to be more desirable than the processes described for SB-CoNi-8, as less of the structural alloy is consumed by the oxidation process, and it would be more likely for any scale spallation

or damage to lead to rapid reformation of the continuous Al_2O_3 layer, instead of restarting non-protective IOZ formation and growth. It should be noted, however, that a γ' denuded zone was observed underneath the formed oxide scale, indicating an Al depletion layer in the alloy that may prevent or delay the onset of continuous Al_2O_3 reformation in the event of spallation. This will be investigated via longer time oxidations and thermal cycling exposure in a future study. It will additionally be of interest to address the effects of lower temperatures, as decreased outward diffusion of Al below 1100 °C may also prevent or delay continuous Al_2O_3 scale formation. Nevertheless, for the purpose of achieving oxidation behavior comparable to that of 2nd generation Ni-base superalloys [14], the present scale behavior after 1 h at 1100 °C is promising for preventing significant metal loss by oxidation.

Overall, the superior oxidation behavior of SB-CoNi-9 in forming continuous Al_2O_3 scale initially without IOZ formation, albeit with small amounts of overlying oxide, was deemed more desirable despite the reduced γ' solvus from increased Cr content. As such, this composition was selected for further modification. SB-CoNi-10 composition was arrived at by slightly decreasing the Al content and increasing the Ni content to shift the alloy towards the two-phase γ/γ' field, preventing formation of the Al-rich β phase.

3.4.3 Final Design: SB-CoNi-10 and -10+

Analysis of the SB-CoNi-10 alloy microstructure (Fig. 3.7a) shows the compositional modifications were successful in preventing the formation of the β phase. Additionally, neither the γ/γ' microstructure, nor the γ' solvus temperature (Table 3.2) were changed appreciably. While removing the ordered B2 - β phase may benefit the mechanical properties of the alloy, one concern is that this will reduce Al reservoirs and hinder continuous Al_2O_3 scale development. Yet upon oxidation, SB-CoNi-10 still displays the formation of

a continuous Al_2O_3 layer with minimal overlying oxides (Fig. 3.7b,c), albeit with slightly greater amounts of refractory oxide. TEM investigation of a FIB lamella taken from the scale (Fig. 3.8, Table 3.3) shows the oxide overlying Al_2O_3 to be $Co(Al,Cr)_2O_4$ and $(Co,Ni)Ta_2O_6$ (points 2-5), with very occasional grains of (Co,Ni)O (point 1). High aspect ratio particles were still observed underneath the oxidation front (point 10) and TEM EDS confirmed the formation of AlN. The effect of this sub-Al_2O_3 morphology on longer-time exposures will need to be investigated.

The single crystal variant SB-CoNi-10+ is found to have a satisfactory balance of high temperature oxidation behavior via the formation of a continuous Al_2O_3 scale with minimal overlying oxides at 1100 °C, high γ' solvus temperature, favorable solidification characteristics, low density, room temperature elastic properties, and high temperature creep strength. While other CoNi-alloys displayed in Table 3.4 have shown high γ' solvus temperatures above 1200 °C [32] or beneficial oxidation response [128], the combinations of both of these properties simultaneously in SB-CoNi-10+ has not yet been achieved to the authors' knowledge in other CoNi-base alloys. The promising creep rupture resistance and elastic properties make this alloy a promising candidate for single crystal alloy components. Additionally, the favorable solute distribution observed after solidification indicates that processing through additive manufacturing pathways such as laser powder bed fusion or electron beam melting may yield crack-free components with high γ'-volume fractions over 60%, which has been difficult to achieve using traditional single crystal Ni-base superalloy compositions [98, 99, 174]. Given the favorable properties of the alloys investigated here, this region of the CoNi-base composition space is promising for future alloy development. Finally, the presented strategy would thus likely be an efficient approach for other alloy systems currently under development, where alumina formation over a large amount of composition space is desirable to achieve the properties of interest.

3.4.4 Yield Strength Anomaly in Co-Ni design space

Since the CoNi-base superalloy design space appears promising for further alloy development, a greater fundamental understanding of the effect of Co on the strength of the Ni_3Al γ' phase at various temperatures is desired. As temperature increases, the 0.2% offset yield strength of pure γ' Ni_3Al alloys increases from less than 100 MPa at room temperature to almost 600 MPa at a peak temperature near 700 °C. This effect is known as the yield strength anomaly, or YSA, and it is responsible for the high strength retained by superalloys at elevated temperatures. Quasi-static compression tests (strain-rate = 1×10^{-4}) on single crystals of SB-CoNi-10+ at room temperature, 750 °C, and 950 °C have resulted in yield strengths of 502 MPa, 592 MPa, and 372 MPa, respectively. While SB-CoNi-10+ does exhibit a YSA, it is currently unclear why this alloy exhibits yield strengths lower than Ni-base single crystals such as CMSX-4 which can be in excess of 1 GPa at the peak temperature with proper heat treatment [175]. Several systematic studies have been performed exploring the effect of various alloying additions on the YSA, including Ti, Zr, Hf, V, Nb, Ta, Mo and W [56], however a similar study investigating systematic additions of Co to Ni_3Al had not yet been performed. This was pursued through a combined experimental and computational approach involving high temperature compression testing, planar fault modeling, and CALPHAD phase stability calculations. The details of this study have been published in a prior article, and the key results are summarized below [176].

Anisotropy in the antiphase boundary energies (APBE) on the {111} and {010} planes and the elastic anisotropy are known to strongly influence the YSA. An expression for the driving force for dislocation cross-slip due to the anisotropy in APBE coupled with

elastic anisotropy between the {111} and {010} planes was derived by Yoo [170]:

$$\frac{\gamma_{APB(111)}}{\gamma_{APB(010)}}(1 + f\sqrt{2}) > \sqrt{3} \tag{3.2}$$

$$f = \frac{\sqrt{2}(A-1)}{A+2} \tag{3.3}$$

where $\gamma_{APB(010)}$ is the APBE of the cube plane, $\gamma_{APB(111)}$ of the close-packed plane, and A is the Zener anisotropy ratio defined as $A = 2C_{44}/(C_{11}\text{-}C_{12})$. Determining the relevant APB energies is difficult experimentally since this often relies on TEM investigations that measure the separation distance of closely-coupled dislocation pairs within the γ' phase. Instead, computational approach based on a diffuse multi-layer model (DMLF) has been employed to calculate the relevant APB energies at various compositions of interest for $(Ni,Co)_3(Al)$ alloys. The details of this model are described more fully in a prior article [11].

Table 3.6: Nominal (measured by ICP) compositions in at.% of alloys for the present study

Alloy	**Nominal γ' composition**	**Al**	**Co**	**Ni**	**RT σ_y (MPa)**
0Co	Ni_3Al	25.0	0.0	75.0	88
		(24.8)	(0.0)	(75.2)	
10Co	$(Ni_0.9Co_0.1)_3Al$	25.0	7.5	67.5	109
		(25.0)	(7.5)	(67.5)	
20Co	$(Ni_0.8Co_0.2)_3Al$	25.0	15.0	60.0	153
		(24.7)	(15.1)	(60.2)	

Three $(Ni_{1-x}Co_x)_3Al$ alloys with increasing Co content were arc-melted and homogenized at 1000 °C for 120 h. The nominal and experimentally measured alloy compositions are shown in Table 3.6. Quasi-static compression tests at various increasing temperatures identified that each of the alloys exhibited a YSA, with the higher Co content alloys exhibiting slightly higher yield strengths across the entire temperature range. This

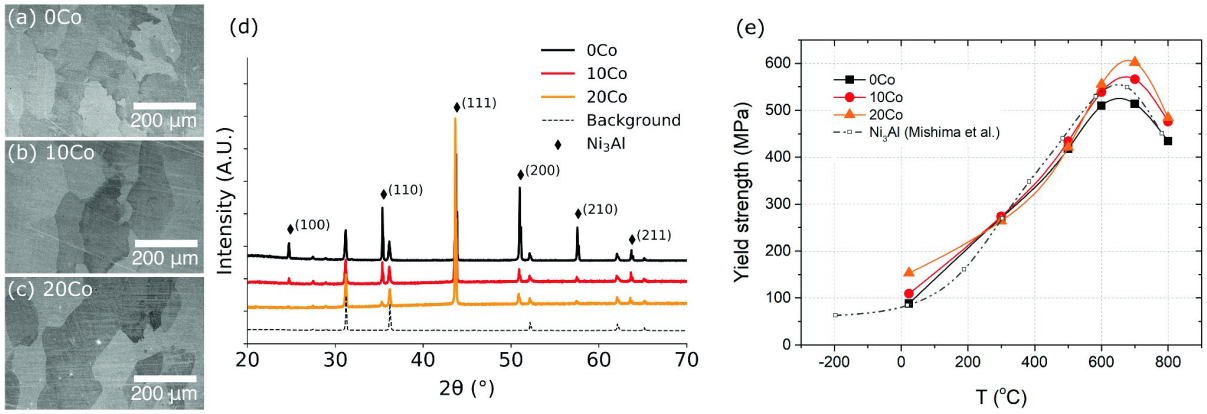

Figure 3.16: BSE micrographs of homogenized (a) 0Co, (b) 10Co, and (c) 20Co samples. (d) XRD spectra of 0Co, 10Co, and 20Co reveal they are single phase $L1_2$. XRD spectra have been scaled such that the background peaks are of comparable intensity in all scans. The peaks present in the background of each diffractogram are due to Pb tape used to isolate each sample during XRD measurements. (e) the yield strength in compression vs. temperature for the alloys investigated in this study, compared to the work of Mishima et al. [56]. Reproduced from "The Yield Strength Anomaly in Co–Ni Design Space" by K.V. Vamsi, S.P. Murray, and T.M. Pollock, 2020, *Superalloys 2020*, p. 948-958. Copyright 2020 by The Minerals, Metals & Materials Society. Reproduced with permission [176].

is presented in Fig. 3.16. XRD measurements confirmed that each of these alloys was single phase γ'. An additional sample denoted as 30Co that had a stoichiometry of $(Ni_{0.7}Co_{0.3})_3Al$ was fabricated and tested, but this alloy was found to contain a small amount of Al-rich β phase and was not considered further in the study. These compression tests validated the DMLF model calculations on the presence of a YSA in this alloy system.

Using the TCHEA3 thermodynamic database, a pseudo-quaternary phase diagram was calculated at 1000 °C to explore the stability of the γ' phase in the Ni_3Al - Ni_3W - Co_3W - Co_3Al system. These calculations are shown in Fig. 3.17 along with regions highlighted that were single-phase γ'. This shows that without additional γ' formers such as W, the Ni_3Al phase can only be alloyed with about 13 at.% Co before the formation of a deleterious β phase. Additionally, these calculations show that at 1000 °C, there is not

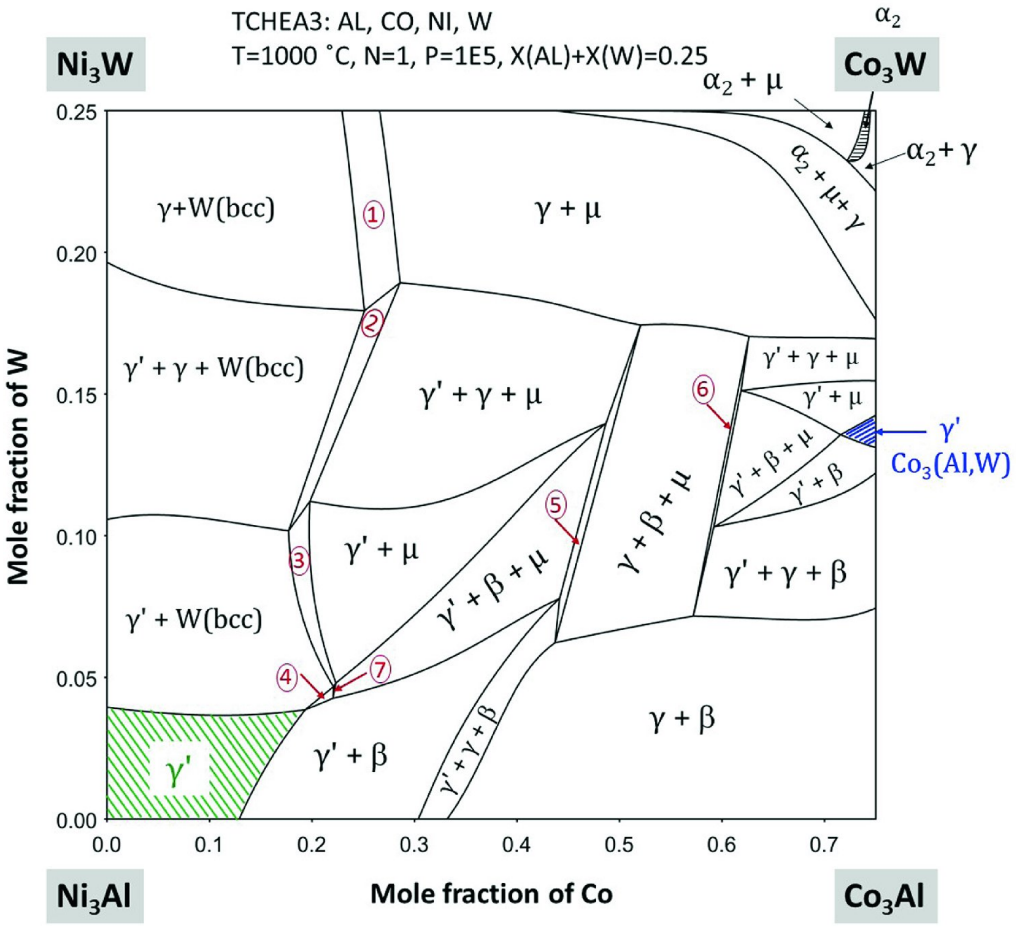

Notation		Phases
1	→	γ + W(bcc) + μ
2	→	γ + γ' + W(bcc) + μ
3	→	γ' + W(bcc) + μ
4	→	γ' + W(bcc) + β
5	→	γ + γ' + β + μ
6	→	γ + γ' + β + μ
7	→	γ' + W(bcc) + β + μ

Phase notation		Structure/Composition
γ	→	fcc/Disordered fcc
γ'	→	$L1_2/(NiCo)_3(Al,W)$
β	→	B2/(Co,Ni)Al
μ	→	Co_7W_6
α_2	→	$D0_{19}/Co_3W$

Figure 3.17: Isothermal pseudo-quaternary phase diagram in the range of Ni_3Al–Ni_3W–Co_3W–Co_3Al at 1000 °C calculated using ThermoCalc with the TCHEA3 database. Reproduced from "The Yield Strength Anomaly in Co–Ni Design Space" by K.V. Vamsi, S.P. Murray, and T.M. Pollock, 2020, *Superalloys 2020*, p. 948-958. Copyright 2020 by The Minerals, Metals & Materials Society. Reproduced with permission [176].

a continuous γ' phase field between Ni_3Al and $Co_3(Al,W)$ within this pseudo-quaternary phase diagram.

DMLF calculations in the above compositional space have shown that additions of Co to Ni_3Al reduces the $\gamma_{APB(111)}$ and $\gamma_{APB(010)}$ up until x = 0.667 (with $(Ni_{1-x}Co_x)_3Al$) above which there is a dramatic increase in the fault energies as Co_3Al is approached. This agrees well with prior studies that have indicated that CoNi-base alloys likely have reduced APB energies compared to Ni-base alloys due to the observations of extended APBs that shear entire γ' particles during the early stages of high temperature creep [68]. The maximum in the APB energies were determined to be at γ' compositions of $(Ni_{0.65}Co_{0.35})_3(Al_{0.5}W_{0.5})$ and $(Ni_{0.6}Co_{0.4})_3(Al_{0.6}W_{0.4})$ for the $\gamma_{APB(111)}$ and $\gamma_{APB(010)}$, respectively. For example, the $\gamma_{APB(111)}$ increases from 209.9 mJ/m^2 for Ni_3Al to ~500 mJ/m^2 for $(Ni_{0.65}Co_{0.35})_3(Al_{0.5}W_{0.5})$. From the perspective of alloy design, alloys with γ' compositions around these maxima should have greater resistance to shearing compared to Ni_3Al. These alloys would be expected to have higher peak yield strengths, due to the following relation between the $\gamma_{APB(111)}$ and the strength [177]:

$$(\sigma_{y_{peak}}) = 0.81M\frac{\gamma_{APB(111)}}{2b}(\frac{3\pi v_{\gamma'}}{8})^{1/2} \tag{3.4}$$

where M is the Taylor factor, b is the magnitude of the $1/2\langle 110\rangle$ Burgers vector, and $v_{\gamma'}$ is the volume fraction of the γ' phase. Applying this combined modeling and experimental approach to other relevant γ' forming alloying additions such as Ta and Ti could result in CoNi-base superalloys with significantly improved strengths due to the increased planar fault energies of resultant γ' compositions. Lastly, the calculations from this study show that the measured Ni:Co ratio of the γ' composition in SB-CoNi-10+ of 0.52Ni:0.48Co (see Fig. 3.14, where the γ' is Ni-rich even though the alloy contains more Co than Ni) is not expected to possess the highest strength compared to γ' compositions with higher

Ni content. Therefore, designing CoNi-alloy γ' compositions with increased Ni contents than are currently expressed would be desirable, but this is likely difficult to achieve without increasing the Ni content such that the alloy becomes a NiCo-base alloy.

3.4.5 Elastic properties as a function of temperature

The SB-CoNi-10+ single crystal alloy has recently been used to validate a new experimental technique to determine the elastic moduli (C_{ij} in Voigt notation) and elastic anisotropy, A, of single crystals as a function of increasing temperature. The approach is based on resonant ultrasound spectroscopy (RUS) where SiC-tipped piezoelectric transducers are used to drive and measure resonance frequencies in a rectangular parallelepiped (RT) superalloy specimen. Through the incorporation of a induction heater and non-contact pyrometer, it was possible to rapidly heat the alloy and collect resonance spectra which were later analyzed using a Bayesian inference RUS code called CmdStan-RUS that uses a self-tuning Hamiltonian Monte Carlo (HMC) sampler to simultaneously determine the elastic constants and the crystal orientation. A schematic of the experimental setup is presented in Fig. 3.18. The details of performing these calculations are presented in prior articles on this topic [121, 178].

Table 3.7: Rectangular parallelepiped specimen geometry, mass, and density measured at RT

Specimen	**X (mm)**	**Y (mm)**	**Z (mm)**	**mass (g)**	**density (kg/m^3)**
SB-CoNi-10+	8.983	9.982	10.815	8.3564	8617

The geometry of the RP must be measured to a high accuracy for high quality elastic modulus measurements. The dimensions, weight, and density at room temperature of the RP that was extracted from a SX bar of SB-CoNi-10+ by EDM are listed in Table 3.7. Since these dimensions must also be understood at elevated temperatures for the high temperature RUS experiment, dilatometry experiments were performed on a

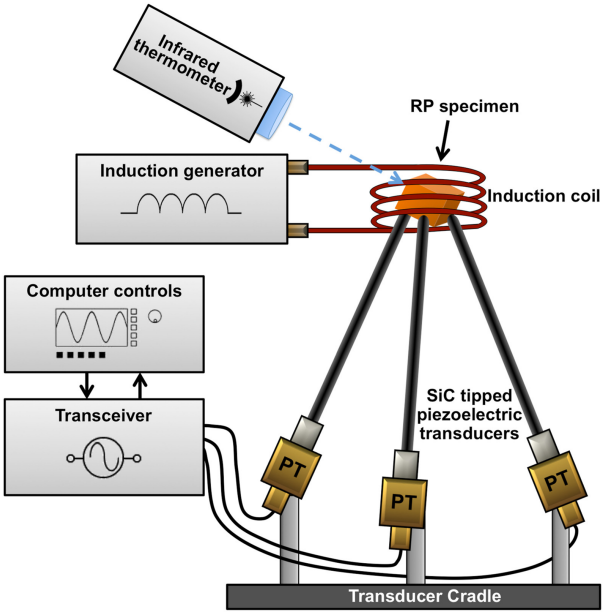

Figure 3.18: Component diagram of the rapid induction heating high temperature RUS setup. Reproduced from "Temperature dependence of single crystal elastic constants in a CoNi-Base alloy: A new methodology" by B.R. Goodlet et al., 2021, *Mater. Sci. Eng. A*, p. 140507. Copyright 2020 by Elsevier B.V. Reproduced with permission [178].

25.4 mm long SX bar of SB-CoNi-10+ in air from room temperature to 1250 °C. The elongation, mean coefficient of thermal expansion (CTE), and the instantaenous CTE for two separate dilatometry runs of SB-CoNi-10+ are displayed in Fig. 3.19 and show good agreement with each other. With this information, the RP dimensions at each hold temperature during the RUS spectra collection could be calculated and used in the CmdStan-RUS code during data analysis.

A summary of the elevated temperature elastic constants along with a RUS noise parameter and a calculation of the Zener anisotropy are presented in Fig. 3.20. A slight hysteresis can be observed between the measurements taken during initial heating and during cooling, which is likely due to the mass gain through oxidation of the initially polished alloy surfaces during the test. A monotonic decrease in the three cubic elastic constants (C_{11}, C_{12}, C_{44}) from (236.4, 150.8, 134.1) GPa to (190.7, 138.1, 95.2) GPa is

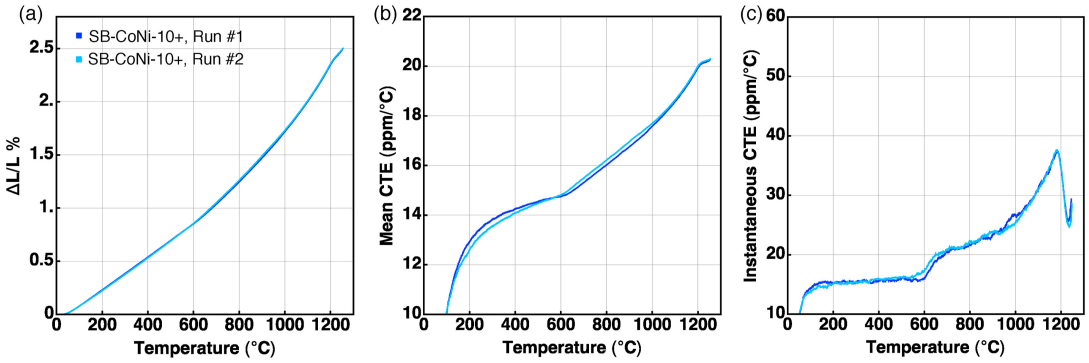

Figure 3.19: Dilatometry data provided as (a) change of RT length in percent, (b) mean CTE from RT in ppm/°C, and (c) instantaneous CTE in ppm/°C. Reproduced from "Temperature dependence of single crystal elastic constants in a CoNi-Base alloy: A new methodology" by B.R. Goodlet et al., 2021, *Mater. Sci. Eng. A*, p. 140507. Copyright 2020 by Elsevier B.V. Reproduced with permission [178].

accompanied by a 15% increase in the elastic anisotropy from A = 3.131 → 3.618 upon heating from RT to 927 °C. Above this temperature, significant damping occurs and resonance mode identification becomes increasingly difficult and unreliable. Compared to similar SX Ni-base superalloys, SB-CoNi-10+ has a 25 GPa lower C_{11} while retaining a high Zener anisotropy near 3.1. This unique combination of elastic properties has not been observed in other Ni-, CoNi-, or Co-base superalloys that have been investigated in the literature.

3.5 Conclusions

A combination of computational and high throughput experimental tools has been deployed to efficiently investigate multicomponent space and design a new single crystal alloy, SB-CoNi-10. This alloy consists of a γ/γ' cuboidal microstructure with a high precipitate volume fraction and a relatively high γ' solvus compared with previously investigated Co-base alloys. Furthermore, SB-CoNi-10 alloy is also able to achieve a very thin TGO scale containing α-Al_2O_3 after 1 h in air at 1100 °C, which has not been

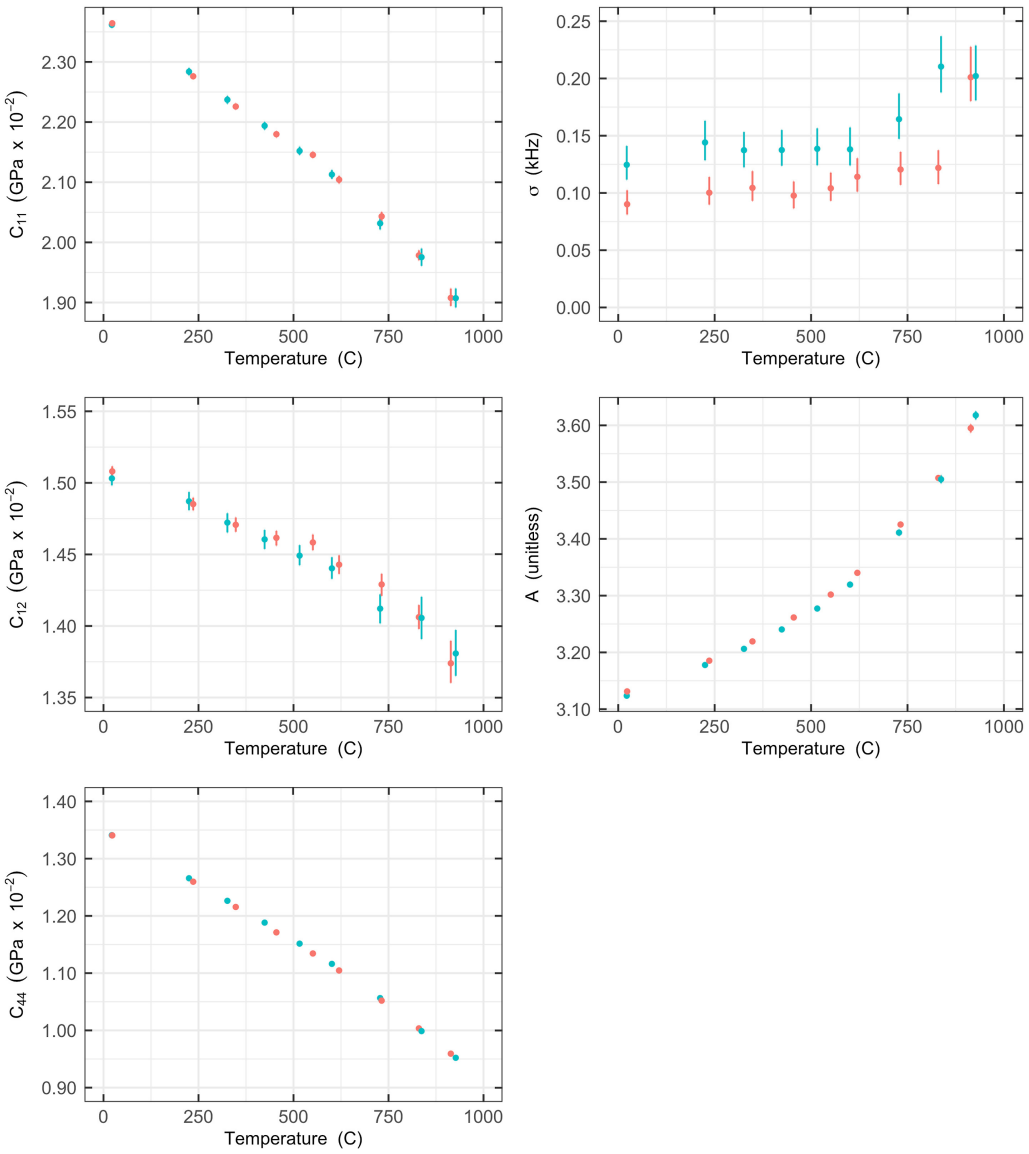

Figure 3.20: Bayesian parameter estimates as a function of temperature for SB–CoNi-10+alloy, with mean values (plotted as points), 68% posterior intervals (height of bars), and color indicating measurements collected upon heating (red) or cooling (blue). Reproduced from "Temperature dependence of single crystal elastic constants in a CoNi-Base alloy: A new methodology" by B.R. Goodlet et al., 2021, *Mater. Sci. Eng. A*, p. 140507. Copyright 2020 by Elsevier B.V. Reproduced with permission [178].

demonstrated in other high-solvus Co-alloys. It is also notable that SB-CoNi-10 has a very comparable density to the 2nd-generation Ni-base superalloys, a desirable trait for potential aero-engine components, combined with favorable solidification behavior and good high temperature creep properties. The new suite of alloy design tools can efficiently explore the design space for complex multicomponent alloys.

Chapter 4

Low cycle fatigue of a CoNi-base superalloy[†]

In this chapter, the low cycle fatigue response of the single crystal γ'-containing CoNi-base superalloy SB-CoNi-10+ described in Ch. 3 has been investigated in air and in vacuum at 950 °C. The fatigue performance is demonstrated to be similar to the 1st-generation single crystal Ni-base superalloy AM1. Fracture surface imaging and cross-sections on both alloys reveal that oxidation-assisted surface cracking is responsible for fatigue crack initiation in air. The fatigue performance improves under vacuum for both alloys as crack initiation transitions to internal casting pores retained from the solidification process. Recrystallized regions on the fracture surfaces of the vacuum-tested samples of both alloys are identified by electron backscattered diffraction, which has not been previously reported for single crystal Ni-base alloys at these test conditions. The role of the base element (Ni- vs. CoNi- vs. Co-base) on the fatigue performance is discussed.

[†]Significant portions of this chapter are reproduced from the following article: S.P. Murray, A. Cervellon, J. Cormier, and T.M. Pollock, Low Cycle Fatigue of a Single Crystal CoNi-base Superalloy. *Mater. Sci. Eng.: A* **827** (2021) 142007. [**doi**] [179]

4.1 Introduction

Single crystal (SX) Ni-base superalloys are the material of choice for blades and vanes in the hot sections of aeroengines and land-based gas turbines where a combination of high stresses and elevated temperatures are present [3]. After appropriate heat treatments, these alloys exhibit a two-phase microstructure that consists of a high volume fraction of sub-micron scale cuboidal precipitates (γ', $L1_2$) that are coherent with a solid-solution strengthened matrix (γ, A1). The compositions of these multi-component alloys have been designed in an evolutionary fashion over several decades to achieve a combination of excellent creep resistance, high strength, and oxidation resistance [1]. Additionally, these alloys must resist failure by cyclic loading, which can result in catastrophic fatigue failures in service. Low cycle fatigue (LCF), which is related to the cyclic stresses imposed by the start-stop cycle of gas turbines (e.g. a flight for an aero-engine), is a significant factor limiting component life [37].

At high temperatures (> 850 °C), the LCF life of directionally solidified and SX Ni-base superalloys is controlled by crack initiation from the surface, assisted by oxidation [77, 81, 180, 181, 182]. This is in contrast to intermediate temperatures (< 850 °C) where crack initiation primarily occurs at microstructural inhomogeneities such as internal casting pores that form during the solidification process [79, 81, 183]. It is possible to increase the fatigue life significantly by reducing the size distribution of the casting pores through higher cooling rates during solidification [79, 184]. However, at high temperatures, similar fatigue life benefits are not realized unless testing is performed in high vacuum where the impact of environmental damage is reduced.

Co- and CoNi-base superalloys that contain a two-phase γ-γ' microstructure have recently been investigated as candidate alloys for high temperature applications where Ni-base superalloys are currently employed in their single crystal form [34, 153, 160].

Novel materials that may be introduced into turbine hot sections must be evaluated for their high temperature LCF resistance. LCF studies on Co-base SXs have found that they exhibit significantly reduced fatigue lives compared to their Ni-base counterparts due to their increased susceptibility to oxidation-assisted surface cracking at intermediate temperatures [117]. This can largely be attributed to the inability for model Co-base superalloys, such as ternary Co-Al-W alloys, to rapidly form a protective α-Al_2O_3 oxide scale during high temperature exposure to air [44], or for these protective oxide scales to form with significant amounts of overlaying oxide [23]. Since CoNi-base alloys have a larger solubility for beneficial alloying elements that can promote the formation of protective oxide scales, recent alloy designs have sought to design multi-component alloys that have balanced mechanical, thermophysical, or environmental properties [33, 153, 185, 186]. One such alloy is SB-CoNi-10+, which possesses an elevated γ'-solvus temperature of approximately 1200 °C and quickly forms α-Al_2O_3 after a 1 hr exposure to air at 1100 °C, resulting in thin overlying oxide scales on the order of 2 µm at this condition [34]. These improved properties allow for fatigue testing at higher temperatures in air without the assistance of a protective overlay coating used in prior studies on Co-base superalloys [117].

In this work, the LCF response of a novel SX CoNi-base superalloy, SB-CoNi-10+, is investigated at 950 °C in air and in high vacuum. Tests in vacuum elucidate the intrinsic LCF resistance of SB-CoNi-10+ without the contribution of oxidation. The fatigue performance is compared to AM1, a 1st-generation SX Ni-base superalloy. Observations on the post-mortem specimens by optical and electron microscopy provide insight into which microstructural features and damage mechanisms control fatigue crack initiation and fatigue life for these test conditions. These results suggest pathways for future improvements in fatigue performance in Co- and CoNi-base superalloys.

4.2 Methods

An alloy ingot of the SB-CoNi-10+ alloy was acquired from Sophisticated Alloys, Inc. Single crystalline bars of ~15 mm diameter and ~175 mm in length were fabricated through the Bridgman growth process with a five-bar investment mold. The mold was pre-heated to 1575 °C and extracted from the furnace hot zone with a withdrawal rate of 3.4 mm min^{-1}. After removal from the mold, the bars were solutionized in vacuum at 1245 °C for 12 h followed by aging at 1000 °C for 50 h to produce a γ/γ' microstructure. Inductively coupled plasma optical emission spectrometry was used to determine the chemical composition of the SB-CoNi-10+ alloy ingot before casting and is displayed in Table 4.1 along with the composition of AM1. Volume fraction of γ' measurements were made on SX pieces of SB-CoNi-10+ that were solutioned in vacuum at 1245 °C for 12 h and subsequently aged at various temperatures for 8 h. Alloy pieces were encapsulated in evacuated quartz before aging and quenched in water by breaking the capsules under water. Area fraction, A_f, measurements were made on BSE images of the alloys using the Yen threshold and despeckle filter in Fiji and then converted into volume fractions, V_f, using $V_f = {A_f}^{3/2}$ which assumes evenly dispersed cuboidal precipitates [124, 125]. Additional details on the SX SB-CoNi-10+ alloy have been reported in a previous publication [34].

Load-controlled fatigue tests were performed on four cylindrical dogbone samples machined from two of the SX bars. The diameter of the gauge sections were ~5 mm with a gauge length of ~16 mm. Each pair of samples produced by a SX bar were tested under similar loading conditions, but one test would be performed in air and the other in vacuum. The R-ratio ($\sigma_{\min}/\sigma_{\max}$) for all tests was R = -1, the test temperature was 950 °C, and the cyclic frequency of the fatigue tests was 0.5 Hz. Tests were performed using the same procedure as presented in Steuer et al. [79]. Stress-strain data was col-

lected with ceramic-tipped extensometers for the tests performed in air due to access to the gauge section during testing. Stress-strain data was not collected for the vacuum tested specimens since placing an extensometer in the vacuum chamber is technically not possible. All fatigue tests were cycled to failure. Elastic stiffness and compliance tensors for single crystal SB-CoNi-10+ were collected by high temperature resonant ultrasound spectroscopy (RUS), and have been reported in a prior publication [178]. The elastic properties of single crystal AM1 with respect to temperature were determined by a dynamic-resonance method (DRM) described in prior publications [187, 188, 189].

Compression testing of SB-CoNi-10+ was performed on 5 mm diameter by 5 mm tall cylindrical samples extracted by electric discharge machining from a heat-treated single crystal bar with the compressive axis along the solidification direction. The compressive strain rate was 1×10^{-4} s^{-1} until a plastic strain of 5-10 % was reached. Testing was performed in air with heat applied by a clamshell furnace, the temperature controlled by a thermocouple placed on the specimen surface, and the platens lubricated with a boron nitride paste to limit frictional effects.

The AM1 fatigue data used for comparison comes from prior studies [79, 190] performed under load-control at the same temperature and stress conditions and on the same fatigue machine. Post-mortem AM1 samples from these studies were acquired for microscopy studies presented here. The primary misorientations of the SB-CoNi-10+ SXs relative to the [001] crystallographic orientation were assessed by electron backscattered diffraction (EBSD) on cross-sections of the grips of the air-tested specimens sectioned perpendicular to the loading direction. Bar #1 had a primary misorientation from the [001] of 21° while Bar #2 had a primary misorientation of 13°. Since load-control testing at high temperatures minimizes the impact of differing crystallographic orientation ([001], [111], [213], etc.) on fatigue life, load-control testing was preferred to strain-control in our study [147].

Table 4.1: Experimentally measured alloy compositions of SB-CoNi-10+ and AM1 in at.%

Alloy	Co	Ni	Al	Cr	Ta	W	C	B	Other
SB-CoNi-10+ [34]	Bal.	36.8	13.3	5.8	3.5	1.0	0.06	0.08	0.026Hf, 0.004Y
AM1 [79]	6.7	Bal.	11.6	9.0	2.6	1.9	-	-	1.3Mo, 1.4Ti

Fracture surface and surface cracking observations were made using 3D-stitching on a Keyence VHX-5000 optical microscope. Cross-sections for scanning electron microscopy (SEM) were metallographically prepared by grinding down to 1200 grit SiC paper and polishing down to 1 µm diamond suspension, with a final polish using 50 nm colloidal silica suspension. Secondary electron (SE) imaging, backscattered electron (BSE) imaging and energy dispersive x-ray spectroscopy (EDX) mapping was performed using a ThermoFisher Apreo C equipped with a Schottky field emission gun at accelerating voltages between 10 and 20 kV. EBSD mapping was performed with an EDAX Velocity camera in a FEI Versa3D microscope at an accelerating voltage of 30 kV. The collected diffraction patterns were indexed by spherical indexing using the EMSphInx software package [191]. Subsequent EBSD map clean-up and partitioning was performed in the OIM Analysis™ v7 software package.

4.3 Results

4.3.1 Stress-life diagram and stress-strain response

The stress-life results for SB-CoNi-10+ are compared to AM1 [79, 190] also tested in load-control at 950 °C in air and vacuum in Fig. 4.1. For the tests performed in air, the CoNi-base alloy had a fatigue life similar to AM1. In high vacuum, the fatigue performance of the CoNi-base alloy improves in a similar way as AM1, however additional tests would be desirable to confirm the relative performance of these two alloys due to the

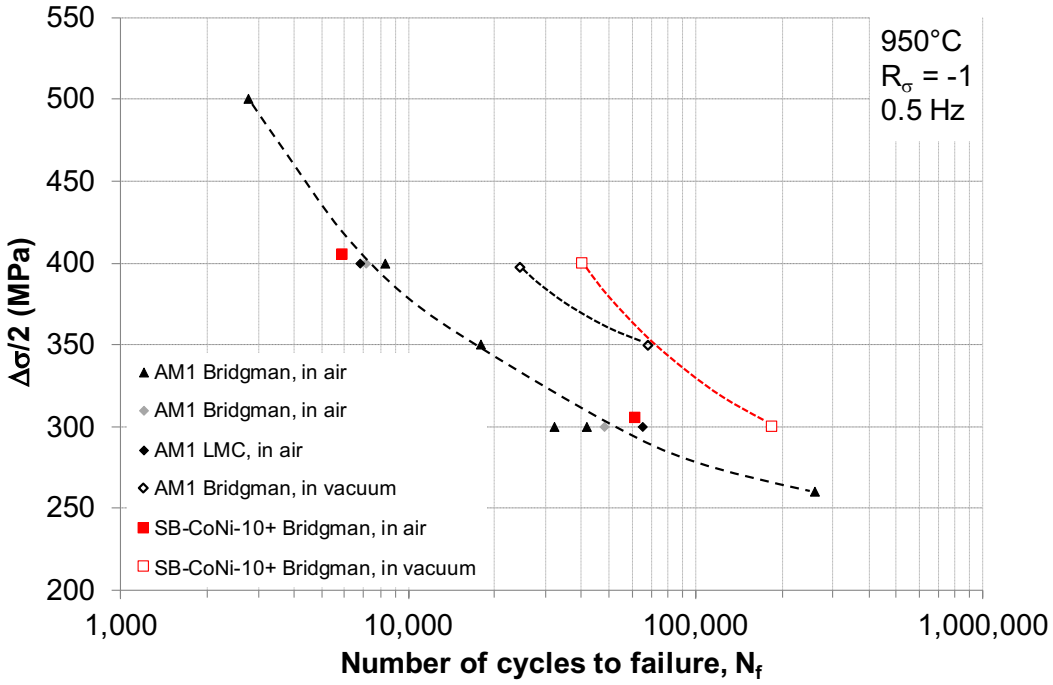

Figure 4.1: S-N diagram of SB-CoNi-10+ at 950 °C / R = -1 / f = 0.5 Hz tested in air and in vacuum compared to 1st-generation SX Ni-base superalloy AM1 [79, 190]. Trendlines are only intended to guide the eye and do not represent a curve fit.

scatter in fatigue-life often observed in this temperature/stress regime. The results for the fatigue tests on SB-CoNi-10+ are also presented in Table 4.2 along with the applied test conditions.

Table 4.2: Test conditions for load-control fatigue tests on SB-CoNi-10+

SX Bar Label	Temp. (°C)	R-ratio	σ_a (MPa)	Environment	Cycles to Failure, N_f
Bar #1	950	-1	305 MPa	Air	61,729
Bar #1	950	-1	300 MPa	Vacuum	184,992
Bar #2	950	-1	405 MPa	Air	5,892
Bar #2	950	-1	400 MPa	Vacuum	40,201

The maximum total strain for the two fatigue tests performed in air are presented in Fig. 4.2. For the test performed at σ_a = 305 MPa, the accumulation and subsequent saturation of ratcheting strains during load-control testing is observed. Loading was in

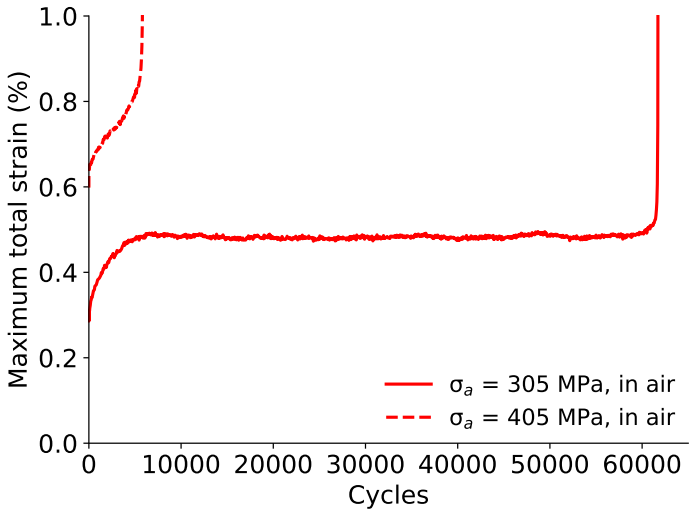

Figure 4.2: Max total strain vs. cycles for each of the LCF tests on SB-CoNi-10+ in air. T = 950 °C, R = -1.

the elastic regime macroscopically for this test, indicated by the closed nature of the hysteresis loops (not shown). After ~5,000 cycles, the alloy ceases to accumulate ratcheting strain and the max strain stabilizes. In the case of the σ_a = 405 MPa cycled sample, sample failure occurred at 5892 cycles, and a saturation point for ratcheting strains was not reached during this test. Once fast crack propagation occurs near the end of the fatigue life, the hysteresis loops in both tests open significantly, indicating large crack opening and plastic damage accumulation. High temperature quasi-static compression tests on single crystalline SB-CoNi-10+ resulted in a 0.2% offset yield strength of 372 MPa at 950 °C. This is consistent with the max total strain plot presented in Fig. 4.2 since the test performed at σ_a = 305 MPa reached a stabilization point while the test performed at σ_a = 405 MPa (slightly above the quasi-static yield strength) never reached a stabilized regime. Additional compression tests at room temperature and 750 °C resulted in measured yield strengths of 502 MPa and 595 MPa, respectively. This indicates the presence of a yield strength anomaly in this CoNi-base alloy around 750 °C, as has been observed in other γ'-containing CoNi-base superalloys [192]. The room temperature

yield strength of SB-CoNi-10+ is lower than AM1 and most other SX Ni-base superalloys [193].

At the max tensile load of the first cycle, the sample loaded to 305 MPa had a max strain of 0.3% and the sample loaded to 405 MPa had a max strain of 0.6%, which is double the value of the lower stress test. This can be partially attributed to differences in the Young's modulus between these two specimens as a result of the elastic anisotropy introduced by the misorientation of both crystals from [001] along the loading direction. The $\sigma_a = 305$ MPa tested sample is more misoriented (21°) from [001] compared to the $\sigma_a = 405$ MPa tested sample (13°) and therefore has a higher stiffness along the loading direction.

A previous study experimentally measured the elastic constants of single crystals of SB-CoNi-10+ from room temperature to 927 °C using RUS [178]. This produced a stiffness tensor (C_{ij}, in Voigt notation) and an associated compliance tensor (S_{ij}) for this alloy. These tensors as a function of temperature are presented in Fig. 4.3. These measurements can be used to estimate the directional Young's modulus for the misoriented single crystals in this work by extrapolating these results to 950 °C, which was accomplished by fitting the C_{ij} and S_{ij} with second-order polynomials of the form $y = a + bx + cx^2$. These curve fits match the data well, with R^2 values above 0.98 for all fits. The [001] Young's Modulus for AM1 and SB-CoNi-10+ are presented in Fig. 4.4. For a single crystal of SB-CoNi-10+ loaded along the [001] direction, the Young's modulus would be 117.8 GPa at room temperature and would decrease to 74.2 GPa at the testing temperature of 950 °C. AM1 exhibits a higher [001] Young's modulus of 128.5 GPa at room temperature which decreases to 92.1 GPa at 950 °C [189]. Other single crystalline CoNi-alloys have been demonstrated to become less stiff with increasing temperature at a faster rate than single crystal Ni-base superalloys [153]. The 13° misoriented bar of SB-CoNi-10+ would be slightly stiffer with a room temperature modulus of 130.1 GPa

that decreases to 85.6 GPa at 950 °C. The 21° misoriented bar has the largest increase in stiffness, as expected, with a room temperature modulus of 151.9 GPa that falls to 108.6 GPa at 950 °C.

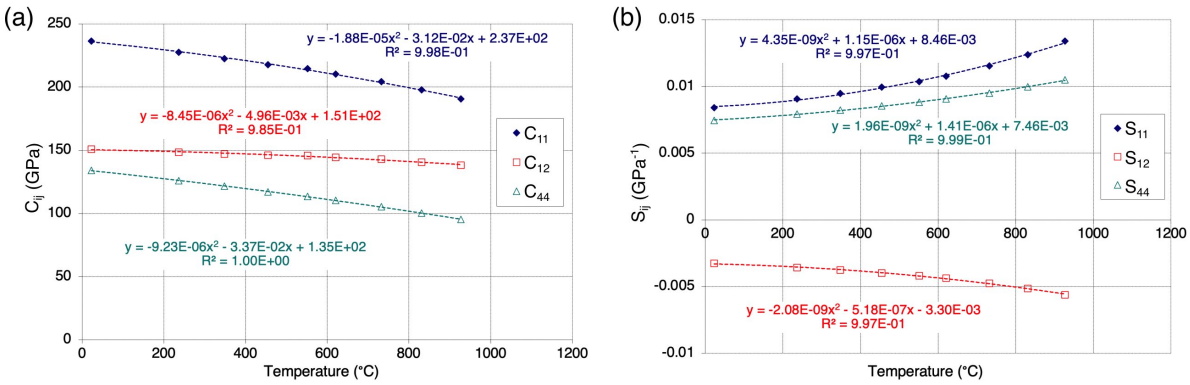

Figure 4.3: (a) C_{ij} and (b) S_{ij} with respect to temperature for single crystal SB–CoNi-10+. Data adapted from Goodlet et al. [178].

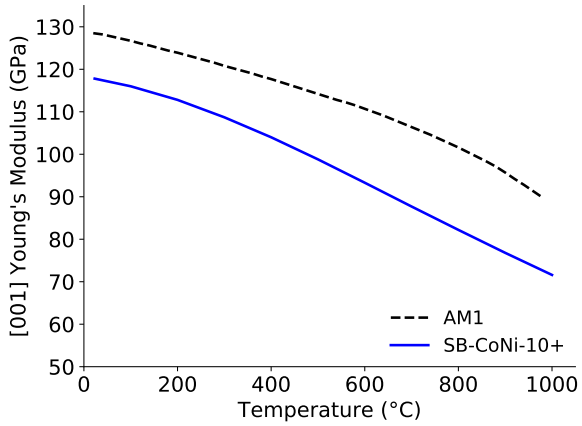

Figure 4.4: Experimentally determined [001] Young's modulus with respect to increasing temperature for Ni-base single crystal alloy AM1 compared to SB-CoNi-10+ [194].

4.3.2 Fracture Surfaces and Surface Cracking

Optical micrographs of the post-mortem fracture surfaces for both SB-CoNi-10+ and AM1 are shown in Fig. 4.5. The samples tested in air (Fig. 4.5a-c) are discolored com-

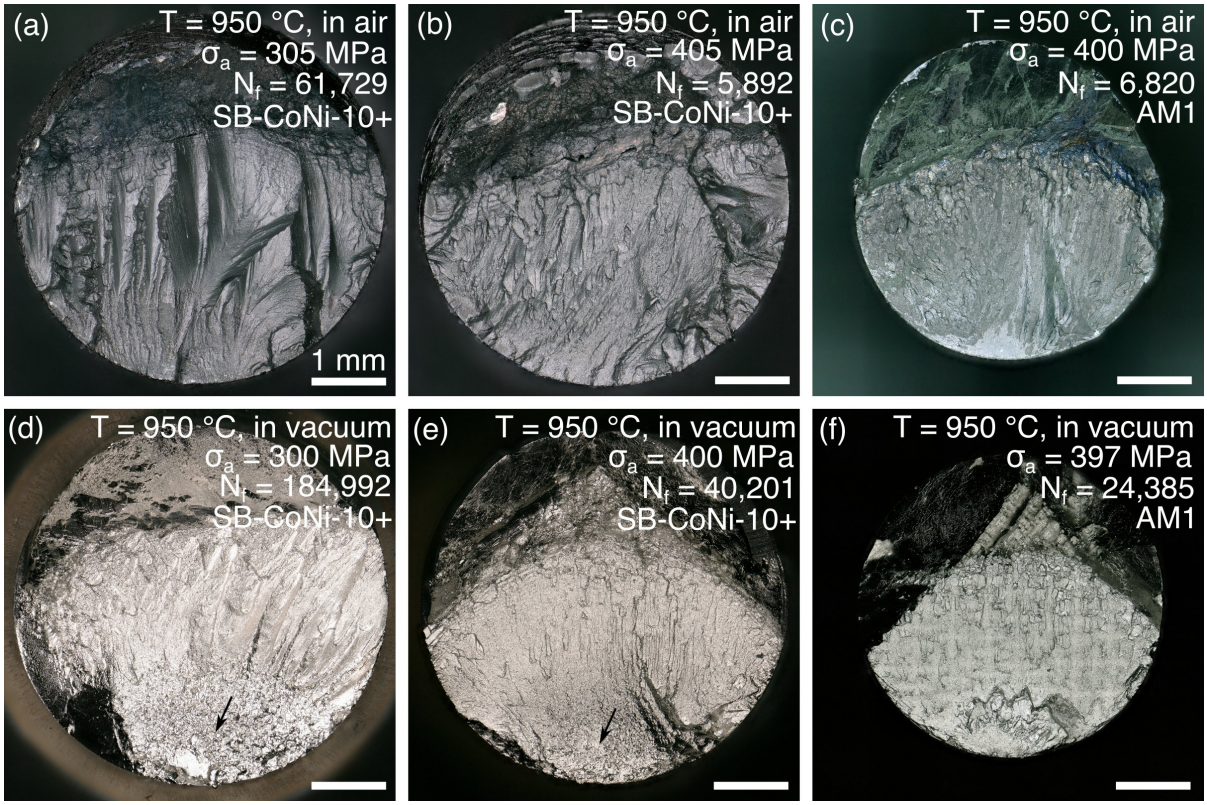

Figure 4.5: Stitched optical micrographs of the post-mortem fracture surfaces of (a,b,d,e) SB-CoNi-10+ and (c,f) AM1 tested at 950 °C with test conditions of: (a) σ_a = 305 MPa in air, (b) σ_a = 405 MPa in air, (c) σ_a = 400 MPa in air, (d) σ_a = 300 MPa in vacuum, (e) σ_a = 400 MPa in vacuum, and (f) σ_a = 397 MPa in vacuum. Small black arrows indicate rough regions in SB-CoNi-10+.

pared to the vacuum-tested samples due to oxidation of the fracture surfaces during testing (Fig. 4.5d-f). For both test environments, crack initiation was observed to occur at the sample surface or internally near the sample surface. These regions are identified by their characteristic semi-elliptical shape [142, 195]. Interestingly, the vacuum-tested SB-CoNi-10+ specimens both feature a region with radius of 1.5 mm centered on the crack initiation site that is more rough than the corresponding regions in AM1 or in any of the air-tested samples. These regions are indicated by small black arrows in Fig. 4.5d,e. This rough region is also rougher than the subsequent region of long crack propagation. This subsequent region has characteristics of ductile fracture followed by tensile fracture.

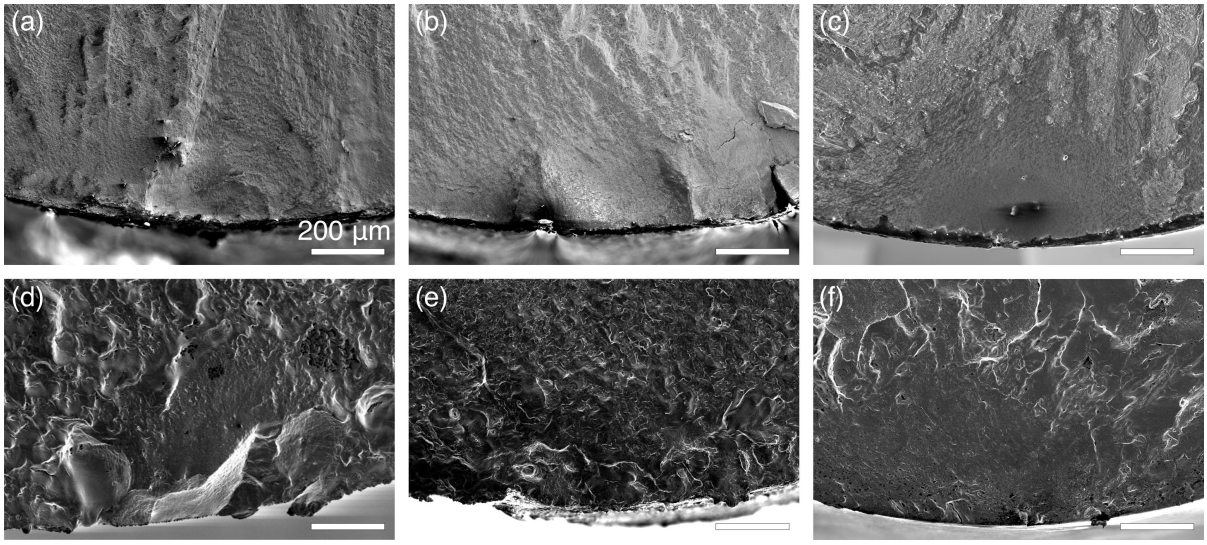

Figure 4.6: SE micrographs of the regions surrounding the crack initiation sites of (a,b,d,e) SB-CoNi-10+ and (c,f) AM1 tested at 950 °C with test conditions of: (a) σ_a = 305 MPa in air, (b) σ_a = 405 MPa in air, (c) σ_a = 400 MPa in air, (d) σ_a = 300 MPa in vacuum, (e) σ_a = 400 MPa in vacuum, and (f) σ_a = 397 MPa in vacuum.

Fig. 4.5f shows contrast of remnant dendrite structure on the fracture surface of AM1 tested in vacuum. Similar dendrite structure is not observed on the vacuum tested CoNi-alloy. This may be due to the persistent chemical microsegregation which is often present in SX Ni-base superalloys after standard solutionizing heat treatments used in industry [196]. The investigated CoNi-alloy is known to have less pronounced dendritic microsegregation compared to SX Ni-base superalloys in addition to an extended solutioning heat treatment (1245 °C / 12 h) above the γ'-solvus [34, 197, 198].

Overview SE images of the regions where crack-initiation occurs are displayed in Fig. 4.6. For the air-tested specimens (Fig. 4.6a-c), the crack initiation was always clearly observed to be from the sample surface. The vacuum tested specimens (Fig. 4.6d-f) did not have clear evidence of distinct microstructural features responsible for the crack initiation that occurred near the sample surface. It is likely that these microstructural features may have become damaged, particularly during the compressive portions of the cycling loading. Despite this, it is thought that near-surface solidification pores or clusters

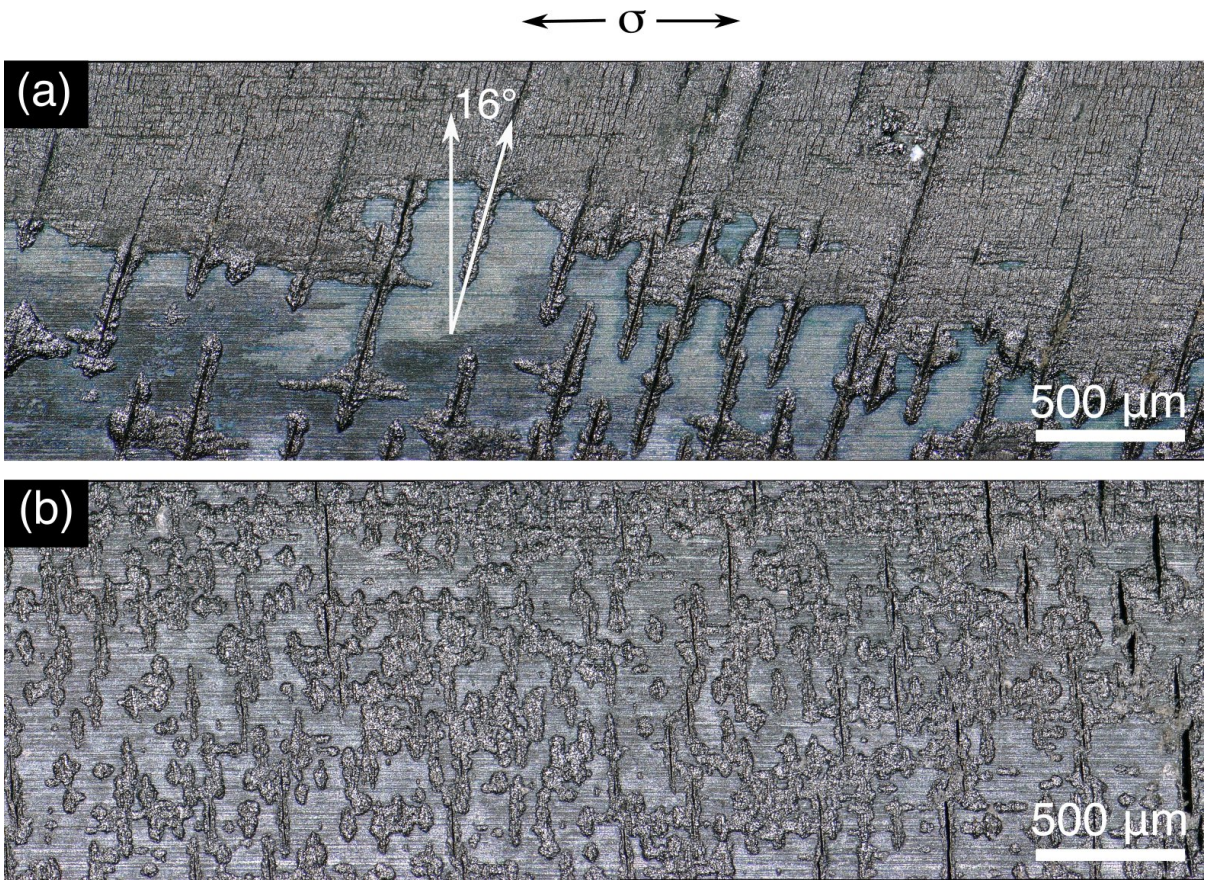

Figure 4.7: Stitched optical micrographs of surface oxidation and cracking along the gauge section of the SB-CoNi-10+ samples tested at 950 °C in air with (a) $\sigma_a = 305$ MPa in air and (b) $\sigma_a = 405$ MPa in air

of solidification pores are responsible for the sub-surface crack initiation in vacuum [79].

Optical observations along the gauge sections reveal arrays of periodic surface cracks on the surfaces of the air-tested SB-CoNi-10+ specimens (Fig. 4.7). The sample in Fig. 4.7a has angled surface cracks that correspond well to the measured primary misorientation of the SX from the [001] orientation. This indicates that the surface cracks likely follow the secondary dendrite arms or the γ/γ' interfaces [10, 182].

4.3.3 Cross-sections

Cross-sections were taken along the loading direction near the surface crack initiation sites of each specimen in order to make observations of oxidation and sub-surface damage after fatigue cycling. Overview images taken along the gauge sections of SB-CoNi-10+ tested in air and vacuum are presented in Fig. 4.8 and detailed views of the regions near where crack initiation occurred are presented in Fig. 4.9. In the case of the air-tested specimens, oxidized surface cracks that penetrate into the sample are observed along the gauge section. The $\sigma_a = 305$ MPa tested sample had an average secondary crack length of 61 µm with a standard deviation of 34 µm on a set of 58 measured cracks, while the $\sigma_a = 405$ MPa tested sample had an average secondary crack length of 61 µm with a standard deviation of 48 µm on a set of 101 measured cracks. The measured crack densities were 4.5 and 7.5 cracks per mm for the $\sigma_a = 305$ MPa and 405 MPa tests, respectively. The longest measured secondary cracks in the 305 MPa and 405 MPa tested samples were 217 µm and 220 µm, respectively. These measurements were made from the tip of the oxidized crack to the original metal sample surface. Fatigue cycling in vacuum did not produce any periodic cracks along the gauge section (Fig. 4.8b,d). Images near the fracture surfaces in Fig. 4.9 show that the air-tested samples have extensive oxidation across the fracture surface as well as near the fatal crack initiation site. In the case of the vacuum tested samples, large regions of fine, equiaxed, recrystallized grains were observed across the initial 1.5 mm of the fatal crack. While the fatal cracks grew perpendicular to the loading direction in all tests, the air-tested samples possessed flatter fracture surfaces compared to the rough, undulating surfaces of the vacuum tested samples close to the crack initiation site, which is displayed in Fig. 4.9a,b.

The qualitative EDX map shown in Fig. 4.10a-h was collected on a characteristic oxidized surface crack in the sample cycled at $\sigma_a = 305$ MPa. A focused region on the

crack tip is shown in Fig. 4.10i-p. Decomposition of the γ-γ' microstructure into other phases around the crack tip is not observed, and the denuded zones of γ' depletion are thin. These scans reveal the presence of a Cr-enriched Al-oxide that limits the extent of the oxidation beneath the alloy surface significantly compared to oxidized cracks previously observed in Co-base superalloys [117]. This oxide has been previously identified as α-Al_2O_3 by TEM diffraction in previous studies of this alloy after isothermal oxidation at 1100 °C [34]. A porous (Co,Ni)O oxide is also present within the crack, along with the presence of a variety of Ta-rich oxides and Co-containing spinels, as expected. The outward diffusion of Co and Ni ions is responsible for the outward protrusion of the (Co,Ni)O oxide seen at the surface. Additionally, a 'scalloped' morphology can be seen in the Al signal in Fig. 4.10d and the Cr signal in Fig. 4.10f, which is thought to occur due to the repeated formation and breaking of the oxide scale during fatigue cycling in air. Similar oxidation behavior is observed in the SB-CoNi-10+ sample tested at the higher cyclic stress of $\sigma_a = 405$ MPa.

To confirm the presence and nature of the recrystallized regions on the vacuum-tested samples, EBSD scans were collected across an 800 micron wide region of the fracture surface and at focused regions of interest. Inverse pole figure (IPF) orientation maps of these regions are displayed in Fig. 4.11, along with grain reference orientation deviation (GROD) maps and kernal average misorientation (KAM) maps of the focused regions. These pockets of recrystallized grains are found in the region of high roughness along the fracture surface observed in Fig. 4.5d-f. The recrystallized grains are found to have low internal misorientation and are surrounded by heavily deformed regions of the underlying SX. The grain sizes of the recrystallized regions were measured as 0.59 µm for the $\sigma_a = 300$ MPa sample and 0.72 µm for the $\sigma_a = 400$ MPa sample. These averages were measured on 30×30 µm^2 and 15×15 µm^2 sized regions, respectively, within the recrystallized pockets.

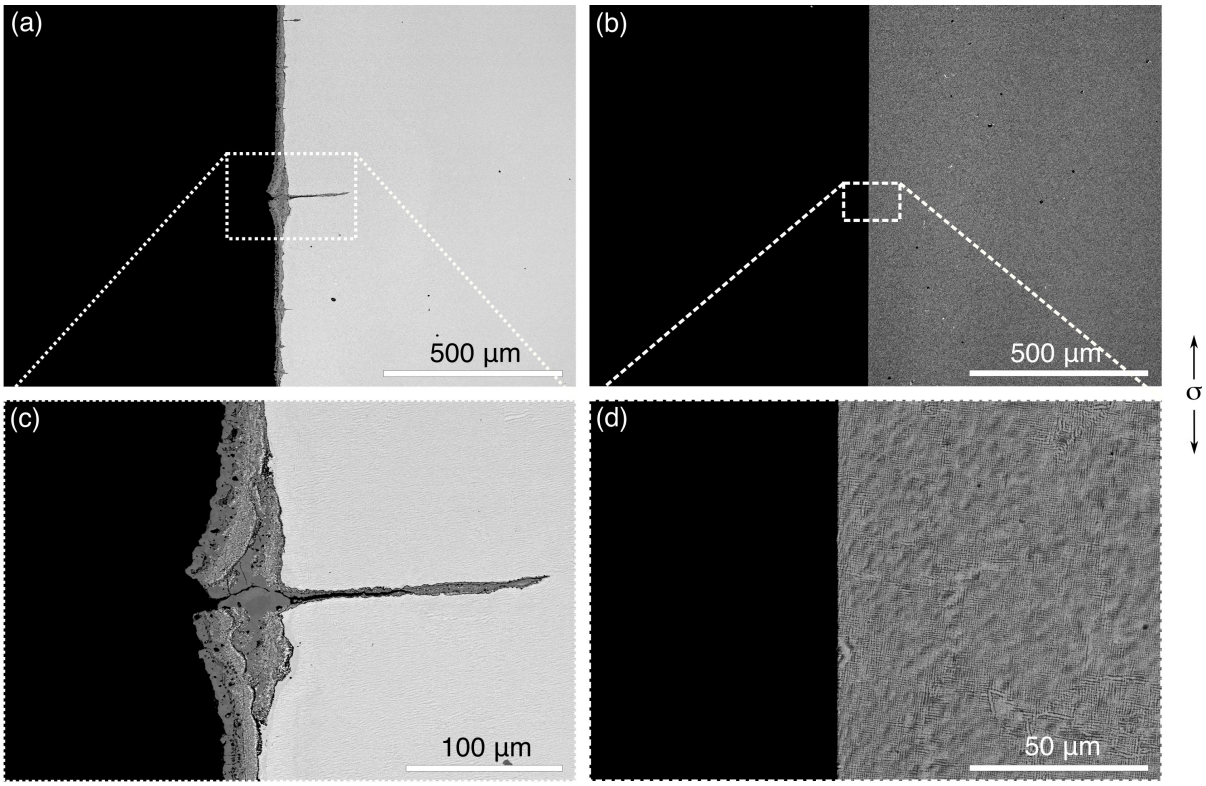

Figure 4.8: BSE micrographs of the gauge sections of cross-sectioned post-mortem SB-CoNi-10+ specimens tested at (a,c) $\sigma_a = 305$ MPa in air and (b,d) $\sigma_a = 300$ MPa in vacuum

Similar LCF tests (T = 950 °C, $\sigma_a = 400/397$ MPa, in air/vacuum) have been performed and previously reported on 1st-generation Ni-base SX superalloy AM1 [79, 190]. After acquiring these previously tested samples, cross-sections along the loading direction allowed for a direct comparison of the oxidized surface cracks in both Ni- and CoNi-alloy classes. Since the observation of large recrystallized regions on the fracture surfaces of the CoNi-base specimens were unexpected, and as these have never been reported in the literature for Ni-based SX superalloys, the previously tested AM1 samples were investigated in a similar fashion to confirm if this recrystallization behavior was unique to the CoNi-base SXs.

Oxidized surface cracks are responsible for fatigue failure of the AM1 sample tested in air, as shown by the oxidized crack on the fracture surface of the AM1 cross-section

in Fig. 4.12. However, the secondary cracks do not penetrate as deeply into the Ni-alloy as they do into the CoNi-alloy and these cracks are not as prevalent in the cross-sections taken through the fatal crack. The average secondary crack length was 11 µm with a standard deviation of 4 µm, with a maximum measured length of 16 µm in the set of only four cracks that were observed. This is interesting since the fatigue lifetime for the Ni-alloy (6,820 cycles) and the CoNi-alloy (5,892 cycles) tested at $\sigma_a = 400$ MPa in air are similar. So, despite the superior oxidation resistance of the AM1 alloy, this appears to have not resulted in a significant difference in fatigue life between these alloy classes.

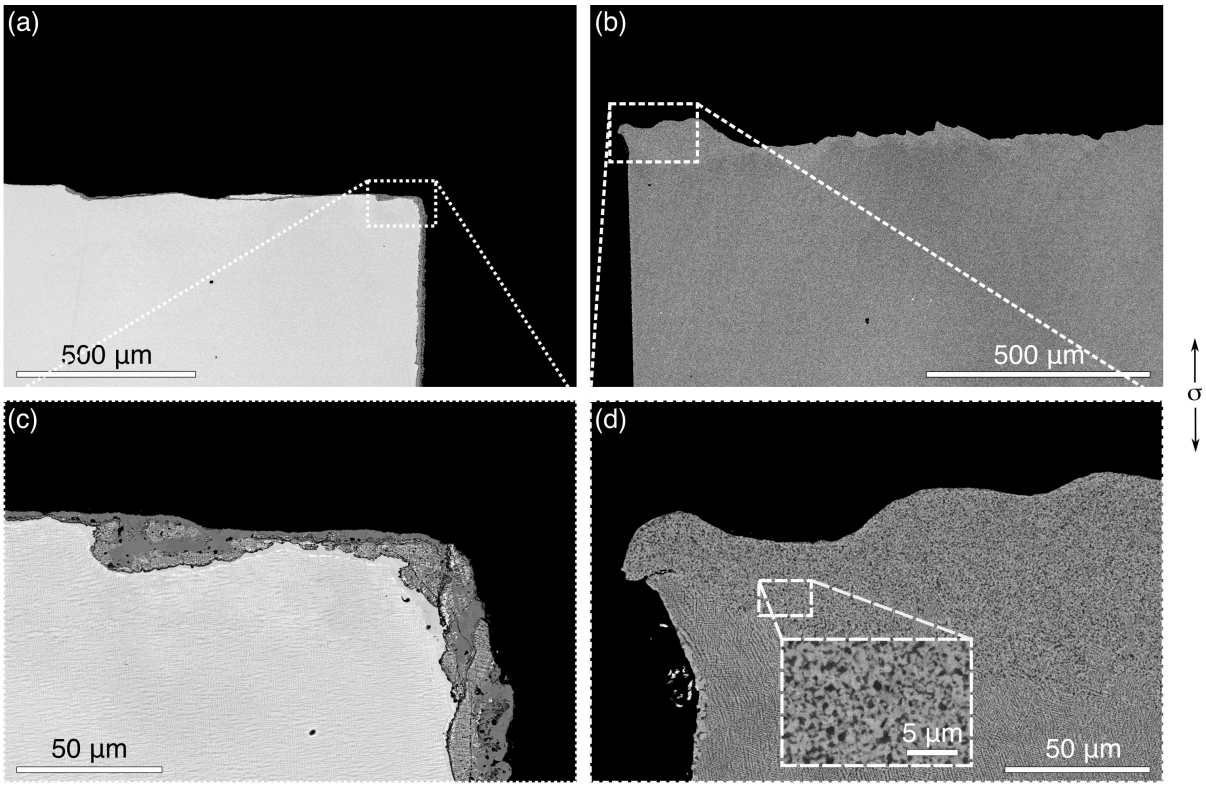

Figure 4.9: BSE micrographs of the fracture surfaces of cross-sectioned post-mortem SB-CoNi-10+ specimens tested at (a,c) $\sigma_a = 305$ MPa in air and (b,d) $\sigma_a = 300$ MPa in vacuum

Interestingly, large recrystallized regions of fine grains were also observed along the fracture surface of the AM1 sample fatigued in vacuum, although these regions were less prevalent than in the CoNi-base material. EBSD maps acquired on these fine grain

regions shown in Fig. 4.13 reveals that the recrystallized grains had low internal misorientations while the base SX below these regions was heavily deformed. The authors are not aware of similar observations on SX Ni-base superalloys that have undergone high-temperature vacuum fatigue cycling in the literature. Using the same grain size measurement method as before, the average grain size was measured as 0.39 µm on a 15 $\times$ 15 µm^2 within a recrystallized grain pocket.

SEM BSE images of vacuum-tested AM1 in Fig. 4.12b and Fig. 4.13a reveal the presence of a bright, W-rich phase that forms along the fracture surface in the heavily deformed fracture surface layer. Observations of these small, spherical precipitates have been observed on the fracture surface of AM1 that has undergone high cycle fatigue testing at 1000 °C [199], however these precipitations are somewhat unexpected since AM1 is known to not be highly susceptible to TCP phase formation, especially when compared to subsequent generations of alloys that contain additions of Re [200]. Similar phases were not observed on the fracture surface of the CoNi-base alloy, or on the AM1 specimens tested in air.

4.4 Discussion

The fatigue performance of SB-CoNi-10+ is found to be similar to AM1 in air and in high vacuum. This comparison is remarkable since AM1 has excellent oxidation resistance in the 900-1100 °C regime and is often used as a baseline comparison for environmental resistance for other SX Ni-base superalloys [201, 202, 203]. These fatigue tests demonstrate a significant improvement in high temperature fatigue response in SB-CoNi-10+ compared to previous studies on Co-base superalloys which exhibited short fatigue lifetimes due to extensive oxidation-assisted surface cracking and inferior strength compared to SX Ni-base superalloys, with fatigue lifetimes being two orders of magnitude shorter

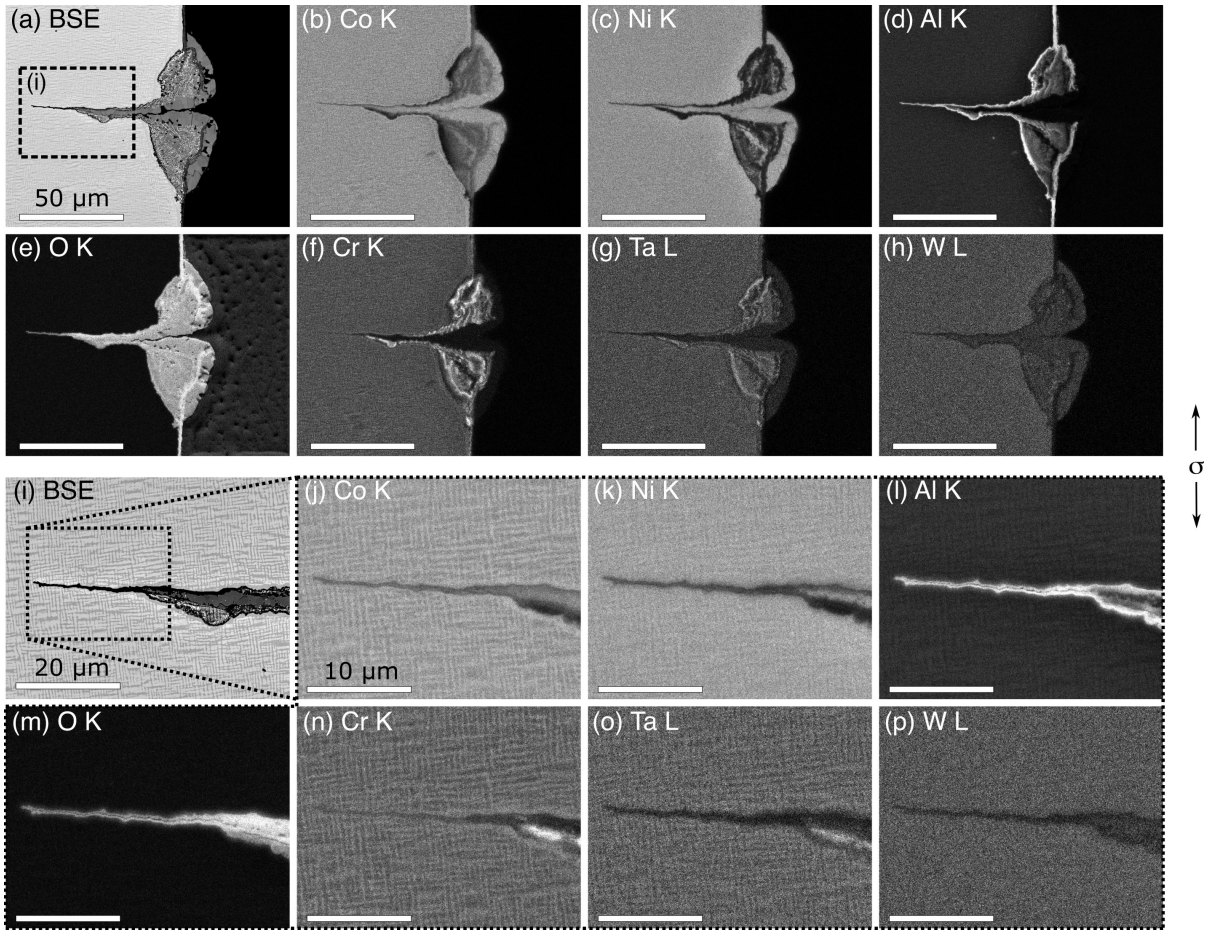

Figure 4.10: Qualitative EDX mapping of an oxidized surface crack in SB-CoNi-10+ tested at $\sigma_a = 305$ MPa in air. The collected x-ray signals were (b,j) Co K, (c,k) Ni K, (d,l) Al K, (e,m) O K, (f,n) Cr K, (g,o) Ta L, and (h,p) W L. The contrast of each map has been adjusted in FIJI so that the minimum and maximum x-ray signal corresponds to black and white, respectively.

compared to Ni-base SX superalloys at the investigated test conditions [117]. This improvement can partially be attributed to (i) the oxidation behavior of the SB-CoNi-10+ alloy and (ii) the improved high temperature strength of the SB-CoNi-10+ alloy. Previous Co-base superalloys were not able to quickly form a protective layer of α-Al_2O_3 after high temperature exposure to air [44]. The formation of a Cr_2O_3 scale has been previously demonstrated for γ'-containing Co-base alloys, however the necessary elevated Cr content can result in destabilisation of the two-phase γ-γ' microstructure near the

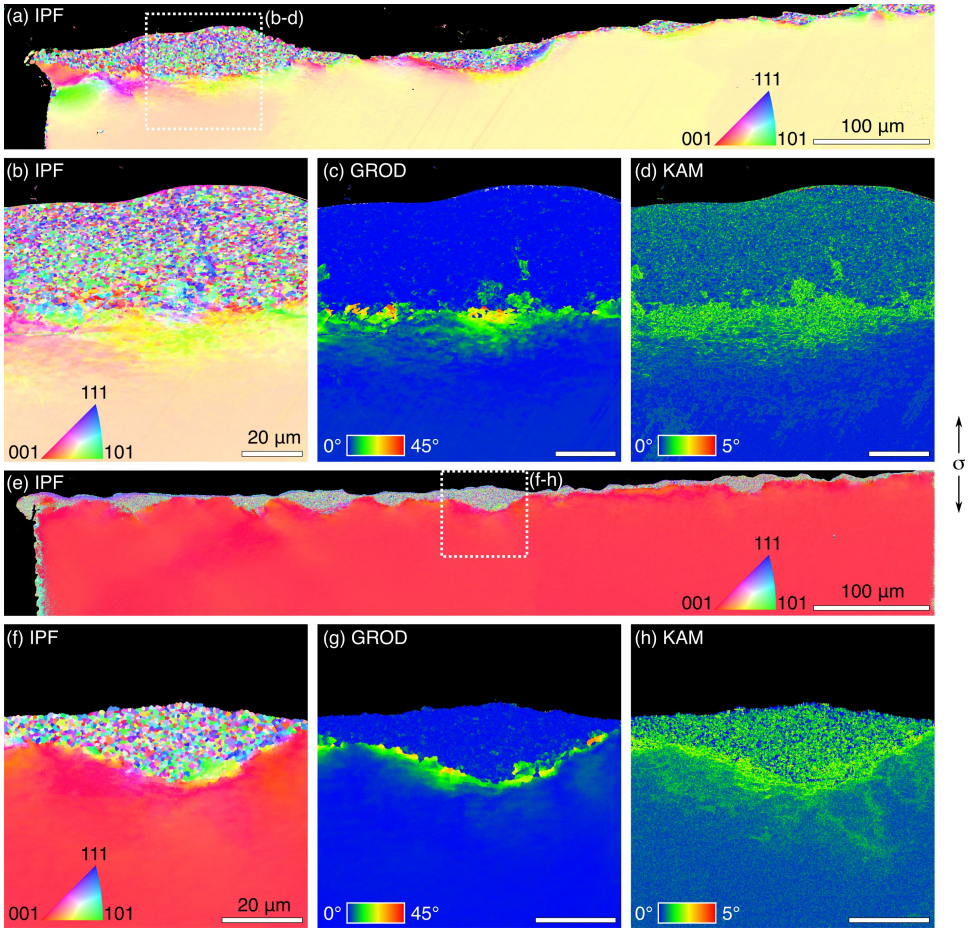

Figure 4.11: EBSD maps showing the formation of recrystallized regions on the fracture surfaces of the SB-CoNi-10+ specimens tested at (a-d) 300 MPa in vacuum and (e-h) 400 MPa in vacuum. (a-b, e-f) IPF maps are presented alongside (c,g) GROD maps with a 0-45° scale and (d,h) KAM maps with a 0-5° scale.

oxidizing sample surface [44]. Additionally, it is known that Cr_2O_3 is susceptible to volatilization in the presence of water vapor at elevated temperatures and is therefore not desirable for alloys that experience these temperatures for extended time periods in service [149, 150, 204]. Similar to other investigated CoNi-alloys, the compositional design of SB-CoNi-10+ relies on elevated amounts of Al and Cr which contributes to the enhanced oxidation response of the alloy [34].

Ternary Co-Al-W alloys exhibit significantly lower γ' volume fractions at the testing temperature of 950 °C, since many of these alloys have a γ'-solvus temperature near 1000

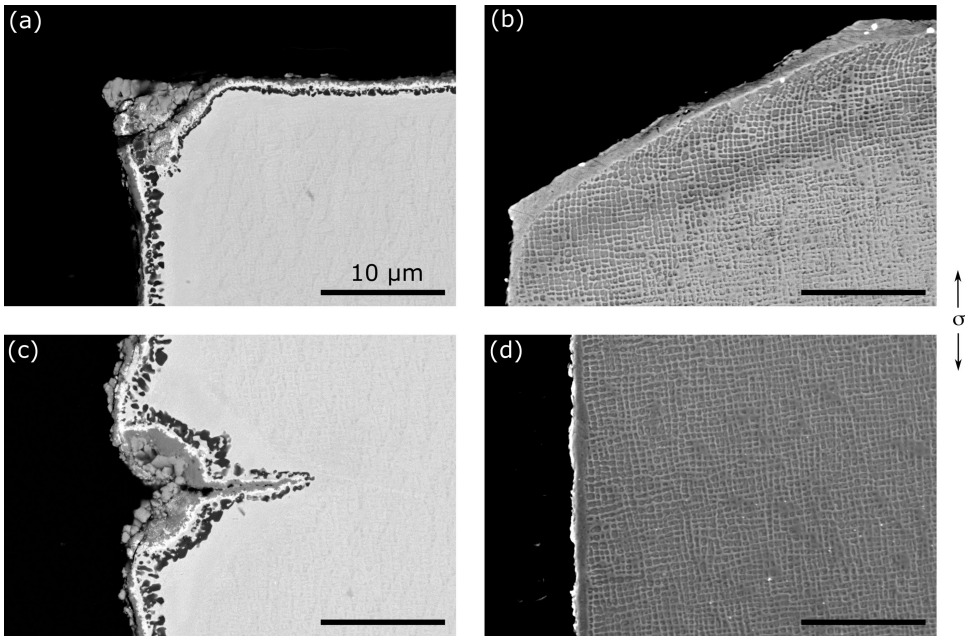

Figure 4.12: SEM BSE images of cross-sections of AM1 at (a-b) regions near the surface crack initiation sites as well as (c-d) images of the gauge section for samples tested at (a,c) T = 950 °C, σ_a = 400 MPa in air and (b,d) T = 950 °C, σ_a = 397 MPa in vacuum.

°C or lower [160, 22, 205]. Fig. 4.14 shows the temperature evolution of the γ' volume fraction at thermodynamic equilibrium of SB-CoNi-10+ compared to AM1, showing that at 950 °C both alloys retain a high volume fraction of γ' near 70 %. The alloying approach and the subsequent properties of SB-CoNi-10+ would not be feasible without the nearly equal Co:Ni ratio in this alloy, which greatly widens the two-phase γ-γ' field and allows for more compositional flexibility in alloy design [27, 30, 34].

Comparing the oxidized surface cracks in SB-CoNi-10+ to AM1, it is apparent that the oxidation resistance would need to be further improved to limit the extent of oxidation into the CoNi-alloy during high temperature fatigue cycling in air. This is suggested by the average measured secondary crack lengths in the CoNi-alloys (61 µm) being significantly longer than the oxidized cracks observed in AM1 (11 µm). It is likely that further enhancement of the oxidation resistance in this compositional space should be

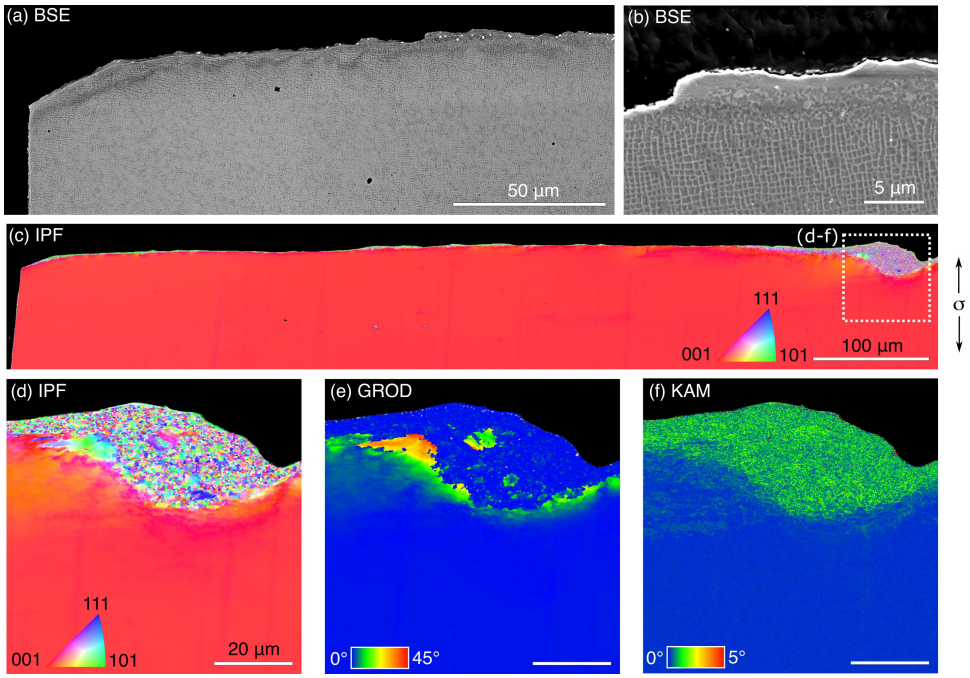

Figure 4.13: SEM BSE images (a-b) and EBSD maps (c-f) of AM1 tested at T = 950 °C, σ_a = 400 MPa in vacuum. The presence of W-rich particles are found along the fracture surface, along with thin regions of recrystallized grains. An IPF map of a focused view of a large region of recrystallized grains is shown in (d), along with a (e) GROD map and a (f) KAM map.

possible, but this may come at the cost of reduced high temperature strength or other desired properties.

From observations of the largest non-fatal cracks in the cross-sections of the air-tested CoNi-alloys, calculations of the stress intensity range at the crack tip, ΔK, can be made. These can be used to estimate a lower bound for the threshold stress intensity range, ΔK_{Th}, necessary for long crack propagation in the steady-state Paris regime since these secondary cracks were likely near threshold length yet still in the crack initiation stage. For an edge crack in a round bar, the stress intensity range can be written as:

$$\Delta K = F \Delta \sigma \sqrt{\pi a}. \tag{4.1}$$

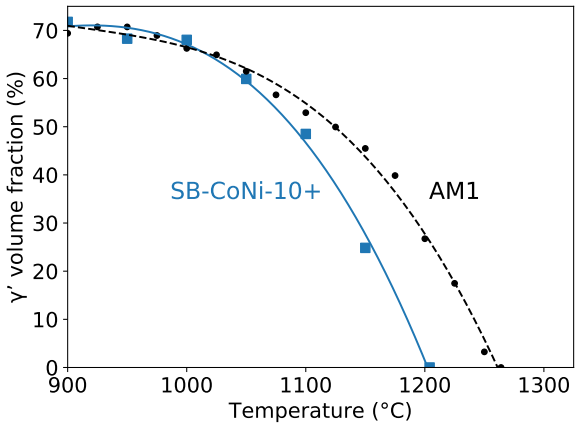

Figure 4.14: Temperature evolution of the γ' volume fraction for SB-CoNi-10+ and AM1 [206, 207]. Applied curve fits are only intended to guide the eye.

where ΔK is the stress intensity range, F is a shape factor based on a semi-elliptical surface crack, $\Delta\sigma$ is the range of the tensile cyclic stresses, and a is the length of the surface crack [142]. The longest measured secondary cracks for the σ_a = 305 MPa and 405 MPa tested CoNi-alloys were 217 and 220 µm, respectively. Inserting these values along with an estimate of the shape factor for a edge crack in a round bar with a curved front, $F = 0.74$, into Eq. 1 results in an estimate for the threshold stress intensity factor for SB-CoNi-10+ tested at 950 °C in air to be $\Delta K_{Th} \approx$ 5.9-7.9 MPa$\sqrt{m}$. For AM1 at 950 °C in air, a value of 10 MPa$\sqrt{m}$ has been reported previously using compact tension crack growth experiments at R = -1 [208]. Therefore, the threshold stress intensity factors are similar in range between SB-CoNi-10+ and AM1, especially after considering that the estimate for SB-CoNi-10+ is likely an underestimate due to the investigated cracks still being in the initiation stage. Compact tension fatigue crack growth experiments at high temperature in air and vacuum would further refine this measurement, and account for factors such as oxide-induced crack closure that can affect the effective stress intensity at the crack tip [82].

We report observations of large regions of recrystallized grains on the fracture sur-

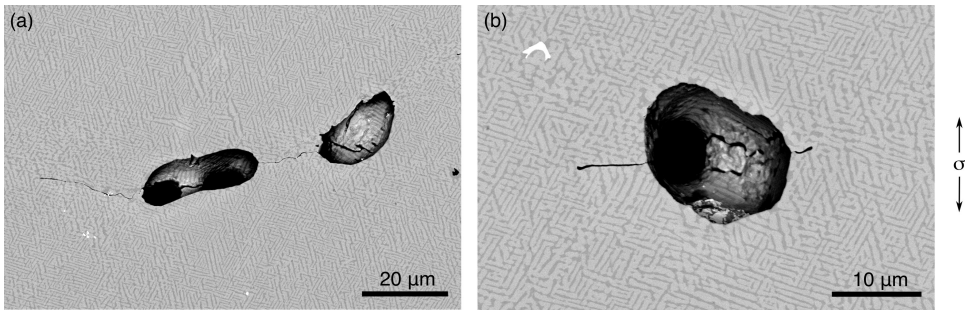

Figure 4.15: SEM BSE images of (a) a group of cracked pores and (b) and isolated cracked pore in SB-CoNi-10+ tested at T = 950 °C, σ_a = 300 MPa in vacuum

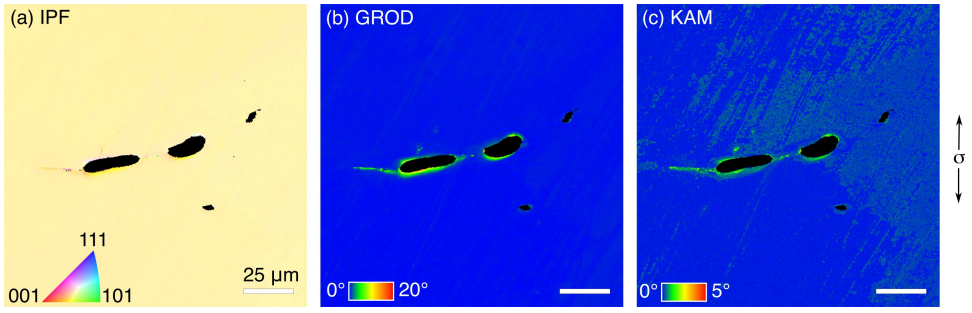

Figure 4.16: (a) IPF, (b) GROD, and (c) KAM EBSD maps of the cracked pores in Fig. 4.15a showing that plastic deformation is present around the pores after testing but has not resulted in recrystallization.

faces of all samples tested in vacuum, which, to the best of our knowledge, have not been reported previously in the superalloy LCF literature. This is most likely due to a lack of fatigue testing on SX superalloys in high vacuum combined with other studies not cross-sectioning these specimens along the loading direction. However, similar recrystallization processes have been observed at high temperatures in SX Ni-base superalloys after very high cycle fatigue (VHCF) [76], out-of-phase thermal-mechanical fatigue (TMF) [209], creep testing to high strain levels [210], and after creep tests where room temperature plastic deformation was introduced by tension before testing [211, 212]. Recrystallization can occur through plastic deformation due to the formation of dense dislocation walls, sub-grain boundaries, and finally new grain boundaries [213]. However, the lack of mis-orientation within the recrystallized grains shown by the GROD maps in Fig. 4.11c,g and

Fig. 4.13e indicates that these fine grains are formed in the wake of the fatigue crack, with recrystallization occurring due to minimization of stored strain energy with the assistance of elevated temperatures present during testing [214]. This is further supported by observations of cracked casting pores in the vacuum-tested CoNi-alloy cycled at σ_a = 300 MPa shown in Fig. 4.15. EBSD mapping displayed in Fig. 4.16 was collected around the pair of cracked pores in Fig. 4.15a and shows that recrystallization has not occurred in the vicinity of the cracks that initiate from the casting pores. This suggests that recrystallization likely occurs in the wake of the crack as a result of the enhanced plastic deformation around the crack tip. This is contrary to the case of high temperature VHCF where the accumulation of plastic deformation and subsequent recrystallization around microstructural inhomogenieties is responsible for crack initiation [76].

The recrystallized grains on the fracture surface are often found in groupings of many grains in addition to a thinner layer of recrystallization that covers the fracture surface. It is proposed that the fatal fatigue cracks are occasionally arrested during their growth, and that the closure of the crack lips under fully-reversed cycling conditions plastically deforms nearby regions. This eventually induces recrystallization due to the combination of high temperature (T = 950 °C) and sufficient plastic deformation. This is further supported by observations that recrystallization does not occur next to crack faces in coated AM1 during fatigue cycling in air at R = 0.05 and T = 950 °C, i.e. when there is no compressive portion of the load-cycle [194]. The size of these recrystallized pockets seems to be correlated with the misorientation between the loading direction and the orientation of the SX from the [001], with crack arrest occurring more frequently and leading to more sub-surface deformation for the misoriented SX shown in Fig. 4.11a-d. Lastly, these recrystallized regions are not observed on any of the tests performed in air. This could imply that recrystallization is further driven by diffusion and chemical segregation within the highly deformed regions, as has been proposed by Hamadi et al. where the

diffusion of γ-forming elements such as Co and Cr are the main driver of recrystallization in AM1 during high temperature creep along slip bands that were introduced by room temperature deformation [211]. The formation of bright TCP precipitates along the fracture surface in AM1 (see Fig. 4.13a,b) further supports that significant chemical diffusion occurs in the heavily deformed layer below the fracture surface, similar to the observation of TCP phases formed in CMSX-4 during out-of-phase TMF as shown by Moverare et al. [209] or during VHCF at 1000 °C as shown by Cervellon et al. [215].

These observations of large recrystallized regions on both the CoNi-base and Ni-base alloys raise interesting questions about the differences in plastic damage accumulation and crack propagation between these two alloy classes. The lack of an oxidizing environment for these tests prevents oxidation-assisted fatigue crack growth, and leads to longer fatigue lifetimes. What is not clear is whether the larger regions of recrystallized grains can be solely attributed to differences in sample orientation, or if chemical composition has a significant effect. It is well known that additions of Co to Ni reduces the stacking fault energy of the alloy [216]. Alloys of higher Co content would promote the dissociation of unit dislocations to partial dislocations, resulting in reduced cross-slip and recovery at high temperatures and a higher susceptibility for recrystallization [217]. The susceptibility to recrystallization of model multi-component Ni-, CoNi-, and Co-base superalloys has been studied by Rockwell hardness indentation testing followed by subsequent supersolvus heat treatment [218]. As the Co content of the alloys increased, the radius of the region of recrystallized grains around the applied hardness indents also increased [218]. However, it is currently unclear whether the higher susceptibility to recrystallization in Co-base alloys affects fatigue crack initiation. Therefore, this behavior may not have a significant effect on the fatigue performance of SX alloys since a significant portion of fatigue life is spent in crack initiation as opposed to propagation [118].

Despite the presence of the large regions of recrystallized grains on the fracture sur-

faces of all vacuum-tested samples, it is still strongly asserted that the size and distribution of casting pores is responsible for fatigue crack initiation and subsequent fatigue life in these alloys. This is strongly supported by the study of Steuer et al. where reducing the pore size distribution through increased cooling rates during liquid metal cooling assisted SX casting resulted in significantly enhanced fatigue life compared to conventionally cast specimens [79]. Observations of cracked casting pores in the vacuum-tested CoNi-base alloys shown in Fig. 4.15 and Fig. 4.16 provide evidence for casting pores being responsible for crack initiation for fatigue performed in vacuum. Despite larger recrystallized regions in the SX SB-CoNi-10+ specimens, LCF lives in vacuum were similar or even slightly better than the AM1 alloy. This is remarkable since it is likely that CoNi-alloys exhibit lower yield strengths compared to Ni-base alloys due to their lower resistance to precipitate shearing [68, 219].

The more desirable solidification characteristics of CoNi-base superalloys may result in a reduction in their pore size distributions, which would result in improved fatigue performance over Ni-base superalloys. More favorable partitioning of highly segregating alloying additions during solidification would result in reduced mushy zone heights [34, 51, 197], which could facilitate liquid flow between primary dendrite arms during solidification and therefore reduce the size distribution of the casting pores [220]. For SX Ni-base superalloys, an estimate for the maximum pore diameter, d_{pore}, has been suggested by Brundidge et al. to be closely related to the secondary dendrite arm spacing (SDAS), λ_2, by the simple relation of $d_{pore} = 1.15\lambda_2$ [118]. A longitudinal cross-section of the region above the pigtail for as-cast SX SB-CoNi-10+ resulted in an average SDAS of 72.7 µm. This is similar to the SDAS in Ni-base superalloys solidified by the Bridgman method at the same withdrawal rate of 3.4 mm min^{-1} [118]. However, while metallographic cross-sections on Ni-base alloys have revealed pore sizes that fulfill the previous relation, measurements of both the as-cast and fully heat-treated CoNi-alloy resulted

in $d_{pore} < 30$ µm. Smaller maximum pore sizes would require more cycles for fatigue crack initiation and longer lifetimes for fatigue in vacuum at these high temperature test conditions. Confirmation of this relationship between alloy chemistry and pore size distribution would require more statistical measurements of the pore size distribution in both alloys through techniques such as x-ray tomography since metallographic cross-sections do not capture the 3D pore shapes and their size distribution.

4.5 Conclusions

In conclusion, this study reports on the LCF response of a SX CoNi-base superalloy. Observations of the post-mortem specimens revealed several different types of damage that form and we have compared these damage mechanisms to those found after similar fatigue testing of SX Ni-base superalloy AM1. The following findings from this study are:

- Load-controlled LCF tests on a novel SX CoNi-base superalloy at T = 950 °C in air and in vacuum reveal a fatigue performance similar to 1st-generation SX Ni-base superalloy AM1.
- Oxidized surface cracks are responsible for fatigue crack initiation in air at T = 950 °C, while sub-surface casting pores are responsible for crack initiation in vacuum. For the same solidification conditions, the CoNi-base alloy possesses smaller solidification pores compared to Ni-base SXs.
- Large recrystallized regions were found along the fracture surface of all alloys tested in vacuum at T = 950 °C and fully-reversed conditions.

Chapter 5

3D printable CoNi-base superalloys[†]

Additive manufacturing promises a major transformation of the production of high economic value metallic materials, enabling innovative, geometrically complex designs with minimal material waste. The overarching challenge is to design alloys that are compatible with the unique additive processing conditions while maintaining material properties sufficient for the challenging environments encountered in energy, space, and nuclear applications. In this chapter, a class of high strength, defect-resistant 3D printable superalloys with approximately equal parts of Co and Ni along with Al, Cr, Ta and W are described. These alloys are amenable to crack-free 3D printing via electron beam melting (EBM) with preheat as well as selective laser melting (SLM) with limited preheat. These alloys possess strengths in excess of 1.1 GPa in as-printed and post-processed forms and tensile ductilities of greater than 13 % at room temperature. Alloy design principles are described along with the structure and properties of EBM and SLM CoNi-base materials.

[†]Significant portions of this chapter are reproduced from the following article: S.P. Murray, K.M. Pusch, A.T. Polonsky, C.J. Torbet, G.G.E. Seward, N. Zhou, S.A.J. Forsik, P. Nandwana, M.M. Kirka, R.R. Dehoff, W.E. Slye, and T.M. Pollock, A defect-resistant Co–Ni superalloy for 3D printing. *Nat. Commun.* **11** (2020) 4975. [**doi**] [197]

5.1 Introduction

Metal-based additive manufacturing (AM), or three-dimensional (3D) printing, has enabled the fabrication of near net shape metal components with optimized geometries that are not achievable through conventional manufacturing techniques. The promise of increased design flexibility has led to significant interest in applying 3D printing methods to commercial alloys currently used in biomedical, automotive, and aerospace applications [3, 88, 221]. However, only a limited number of existing alloys are amenable to the complex thermal conditions present during metal-based AM, where layer-by-layer growth of the component is achieved through local melting of metal powder by either a laser or electron beam energy source [94, 97, 222, 223]. AM of metals is fundamentally a repeated welding process, in which a directed energy source is used to locally melt and join material. Candidate materials for AM therefore tend to be weldable alloys, which are less susceptible to cracking mechanisms that originate in the liquid phase, such as liquation cracking or hot tearing, or due to stresses that develop in the solid state, resulting in, for example, strain-age cracking and ductility-dip cracking [99].

Due to their excellent mechanical properties at elevated temperatures, Ni-base superalloys are the material of choice for structural components such as single crystal (SX) turbine blades and vanes used in the hot sections of aircraft engines and land-based natural gas turbines [1]. These alloys consist of a high volume fraction (> 60 %) of sub-micron size cuboidal precipitates of the γ' phase (Ni_3(Al,Ti), $L1_2$) that are coherent with a solid solution strengthened matrix, or γ phase (Ni, A1). However, many of the highest-performing Ni-base superalloys are observed to be non-weldable due to the rapid precipitation of the γ' phase shortly after solidification, which impedes the relaxation of thermal stresses by strengthening the recently solidified material, resulting in strain-age cracking [224]. This behavior is captured in Prager-Shira weldability diagrams that

show how increasing Al or Ti content, which both increase the volume fraction of the γ' strengthening phase, is a reliable proxy for decreasing alloy weldability [225].

As the γ phase solidifies, the liquid becomes locally enriched by the rejection of γ' forming elements such as Al, Ti, and Ta [226]. This solute segregation lowers the local liquidus temperature, creating solute-enriched liquid films between solid dendrites that contract at differential rates in the melt pool during cooling, resulting in tensile stresses and cracking [111, 227, 228]. This susceptibility to liquid-mediated cracking can be influenced by control of the liquid composition and liquid fraction at a given temperature via changes in the alloy composition. Just below the melting point, stresses can be accommodated by plastic deformation in the solid state, which is very sensitive to the temperature at which the strengthening precipitates appear. Therefore, many of the desirable high γ' volume fraction Ni-base superalloys, which have a narrow temperature window from the point at which the material solidifies to the temperature at which the precipitates become thermodynamically stable, are susceptible to both cracking in the nearly-solidified state and in the solid state. The solute segregation and precipitation processes can, in principle, be modified by global changes in composition.

The cracking susceptibility of high-performance engineering alloys including high γ' volume fraction Ni-base superalloys, high strength aluminum alloys and refractory alloys [99, 113, 174, 229, 230, 231] represents the major barrier to the use of these alloys for AM components in critical applications. For alloys that operate at relatively low temperature, such as high strength aluminum alloys, control of grain nucleation in the melt pool via functionalization of powder surfaces can mitigate the cracking problem [100]. However, this results in a small grain size, which is unfavorable for high temperature operation. Thus, innovative alloy designs are needed for AM, especially for more severe environments [232].

Several different strategies have recently been pursued for the development of alloys

for AM [233]. By increasing the solid solution strengthening elements in the Ni-base superalloy Hastelloy X within the existing commercial alloy composition range, a reduction in microcracking in AM was observed [114]. To control material anisotropy, Haines et al. performed a sensitivity analysis with a focus on adjusting alloy composition to control the columnar to equiaxed transition in Ni-base alloys [234]. Similarly, control of the columnar to equiaxed transition through AM process control has been employed by Kontis et al. to successfully fabricate a non-weldable Ni-base superalloy through atomic-scale grain boundary engineering [101]. Additionally, AM allows for the mixing of alloy powders before printing, resulting in the fabrication of metal-metal composites with unique microstructures that would be difficult to fabricate by other means [235]. Since the γ–γ' microstructure present in modern Ni-base superalloys is desirable due to the excellent mechanical properties it confers, the goal of this research was to design an alloy that contains a high γ' volume fraction while retaining good printability.

Recent interest in Co-base superalloys commenced with the study of Sato et al. that revealed the possibility of precipitation strengthening in the Co-Al-W ternary system [22]. These Co-base alloys are morphologically identical to their Ni-base counterparts, except the γ' strengthening phase is based on Co_3(Al,W). The γ'-strengthened Co-base superalloys have recently been fabricated as single crystals via Bridgman growth and polycrystals via wrought processing [51, 129, 163, 164].

In this work, a CoNi-base superalloy that can be processed through both selective laser melting (SLM) and electron beam melting (EBM) manufacturing pathways is demonstrated, resulting in crack-free components in spite of the presence of a high volume fraction of the desirable γ' phase. A low degree of solute segregation during solidification reduces the susceptibility for liquid-mediated cracking, and the reduced γ'-solvus temperature alleviates cracking once solidification is complete. Room temperature tensile testing reveals that CoNi-base superalloys have an excellent combination of ductility and

strength compared to other Ni-base superalloys currently being investigated for AM. This research demonstrates that the CoNi-base superalloy compositional space provides opportunities for the development of superalloys that can leverage the potential of additive manufacturing.

5.2 Methods

3D printing parameters and heat treatment. Metal powder of SB-CoNi-10 for the additive manufacturing trials was produced in 136 kg batches by vacuum induction melting and argon gas atomization. Table 5.1 lists the nominal SB-CoNi-10 composition along with the composition of the powder and the composition of the as-printed alloy processed by EBM as measured by inductively coupled plasma mass spectrometry (ICP), glow discharge mass spectrometry (GDMS), and combustion analysis. It should be noted that the designation of SB-CoNi-10+ is used exclusively to refer to single crystal variants of this alloy throughout this dissertation, for even though the nominal compositions of the two alloys are identical, the minor element and tramp element compositions are measurably different. The reader is referred to Table 3.4 in Ch. 3 for the composition of SB-CoNi-10+ single crystal alloys and is referred to to Table 5.1 in this chapter for the SB-CoNi-10 composition relevant to the additive manufacturing studies. Powder was separated into size ranges of -53/+15 µm for SLM and -177/+53 µm for EBM. The EBM fabricated samples were produced on an Arcam Q10+ system at Oak Ridge National Laboratory running 4.2.89 EBM control software under a controlled He vacuum with an applied preheat temperature of 1000 °C. Other EBM printing details include: max current = 18 mA, speed function = 63 (unitless), hatch spacing = 125 µm, layer thickness = 75 µm, using a standard Arcam raster scan strategy. The SLM fabricated samples were produced on a SLM Solutions SLM125 at Carptenter Technology Corporation with

an applied preheat of 200 °C in an inert gas atmosphere. Other SLM printing details include: layer thickness = 30 µm, laser power = 176 W, hatch spacing = 80 µm, laser speed = 1137 mm s^{-1}, using a bidirectional raster scan strategy. The EBM specimens underwent hot isostatic pressing at 1245 °C for 4 h under 103.4 MPa of isostatic pressure in Ar, followed by a solution heat treatment at 1245 °C for 2 h and aging at 1000 °C for 50 h under vacuum. The EBM fabricated samples were cooled by furnace shut-off quenching after each heat treatment step. The SLM specimens underwent hot isostatic pressing at 1177 °C for 4 h under 103.4 MPa of isostatic pressure in Ar, followed by a solution heat treatment at 1245 °C for 1 h and aging at 1000 °C for 50 h. In the case of the SLM samples, these samples were cooled by an oil quench after the solution heat treatment, followed by a furnace quench after the aging heat treatment.

Microstructural characterization. Samples were prepared for microscopy using standard metallographic techniques consisting of grinding with SiC papers down to 1200 grit followed by polishing down to a 50 nm colloidal alumina suspension using a Vibromet polisher for 4 h. Scanning electron microscopy with secondary electron (SE) imaging and backscattered electron (BSE) imaging was performed on a ThermoFisher Apreo C at accelerating voltages between 5 kV and 20 kV using a Schottky field emission gun. Electron backscatter diffraction (EBSD) maps were acquired using an EDAX Velocity EBSD camera in a FEI Versa3D microscope at an accelerating voltage of 30 kV. All inverse pole figure (IPF) maps are defined such that the ⟨001⟩ is aligned with the build direction. The collected diffraction patterns were indexed by spherical indexing using the EMSphInx v0.2 software package [191] and Hough indexing within OIM Analysis™ v8 software. Fracture surfaces were imaged using the aforementioned scanning electron microscopes at similar accelerating voltages.

Table 5.1: Nominal SB-CoNi-10 composition and compositions of the powder and the as-printed EBM alloy in at.% measured by ICP, GDMS (*), and combustion analysis (†).

Alloy	Co	Ni	Al	Cr	Ta	W	C†	B*	Hf*	Y*	Fe*	Ti*
Nominal	Bal.	36.4	13.2	6.0	3.5	1.0	0.08	0.08	0.018	0.002		
Powder	Bal.	36.44	13.13	5.63	3.53	0.98	0.16	0.10	0.028	0.006	0.28	0.12
As-printed (EBM)	Bal.	36.54	13.12	5.53	3.61	1.00	0.14	0.10	0.037	0.009	0.27	0.09

As-printed chemical segregation characterization. Electron probe microanalysis (EPMA) was performed using a Cameca model SX100 with five wavelength dispersive spectrometers and a CeB_6 thermionic emission gun. To quantify the amount of chemical segregation present after printing in both the EBM and SLM samples, a 20 × 20 grid scan of evenly spaced points with long dwell times (1 min of collection time per point) was collected in a 100 × 100 micron area on cross-sections taken 1 mm below the final build layer perpendicular to the build direction. Chemical maps with a reduced dwell time were used for visualization of this chemical segregation. Probe Image and Probe for EPMA software packages developed by Probe Software, Inc. were used for quantification of the collected spectra. All EPMA data underwent standards-based quantification with a combination of pure alloy standards and a reference alloy sample with composition Co–6.7W–8.9Al–3.3Cr–1.5Ta at.% that was previously characterized to high accuracy by inductively coupled plasma compositional analysis.

The collected EPMA grid scan data were sorted from highest Co concentration to lowest and assigned an apparent fraction solidified (f_s) from 0 to 1, as shown in Fig. 5.2(c)-(d). It is assumed that point with the highest Co content can be assigned an apparent $f_s = 0$ since Co partitions to the dendrite core during solidification, as shown in Fig. 5.2(e), resulting in the liquid becoming depleted of Co as solidification continues. Co was selected for sorting since it has the highest concentration in SB-CoNi-10 compared to the other alloying additions. In order to determine the apparent distribution coefficient, k, for each major alloying addition, the sorted concentration of the solid vs. apparent fraction solidified curves were fit using the Scheil equation [55],

$$C_s = kC_o(1 - f_s)^{k-1} \tag{5.1}$$

where C_s is the concentration of the solid, C_o is the starting composition of the melt, f_s is the fraction solidified, and the distribution coefficient is defined as $k = C_s/C_l$. Curve fits to the Scheil equation were made using a least squares regression using data with apparent fraction solidified vales between $f_s = 0.1$ and $f_s = 0.9$ for both the EBM and SLM datasets. These curve fits provided values for C_o and k using the values of C_s and f_s as inputs determined experimentally by the EPMA grid scan.

Mechanical testing. Sheet dogbones for mechanical testing were removed from the EBM fabricated bars using electric discharge machining. The dogbones were 44 mm long with gauge dimensions of 2 mm × 3 mm × 14 mm. To remove the EDM-affected zone on the surface of the specimens, the gauge sections were ground down to 1200 grit using SiC grinding papers. Tensile tests on the EBM manufactured specimens were performed along the build direction (i.e. Z-orientation) at a strain-rate of 1×10^{-4} s^{-1} using an Instron 5582 universal testing machine. The SLM manufactured specimens were mechanically tested in the XY-orientation according to ASTM E8/E8M using machined cylindrical threaded dogbones with a gauge diameter of 6.35 mm. The strain-rate was 3×10^{-5} s^{-1} before yield and 1×10^{-4} s^{-1} after yield. All mechanical tests were performed at room temperature and taken to rupture. EBSD maps of post-mortem specimens were collected after cross-sectioning the samples in half along the build direction.

5.3 Results

Design Approach. The primary goals for alloy design were good high temperature strength, achieved via stabilization of a high volume fraction of the γ' phase to at least 1100 °C, solidus and liquidus temperatures above 1300 °C with a narrow equilibrium freezing range, high resistance to oxidation provided by formation of alumina in oxidizing

environments and favorable printability. Ni-base alloys strengthened with high volume fractions of γ' phase are well known for their tendency to crack during powder-bed fusion (PBF) printing [98]. In these alloys the Ni_3Al phase is thermodynamically stable up to a few degrees below the solidus temperature, thus it was hypothesized that a gap of > 50 °C between the solidus and solvus temperatures would increase cracking resistance while still maintaining a high volume fraction of precipitates at elevated temperatures.

The emergence of this class of cobalt-base alloys coincides with a recent thrust to develop computational and high-throughput alloy design tools [236]. This has enabled a suite of tools to be developed and integrated for exploration of the large multicomponent composition-space necessary to discover alloys for AM. These tools were used to expand compositions from the original Co-Al-W ternary to the multicomponent composition of the printed alloy investigated here. Below are brief descriptions of the tools and their role in the alloy design process.

The strength of the two-phase γ–γ' microstructure is governed by the resistance of the $L1_2$ γ' phase to shearing by ordinary or partial dislocations entering from the γ, creating either superlattice intrinsic stacking faults (SISF) or antiphase boundaries (APBs). Prior research on the role of solutes on these planar fault energies, consisting of density functional theory (DFT) calculations within the Vienna Ab Initio Simulation Package (VASP) along with Special Quasi-random Structures (SQSs), the ANNNI (Axial Next-Nearest Neighbor Ising) model [157, 237], and the Diffuse Multi-Layer Fault (DMLF) model with a proximate structure for the (111) APB [11, 238], indicated that Ti, Ta, Nb and Ni were favorable alloying additions. Creep experiments on several single crystal variants of these materials confirmed that alloys with these elements did possess creep strengths that exceed 1^{st}-generation Ni-base single crystal levels [34, 160].

To validate fault energy assessments and understand the complex precipitate shearing mechanisms observed across individual and groups of precipitates following mechanical

testing, ab-initio calculations of the generalized-stacking-fault (GSF) potential energy were used for phase field dislocation calculations [219, 239].

An early thermodynamic database in the compositional space adjacent to the $Co_3(Al,W)$ phase was developed and subsequently incorporated into the CompuTherm PanCobalt database [156]. Thermodynamic calculations were used to adjust the Ni content to increase the $L1_2$ solvus temperature to the desired range, to predict phases present across composition space in the combinatorial studies described below and to predict solidification paths and their likely influence on printability.

Ternary Co-Al-W alloys have limited oxidation resistance due to the formation of non-protective CoO and mixed spinels [23, 43]. Because first principles modeling of non-stoichiometric oxides is extremely challenging, a combinatorial library approach was developed. The combinatorial approach [46, 49] was coupled with rapid oxide screening based on Photo Stimulated Luminescence Spectroscopy (PSLS) [48] and the Calphad database [156] to outline regions of composition space giving rise to α-Al_2O_3 scales and two-phase γ–γ' microstructures. Ion plasma deposition (IPD) using five cathodes of different compositions was used to create three libraries covering a spectrum of Co-Ni-Al-W-Cr-Ta alloy compositions with 234 samples.

Starting from the composition of an alumina-forming IPD alloy of composition Co-32.4Ni-11.7Al-4.4W-3.3Cr-1.5Ta (at.%), three additional alloys with small variations in composition were arc melted into 40 g buttons [34]. After analysis of microstructure and phases present, a final composition, SB-CoNi-10, possessing a desirable two phase microstructure was selected for (a) single crystal growth to measure basic properties and (b) 3D printing to assess its behavior in both laser and electron beam based PBF build approaches.

The SB-CoNi-10 alloy has a nominal composition of Co–36.4Ni–13.2Al–6Cr–3.5Ta–1W in atomic percent, along with minor additions of 0.08B–0.08C–0.018Hf–0.002Y which are

included for grain boundary strengthening, carbide formation, and oxide scale adhesion [34]. It possesses a high volume fraction of γ' of approximately 0.7 after aging at 1000 °C, a mass density similar to Ni-base superalloys (8.65 g cm^{-3}), and is able to form environmentally protective α-Al_2O_3 after high temperature exposure in air [34, 240]. The γ'-solvus, solidus, and liquidus values for this alloy have been measured by differential thermal analysis as 1204, 1329, and 1381 °C, respectively, resulting in a window of 125 °C where the material is single phase γ and an equilibrium freezing range of 52 °C.

Alloy synthesis. A 136 kg lot of SB-CoNi-10 powder was fabricated by Carpenter Technology Corporation by vacuum induction melting and argon gas atomization. A powder size range of 15 to 53 µm was used for SLM printing, while a larger size distribution of 53 to 177 µm from the same heat was used for the EBM process, as shown in Fig. 5.1(a)-(b). Rectangular blocks and blade-shaped samples were printed in both processes with process parameters that are typical of those employed for printing of Ni-base alloys. The laser printing was conducted at Carpenter Technology Corporation with a preheat temperature of 200 °C applied to the powder bed, while the EBM printing was performed at Oak Ridge National Laboratory and utilized the electron beam to preheat the powder bed to approximately 1000 °C.

The 3D printing trials with both the EBM and SLM approaches resulted in crack-free blocks and blade-shaped samples in the as-printed state, Fig. 5.1(c)-(f). Due to the favorable solvus temperature and the thermal conditions present during printing, the block samples were suitable for tensile tests without the need for post-processing heat treatments. Additional tensile tests were performed after subjecting the alloy to a standard processing route for additively manufactured components, which consists of (i) hot isostatic pressing (HIP) to close any residual gas or shrinkage porosity, (ii) solution heat treatment (SHT) above the γ'-solvus to homogenize the alloy, and (iii) a lower temperature aging to precipitate and coarsen the γ' phase. These specimens are denoted

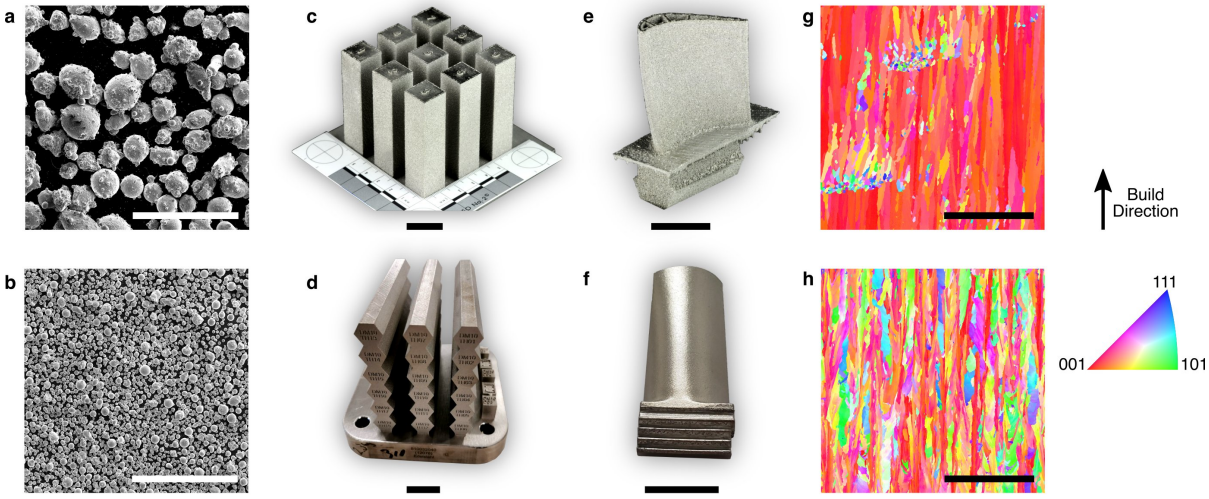

Figure 5.1: **Additive manufacturing of a CoNi-base superalloy through EBM and SLM.** SEM micrographs of metal powder of SB-CoNi-10 used for (**a**) EBM and (**b**) SLM printing trials. Simple bar geometries have been printed for uniaxial tensile testing (**c-d**) in addition to complex geometries such as prototype turbine blades with (**e**) internal cooling channels or (**f**) thin, over-hanging platforms. IPF maps acquired through EBSD show the grain structure of the as-printed CoNi-base superalloy along the build direction manufactured through (**g**) EBM and (**h**) SLM. The scale bars for (**a-b**) and (**g-h**) are 500 µm. The scale bars for (**c-f**) are 2 cm.

as HIP+SHT+aged. Further details on printing and post processing are given in the Methods section.

The as-printed grain structure characterized by electron backscatter diffraction (EBSD) in the scanning electron microscope (SEM) is shown for both the SLM and EBM processes with inverse pole figure (IPF) maps in Fig. 5.1(g) and (h). In the higher preheat EBM process, there is a greater tendency for grains to be columnar and to assume the preferred solidification growth direction of $\langle 001 \rangle$ aligned with the build direction. There are occasional clusters of equiaxed grains, which are associated with fluctuations in thermal conditions, and are not due to lack of fusion locally. In the low preheat SLM process, the grains are also columnar but have greater variation in their crystallographic orientation relative to the build direction.

As-printed chemical segregation. In order to evaluate solute segregation in the as-printed condition, both EBM and SLM alloys were investigated by electron probe microanalysis (EPMA) along the XY-plane, i.e. perpendicular to the build direction, from cross-sections taken 1 mm below the final build layer (Fig. 5.2). By collecting a 20 × 20 point grid of compositional data over a 100 × 100 µm area in the center of the regions shown in Fig. 5.2(b)-(c), statistics on the alloy composition at various stages of the solidification process were collected. These measurements have been repeated on a version of SB-CoNi-10 that was fabricated into a single crystal by the Bridgman method using a 1 mm × 1 mm area grid for data collection over the dendrite florets shown in Fig. 5.2(a). Accurate compositional measurement requires that the electron probe (and subsequently detected x-rays) interacts with a volume of sample that is homogeneous in composition. The interaction volume of the electron probe with the alloy surface is non-negligible at the accelerating voltages necessary for sufficient characteristic x-ray signal from elements such as W or Ta. Therefore, compositional measurements were taken on the XY-plane for all specimens to reduce the impact of compositional fluctuations beneath the alloy surface on the measured values. By sorting this compositional data from highest Co content to lowest Co content, the composition of the solid at each apparent solid fraction, or f_s, for each of the major alloying additions can be estimated and is shown in Fig. 5.2(d)-(f). By fitting these curves with the Scheil equation [55], which describes solute segregation during solidification under the assumption of no diffusion in the solid and infinite diffusion in the liquid, the apparent distribution coefficients that describe the intensity of solute segregation, k, can be experimentally determined. The distribution coefficient k is defined as $k = C_s/C_l$ where C_s and C_l are the composition of the liquid and solid on either side of the solid-liquid interface during solidification. These results are shown in Table 5.2. Apparent distribution coefficients measured in Bridgman-grown single crystals of SB-CoNi-10 show the same partitioning tendencies as the EBM sample [34]. The degree of

partitioning in SB-CoNi-10 is much lower in comparison to conventional Ni-base alloys, resulting in the variation of the fraction liquid with temperature also being lower [34]. Since the length-scale of the segregation present in the as-printed cellular structure is smaller than the interaction volume of the EPMA electron probe, it is not possible to resolve the apparent distribution coefficients for the SLM sample. This is demonstrated by the flat Scheil curves in Fig. 5.2(f) where Scheil curve fits are not applied in this case.

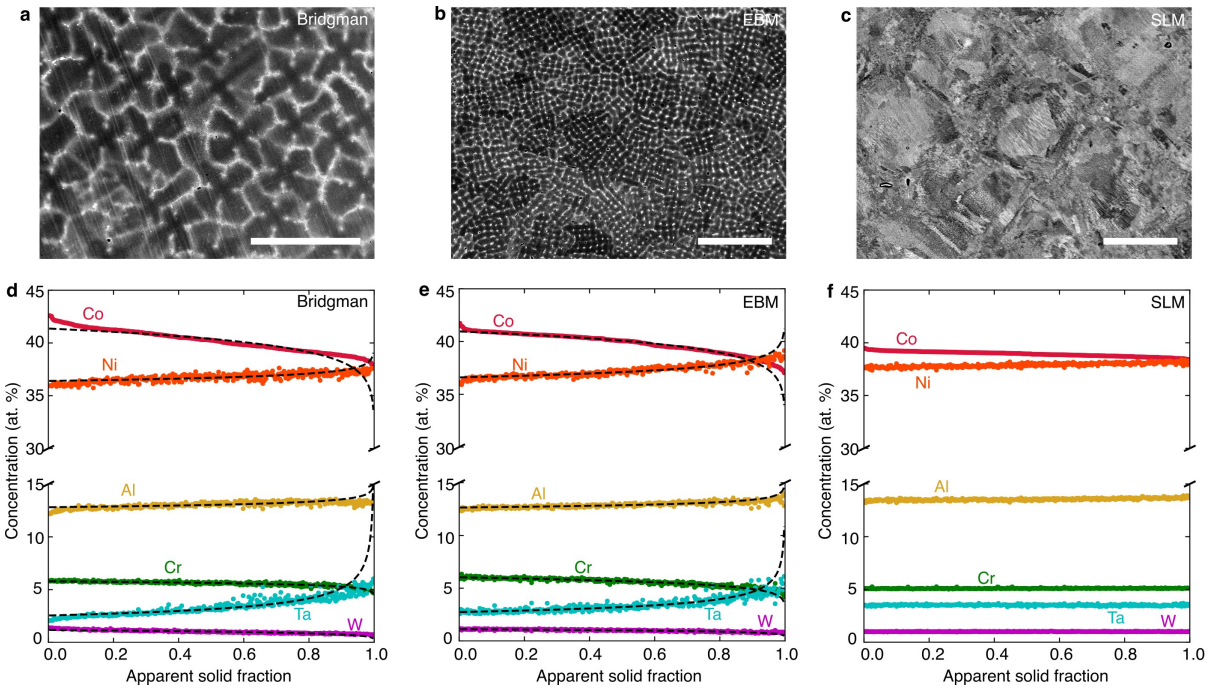

Figure 5.2: **As-printed chemical segregation after Bridgman Casting, EBM, and SLM.** BSE micrographs of the XY-plane microstructures of SB-CoNi-10 after fabrication through (**a**) Bridgman casting, (**b**) EBM, and (**c**) SLM. Quantitative compositional data and Scheil curve fits for the apparent distribution coefficients are shown for the (**d**) Bridgman, (**e**) EBM, and (**f**) SLM samples. EPMA grid scans of 20 × 20 evenly spaced points were collected in the centers of the BSE images shown in (**a-c**) with dimensions of (**a**) 1 × 1 mm and (**b-c**) 100 × 100 µm. Scale bars for (**a**), (**b**), and (**c**) are 500 µm, 50 µm, and 50 µm respectively.

Quantitative chemical maps of the EBM and SLM material are provided in Fig. 5.3(a)-(b) for visualization of this solute segregation, showing that Co, Cr, and W segregate to the dendrite cores and that Ni, Al, and Ta segregate to the interdendritic regions. As

Table 5.2: Experimentally measured distribution coefficients (k_i) using the EPMA grid technique

Alloy name	Alloy class	k_{Co}	k_{Al}	k_W	k_{Ta}	k_{Cr}	k_{Ni}	k_{Re}
11W[51]	Co-, SX	1.01	0.94	0.99	-	-	-	-
2Ta[51]	Co-, SX	1.01	0.95	1.02	0.63	-	-	-
CrTa[51]	Co-, SX	1.01	0.96	1.01	0.61	0.99	-	-
SB-CoNi-10	CoNi-, EBM	1.03	0.98	1.14	0.77	1.09	0.98	-
SB-CoNi-10[34]	CoNi-, SX	1.03	0.97	1.20	0.69	1.04	0.99	-
CMSX-4®[241]	Ni-, SX	1.06	0.91	1.29	0.76	1.05	0.97	1.47
SX-series [53]	Ni-, SX	1.05-1.10	0.81-0.89	1.52-1.54	0.69-0.80	1.07-1.17	0.94-0.95	1.38-1.60
SX-series+C [53]	Ni-, SX	1.03-1.13	0.86-0.90	1.36-1.44	0.76-0.89	1.05-1.13	0.93-0.96	1.33-1.49

noted above, the fine-scale segregation in the SLM samples can not be resolved with this technique.

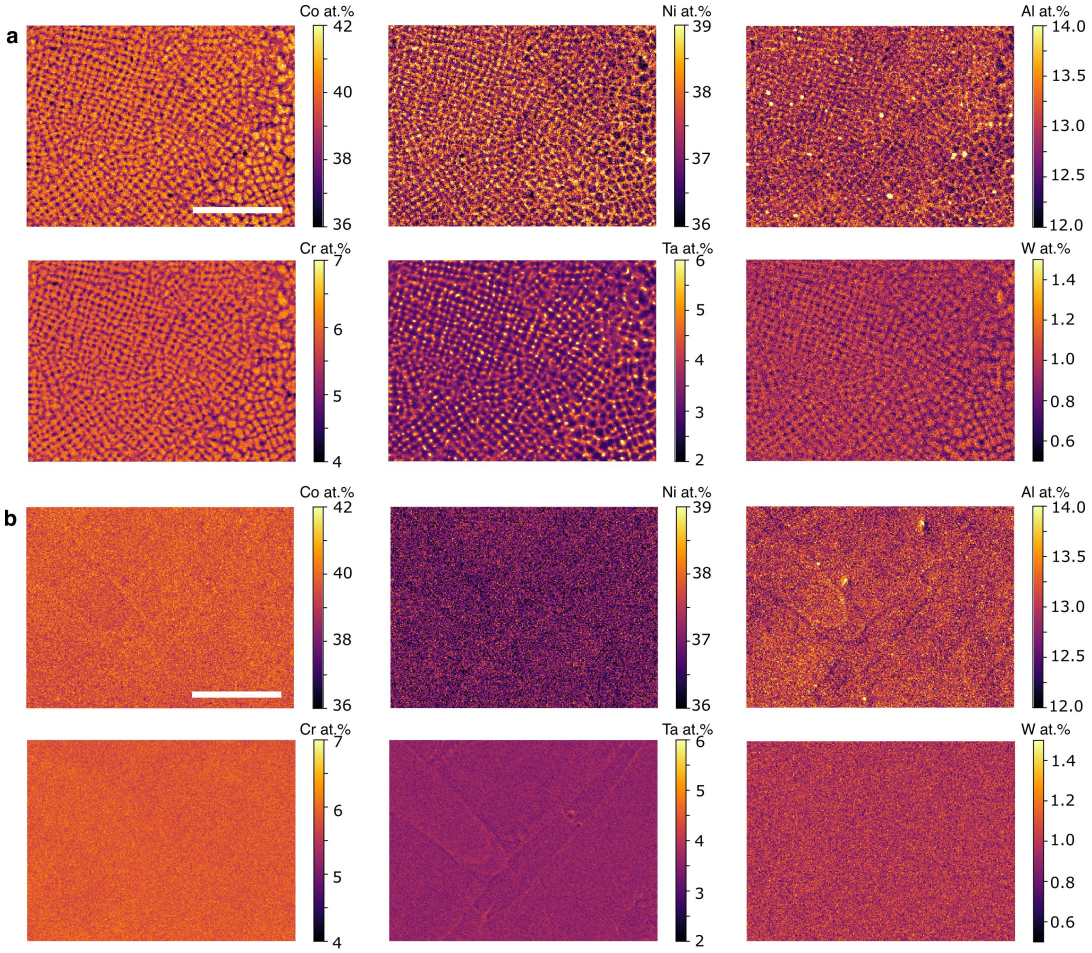

Figure 5.3: **Quantitative EPMA maps.** EPMA elemental composition maps of the XY-plane microstructures for the (**a**) EBM and (**b**) SLM samples. Co, Cr, and W segregate to the dendrite core while Ni, Al, and Ta segregate to the interdendritic regions. Each map has a step size of 0.5 µm. The scale bar for (**a-b**) is 100 µm.

Microstructure evolution. The high preheat temperature employed in EBM (1000 °C) reduces the thermal stresses that develop during solidification, with low orientation gradients present within individual grains (Fig. 5.1(g) and 5.4(f)). In the case of precipitation strengthened alloys such as SB-CoNi-10, preheating results in γ' microstructural evolution that varies with the build height [242]. Investigations at varying heights in the

EBM build (Fig. 5.4(b)-(e)) reveal that near the top of the build the γ' phase precipitates are at a length-scale that is difficult to resolve by scanning electron microscopy, and that the γ' phase and coarsens along the depth of the build. Traditional post-processing can be applied to this alloy in order to homogenize the chemical segregation and eliminate gradients in precipitate size. Hot isostatic pressing applied above the γ'-solvus temperature (T_{HIP} = 1245 °C) resulted in a microstructure that was free from porosity and also resulted in recrystallization of the microstructure into a coarse-grained equiaxed microstructure. While the γ' phase has a non-uniform size distribution along with non-cuboidal precipitate shapes after the HIP, a short 2 h solution heat treatment at 1245 °C followed by aging at 1000 °C for 50 h produces the γ' morphology shown in Fig. 5.4(i)-(j) with a measured volume fraction of approximately 0.7. This heat treatment schedule has also been applied to single crystals of CoNi-alloys grown by the Bridgman method, and could be modified if changes in the grain structure or precipitate sub-structure are desirable [34].

The limited preheat used during SLM (200 °C) does not promote the formation and coarsening of the γ' phase during printing as occurs in EBM. The prior weld pools are visible in Fig. 5.5(a) with columnar grains that grow along the build direction from the bottom of the melt pools and grains that grow laterally from the walls of the weld pools towards the laser track centerline, along with limited amounts of porosity. BSE micrographs at various depths below the final build layer shown in Fig. 5.5(b)-(e) reveal that the cellular microstructure persists throughout the build. Additionally, where the EPMA mapping in Fig. 5.3(b) does not detect chemical segregation, these micrographs reveal that chemical segregation does persist at the cellular level along with the formation of bright Ta-rich carbides. A sub-solvus HIP at 1177 °C resulted in recrystallization of the as-printed microstructure (Fig. 5.5(f)-(g)) and solution heat treatment and aging produced the γ' morphology shown in Fig. 5.5(h)-(i).

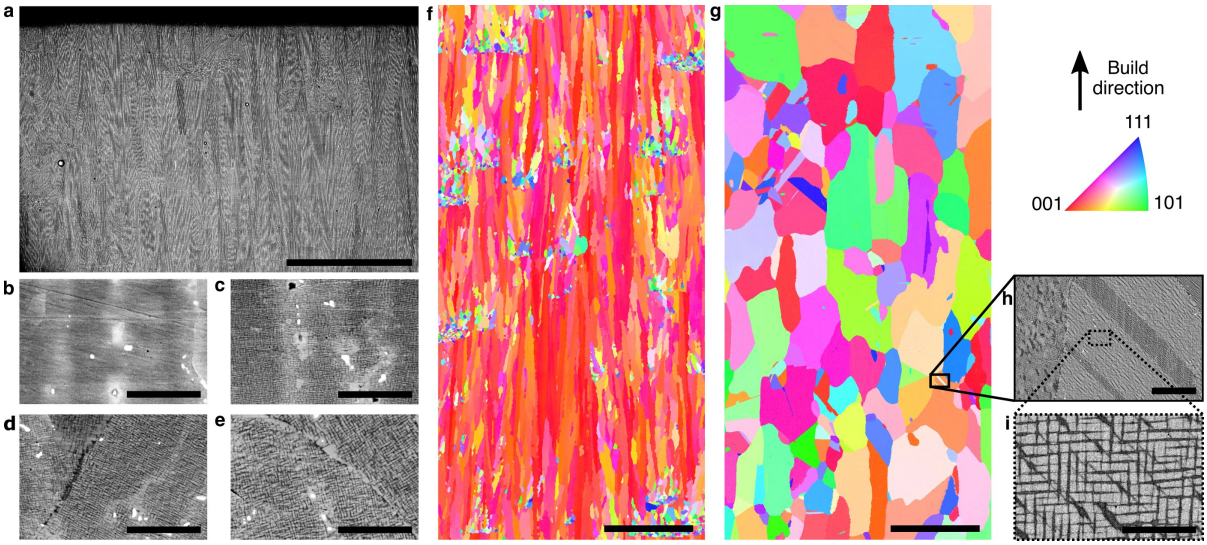

Figure 5.4: **EBM microstructural evolution before and after post-processing.** **a**) Stitched BSE image of the final build layers in as-printed EBM SB-CoNi-10. BSE micrographs of the as-printed EBM alloy at different depths below the final build layer: (**b**) near the final build layer, (**c**) 1 mm below, (**d**) 2 mm below, and (**e**) 4 mm below. (**f**) IPF map of the as-printed EBM alloy and (**g**) IPF map of the fully heat-treated material. Both EBSD scans were acquired at a similar distance from the final build layer (~22 mm) that was representative of the center of the tensile specimen gauge sections. (**h-i**) Additional BSE micrographs of the γ–γ' microstructure after post-processing. The bright particles are Ta-rich carbides which are a result of the intentional addition of carbon. The scale bar for (**a**) is 500 µm. The scale bars for (**b-e**) are 5 µm. The scale bars for (**f-g**) are 500 µm. The scale bar for (**h**) is 25 µm. The scale bar for (**i**) is 5 µm.

Mechanical testing of as-printed and post-processed alloys. Room temperature quasi-static tensile tests were performed on both the SLM and EBM printed material. The specimens were machined from bars such as the ones presented in Fig. 5.1(c)-(d) and tests were performed on both the as-printed and fully heat treated microstructures. A summary of the mechanical strength results are shown in Table 5.3 [98, 243]. Samples tested with the tensile axis along the build direction are indicated as Z-orientation, whereas samples that were tested perpendicular to the build direction are indicated as XY-orientation. Typically, additively manufactured alloys that contain a high density of cracks after printing fail shortly after the yield point. The SB-CoNi-10 alloy demonstrates

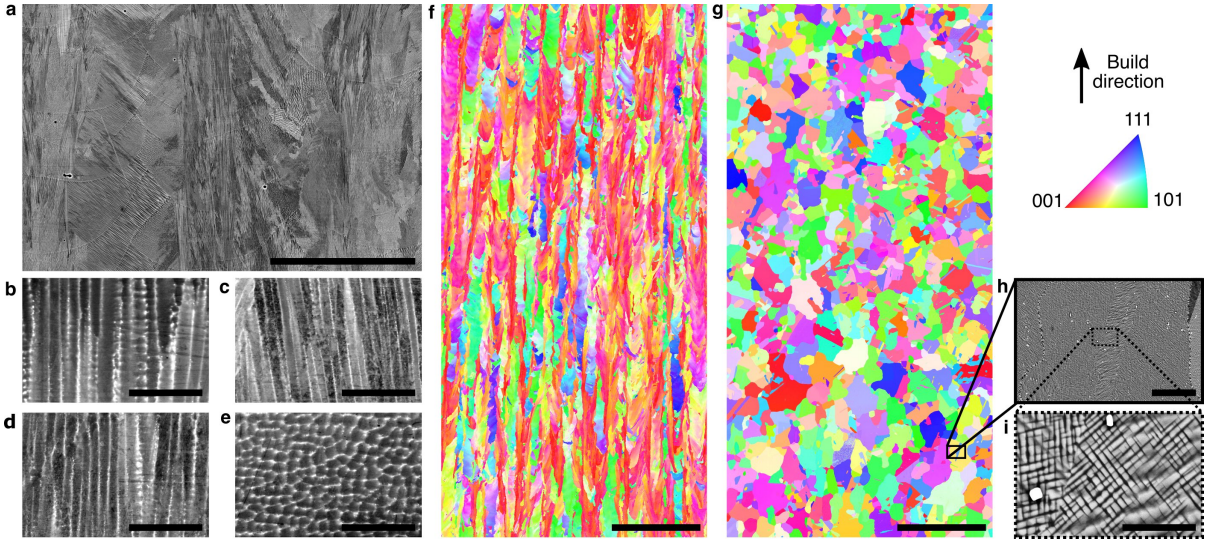

Figure 5.5: **SLM microstructural evolution before and after post-processing.** (**a**) Stitched BSE image of the as-printed SLM microstructure of SB-CoNi-10 with characteristic melt pool boundaries visible. BSE micrographs of the as-printed EBM alloy at different depths below the final build layer: (**b**) near the final build layer, (**c**) 1 mm below, (**d**) 2 mm below, and (**e**) 4 mm below. (**f**) IPF map of the as-printed SLM alloy and (**g**) IPF map of the fully heat-treated material. (**h-i**) Additional BSE micrographs of the γ–γ' microstructure after post-processing. The scale bar for (**a**) is 50 µm. The scale bars for (**b-e**) are 5 µm. The scale bars for (**f-g**) are 500 µm. The scale bar for (**h**) is 25 µm. The scale bar for (**i**) is 5 µm.

significantly improved ductility and resistance to cracking compared to similar Ni-base superalloys produced by PBF, as shown by the engineering stress-strain curves in Fig. 5.6(a) and Fig. 5.6(f). SEM investigations of the fracture surfaces after testing revealed that failure was ductile and intragranular in all room temperature tests (Fig. 5.6(b-e,g-j)). This is evidenced by the tendril-like features that are indicative of microvoid coalescence, along with the significant reductions in cross-sectional area of all specimens after testing. Severe elliptical distortions in the fracture surfaces of the as-printed specimens are visible in Fig. 5.6(b) and 5.6(g). This is a result of rotations of the columnar grains where the slip planes of the dominant slip system reorient in order to maximize the resolved shear stress they experience [244, 245]. EBSD maps along the build direction of the post-mortem EBM specimens reveals this grain rotation by showing how the $\langle 001 \rangle$

crystallographic direction of the columnar grains are now more strongly aligned with the loading direction after the test (Fig. 5.4f and Fig. 5.7a). Additionally, these EBSD maps show how strain accumulates in grains oriented favorably for dislocation slip in the HIP+SHT+aged samples (Fig. 5.7c-d) and that the post-test microstructures of both specimens are free from cracking along grain boundaries (Fig. 5.7(a-d)).

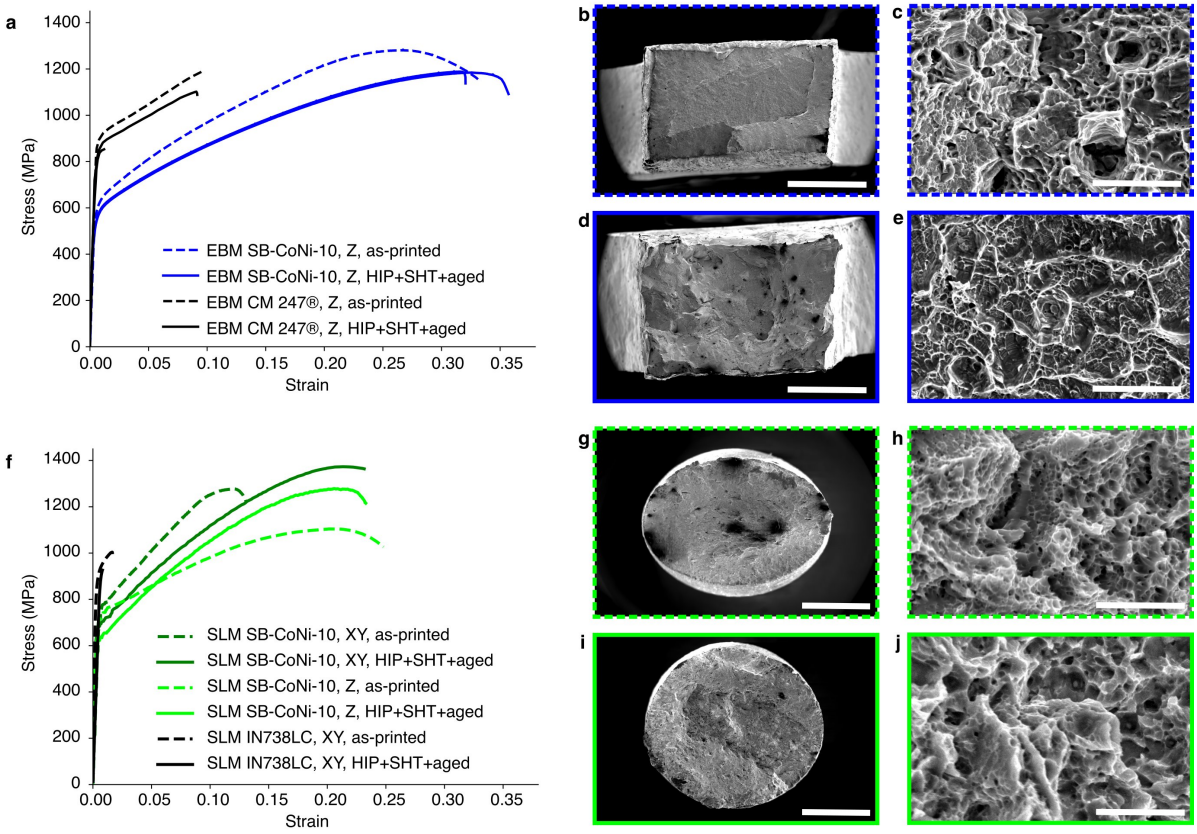

Figure 5.6: **Tensile testing of EBM and SLM SB-CoNi-10 at room temperature.** Stress-strain curves for quasi-static tensile tests at room temperature on the (**a**) EBM and (**f**) SLM materials in the as-printed and fully processed conditions compared to EBM CM 247[98] and SLM Inconel® 738 LC [243]. SEM fractography of the (**b-e**) EBM samples and the (**g-j**) SLM samples in the as-printed (**b-c**, **g-h**) and fully post-processed (**d-e**, **i-j**) conditions reveal features indicative of ductile fracture in all specimens. The higher magnification images are taken near the center of each fracture surface. The scale bars for (**b**, **d**) are 1 mm. The scale bars for (**g**, **i**) are 2 mm. The scale bars for (**c**, **e**, **h**, **j**) are 5 µm.

Table 5.3: Results of room temperature tensile testing

Alloy	Heat Treatment	Orientation	σ_y (MPa)	UTS (MPa)	Elongation (%)
EBM SB-CoNi-10	As-printed	Z	593	1281	33.2
EBM SB-CoNi-10	HIP+SHT+aged	Z	525	1185	35.7
EBM SB-CoNi-10	HIP+SHT+aged	Z	518	1183	32.0
EBM CM 247® [98]	As-printed	Z	894	1196	9.8
EBM CM 247® [98]	HIP+SHT+aged	Z	825	1102	9.2
EBM CM 247® [98]	HIP+SHT+aged	Z	838	853	1.2
SLM SB-CoNi-10	As-printed	XY	753	1289	13.1
SLM SB-CoNi-10	HIP+SHT+aged	XY	689	1379	23.2
SLM SB-CoNi-10	As-printed	Z	717	1110	24.8
SLM SB-CoNi-10	HIP+SHT+aged	Z	621	1289	23.3
SLM Inconel® 738 LC [243]	As-printed	XY	895	1010	1.6
SLM Inconel® 738 LC [243]	HIP+SHT+aged	XY	926	926	0.8

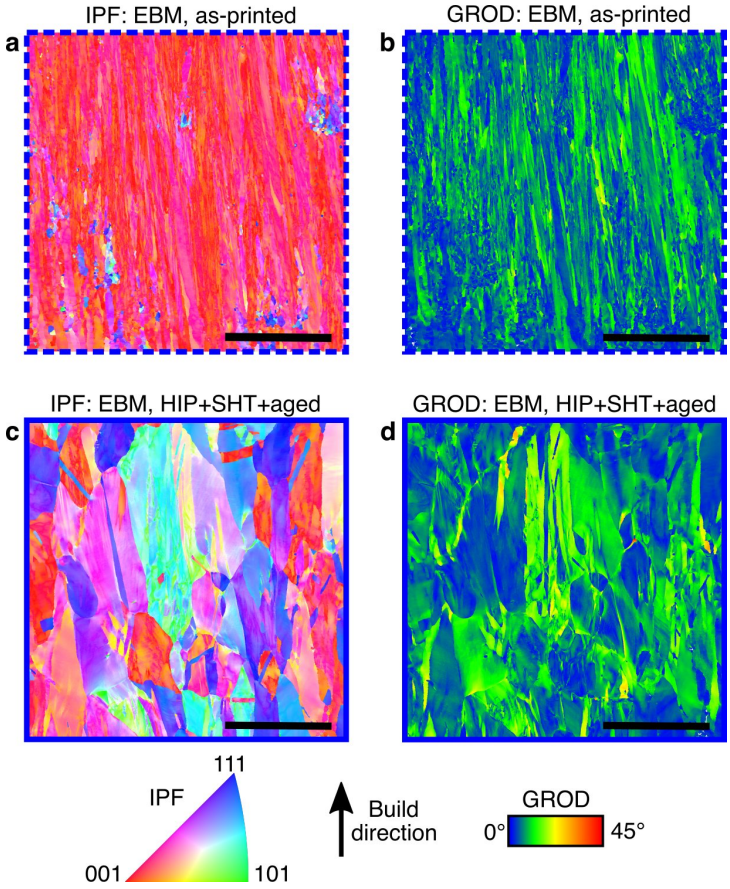

Figure 5.7: **EBSD of post-mortem EBM tensile specimens.** IPF maps (**a**,**c**) and grain reference orientation deviation (GROD) maps (**b**,**d**) show the accumulation of plastic strain after tensile testing of the EBM material in the (**a**-**b**) as-printed and (**c**-**d**) fully heat-treated conditions. The scale bars are 500 µm.

5.4 Discussion

By utilizing a suite of modern research tools, including first-principles calculations [46, 157, 237, 246, 247], high-throughput thermodynamic database calculations [34, 156], combinatorial alloy synthesis [46, 49] and non-destructive characterization techniques [48], a complex multicomponent space for Co-Ni alloy compositions that are favorable for AM and also possess favorable mechanical and environmental properties has been rapidly explored. A particular challenge for alloy design in the additive domain is the need to fabricate expensive powders in significant quantities (typically greater than 100

kg); thus the computational suite of design tools was essential for efficient exploration and selection of a composition likely to be favorable for additive manufacturing. By fabricating the alloy SB-CoNi-10 with both SLM and EBM methods, it is suggested that this region of compositional space may yield alloys that are easier to process through additive manufacturing, compared to current Ni-base superalloys. Importantly, it has been demonstrated that the SB-CoNi-10 alloy can printed in a simple bar form (Fig. 5.1c-d), which is subject to less mechanical constraint during printing, and in a blade-shaped form (Fig. 5.1e-f), which would be more prone to cracking due the added thermomechanical gradients associated with this geometry.

The EPMA grid technique described above is often used on single crystal castings of superalloys fabricated using the Bridgman method to study the microsegregation of various elements during directional solidification, which strongly affects the liquid density during solidification and can promote casting defects such as stray grains and freckle chains [51, 53, 241]. The solidification segregation in the SB-CoNi-10 alloy and related Co-base alloys is much less pronounced compared to Ni-base alloys (Table 5.2) with distribution coefficients near 1 for all elements except for Ta which is approximately 0.75. The less pronounced segregation in the Co-rich alloys, particularly in the late stages of solidification is beneficial for cracking resistance [227, 228]. The intensity of the segregation is similar in the EBM material compared to the single crystal material, though the scale of the dendritic structure is clearly refined in the EBM material due to the higher cooling rates in the EBM process [248]. Similar to single crystal growth processes which exhibit an annealing effect due to slow withdrawal rates, the layer-by-layer thermal excursions in the EBM process might be expected to influence the observed solute segregation due to solid-state diffusion. However, prior research on segregation in these materials has shown these effects to be minor [51]. In the SLM process, with even higher thermal gradients and cooling rates ($> 10^6$ K/m at the solid-liquid interface [249]),

the structure is refined further still. Finer scale chemical maps acquired by transmission electron microscopy are required to conclusively measure the degree, if any, to which segregation is suppressed in the SLM processed samples.

The alloys described above are readily modified through standard post-processing such as HIP and heat treatment to remove microstructural inhomegeneites present after printing, such as chemical segregation and porosity, and to promote a more equiaxed grain structure after recrystallization. In the case of EBM, where long columnar grains aligned with $\langle 001 \rangle$ along the build direction are observed in the as-printed state, modified heat treatments may be desirable to preserve the as-printed grain structure while removing as-printed segregation and pores, as has been demonsrated in EBM processed CMSX-4®* [250]. The microstructure after EBM resembles the columnar grain structure formed in directionally solidified (DS) castings used in the aerospace industry for superalloy turbine blades. The elimination of transverse grain boundaries in DS castings significantly improves the high temperature creep response (T >900 °C) compared to equiaxed castings, which extends the usable life of alloys employed where a combination of high temperature and stress are present [251, 252]. This is partially attributed to enhanced creep-rupture ductility with columnar microstructures, which has been hypothesized to be due to the reduction of grain boundary intersections with the surface which are susceptible to stress-assisted grain boundary oxidation and intergranular cracking [251]. Since these columnar grain structures are industrially relevant, this motivated the printing of the limited amount of EBM powder available for this study in the Z-orientation for microstructural investigations and mechanical testing.

The mechanical response at room temperature demonstrates the excellent printability of the SB-CoNi-10 alloy. The ultimate tensile strength (UTS) and elongation at failure was high with both Z samples with the tensile axis oriented along the build direction

*CMSX-4® is a registered trademark of Cannon-Muskegon Corporation

(EBM, SLM) and XY samples with the tensile axis oriented normal to the build direction (SLM), demonstrating good properties both parallel and transverse to the axis of the columnar microstructure. In spite of their high ultimate tensile strength after significant strain-hardening during plastic flow, tensile ductilities in excess of 32 % are observed for EBM SB-CoNi-10, which is higher compared to the standard precipitation strengthened Ni-base alloy CM 247®[†] fabricated by EBM [98]. For the SLM SB-CoNi-10 specimens, tensile ductilities in excess of 13 % are observed, which is again greater than the standard precipitation strengthened Ni-base alloy Inconel®[‡] 738 LC manufactured by SLM [243]. An anisotropy in the tensile properties is apparent in the SLM samples that depends on build orientation. The as-printed XY-oriented samples exhibit higher strength and lower ductility than their Z-oriented counterparts, which has been observed in other additively manufactured superalloys with columnar microstructures [253]. This behavior is often reversed when a high density of cracks is present in the as-printed microstructure, resulting in reduced yield strengths as the print orientation changes when the preexisting cracks become oriented perpendicular to the loading direction [254]. The single crystal Ni-base superalloy CMSX-4® has recently been printed in cylindrical bar form by EBM, producing a single crystal core with equiaxed grains at the surface [108]. Removing samples from the as-printed single crystal core yielded a room temperature yield strength of 829 MPa and elongation of 6.1 %, with no apparent cracking. However, it is unclear whether the techniques used to create the single crystalline core could be used to print this alloy into more complex blade shapes. While the SB-CoNi-10 alloy has a lower yield strength compared to CMSX-4®, the CoNi-base superalloy compositional space is under-explored and it is likely that future alloy compositions could be designed with higher yield strengths.

[†]CM 247® is a registered trademark of Cannon-Muskegon Corporation
[‡]Inconel® is a registered trademark of Huntington Alloys Corporation

5.5 Conclusions

In conclusion, a recently developed CoNi-base superalloy, SB-CoNi-10, has been successfully printed using both EBM and SLM. Compositional mapping of the as-printed microstructures reveals that solute partitioning is favorable for suppression of cracking across the range of solidification conditions encountered in the EBM and SLM processes. The high thermal gradients and cooling rates in the printing process results in substantial refinement of the as-solidified structure compared to conventional processing routes, reducing the necessary time for a solution heat treatment. The alloys are processable through standard post-processing and heat treatments where a fine dispersion of a high volume fraction of the γ' phase is precipitated. Tensile testing reveals that these alloys exhibit excellent ductility and a high ultimate tensile strength due to a low propensity for defect formation during printing compared to other high γ' volume fraction Ni-base superalloys fabricated by EBM and SLM. This study suggests that further investigation of the CoNi-base superalloy compositional space will be promising for future AM applications. Emerging high throughput experimental and computational tools now enable rapid exploration of the high-dimensional composition-spaces needed to discover alloys for additive manufacturing.

Chapter 6

Structure evolution and mechanical properties of a CoNi-base alloy processed by EBM[†]

In the following two chapters, more detailed investigations on the use of electron beam melting (EBM) and selective laser melting (SLM) to process SB-CoNi-10 are presented. These two powder-bed fusion based AM techniques produce alloys with unique grain structures, cellular/dendritic substructures, and as-printed chemical segregation. The relative strengths of the two approaches are described in more detail in Section 1.4. The as-printed microstructures are presented for both techniques along with the structure evolution due to various heat treatments. Hardness and tensile mechanical properties for select alloys are presented at both room temperature and elevated temperatures. These alloys exhibit excellent tensile ductility compared to Ni-base superalloys which often

[†]Significant portions of this chapter are reproduced from the following article: S.P. Murray, K.M. Pusch, A.T. Polonsky, C.J. Torbet, G.G.E. Seward, P. Nandwana, M.M. Kirka, R.R. Dehoff, N. Zhou, S.A.J. Forsik, W. Slye, and T.M. Pollock, Microstructure and Tensile Properties of a CoNi-Based Superalloy Fabricated by Selective Electron Beam Melting. In S. Tin et al. (Eds.) *Superalloys 2020*, (2020) pp. 880-890. [**doi**] [198]

experience extensive cracking due to the extreme thermal conditions present in additive manufacturing which severely degrades their mechanical properties.

In this chapter, SB-CoNi-10 is successfully produced through EBM. The elevated preheat temperature of 1000 °C results in an in situ heat treatment that promotes a build-height dependent γ' distribution. The microsegregation of the fine dendritic structure is assessed by EPMA and compared to previous single crystal castings of SB-CoNi-10+. Room temperature and elevated temperature tensile testing demonstrates that these alloys have an excellent combination of strength and ductility. Elevated temperature tensile tests demonstrate that the textured as-printed microstructure performs better compared to the recrystallized microstructures formed by super-solvus heat treatment. High strain-rate tensile tests on as-printed and heat treated specimens suggest that a time-dependent process such as grain boundary oxidation contributes strongly to the observed reduction in ductility at elevated temperatures.

6.1 Introduction

Selective electron beam melting (SEBM, or EBM) is a powder bed based additive manufacturing (AM) technique for the fabrication of fully dense metallic components [97]. This process employs a finely-focused electron beam directed by electromagnetic lenses to sinter and subsequently melt 50-100 µm thick layers of metal powder in a build chamber under a controlled vacuum. Rapid manipulation of this directed energy source allows for innovative scan strategies and reduced build times for components with complex designs that would be difficult to achieve through other manufacturing techniques. EBM has been successfully applied to a variety of commercial alloys currently used in energy, biomedical, automotive, and aerospace applications, such as Ti-6Al-4V, CoCrMo alloys, 316L stainless steel, γ-TiAl, Inconel 625, and Inconel 718 [97].

Due to their excellent mechanical properties at elevated temperatures, there is a strong desire to apply additive manufacturing techniques to the high γ' volume fraction Ni-based superalloys [98]. However, these Ni-based superalloys are highly susceptible to cracking during the EBM process, resulting in as-printed microstructures that contain a high density of pre-existing flaws and cracks that severely degrade the mechanical properties of the final component [98]. These cracks typically extend across multiple build layers and are located between misoriented columnar grains that grow epitaxially from the previous build layer due to the high thermal gradients present during printing [101]. Hot isostatic pressing (HIP) is normally applied after EBM in order to eliminate process-induced porosity, but this post-processing is often ineffective for closing cracks once they have formed [99, 174]. Therefore, in order to fabricate components by EBM for elevated-temperature applications without pre-cracked, as-printed microstructures, it is necessary to either (i) modify the microstructure through innovative scanning strategies and process parameters [101] or (ii) develop novel alloy compositions that are less susceptible to cracking while retaining the desirable high γ' volume fraction.

The favorable solidification behavior of Co-based superalloys makes them interesting candidates for additive manufacturing. Cracking during the EBM process is promoted by large freezing ranges resulting in liquid films between solidifying dendrites in the late stages of melt pool solidification, accompanied by tensile stresses due to thermal contraction. The liquid films are solute enriched due to strong rejection of γ'-forming elements to the liquid. Single crystal casting studies on Co-based superalloys have demonstrated that Co-based superalloys have a more even distribution of alloying additions between the solid and liquid, i.e. the distribution coefficients ($k_i = C_s/C_l$) are closer to unity [51]. In the case of CoNi-based superalloys, the distribution coefficients lie between those for Co- and Ni-based superalloys, indicating that the solidification behavior for CoNi-based superalloys should also be favorable, which may result in a reduced susceptibility for

cracking [34].

For these reasons, a recently developed γ'-containing CoNi-based superalloy named SB-CoNi-10 has been fabricated via EBM to investigate whether CoNi-based superalloys are promising candidates for future alloy development for AM. This alloy exhibits a γ'-solvus of 1204 °C, a low density of 8.65 g cm^{-3}, and can form a continuous Al_2O_3 scale upon high temperature exposure to air at 1100 °C [34]. The microstructure and mechanical properties of this alloy have been investigated in the as-printed and post-processed conditions.

6.2 Methods

A 51.7 kg powder heat of SB-CoNi-10 powder was fabricated at Carpenter Technology Corporation through vacuum induction melting and inert gas atomization with a -177/+53 µm particle size distribution. Table 5.1 in Ch. 5 lists the nominal SB-CoNi-10 composition along with the composition of the powder and the composition of the as-printed alloy processed by EBM asmmeasured by inductively coupled plasma mass spectrometry (ICP), glow discharge mass spectrometry (GDMS), and combustion analysis. An Arcam Q10+ system at Oak Ridge National Laboratory running 4.2.89 EBM control software was used in this work with the following print parameters: max current = 18 mA, speed function = 63 (unitless), hatch spacing = 125 µm, layer thickness = 75 µm, pre-heat = 1000 °C. A 3 × 3 array of rectangular bars were printed for tensile testing experiments along the build direction. These bars had dimensions of 6.4 cm × 1.6 cm × 1.6 cm. Several of these bars underwent a hot isostatic pressing (HIP) at 1245 °C / 100 MPa / 4 h followed by a 1245 °C solution heat treatment (SHT) for 2 h and a 1000 °C age for 50 h under vacuum.

Tensile testing was performed at room temperature and elevated temperatures in lab-

oratory air with an Instron 5582 universal testing machine. Tests were also performed at quasi-static (1×10^{-4}) and rapid (1×10^{-2} strain rates at elevated temepratures. Sheet dogbone-shaped samples with gauge dimensions of 2 mm × 3 mm × 14 mm and total length of 44 mm were extracted from the top of the printed bars by electric discharge machining (EDM). Samples were ground with SiC papers down to 1200 grit after machining to remove any heat-affected zone from EDM. Heat was applied by induction with an Ambrell 800S series heater with a custom-built water-cooled copper coil. Test temperatures were maintained with a Pyrofiber Lab infrared pyrometer rated for 320–1200 °C focused on sample gauge sections where a black high temperature paint was applied.

Samples were prepared for microscopy by grinding with SiC papers down to 1200 grit followed by vibratory polishing down to a 50 nm colloidal alumina suspension. Optical microscopy of the as-printed microstructure was acquired with a Keyence VHX-5000 digital microscope after a 20 s immersion etch with Kallings No. 1 etchant (33 ml water, 33 ml concentrated hydrochloric acid, 33 ml ethyl alcohol, and 1.5 g cupric chloride dihydrate). 2D optical image stitching was used to acquire photographs along the entire length of a bar cross-section and 3D-stitching was used for in-focus imaging of post-mortem dogbone fracture surfaces.

Scanning electron microscopy (SEM) using both secondary electron (SE) and backscattered electron (BSE) imaging was performed at accelerating voltages between 5 kV and 20 kV with a ThermoFisher Apreo C. The primary dendrite arm spacing (PDAS) of the as-printed alloy were measured using Delauney triangulation within FIJI using BSE micrographs taken perpendicular to the build direction. Electron backscattered diffraction (EBSD) maps were acquired using an EDAX Velocity EBSD camera in a FEI Versa3D microscope at 30 kV. Indexing of the collected diffraction patterns was accomplished using the EMSphInx software package in addition to traditional Hough indexing within OIM Analysis software [191]. All inverse pole figure (IPF) maps shown in this article

are indexed with the ⟨001⟩ crystallographic direction along the build direction. Elastic stiffnesses were calculated by considering loading along the build direction using single crystal elastic stiffnesses experimentally determined by resonant ultrasound spectroscopy (RUS) at 850 °C in air on a single crystal variant of SB-CoNi-10: C_{11} = 198.3 GPa, C_{12} = 141.9 GPa, C_{44} = 99.5 GPa, with Zener anisotropy ratio = 3.53. Further details on performing RUS measurements have been reported in a previous publication [121]. Schmid factors for $\{111\}\langle 1\bar{1}0\rangle$ slip were calculated by considering loading along the build direction.

Chemical segregation was assessed by electron probe microanalysis (EPMA) on a Cameca model SX100 with five wavelength dispersive spectrometers and a CeB_6 thermionic emission gun at 20 kV. Standards-based quantification was performed with a reference alloy of Co-6.7W-8.9Al-3.3Cr-1.5Ta at.% that was characterized by ICP. The bright spots in the Al maps (and corresponding dark spots in the Co maps) are a result of porosity where alumina polishing media persisted after metallographic preparation. Scheil solidification simulations were performed on the nominal alloy composition using a 2011 version of the commercial PANDAT PanCobalt thermodynamic database of the Co-Ni-Al-W-Ta-Cr system. No phases were suppressed during the calculation, even if the predicted phases were not experimentally observed. The equilibrium freezing range was measured by differential thermal analysis (DTA) at a heating rate of 5 °C s^{-1} on 0.179 g of heat treated alloy using a Setaram Setsys 16/18 calibrated with high purity Sn, Ag, Au, Ni, and Pd.

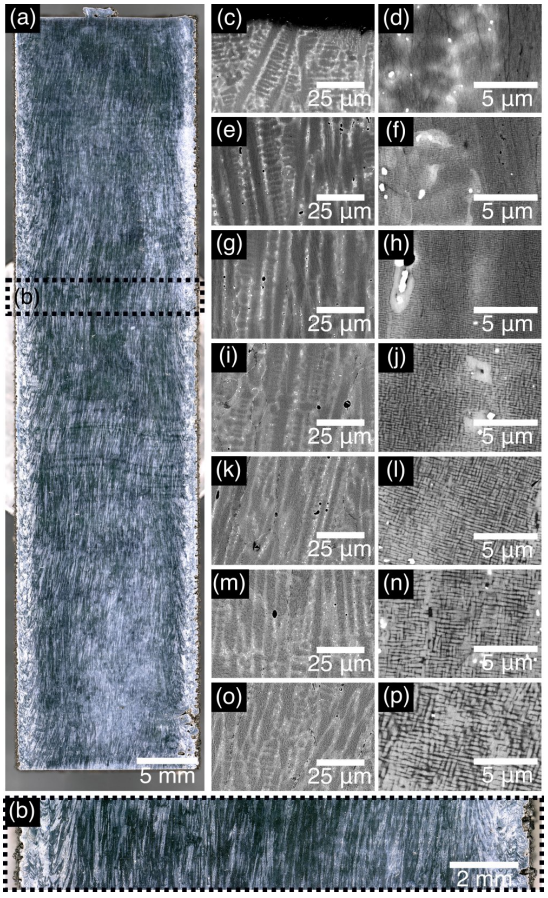

Figure 6.1: (a,b) Stitched optical micrographs of an etched cross-section along the build direction of an as-printed bar of EBM SB-CoNi-10. BSE micrographs at different depths below the final build layer of (c,d) 0 mm, (e,f) 1 mm, (g,h) 2 mm, (i,j) 4 mm, (k,l) 8 mm, (m,n) 16 mm, and (o,p) 32 mm.

6.3 Results

6.3.1 As-Printed and Fully Heat Treated Microstructure

Optical microscopy on an etched cross-section of an as-printed EBM SB-CoNi-10 bar reveals the grain structure across the entire length of the bar (Fig. 6.1a). The samples exhibit a 1 mm thick layer of surface equiaxed grains that are associated with the rough, powder-sintered surface. Similar to other Ni-based superalloys fabricated through EBM, a primarily columnar microstructure is present with grains aligned along the build di-

rection that span multiple build layers [98]. Cracks between these columnar grains were not observed. Other classes of flaws such as lack-of-fusion defects were also not observed. Chemical segregation is present between the dendrite cores and interdendritic regions (Figs. 6.1c, e, ..., o). Additions of carbon in the alloy result in the formation of small, blocky Ta-rich carbides within the interdendritic regions and along grain boundaries. EPMA point measurements (not shown) indicate that these carbides are likely MC carbides of composition TaC. Columnar grains consist of several well-aligned dendrites with an average PDAS of 7 µm, which is over an order of magnitude finer than the PDAS observed after solidification using the Bridgman method [51, 255]. A small amount of porosity is observed throughout the specimen, usually located within the interdendritic regions. This porosity is likely gas porosity due to its spherical morphology.

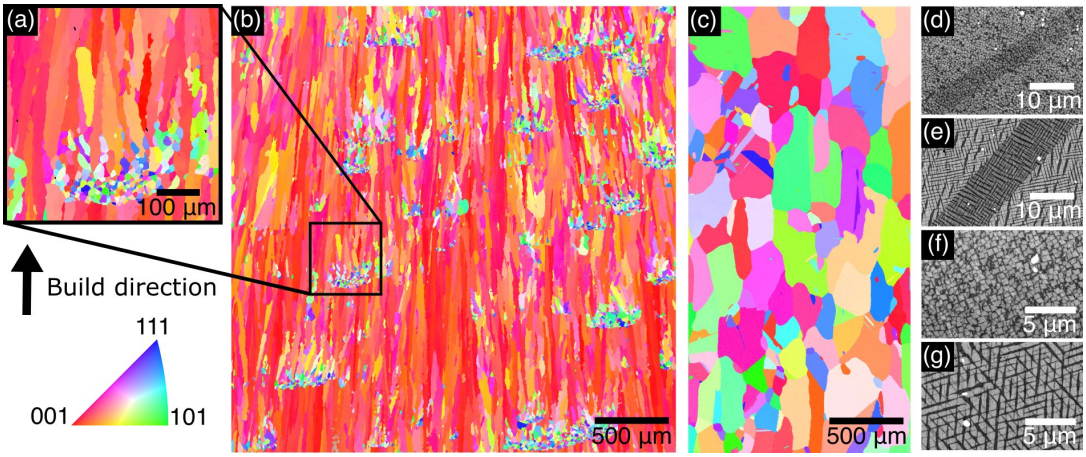

Figure 6.2: IPF maps of (a-b) as-printed and (c) HIP+SHT+Aged EBM SB-CoNi-10. A focused view of an equiaxed grain region is shown in (a). BSE micrographs of (d,e) annealing twins and (f,g) the γ' morphology are from the (d,f) HIP-only condition and the (e,g) HIP+SHT+Aged condition.

The γ' size varies across the build direction due to the applied pre-heat temperature of 1000 °C used for pre-sintering the metallic powder before melting of each layer. This pre-heating results in regions far from the final build layer experiencing more time at elevated temperatures than regions near the final build layer. This results in a gradient

of γ' size that is a function of the build height (Figs. 6.1d, f, ..., p). Additionally, there is a non-uniform γ' size distribution at each build height perpendicular to the build direction that depends on whether γ' are located within the dendrite cores or the interdendritic regions.

The IPF map in Fig. 6.2b shows that the columnar grains are strongly $\langle 001 \rangle$ textured along the build direction in the as-printed condition. However, the columnar grained microstructure is frequently interrupted by isolated clusters of fine equiaxed grains. A focused view of one of these equiaxed grain regions is shown in Fig. 6.2a. These regions are often contained within a single build layer (75 µm) in height, where the columnar texture is eventually recovered over subsequent build layers. These equiaxed grain regions are not thought to occur due to lack-of-fusion, since in-plane process-induced porosity that is characteristic of lack-of-fusion was not observed around these features [256].

To homogenize the alloy and reduce porosity, printed bars underwent a HIP followed by SHT and aging (HIP = 1245°C / 100 MPa / 4 h, SHT = 1245 °C / 2 h, age = 1000°C / 50 h). These processing steps resulted in a unimodal distribution of the γ' phase, which is displayed in Fig. 6.2e and Fig. 6.2g. Since the slow-cooling from the HIP temperature leads to a variety of non-cuboidal precipitate shapes (Fig. 6.2d and Fig. 6.2f), additional SHT and aging are necessary to create the desired unimodal distribution of cuboidal γ' precipitates [257]. This post-processing led to a complete recrystallization of the columnar microstructure, resulting in large, slightly-elongated equiaxed grains containing annealing twins that were not present in the as-printed condition. This new microstructure is compared to the as-printed microstructure in Fig. 6.2c. Microstructural investigations in the HIP-only condition revealed that the recrystallization occurs during the HIP process, indicating that modifications to the HIP procedure would be necessary if the columnar microstructure is to be preserved throughout post-processing, or if a finer equiaxed grain structure is to be produced. The average grain size measured by

EBSD for the as-printed, HIP-only, and HIP+SHT+Aged conditions were 67, 248, and 262 µm, respectively. Grain reference orientation deviation maps (not shown) revealed that the as-printed microstructure contains grains with large gradients in misorientation, which likely provide sufficient stored strain energy to induce recrystallization at elevated temperature.

6.3.2 As-Printed Chemical Segregation

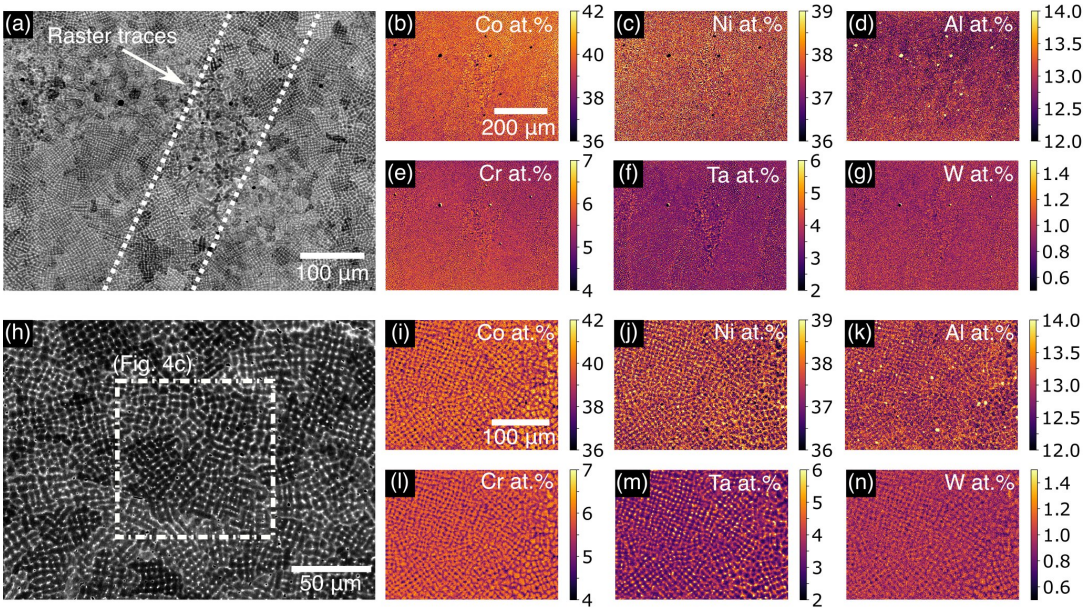

Figure 6.3: BSE micrographs of the as-printed chemical segregation perpendicular to the build direction within (a) an equiaxed grain region and (h) the dendritic-scale microstructure taken from cross-sections 1 mm below the final build layer. Compositional heat maps (in at.%) collected by EPMA of both regions are shown for: (b,i) Co, (c,j) Ni, (d,k) Al, (e,l) Cr, (f,m) Ta, and (g,n) W. The EPMA scan for (b-g) had a 1 µm step size and the scan for (i-n) had a 0.5 µm step size.

EPMA chemical maps of the as-printed microstructure 1 mm below the final build layer are presented in Fig. 6.3 along with BSE micrographs of the investigated regions. These chemical maps describe the chemical segregation of the six major elements in SB-CoNi-10 (i.e. Co-Ni-Al-Cr-Ta-W) in an equiaxed grain region at lower magnification

(Fig. 6.3a) and in the dendritic microstructure within the columnar grains (Fig. 6.3h). The γ-formers such as Co, Cr, and W are observed in higher concentrations in the dendritic cores, while the γ'-formers Ni, Al, and Ta are observed to segregate to the interdendritic regions [34]. The higher magnification chemical maps were displayed alongside similar maps from an SLM-printed alloy in Ch. 5, and are reproduced here for comparison with the lower magnification map collected on the EBM printed alloy. Line traces of the raster scan strategy can be observed in the lower magnification EPMA maps, with the equiaxed grain region appearing to be bounded by these line traces. This suggests that these equiaxed grain regions are promoted by AM process parameters and the corresponding local thermal conditions, and may be eliminated through appropriate process control.

Table 6.1: Experimental and simulated distribution coefficients (k_i) of SB-CoNi-10

Method	k_{Co}	k_{Ni}	k_{Al}	k_{Cr}	k_{Ta}	k_W
SX casting, bottom of bar [34]	1.03	0.99	0.97	1.04	0.69	1.20
SX casting, top of bar [34]	1.03	0.99	0.97	1.04	0.73	1.17
EBM, top of bar	1.03	0.98	0.98	1.09	0.77	1.14
PANDAT Scheil simulation	1.09	0.97	0.84	1.04	0.31	1.80

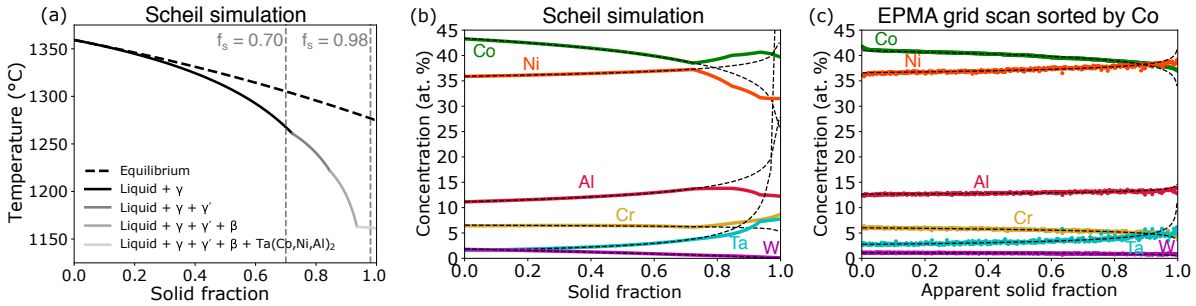

Figure 6.4: (a) Scheil solidification simulation using the major elements of nominal SB-CoNi-10. (b) The composition of each major alloying addition vs. solid fraction predicted by the Scheil simulation in (a). (c) The composition of each major alloying addition vs. apparent solid fraction measured by EPMA with a 20 × 20 point grid scan in the boxed region shown in Fig. 6.3h. The dashed black lines in (b-c) are curve fits using Eq. 1 to determine the distribution coefficient for each element, k_i. These coefficients are compared in Fig. 6.10.

Quantitative measurement of the as-printed segregation by EPMA was collected in the 100 × 100 µm region outlined in Fig. 6.3h. A 20 × 20 point grid of compositional measurements were collected. These EPMA data were also presented previously in Ch. 5 compared to SLM and single crystal versions of SB-CoNi-10 alloys, and they are reproduced here for the following discussion of using Scheil solidification simulations to further study the solute partitioning behavior. As explained previously in Ch. 5, since Co is the majority element in the alloy, the collected data were sorted and assigned an apparent solid fraction (f_s) by the Co content assuming that the dendrite core solidifies first with the highest Co content (apparent $f_s = 0$) and the interdendritic liquid solidifies last with the lowest Co content (apparent $f_s = 1$). By applying the Scheil equation [55],

$$C_s = kC_o(1 - f_s)^{k-1} \tag{6.1}$$

where C_s is the concentration of the solid, C_o is the starting composition in the melt, f_s is the solid fraction, and k is the distribution coefficient, these sorted experimental curves can be fit to determine the distribution coefficient for each major element. The experimental EPMA data along with the Scheil curve fits are displayed in Fig. 6.4c in comparison to simulated results from the Scheil simulation in Fig. 6.4b.

A Scheil solidification simulation using PANDAT (Fig. 6.4a) was performed using the major elements of the nominal SB-CoNi-10 composition to determine the equilibrium freezing range, ΔT_{eq}, and the effect of chemical segregation on this freezing range, ΔT_{Scheil}. The simulation predicts the formation of the γ phase followed by the γ' phase, a B2-ordered β phase, and a Ta-rich Laves phase (AB_2) with a composition of Ta(Co,Ni,Al)$_2$. However, the β phase and the Laves phase are not observed experimentally in the as-printed microstructures described above. The simulated value for $\Delta T_{eq,PANDAT}$ was 84 °C, whereas DTA measurements on the HIP+SHT+Aged alloy mea-

sured the equilibrium freezing range as $\Delta T_{eq,DTA}$ = 48 °C, showing that PANDAT overestimates the equilibrium freezing range. The effect of segregation during solidification widens this solidification range further, resulting in a PANDAT prediction of ΔT_{Scheil} = 198 °C. The simulation accurately predicts the direction of partitioning of each alloying addition (i.e. whether an element segregates to the liquid or the solid). However, the β and Laves phase predictions are likely promoted by the inaccurate intensity of the partitioning of elements such as Ta and Al to the liquid, with $k_{Ta,PANDAT} = 0.31$, $k_{Al,PANDAT} = 0.84$. Experimental measurements of the Ta and Al segregation in this study have yielded values of $k_{Ta,EBM} = 0.77$ and $k_{Al,EBM} = 0.98$, which are closer to unity than predicted by PANDAT. Therefore, it is likely that the freezing range predicted by PANDAT is wider than experimentally observed due to differences in the predicted solute partitioning during solidification.

6.3.3 Room Temperature Tensile Testing

A summary of the mechanical testing results on EBM SB-CoNi-10 are displayed in Table 6.2, with the stress-strain curves shown in Fig. 6.5 for the quasi-static tensile tests at room temperature and elevated temperature. Both the as-printed alloy and the the HIP+SHT+Aged alloy were tested. These results are compared to Ni-based CM 247®* that was also processed by EBM and tested under similar conditions [98].

In the as-printed condition, the CoNi-alloy exhibits excellent tensile ductility at room temperature exceeding 30 % strain before failure. High ultimate tensile strengths in excess of 1200 MPa were observed due to significant strain hardening. The effect of the post-processing heat treatments results in reduced yield strengths and ultimate tensile strengths along with further enhanced ductility. A repeated tensile test on the CoNi-based superalloy at room temperature in the HIP+SHT+Aged condition demonstrated

*CM 247® is a registered trademark of Cannon-Muskegon Corporation

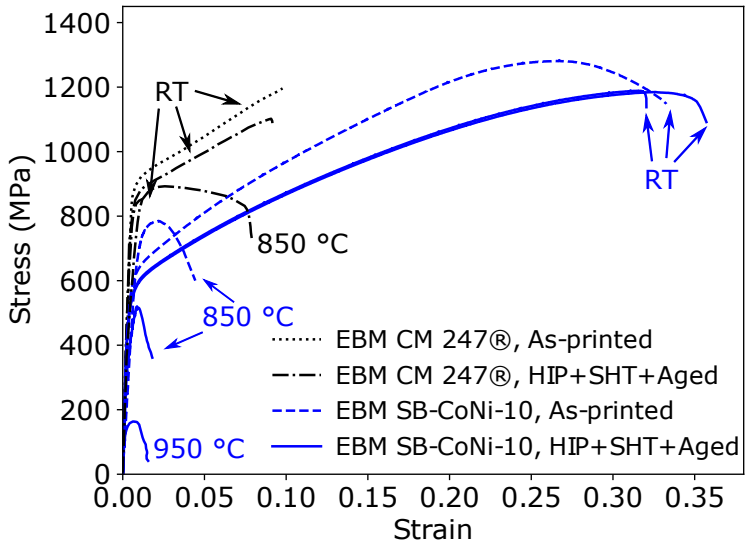

Figure 6.5: Engineering stress-strain curves from quasi-static tensile tests at room temperature and elevated temperatures on EBM SB-CoNi-10 compared to the Ni-based EBM CM 247® [98].

consistent mechanical properties. This is in contrast to EBM fabricated Ni-based superalloys that exhibit a large variability in their mechanical properties when a high density of cracks are present after printing [98, 99]. In both the as-printed and heat treated conditions, fracture was observed to be ductile and intragranular (Figs. 6.6a,c), which is evidenced by the characteristic tendril-like features observed on the fracture surfaces by SEM in Figs. 6.6b,d.

6.3.4 Elevated Temperature Tensile Testing

A tensile test performed at 850 °C on the HIP+SHT+Aged alloy reveals that there is a significant drop in tensile ductility at elevated temperatures, with the ultimate tensile strength falling to a value below the room temperature yield strength. An additional test at 950 °C was performed to investigate if this ductility reduction was due to an intermediate temperature ductility drop, however the ductility was reduced even fur-

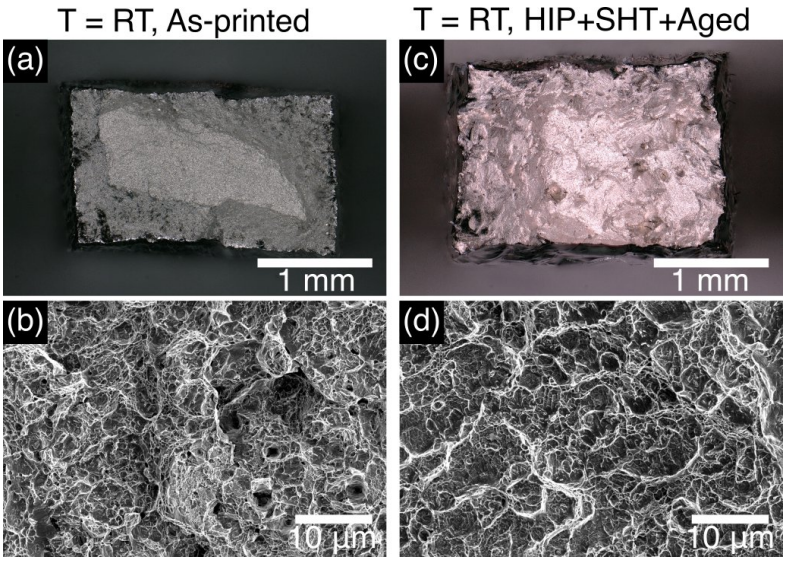

Figure 6.6: (a,c) Optical micrographs and (b,d) SEM micrographs of the fracture surfaces after room temperature tensile tests on (a-b) as-printed and (c-d) HIP+SHT+Aged EBM SB-CoNi-10 (HIP+SHT+Age = 1245°C / 100 MPa / 4 h + 1245 °C / 2 h + 1000 °C / 50 h). SEM micrographs reveal tendril-like features indicative of ductile fracture in both the (b) as-printed and (d) HIP+SHT+Aged conditions.

ther at this higher temperature. A similar reduction in ductility is observed in the as-printed SB-CoNi-10 alloy at 850 °C, but this ductility reduction is not as severe as in the HIP+SHT+Aged alloy. The as-printed SB-CoNi-10 alloy has a similar response at 850 °C to EBM CM 247® in Fig. 6.5, which also possesses a fine, columnar grained microstructure.

Observations of the fracture surfaces displayed in Fig. 6.7 reveal that some amount of intergranular fracture occurs above 850 °C for both sets of samples, with the HIP +SHT+Aged specimens being completely intergranular at 950 °C and the as-printed specimens showing intergranular fracture over roughly 50 % of the fracture surface at 850 °C (Fig. 6.7a). The center of the as-printed specimen remained ductile at 850 °C, which likely contributes significantly to the superior ductility compared to the HIP+SHT+Aged specimens. A combination of intergranular and intragranular fracture present on a single fracture surface will be referred to as a "mixed-mode" failure for clarity.

Table 6.2: Results of Tensile Testing Along the Build Direction

Alloy	Condition	Temp. (°C)	$\dot{\epsilon}$ (s^{-1})	σ_y (MPa)	UTS (MPa)	ϵ_f (%)
EBM SB-CoNi-10	As-printed	RT	1×10^{-4}	593	1281	33.2
	As-printed	850	1×10^{-4}	698	785	4.4
	As-printed	850	1×10^{-2}	670	975	12.7
	HIP+SHT+Aged	RT	1×10^{-4}	518	1183	32
	HIP+SHT+Aged	RT	1×10^{-4}	525	1185	35.7
	HIP+SHT+Aged	850	1×10^{-4}	420	516	1.8
	HIP+SHT+Aged	850	1×10^{-2}	561	835	5.5
	HIP+SHT+Aged	950	1×10^{-4}	149	163	1.4
EBM CM 247® [98]	As-printed	RT	1×10^{-4}	894	1196	9.8
	HIP+SHT+Aged	RT	1×10^{-4}	825	1102	9.2
	HIP+SHT+Aged	RT	1×10^{-4}	838	853	1.2
	HIP+SHT+Aged	850	1×10^{-4}	851	891	7.9

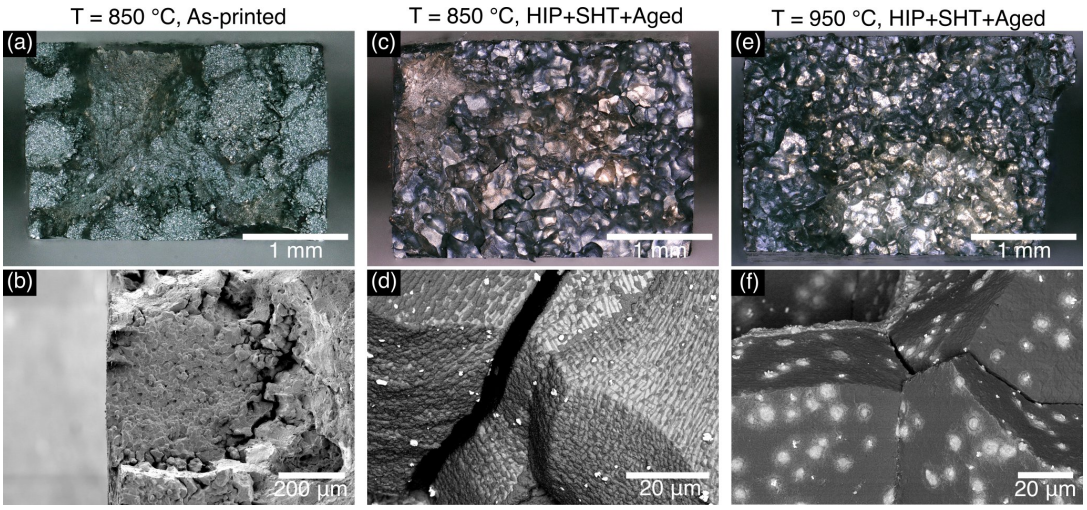

Figure 6.7: (a,c,e) Optical micrographs and (b,d,f) SEM micrographs of the fracture surfaces after high temperature tensile tests: (a-b) as-printed with T = 850 °C, (c-d) HIP+SHT+Aged with T = 850 °C, and (e-f) HIP+SHT+Aged with T = 950 °C.

Higher magnification SEM images of the fracture surfaces in Fig. 6.7 show the regions on each fracture surface where intergranular fracture is occurring for the high temperature tests. Notably, intergranular failures only occur at surface-connected grains in the as-printed condition, with fracture occurring along transverse grain boundaries perpendicular to the loading direction below the equiaxed grain regions described in Figs. 6.2a,b. This is visualized in the IPF map presented in Fig. 6.8a, which was taken across the entire width of the gauge section of the post-mortem as-printed specimen tested at 850 °C. The fracture surface has a jagged, stair-case morphology that connects many separate equiaxed grain regions. Additionally, cracks are observed underneath equiaxed grain regions far from the fracture surface as well.

Fig. 6.8b shows a BSE micrograph of one of these surface-connected cracks below an equiaxed grain region, along with an associated IPF map in Fig. 6.8c. The elastic stiffness map in Fig. 6.8d shows how certain grains are many times more stiff than the elastically compliant columnar grains that are aligned with the build direction. Additionally, by considering the Schmid factor (Fig. 6.8e) for $\{111\}\langle 1\bar{1}0\rangle$ slip for loading applied along

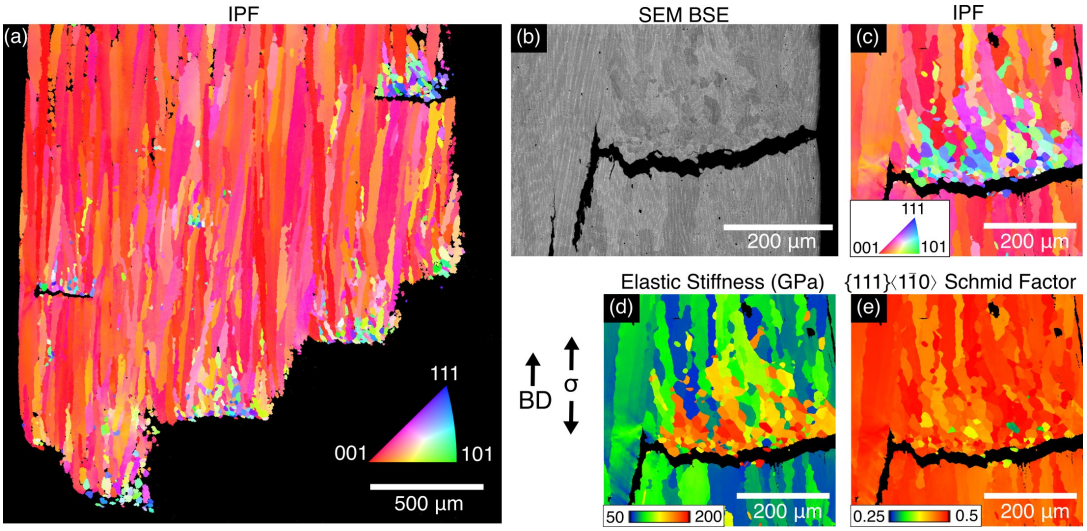

Figure 6.8: (a) IPF map taken across the entire gauge width of the as-printed alloy after tensile testing at 850 °C. (b) BSE micrograph and (c-e) EBSD dataset collected around a surface crack observed in the as-printed alloy after tensile testing at 850 °C.

the [001] direction, it is apparent that a portion of the equiaxed grains are oriented unfavorably for slip, i.e. have a low Schmid factor. The combination of an elastic modulus mismatch along with grains not oriented favorably for slip could explain how these regions are susceptible to fracture. Energy dispersive spectroscopy mapping of similar surface-connected cracks (not shown) revealed the formation of Co-rich oxides within these cracks that likely embrittle the grain boundaries and promote intergranular failure. Oxygen was also observed to be enriched along the grain boundaries ahead of the crack tips. Interrupted testing at elevated temperatures in air or testing under high vacuum would clarify the role of these oxides and oxygen enrichment in the fracture process.

In order to investigate the effect of rate-dependent processes such as grain boundary oxidation, the as-printed and HIP+SHT+Aged samples were subjected to high strain-rate tensile tests at 850 °C. The results of these experiments are shown in Fig. 6.9. Increasing the strain-rate from 1×10^{-4} s^{-1} to 1×10^{-2} s^{-1} roughly tripled the tensile ductility at 850 °C in both sets of samples. Observations of the fracture surfaces revealed a transition to "mixed-mode" failures for both the as-printed and HIP+SHT+Aged alloy,

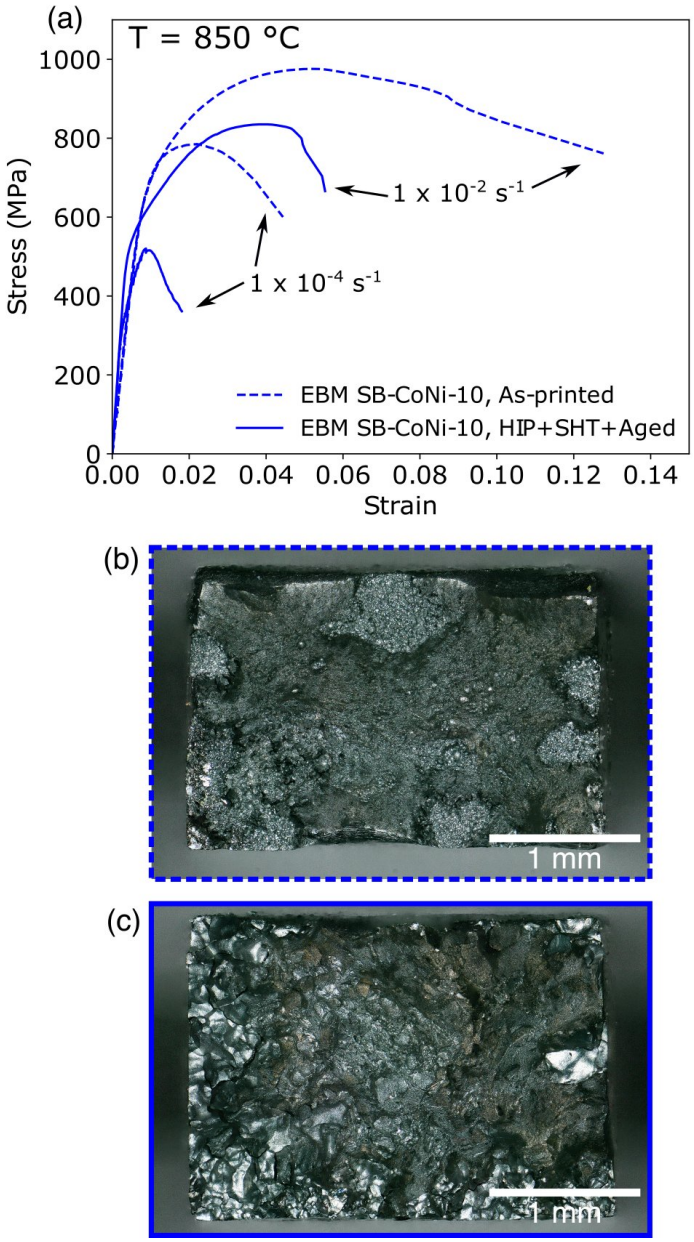

Figure 6.9: (a) Engineering stress-strain curves acquired at quasi-static strain rates and elevated strain rates on EBM SB-CoNi-10 with T = 850 °C. Optical micrographs of the fracture surfaces for tests at elevated strain-rates for (b) as-printed and (c) HIP+SHT+Aged EBM SB-CoNi-10 reveal that a "mixed-mode" failure occurs in both specimens with intergranular fracture at the surface and ductile fracture at the center of the test specimens.

with intergranular fracture limited only to surface-connected grains. These high strain-rate tensile tests provide strong evidence for a time-dependent process such as grain boundary oxidation contributing strongly to the observed reduction in ductility in these alloys at temperatures above 850 °C.

6.4 Discussion

The fabrication of crack-free high γ' volume fraction superalloys through additive manufacturing is difficult to achieve due to a variety of cracking mechanisms that are active. These include, but are not limited to, strain-age cracking, liquation cracking, ductility dip cracking, and solidification cracking [99]. There are several factors that make γ'-containing CoNi-based superalloys suitable for development as alloys for additive manufacturing due to their potentially reduced cracking susceptibility in the late stages of solidification and in the fully-solid state.

Due to the wider processing range between the solidus and the γ'-solvus temperature exhibited by Co- and CoNi-based superalloys, these alloys are likely less prone to cracking in the solid state. This "strain-age" cracking mechanism is promoted by the precipitation of the γ' phase during cooling below the solidus, resulting from the strengthening due to the generation of a dislocation substructure before the γ'-solvus is encountered. This cracking is commonly observed in high γ' volume fraction Ni-based superalloy welds during post-weld heat treatment [258]. In Co-based superalloys, the precipitation of γ' is delayed to lower temperatures compared to Ni-base alloys such as CM 247®. In the case of SB-CoNi-10, this processing range is relatively wide with $T_{solidus} - T_{\gamma'\text{-solvus}} = 1328$ °C-1204 °C $= 124$ °C. This processing range is smaller in high γ' volume fraction Ni-based superalloys, often on the order of 50 °C due to the elevated γ'-solvus in these alloys [259]. Several studies have developed alloying strategies that seek to elevate the

γ'-solvus of Co-based superalloys in order to improve high temperature strength and creep resistance [33, 153]. However, it is possible to control the γ'-solvus within a desired range for additive manufacturing in order to provide a wider processing window, resulting in a combination of processability and high temperature strength.

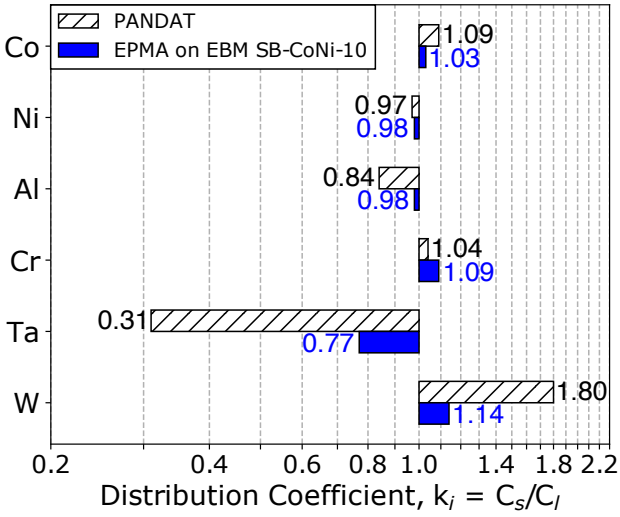

Figure 6.10: The distribution coefficients, k_i, of each major element determined from the curve fits shown in Fig. 6.4.

The favorable solute segregation during solidification also likely reduces the susceptibility for cracking by reducing the length of solute-enriched liquid films between columnar dendrites [112]. A qualitative index for cracking susceptibility has been described for other high γ' volume fraction alloys by the critical temperature range (CTR) between $f_s = 0.70$ and $f_s = 0.98$ [231, 260]. The exact values for the start and end of this critical temperature range are somewhat arbitrary, but they are related to the end stages of solidification where liquid feeding to the solidifying dendrites becomes increasingly difficult and stresses induced from solidification shrinkage and cooling result in tensile stresses that promote cracking. The critical temperature range of SB-CoNi-10 predicted by PANDAT is $\Delta T_{CTR} = 105$ °C. This value indicates a reduced susceptibility to cracking during solidification, since similar Scheil simulations on Ni-based CM 247® result

in ΔT_{CTR} = 125 °C [231]. If we next consider that the simulated solute partitioning in SB-CoNi-10 is much stronger than the experimentally determined values, we can infer that this critical temperature range is likely further reduced. For example, by taking the predicted β-phase precipitation temperature (1222 °C) as a lower bound for f_s = 0.98, then a curve of a similar shape can be drawn between the liquidus and this value producing an estimate of the critical temperature range for SB-CoNi-10 that is reduced to ΔT_{CTR} = 1306 °C − 1222 °C = 84 °C. The combined computational and experimental findings presented above indicate that the freezing range and therefore critical temperature range is likely reduced in this CoNi-based alloy compared to Ni-based superalloys, providing additional resistance to commonly observed cracking mechanisms during additive manufacturing.

The mechanical testing results demonstrate that these alloys exhibit excellent ductility along the build direction greater than 30 % at room temperature along with high ultimate tensile strengths above 1.1 GPa. The crack-free microstructures paired with the precipitation and coarsening of the γ' phase during printing enabled tensile testing of as-printed specimens showing high strengths compared to the large-grained, recrystallized version of the alloy. High temperature tensile tests revealed that the microstructure has a strong effect on elevated temperature mechanical properties, with the columnar as-printed microstructure out-performing the equiaxed grain microstructure in yield strength, UTS, and ductility. In particular, the presence of transverse grain boundaries perpendicular to the loading direction have a substantial effect at slow strain-rates, resulting in a ductility drop from 35.7 % at room temperature to 1.4 % at 950 °C for the HIP+SHT+Aged alloy. The high strain-rate tensile testing suggests that grain boundary oxidation is largely responsible for this ductility drop, since intergranular fracture is significantly reduced at elevated strain-rates. Therefore, it is likely desirable to retain the columnar grained microstructure after HIP and heat treatment for improved high temperature mechanical

properties along the build direction. Alloy designs with modifications of the minor elements are currently being investigated. Further research on EBM processing parameters such as beam power, scan speed, hatch spacing, and pre-heat temperature and their influence on as-printed microstructure are needed in this novel class of CoNi-base alloys. The mechanisms by which the equiaxed grains periodically form within the columnar microstructure are of specific interest, as they clearly affect crack nucleation and the tensile properties of the microstructure. Performing a design-of-experiments with multiple print parameters and evaluating the resultant microstructures could provide insight into the formation of these equiaxed grains during printing.

6.5 Conclusions

The conclusions of this study are as follows:

- The CoNi-based superalloy named SB-CoNi-10 with low density (8.65 g cm^{-3}) is amenable to fabrication by EBM, resulting in crack-free as-printed microstructures in spite of the ability to form a high volume fraction of the γ' phase after heat treatment
- Tensile testing at room temperature revealed exceptional ductility greater than 30 % along with ultimate tensile strengths above 1.1 GPa
- The combination of favorable solidification path and γ'-solvus temperature of 1204 °C, which is 124 °C below the solidus temperature, promotes favorable printing characteristics in the EBM process
- Post-processing consisting of a super-solvus HIP, SHT, and aging removes microstructural inhomogeneities and promotes recrystallization of the as-printed columnar microstructure

- The high temperature strength and ductility are strongly dependent on the alloy microstructure, with the as-printed alloy exhibiting more favorable mechanical properties compared to the HIP+SHT+Aged alloy

Chapter 7

Structure evolution and mechanical properties of a CoNi-base alloy processed by SLM[†]

In this chapter, the high γ' volume fraction CoNi-base superalloy SB-CoNi-10 along with a high C containing variant called SB-CoNi-10C were successfully processed through selective laser melting. Heat treatment optimization studies for the SLM version of this alloy are performed and tensile tests at elevated temperatures are performed and compared to previous results from Ch. 5. In the as-printed state, the alloys have a fine cellular structure with segregation of Ta and significant built-in misorientation within the columnar grain structure. Super-solvus homogenization promotes complete recrystallization of the microstructure which degrades elevated temperature tensile ductility. The elevated temperature tensile ductility can be improved in SB-CoNi-10C compared to SB-CoNi-10

[†]Significant portions of this chapter are reproduced from the following article: S.P. Murray, E.B. Raeker, K.M. Pusch, C. Frey, C.J. Torbet, N. Zhou, S.A.J. Forsik, A.D. Dicus, G.A. Colombo, M.M. Kirka, and T.M. Pollock, Microstructure evolution and tensile properties of a selectively laser melted CoNi-base superalloy. In preparation.

by increasing the C content and modifying the heat treatment procedure. An aging study at 950 °C for various times identified the peak hardness and a sub-solvus heat treatment schedule involving hot isostatic pressing, solution heat treatment, and aging produces a bimodal γ' distribution while retaining the texture of the as-printed alloy. Room temperature and intermediate temperature (760 °C) tensile testing measured parallel and perpendicular to the build direction revealed that the new heat treatments resulted in improved yield strengths, ultimate tensile strengths, and ductilities compared to previous iterations of the alloy. Similar heat treatment strategies could be applied to other additively manufactured superalloys in order to optimize their mechanical properties at elevated temperatures.

7.1 Introduction

Selective laser melting (SLM) is a powder-bed fusion based technique where a laser heat source locally melts and joins metallic powder in a layer-by-layer fashion [94, 261, 262, 263]. SLM has been successfully applied to a variety of structural alloys, such as 316L stainless steel [264, 265, 266], Ti6Al4V [267, 268, 269], AlSi10Mg [270, 271, 272, 273], Inconel® 625* [274, 275, 276], and Inconel® 718 [277, 278, 279, 280]. Many of these alloys have been previously studied and developed for their good weldability, which makes them excellent candidates for SLM, since this fusion-based technique can be considered as a repetitive micro-welding process.

For high temperature applications, there is a strong desire to apply SLM to high γ' volume fraction Ni-base superalloys due to their microstructural stability at high temperatures, excellent creep strength, and intrinsic oxidation resistance [1, 98, 281]. High γ' volume fraction Ni-base superalloys are often described as 'un-weldable' due to their

*Inconel® is a registered trademark of Huntington Alloys Corporation

susceptibility to a variety of cracking mechanisms that are active during the solidification process and when the alloys are cooling after solidification [95, 227, 228, 282, 283]. A significant amount of microcracking can severely debit the mechanical properties [101]. These microcracks can be difficult to alleviate through hot isostatic pressing (HIP) if they are connected with the sample surface or if the cracks were formed in the liquid-state during solidification [174]. A particular challenge for Ni-base superalloys is the intermediate temperature ductility minimum that occurs at temperatures between 600 and 800 °C [284, 285, 286, 287, 288, 289]. This ductility minimum is thought to be caused by a combination of enhanced grain boundary oxidation at elevated temperatures [284], increased alloy strength near the yield strength anomaly [175], and slip-assisted grain boundary sliding which results in the accumulation of dislocations near grain boundaries [285]. These factors combine to raise the local stresses in the vicinity of oxygen-influenced grain boundaries, promoting intergranular crack propagation. It is hypothesized that as the temperature increases above 800 °C, increased grain boundary mobility delays the accumulation of local stresses and ductility is often restored [285]. The intermediate temperature ductility minimum is more severe in AM versions of Ni-base alloys due to the presence of pre-existing microcracks on high angle grain boundaries (HAGBs) along the build direction of many SLM-fabricated high γ' volume fraction alloys [282]. This results in particularly poor ductility at intermediate temperatures for AM versions of these alloys when tested in the XY-orientation, i.e. perpendicular to the build direction, whereas tensile testing along the Z-orientation, i.e. parallel to the build direction, often results in higher ductility [290].

In order to leverage AM for components in high temperature operating environments, novel alloying strategies and processing methods are currently being investigated [233]. High γ'-volume fraction CoNi-base superalloys that contain roughly equal amounts of Co and Ni have recently been demonstrated to be successfully printed with both SLM and

electron beam melting (EBM) [197, 198]. Near fully-dense CoNi-base alloys with limited porosity have been produced, resulting in excellent tensile ductility at room temperature [197]. CoNi-base alloys have more favorable solidification characteristics with less severe partitioning of alloying additions compared to their Ni-base counterparts [34, 52, 218], similar to what has been observed in Co-base alloys with no Ni content [51], which is expected to promote both improved castability during single crystal Bridgman growth and more amenability to the thermal conditions present in additive manufacturing. Additionally, these alloys often exhibit lower γ'-solvus temperatures by 50 - 100 °C which is thought to alleviate thermal stresses in the recently solidified material and reduce the severity of strain-age cracking [197].

After identification of the range of process parameters for SLM (laser speed, laser power, hatch spacing, scan rotation, pre-heat temperature) that produces near fully-dense alloys with limited porosity, appropriate heat treatments must be developed to promote the formation of the γ' phase and control the grain structure of the printed alloy. Several studies have been published on the effect of HIP, solution heat treatment (SHT), and aging on similar high γ' volume fraction Ni-base superalloys produced by AM, including CMSX-4®[†] [104], CM 247 LC® [290], and Inconel® 738 LC [243]. Preferable heat treatments for SLM versions of legacy alloys may not necessarily be identical to those used on cast versions since AM alloys have additional complications of residual stresses, as-built microstructures with largely suppressed γ' content, and the need for HIP in order to ensure that microcracks are eliminated as much as possible. Due to the fine scale of the as-printed segregation produced by the large thermal gradients and high interfacial velocities in AM, the time needed for solutioning heat treatments can be reduced, resulting in potential cost savings in processing these alloys [250].

The prior study in Ch. 5 on SLM SB-CoNi-10 applied a super-solvus (1245 °C) HIP to

[†]CMSX-4® & CM 247 LC® are registered trademarks of Cannon-Muskegon Corporation

ensure closure of any possible microcracks and porosity reduction, followed by a shorter 2 h SHT at 1245 °C and 50 h age at 1000 °C to precipitate and coarsen a unimodal distribution of sub-micron cuboidal γ' precipitates [197]. This heat treatment procedure resulted in a fully recrystallized and equiaxed grain structure. This had the benefit of reduced mechanical anisotropy at room temperature such that the yield strength, ultimate tensile strength, and ductility were similar whether the loading direction during tensile testing was parallel to the build direction (BD) or perpendicular to the BD. However, these alloys exhibited limited ductility at elevated temperatures, in particular at an intermediate temperature of 760 °C where the engineering strain at failure was less than 1%. Elevated temperature tensile testing on EBM processed SB-CoNi-10 found that high temperature ductility was superior in the as-printed condition compared to the super-solvus HIP+SHT+aged condition [198], suggesting that complete recrystallization of the previously textured fine-grained microstructure may not be desirable in the case of SLM processed SB-CoNi-10. However, due to the elevated pre-heat temperatures possible in EBM, which are on the order of the aging temperature of 1000 °C, the as-printed EBM alloy contained a significant volume fraction of γ' phase with varying degrees of coarsening dependent on the build height. This is not the case in SLM processed alloys, with the γ' phase being largely suppressed due to the high cooling rates present in SLM and limited pre-heat temperatures of 200 °C.

In the present investigation, microstructure evolution from the as-printed state through a series of HIP and heat treatment schedules is studied in a CoNi-base superalloy designated as SB-CoNi-10. The microstructure in the as-printed condition is investigated via scanning electron microscopy (SEM) and transmission electron microscopy (TEM). The alloy grain structure and γ' distribution at various steps of the heat treatment process and after various times of aging are observed and described. An alloy variant with increased carbon content designated as SB-CoNi-10C was processed according to the

findings of these experiments and was tensile tested at room temperature and elevated temperatures. By applying sub-solvus HIP and SHT as opposed to super-solvus heat treatments, optimizing the γ' distribution with aging, making additions of carbon to the base alloy composition, improvements in the room temperature yield strength and ultimate tensile strength of SB-CoNi-10C along with a negligible decrease in ductility were demonstrated. An additional lower temperature aging heat treatment (i.e. double-age heat treatment) further increased the yield strength and ultimate tensile strength. Additionally, an improvement in tensile ductility at intermediate temperatures after these modifications has been demonstrated.

7.2 Methods

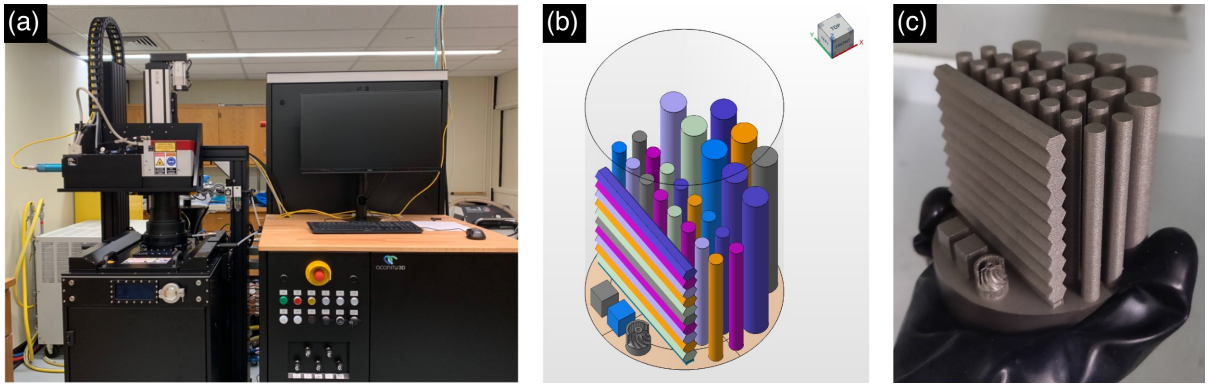

Figure 7.1: (a) The Aconity3D AconityMINI laser powder-bed fusion system at UC-Santa Barbara, (b) build set up of bars for mechanical testing of SB-CoNi-10C, and (c) finished print of SB-CoNi-10C on the build plate after extraction from the build chamber.

SB-CoNi-10 and SB-CoNi-10C powder was fabricated by Carpenter Technology Corporation in a 300 lb. vacuum induction melting inert gas atomizer (VIGA). The compositions of the powders are displayed in Table 7.1. The major alloying additions were measured by x-ray fluorescence. C and O were measured by LECO combustion analysis, tramp elements such as B were measured by mass spectrometry, and Y was measured

via a wet chemical anaysis. The SB-CoNi-10C alloy has a higher nominal C content compared to SB-CoNi-10, at 0.35 at.% compared to 0.08 at.%. A standard powder size range of -53/+15 µm was selected for SLM printing studies. Density blocks and bars for tensile testing of SB-CoNi-10 were fabricated by Carpenter Technology Corporation on a SLM Solutions SLM 125®[‡]. Printing was performed with an applied preheat of 200 °C in an inert gas atmosphere. A variety of density blocks were printed with varying scan speeds, laser powers, and hatch spacings. All SB-CoNi-10 samples were printed with a 30 µm layer thickness and a bidirectional raster strategy with 66.6° scan rotations between layers. Additional microstructure investigations were performed on two sets of samples which were both produced with an 80 µm hatch spacing but varying laser parameters. One set was produced with lower laser power and lower scan speed (134 W, 744 mm s^{-1}) and the other with higher laser power and higher scan speed (176 W, 1137 mm s^{-1}). SB-CoNi-10C specimens were printed at UC-Santa Barbara with an Aconity3D AconityMINI laser powder-bed fusion system. A photograph of the AconityMINI is displayed in Fig. 7.1a, along with the build set up for the bars in Netfabb (Fig. 7.1b) and the build plate containing the finished bars, density cubes, and an example printing artifact (Fig. 7.1c). Samples for mechanical testing were printed using the higher power and higher laser speed settings described previously except with a 16° scan rotation between build layers. The raster strategy, pre-heat temperature, and hatch spacing were not modified with respect to the previous builds.

Super-solvus (1245 °C) and sub-solvus (1177 °C) HIP treatments for 4 h at 103 MPa were applied. Additional heat treatments were performed in air and were followed by either oil quench (OQ), furnace cooling (FC) or air cooling (AC). The full heat treatment schedules are described in Table 7.2. HT1 represents the heat treatment from a prior study on SLM SB-CoNi-10 [197] and HT2 and HT3 were applied to the SB-CoNi-10C

[‡]SLM 125® is a registered trademark of SLM Solutions Group AG Stock Corporation

Table 7.1: Experimentally measured (and nominal) powder compositions of SB-CoNi-10 and SB-CoNi-10C in at.% after fabrication by VIGA

Alloy	**Co**	**Ni**	**Al**	**Cr**	**Ta**	**W**	**C**	**B**	**Other**
SB-CoNi-10[198]	Bal.	37.09	12.10	5.99	3.49	0.98	0.15	0.06	0.013Hf, 0.02O
	(Bal.)	(36.40)	(13.20)	(6.00)	(3.50)	(1.00)	(0.08)	(0.08)	(0.018Hf, 0.002Y)
SB-CoNi-10C	Bal.	36.20	13.11	5.96	3.40	0.98	0.34	0.07	0.02Hf, 0.004Y, 0.06O
	(Bal.)	(36.27)	(13.20)	(6.00)	(3.50)	(1.00)	(0.35)	(0.08)	(0.018Hf, 0.002Y)

tensile specimens for tensile testing. For the aging study at 950 °C shown in Fig. 7.9, samples were previously HIP'd at 1177 °C / 4 h / 103 MPa and solutioned for 1 h at 1177 °C followed by AC. After the desired aging time was reached, samples were water quenched (WQ) before microscopic investigations. Area fraction of γ' measurements were performed at Carpenter Technology through an automated workflow for Fiji that was performed independently by six separate researchers and subsequently averaged [125]. Binarized images of porosity in Fig. 7.2a-c were processed by applying the Yen threshold in Fiji to light optical microscopy images [124]. Binarized images of the carbide content in Fig. 7.11b,d were created by applying the Minimum threshold in Fiji to the BSE micrographs presented in Fig. 7.11a,c. Alumina inclusion area fraction measurements were performed in FIJI on stitched SEM images of alloy cross-sections that were collected on areas >6 mm^2.

Table 7.2: Heat treatment conditions

Label	**HIP**	**Solutioning**	**Aging**
HT1	1245 °C / 4 h / 103 MPa	1245 °C / 1 h OQ	1000 °C / 50 h FC
HT2	1177 °C / 4 h / 103 MPa	1177 °C / 1 h OQ	950 °C / 4 h WQ
HT3	1177 °C / 4 h / 103 MPa	1177 °C / 1 h OQ	Above + 800 °C / 20 h AC

Bars of SB-CoNi-10 and SB-CoNi-10C that were printed in the Z-orientation and XY-orientation were machined for mechanical testing. Room temperature and elevated temperature tensile testing of SB-CoNi-10 and room temperature tensile testing of SB-CoNi-10C was performed at Carpenter following the ASTM E8 standard. Sub-size tensile specimens of SB-CoNi-10C with 4 mm gauge width and 20 mm gauge length were machined for elevated temperature testing which was performed at UC-Santa Barbara on an Instron®[§] 5582 load frame with an induction heater. All tensile tests were taken to rupture. For tensile tests performed at Carpenter Technology, ductility was measured as

[§]Instron® & Vibromet® are registered trademarks of Illinois Tool Works Inc. Corporation

percent elongation of the post-mortem specimens, while engineering strain at failure was used for the SB-CoNi-10C elevated temperature tests performed at UC-Santa Barbara. Post-mortem fracture surface imaging was performed using 3D stitching on a Keyence®[¶] VHX-5000 optical microscope.

Samples were prepared for SEM and electron backscattered diffraction (EBSD) mapping through grinding to 1200 grit SiC paper, colloidal diamond suspension polishing down to 1 µm, followed by a colloidal 50 nm silica suspension using a Vibromet® polisher for 4 h. Backscattered electron (BSE) imaging was performed on both a Thermo Fisher Scientific®[‖] Apreo C and a FEI™ Versa™[**] 3D at accelerating voltages between 10 and 20 kV. EBSD maps were collected on a FEI™ Versa™ 3D at an accelerating voltage of 30 kV and were indexed using either spherical indexing in the EMSphInx v0.2 software package or Hough indexing within OIM Analysis™[††] v8 software [191, 291]. All inverse pole figure (IPF) maps are shown with the ⟨001⟩ aligned along the BD and were collected over 500 × 500 µm^2 areas with a 0.5 µm step size. Kernal average misorientation (KAM) maps were calculated from these data-sets with a 1st nearest neighbor kernal using only the perimeter pixels. All EBSD data-sets were cleaned using 2-3 grain dilation procedures with a 5° grain tolerance angle and a minimum grain size of at least 5 pixels. This typically resulted in 1 to 2% of pixel orientations changed, although especially noisy data-sets (e.g. SR 1000 °C for 2 h + 1215 °C for 10 min in Fig. 7.7) had approximately 20% of the pixels modified. Electron transparent lamella 20 µm in length were extracted from the regions indicated in Fig. 7.3 by focused ion beam (FIB) lift-out on a FEI™ Helios Dualbeam™[‡‡]. Bright-field TEM and scanning transmission electron microscopy energy dispersive spectroscopy (STEM-EDS) were performed on a Thermo

[¶]Keyence® is a registered trademark of Keyence Corporation
[‖]Thermo Fisher Scientific® is a registered trademark of Thermo Fisher Scientific Inc. Corporation
[**]FEI™ & Versa™ are trademarks of Thermo Fisher Scientific Inc. Corporation
[††]OIM Analysis™ is a trademark of AMETEK Inc.
[‡‡]FEI™, Dualbeam™, and Talos™ are trademarks of Thermo Fisher Scientific Inc. Corporation

Fisher Scientific Talos™ G2 at accelerating voltages of 200 kV. The collected x-ray signals were quantified using the Velox software package and the data-sets were normalized to 100%.

7.3 Results

7.3.1 As-printed microstructure

Binarized optical images of the as-printed SB-CoNi-10 and SB-CoNi-10C alloys over a 25 mm^2 area are shown in Fig. 7.2a-c. Cracks were not observed in any of the collected fields of view, although porosity was observed in all specimens with a maximum measured pore diameter of 51 µm in the SB-CoNi-10C (Fig. 7.2c). All of the printed alloys exhibited a measured density of over 99.6 area % as shown in Fig. 7.2b,e. Focused view EBSD maps in Fig. 7.2d-f suggest that each of the alloys exhibits a ⟨001⟩//BD texture which are distinct from each other depending on the scan settings applied. The sample printed with laser power of 134 W and scan speed of 744 mm s^{-1} in Fig. 7.2a,d was chosen for TEM investigations due to the alignment of the columnar grains with the BD. The scan settings of laser power of 176 W and scan speed of 1137 mm s^{-1} that produced the highest density alloy (Fig. 7.2b,e) were chosen for additional study through heat treatment trials.

The as-printed microstructure of SB-CoNi-10 printed with laser power of 134 W and scan speed of 744 mm s^{-1} is shown in Fig. 7.3. An EBSD map of a characteristic region is shown in Fig. 7.3a. BSE microscopy in Fig. 7.3b shows the columnar grains in relation to the melt pool boundaries. The grain-scale microstructure is textured with regions of columnar grains with ⟨001⟩//BD along the center of the melt pools, with larger grains in-between the columnar grains that have their ⟨001⟩ tilted towards the centers of the melt pools. Two FIB lamella were extracted from the indicated regions in Fig. 7.3b, with

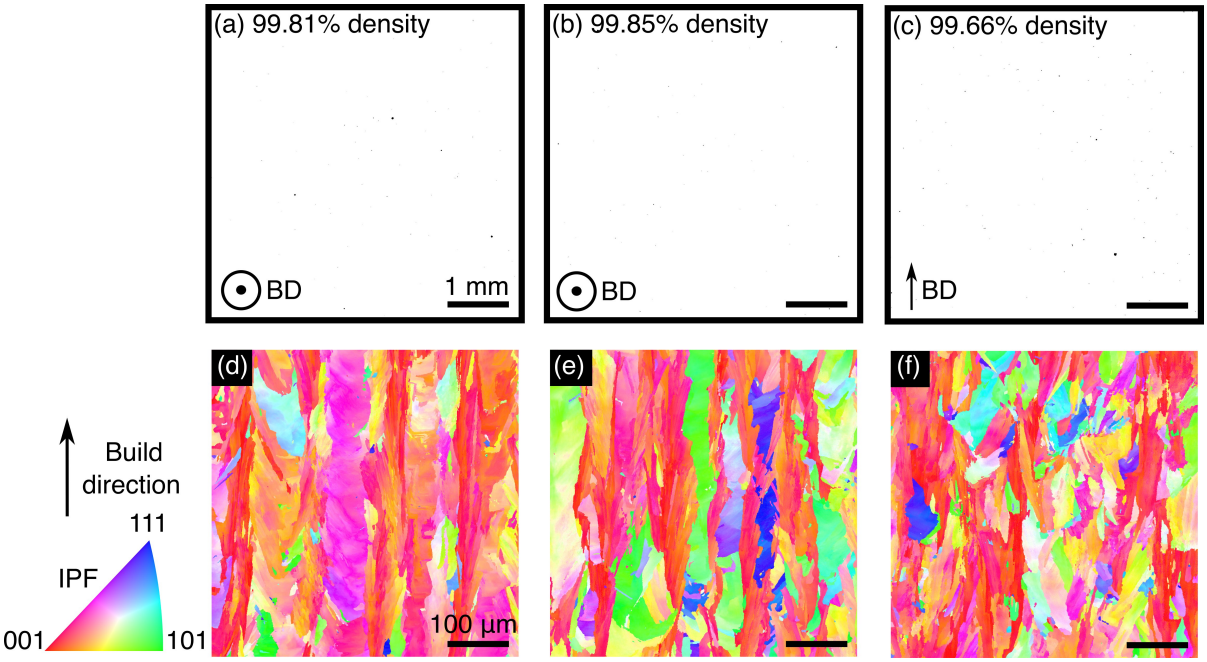

Figure 7.2: (a-c) Binarized optical microscopy images and (d-f) EBSD maps of (a,d) SB-CoNi-10 printed on a SLM125 with laser power of 134 W and scan speed of 744 mm s^{-1}, (b,e) SB-CoNi-10 printed on a SLM125 with laser power of 176 W and scan speed of 1137 mm s^{-1}, and (c,f) SB-CoNi-10C on the AconityMINI printed with laser power of 176 W and scan speed of 1137 mm s^{-1} with a 16° scan rotation between layers.

one lamella having the growth direction of the solidification cells oriented perpendicular to the foil and the other with the solidification cells oriented close to the plane of the foil. BF TEM images of these two foils are shown in Fig. 7.3c,d.

High angle annular dark field (HAADF) imaging in Fig. 7.4 shows the regions in each foil where STEM-EDS mapping was performed. A significant dislocation density in the as-printed microstructure exists, with a greater dislocation density near the cell boundaries compared to the cell centers. Similar to previous investigations of chemical segregations in Bridgman cast and EBM SB-CoNi-10 [34, 197], enrichment of Al and Ta and depletion of Co and Ni was observed in the intercellular region. Based on the maps shown in Fig. 7.4, the segregation of Cr and W are not detectable and the segregation of Ni is less pronounced compared to EBM and single crystal crystal variants of this

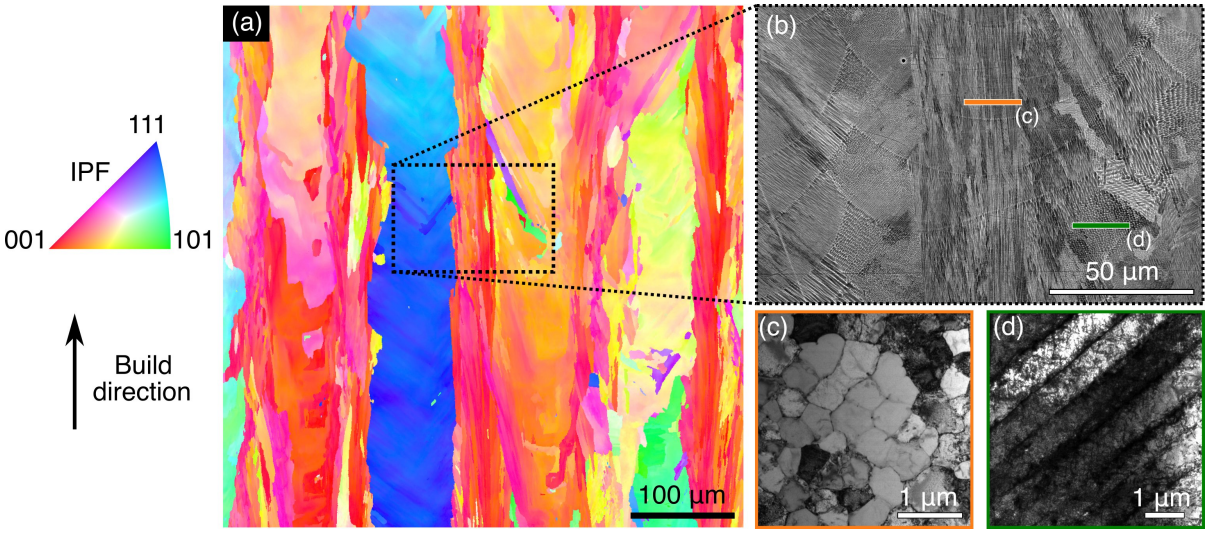

Figure 7.3: As-printed microstructure of SB-CoNi-10 printed on a SLM125 with laser power of 134 W and scan speed of 744 mm s^{-1}. (a) IPF map, (b) BSE image showing location of lamella lift-outs, (c) BF TEM looking down the solidification cells, (d) BF TEM looking along the solidification cells

alloy [34, 198]. Particles rich in Ta and C shown in Fig. 7.4f,h are carbides of the MC stoichiometry, and appear bright in the HAADF images in Fig. 7.4a,j. The particles that are enriched in Al and O in Fig. 7.4 are Al_2O_3 oxide particles that likely formed during the printing process. Due to their relatively low Z-number, these particles appear dark in the HAADF image in Fig. 7.4a. The boxed region in Fig. 7.4a indicates where x-ray signal was integrated for a STEM-EDS line scan across a single cell boundary. This cell boundary was selected for analysis since there were no carbide or oxide particles in the vicinity that may have affected the local chemical composition. This data is plotted in at.% in Fig. 7.5. The enrichment of Ta and Al is clearly shown in addition to the depletion of Co. Measurable changes in the other elements are not obvious at this specific cell boundary, although depletion of Ni was seen in several other boundaries.

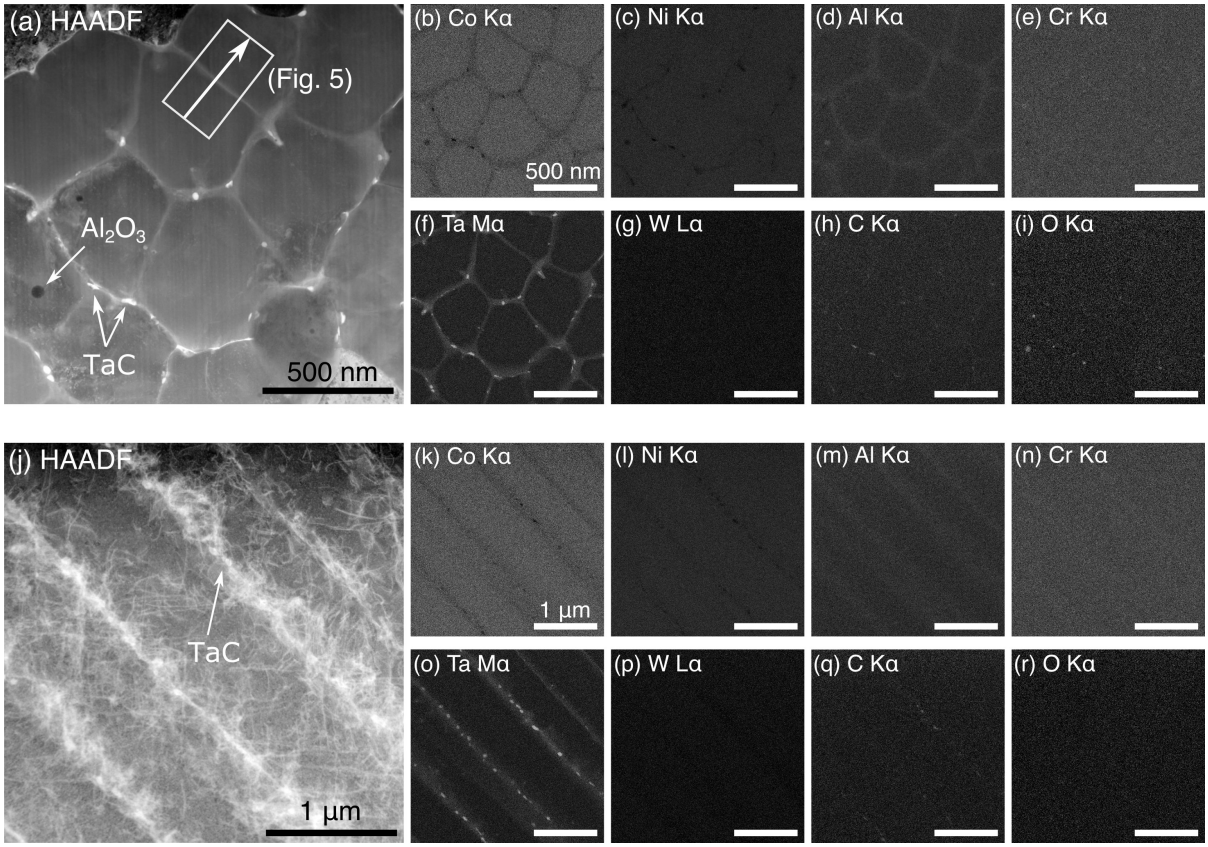

Figure 7.4: STEM-EDS measurements of as-printed SB-CoNi-10 from the foils extracted from Fig. 7.3b

.

7.3.2 Solution heat treatment: Recovery and recrystallization

A solution heat treatment near the γ'-solvus is required to homogenize the chemical segregation introduced during solidification and to control the final size and distribution of the γ' precipitates. Therefore, a series of heat treatment trials were performed on SLM SB-CoNi-10 in order to assess how the grain structure and precipitate structure can be controlled in order to produce alloys with balanced mechanical properties. These heat treatment studies were performed on the SB-CoNi-10 alloys produced on a SLM125 with laser power of 176 W and scan speed of 1137 mm s^{-1}.

The effect of a sub-solvus HIP of 1177 °C for 4 h at 103 MPa followed by a short 1 h super-solvus SHT at 1245 °C is shown in Fig. 7.6. As the HIP temperature does not

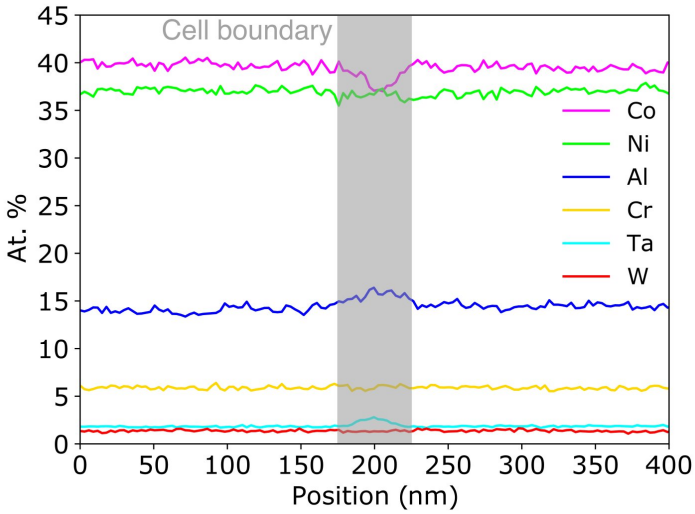

Figure 7.5: STEM-EDS chemical measurement of the major elements in SB-CoNi-10 across the solidification cell boundary outlined in Fig. 7.4a.

exceed the γ'-solvus temperature (approximately 1200 °C [34]), recrystallization of the grain structure after HIP does not occur and the columnar morphology is maintained. KAM maps shown in Fig. 7.6d and Fig. 7.6e show that the sub-solvus HIP reduced the amount of local misorientation but has not completely removed local misorientations throughout the grain structure. A subsequent super-solvus heat treatment shown in Fig. 7.6c,f shows that complete recrystallization can occur despite the reduction of local misorientation, resulting in an equiaxed grain structure with coarser grains and minimal misorientations within the grains.

7.3.3 Stress relief, short time solutioning, and aging

It was hypothesized that recrystallization can be suppressed with appropriate stress relief heat treatments combined with shorter time excursions above the γ'-solvus temperature. This could allow for the retention of the textured grain structure produced by SLM combined with the improved high temperature mechanical performance of a unimodal γ' precipitate distribution. In order to investigate this hypothesis, a series of

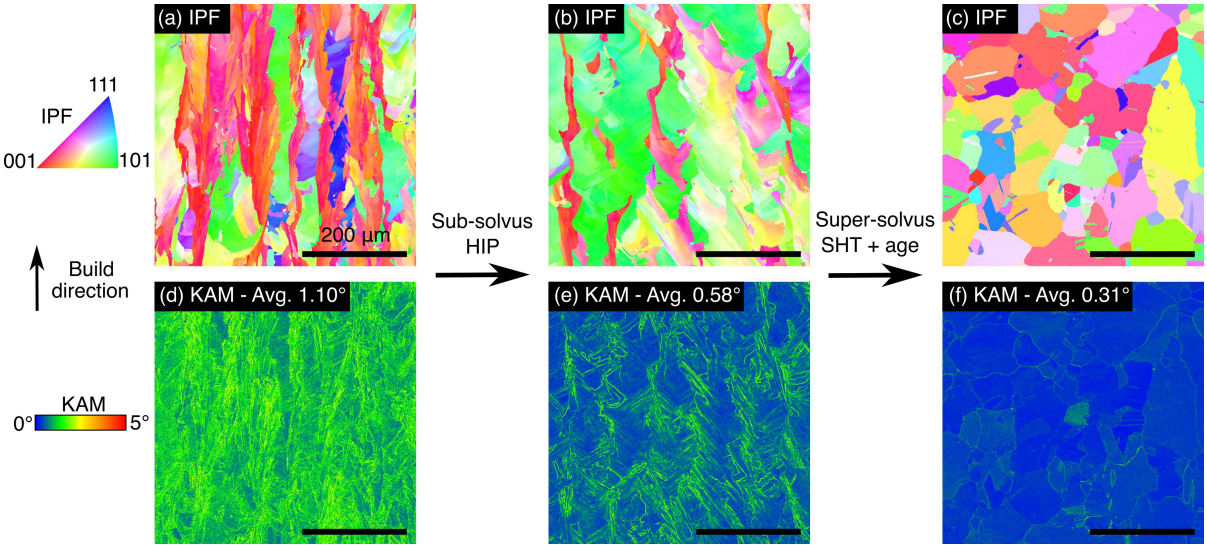

Figure 7.6: Microstructure evolution of SB-CoNi-10. (a-c) IPF maps and (d-f) KAM maps of SB-CoNi-10 in the (a,d) as-printed condition, (b,e) sub-solvus HIP at 1177 °C for 4 h at 103 MPa, and (c,f) subsequent super-solvus solutioning at 1245 °C 1 h and aging at 1000 °C for 50 h.

heat treatments were applied on as-printed SLM SB-CoNi-10 with increasing temperature stress-relieving heat treatments of 1000, 1050, and 1100 °C for 2 h followed by SHT for 10 minutes at temperatures just below the γ'-solvus (1190 °C) and just above the γ'-solvus (1215 °C). The impact of this matrix of heat treatment conditions on the grain scale microstructure is shown in Fig. 7.7, and the associated γ' morphology after heat treatment is shown in Fig. 7.8.

The heat treatments performed below the γ' solvus temperature did not result in recrystallization of the microstructure. All heat treatments that had a segment that exceeded the γ' solvus resulted in complete recrystallization after 10 minutes, even with a stress-relieving heat treatment performed before the solutioning. The γ' precipitate structure varied between the three different stress relief heat treatment conditions, shown in the "No solutioning" row of Fig. 7.8. The chemical segregation in the intercellular regions promotes the formation of interconnected γ' networks upon stress-relieving. As the temperature of the stress relief treatment increased, these networks coarsened to

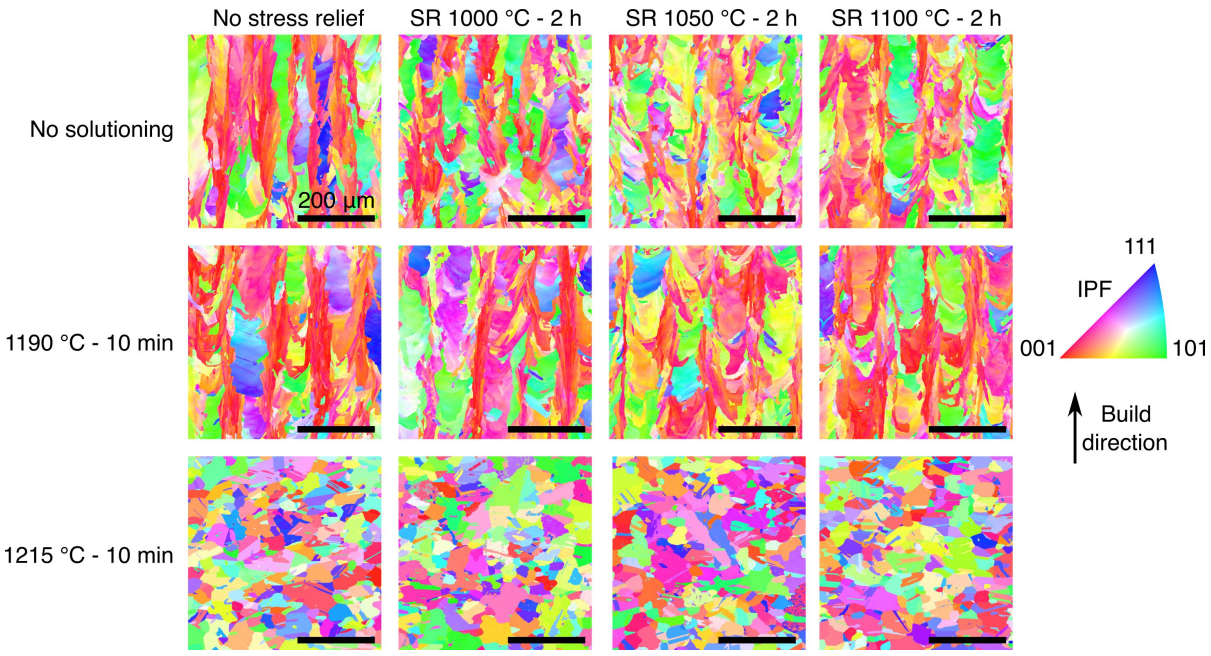

Figure 7.7: IPF maps of SB-CoNi-10 subjected to an array of heat treatment conditions including stress-relieving at 1000, 1050, and 1100 °C for 2 h and solutioning for 10 min at 1190 °C and 1215 °C followed by water quenching.

wavelengths larger than the original cellular spacing. Additionally, carbide precipitation occured on the grain boundaries after all stress-relieving conditions. A sub-solvus SHT at 1190 ° C results in solutioning of a significant amount of γ' such that these γ' networks are no longer continuous, however the remaining γ' content during sub-solvus solutioning coarsens significantly leading to a population of large, elongated γ' precipitates. The short super-solvus SHT at 1215 °C results in a more complete solutioning and a unimodal distribution of fine γ' upon water quenching, as shown by the bottom row labeled as "1215 °C / 10 min" in Fig. 7.8. These heat treatment trials indicate that if the textured, as-printed grain structure is to be retained throughout the heat treatment process, the temperature can not exceed the γ' solvus, even for short times.

After performing a 1177 °C for 1 h SHT on as-printed SLM SB-CoNi-10, an aging study was performed at 950 °C for various times to investigate the ability to develop a bimodal precipitate structure by precipitating and coarsening γ' in-between the primary

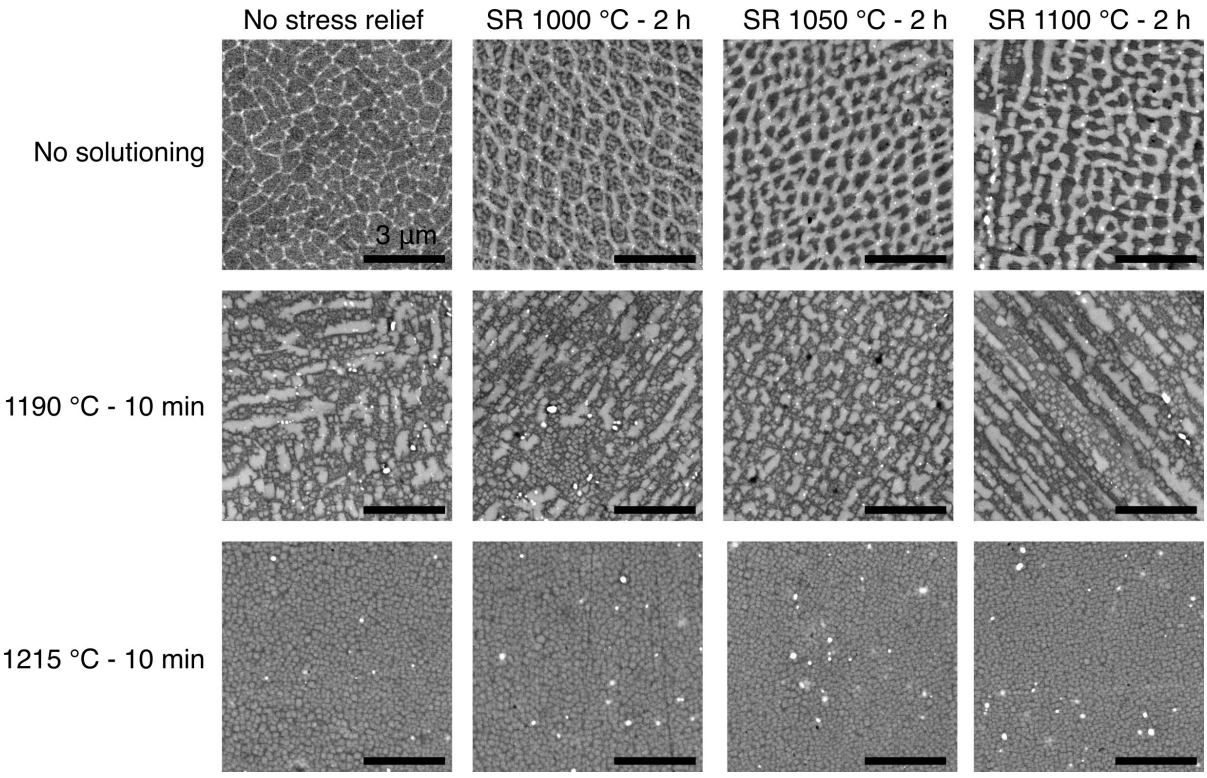

Figure 7.8: BSE micrographs of SB-CoNi-10 subjected to an array of heat treatment conditions showing the γ' distributions at each heat treatment condition followed by water quenching. The images correspond to each of the EBSD maps in Fig. 7.7.

γ' formed during sub-solvus heat treatments. Vickers hardness tests revealed that a peak hardness occurs at some time between 0 and 4 h of aging, with the highest recorded hardness measured at 2 h of aging. Imaging of the samples used for the aging study revealed that in the sub-solvus solutioned state there is a population of larger primary γ' with finer secondary γ' formed upon air cooling. The aging heat treatments clearly affect the size and volume fraction of the secondary γ', which continues to coarsen with aging at 950 °C until it reaches a similar size to the pre-existing primary γ', as shown in Fig. 7.9f. The drop in hardness that occurs at 24 h of aging and beyond appears to be correlated with the coalescence of the two populations of γ' precipitates. From these studies, an aging heat treatment of 950 °C for 4 h was selected based on the combination of high hardness at this condition and the size of the secondary γ' precipitates present in

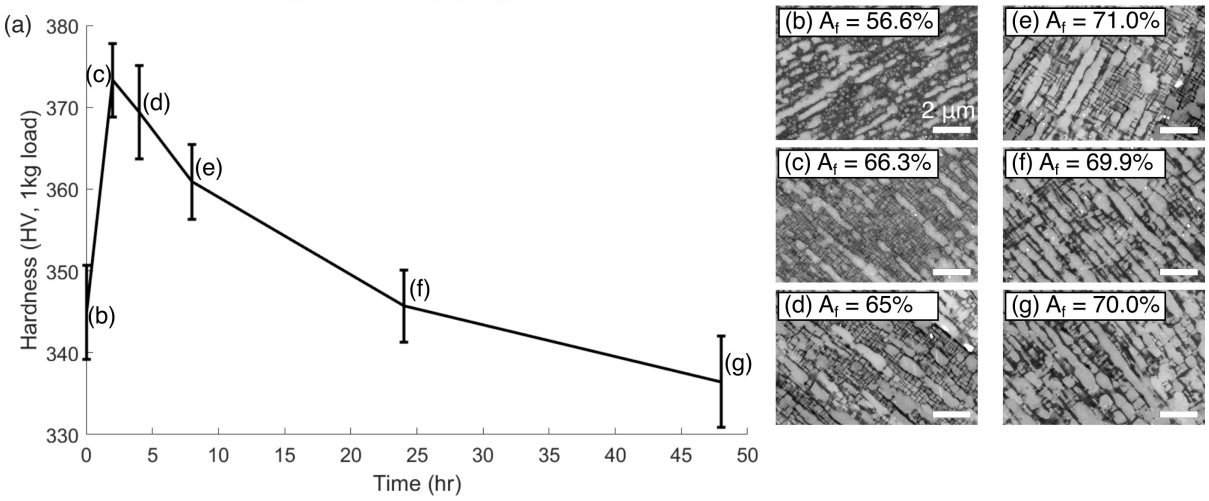

Figure 7.9: (a) Vickers hardness of SB-CoNi-10 after aging at 950 °C for varying times. All samples were sub-solvus HIP'd and solutioned for 1 hr at 1177 °C before aging. Each measurement consists of 12 indentations with a 1 kg load and the error bars represent 95% confidence intervals. (b-g) BSE micrographs of the γ' distributions after different times at 950 °C: (b) 0 h, (c) 2 h, (d) 4 h, (e) 8 h, (f) 24 h, (g) 48 h.

the microstructure. An additional aging heat treatment at 800 °C for 20 h was applied to several samples for mechanical testing to investigate the effect of increasing the γ' volume fraction on alloy strength. This resulted in the two heat treatment conditions considered for further mechanical testing, which are displayed in Table 7.2 as HT2 and HT3. In comparison to the original HT1 applied to previous versions of SB-CoNi-10, these new heat treatments remain sub-solvus throughout the HIP and SHT processes and apply a lower temperature age to increase the γ' volume fraction and increase alloy hardness.

The microstructural evolution of SB-CoNi-10C after HT2 is shown in Fig. 7.10. The texture of the as-printed grain structure is largely preserved after HT2, with occasional instances of recrystallized grains and recovered grains similar to the sub-solvus HIP-only microstructure shown in Fig. 7.6b,e. The average KAM value reduces from 1.19° in the as-printed condition to 0.70° in the fully sub-solvus HIP+SHT+aged condition, indicating that the elevated temperature of the sub-solvus HIP is sufficient in place of a dedicated stress relieving heat treatment to relieve some thermal stresses. The γ'

precipitate structure is expected to be similar to what was demonstrated in SLM SB-CoNi-10 for aging at 950 °C for 4 h shown in Fig. 7.9d. The effect of increased carbon content on carbide formation in SB-CoNi-10C is shown in Fig. 7.11 compared to SB-CoNi-10. A stress-relieving heat treatment of 1100 °C for 2 h followed by AC was applied to both as-printed alloys. After this heat treatment, the SB-CoNi-10C alloy possessed a carbide content of 0.79 area % compared to 0.26 area % for SB-CoNi-10.

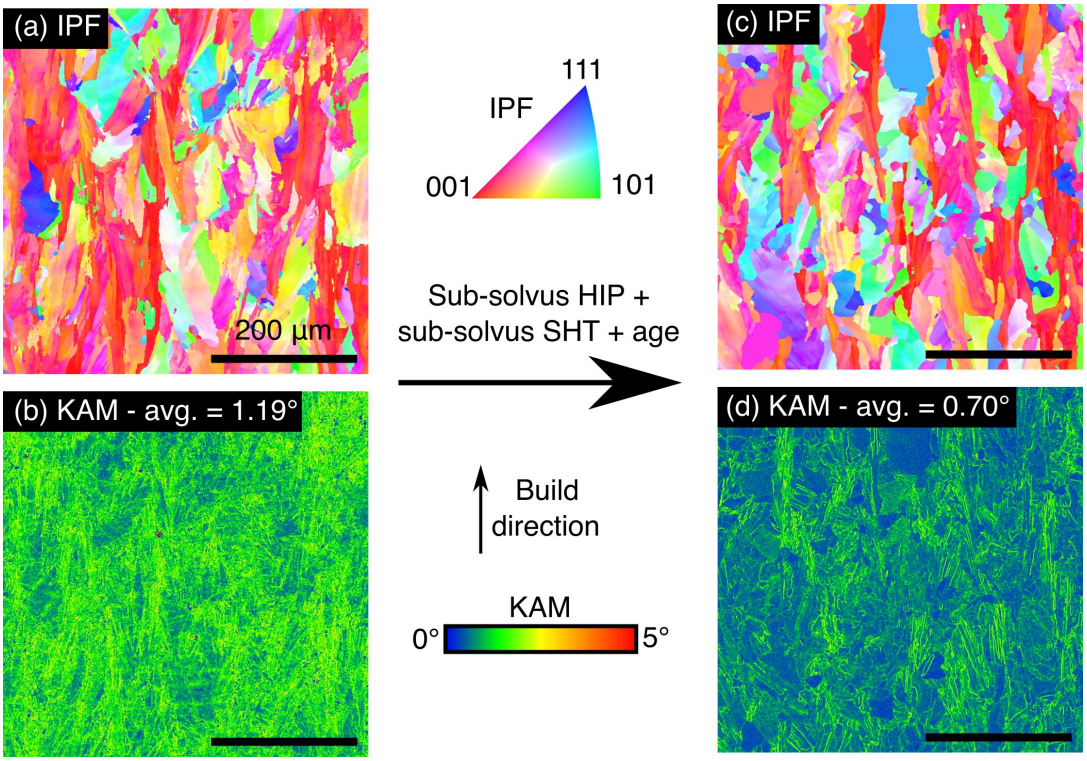

Figure 7.10: Microstructure evolution of SB-CoNi-10C. (a,c) IPF maps and (b,d) KAM maps of SB-CoNi-10C in the (a-b) as-printed condition and (c-d) after heat treatment using the HT2 condition.

7.3.4 SB-CoNi-10C tensile testing

The tensile testing results at room temperature (RT) and elevated temperature for SB-CoNi-10C are compared to the previously reported version of SLM SB-CoNi-10 in Table 7.3. The 0.2% offset yield strength, ultimate tensile strength, and ductility are also

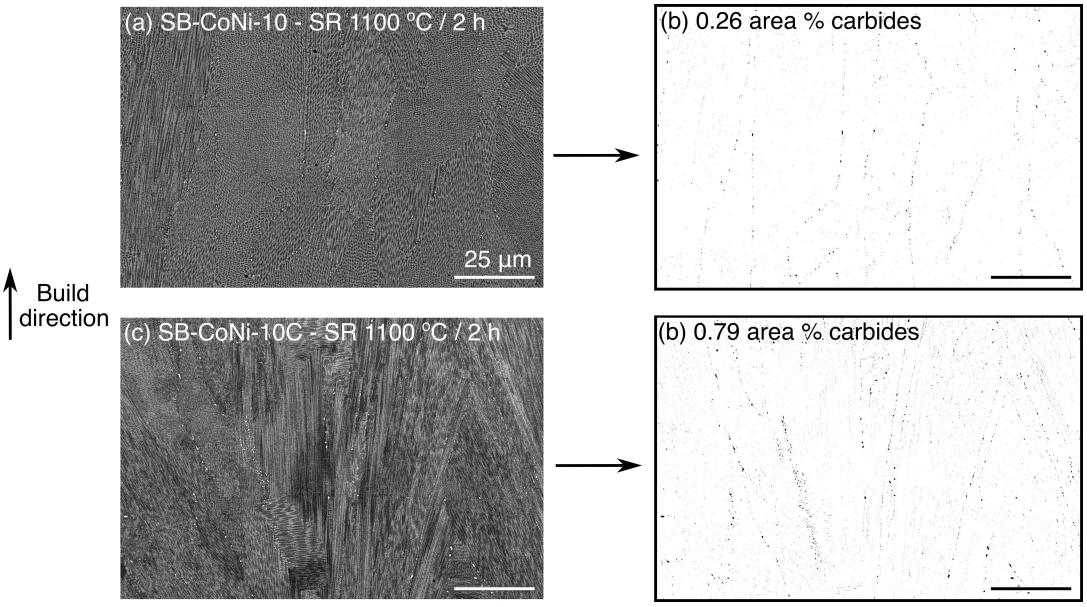

Figure 7.11: (a,c) BSE micrographs and (b,d) binarized thresholded images of (a,b) SB-CoNi-10 compared to (c,d) SB-CoNi-10C after a 2 h stress relieving heat treatment at 1100 °C followed by air cooling. The higher carbon content alloy contains a higher carbide area fraction.

presented in graphical form in Fig. 7.12. The stress-strain curves for the elevated temperature tests on SB-CoNi-10C at 760 °C are presented in Fig. 7.13 along with stitched optical micrographs of selected fracture surfaces. The SB-CoNi-10C alloy exhibits improved ductility at 760 °C compared to the previous version of SB-CoNi-10 that contained a low carbon content and a fully recrystallized grain structure, with the XY-oriented SB-CoNi-10C specimens exhibiting an average engineering strain at failure of 3.0% at 760 °C.

It is demonstrated that the yield strength and ultimate tensile strength are tunable by the application of an additional lower temperature age at 800 °C for 20 h (this heat treatment is denoted as HT3, see Table 7.2). This additional heat treatment has a small negative effect on tensile ductility. Additionally, the benefits to the strength are expected to not be as effective at testing temperatures above 800 °C.

For the Z-oriented specimens, a wide variation in the tensile ductility was observed.

For example, the Z-oriented HT2 specimen had a tensile ductility of 5.8 % at 760 °C and 13.5 % in a duplicate tensile test. The fracture surfaces of these two specimens are shown in Fig. 7.13b for the higher ductility specimen and in Fig. 7.13c for the lower ductility specimen. The higher ductility specimen exhibited a smoother fracture surface compared to the rougher surface of the lower ductility specimen. SEM investigations of the fracture surfaces revealed that all specimens had regions of intergranular failure that were associated with oxidation of the fracture surface. A fracture surface from an XY-oriented specimen is shown in Fig. 7.13d perpendicular to the loading direction and in Fig. 7.13e along the loading direction. The XY-oriented specimens often exhibited cracking along the gauge length, and the fracture surfaces had features that resembled the textured grain structure that is characteristic of SLM printed alloys.

Cross-sections of the Z-oriented HT2 specimens shown in Fig. 7.13b,c were made to investigate the cause of the difference in ductility between these two tests that were performed at the same test condition. BSE images of these cross-sections from the grips (Fig. 7.14a-b, e-f) and near the fracture surfaces (Fig. 7.14c-d, g-h) show that the samples had different amounts of alumina oxide inclusions. The sample with high ductility had fewer oxide inclusions (0.025 area %) (Fig. 7.14e-h) while the sample with reduced ductility had many inclusions (0.098 area %) that were present before tensile testing (Fig. 7.14a-d). Qualitative EDX mapping of one of these inclusions is displayed in Fig. 7.15 which displayed strong Al and O signals. The inclusions within the gauge section often contained cracks that were normal to the loading direction while inclusions located in the grips were uncracked. The cause of the high inclusion density in some of the SB-CoNi-10C specimens is currently under investigation. Cross-sections of the virgin alloy powder did not reveal the presence of alumina inclusions before printing. Periodic oxygen contamination of the build chamber atmosphere was observed in levels of approximately 1000 ppm O_2 which coincided with an excess powder removal procedure

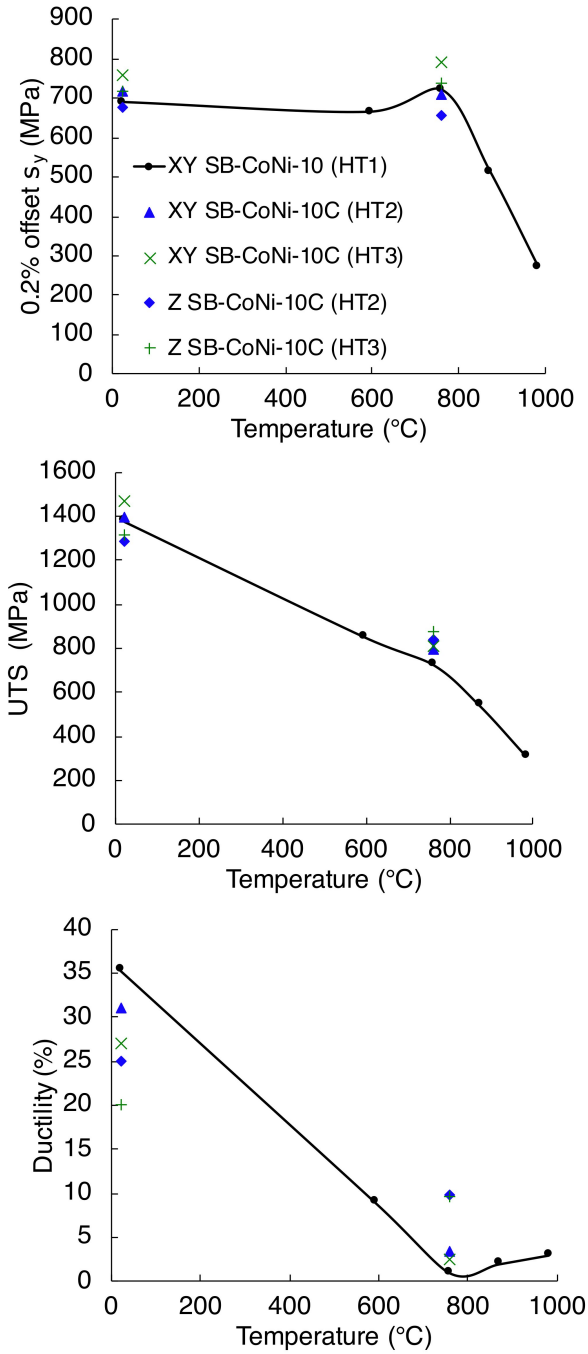

Figure 7.12: Comparison of the 0.2% offset yield strength, ultimate tensile strength, and ductility between XY-printed SB-CoNi-10 with the original HT1 heat treatment and XY- and Z-printed SB-CoNi-10C with the modified HT2 and HT3 heat treatment schedules.

Table 7.3: Tensile testing results on SB-CoNi-10, SB-CoNi-10C, and Ni-base alloys from the literature

Alloy	Treatment	T (°C)	Orientation	σ_y (MPa)	UTS (MPa)	Ductility (%)
SB-CoNi-10 [197]	As-printed	RT	XY	753	1289	13.1
	As-printed	RT	Z	717	1110	24.8
	HT1	RT	XY	689	1379	23.2
	HT1	RT	Z	621	1289	23.3
SB-CoNi-10C	HT2	RT	XY	717	1393	31.0*
	HT2	RT	Z	676	1282	25.0*
	HT3	RT	XY	758	1469	27.0*
	HT3	RT	Z	717	1310	20.0*
SB-CoNi-10	HT1	593	XY	665	855	9.0*
	HT1	760	XY	721	728	1.0*
	HT1	871	XY	514	543	2.0*
	HT1	982	XY	273	312	3.0*
SB-CoNi-10C	HT2	760	XY	718	790	3.6
	HT2	760	XY	696	796	2.9
	HT2	760	XY	708	783	3.8
	HT2	760	Z	647	811	5.8
	HT2	760	Z	663	951	13.5
	HT3	760	XY	787	844	1.4
	HT3	760	XY	791	878	3.1
	HT3	760	XY	790	887	3.1
	HT3	760	Z	734	1032	14.5
	HT3	760	Z	736	953	4.4
Hastelloy® X[292]	†	750	XY	194	396	19.3
	†	750	Z	188	374	25.0
Inconel® 939[293]	†	750	XY	733	867	3.0
	†	750	Z	779	885	6.0
CM 247 LC®[290]	†	760	XY	926	N/A	1.4
[294]	†	760	Z	856	1086	3.5

*ductility measured by post-mortem elongation at Carpenter Technology. Otherwise, ductility is measured as elongation at failure. † refer to citation for specific heat treatment details.

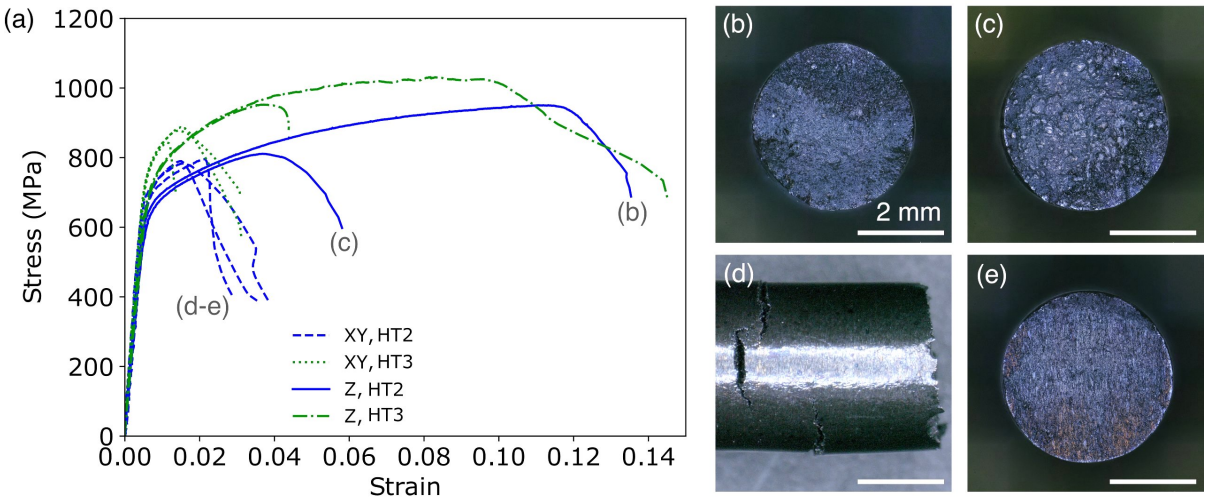

Figure 7.13: (a) Stress-strain curves for tensile tests performed on SB-CoNi-10C at 760 °C. Optical images of post-mortem fracture surfaces the following conditions: (b) Z, HT2 with high ductility, (c) Z, HT2 with low ductility, (d,e) XY, HT2 with low ductility.

during printing, but it is still unclear why certain tensile bars contained more inclusions compared to others printed in the same build chamber.

7.4 Discussion

A high γ' volume fraction CoNi-base superalloy (SB-CoNi-10) and a high carbon containing variant (SB-CoNi-10C) have been successfully processed through SLM. As novel alloys are designed that are compatible with the extreme thermal conditions present in powder-bed fusion AM, new post-processing heat treatment paths also need to be developed to leverage the unique as-printed structure. This is especially true in high γ' volume fraction superalloys that were originally designed for fabrication through directional solidification and single crystal Bridgman growth. Super-solvus heat treatments that create a well-controlled unimodal γ' distribution are employed after single crystal growth without recrystallization in the bulk of the alloy. Since recrystallized versions

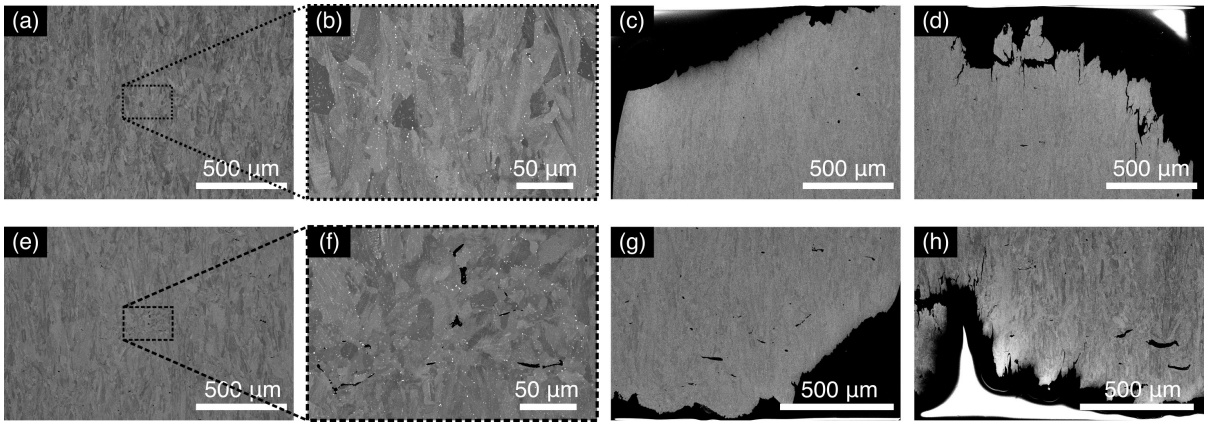

Figure 7.14: BSE micrographs of cross-sections along the loading direction of the post-mortem tensile specimens tested at 760 °C shown in (a-d) Fig. 7.13b and (e-h) Fig. 7.13c. Micrographs are taken from (a-b, e-f) the center of the sample grips and (c-d, g-h) near the fracture surface.

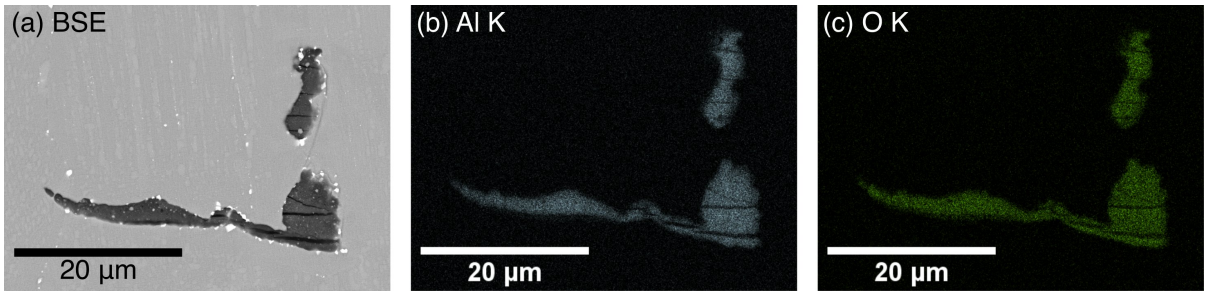

Figure 7.15: (a) BSE micrograph and (b,c) qualitative EDX maps of an alumina inclusion within the lower ductility SB-CoNi-10C sample shown in Fig. 7.14e-h.

of SB-CoNi-10 have been demonstrated to have poor tensile ductility at intermediate temperatures, modifications to the heat treatment procedure and modifications to the minor element concentrations have been studied.

One reason for the improved 3D printability of high γ' volume fraction CoNi-base superalloys compared to Ni-base superalloys is the more favorable solute segregation during solidification [34, 51, 198]. The distribution coefficient ($k = C_s/C_l$, where C_s is the concentration of the solid and C_l is the concentration of the liquid on either side of the solid-liquid interface) for each of the major alloying additions in SB-CoNi-10 has been experimentally measured in Bridgman grown single crystals and EBM processed alloys

using electron probe microanalysis (EPMA) [197]. Since EPMA is a surface-based SEM technique, the interaction volume of the electron beam with the metal surface is large enough such that measurement of the fine scale segregation along cellular boundaries in as-printed alloys processed by SLM is not possible. Individual point measurements likely contain signal from both the intracellular and intercellular regions and result in the false appearance of homogeneous chemical maps of the alloy [197]. This is further complicated by the fact that the thermal gradients, G, and interfacial velocities, V_i, present in SLM are very large with G on the order of 10^6 K/m and V_i on the order of 0.4 m/s [114, 223]. These extreme thermal conditions result in a non-equilibrium condition at the solid-liquid interface such that the distribution coefficient depends on the interfacial velocity. The Aziz model describes the velocity dependent distribution coefficient as [295]:

$$k_v = \frac{k_o + Pe}{1 + Pe} \tag{7.1}$$

where k_o is the equilibrium distribution coefficient and Pe is the solutal Peclet number given as:

$$Pe = \frac{a_o V_i}{D_l} \tag{7.2}$$

where a_o is the width of the zone at the liquid-solid interface where diffusion occurs, V_i is the velocity of the solid-liquid interface, and D_l is the mass diffusivity of solutal elements in the liquid. As V_i increases, the Peclet number increases such that the velocity dependent distribution coefficient approaches $K_v = 1$ at high velocities where solute trapping occurs and microsegregation is suppressed. Solute trapping is expected to occur at interfacial velocities in excess of 3 m/s, and deviations from equilibrium solidification conditions become noticeable above 0.1 m/s [296]. The interfacial velocities typical for the SLM process are on the order of 0.4 m/s [114], therefore the magnitude of the chemical

segregation is expected to decrease and chemical differences between the intracellular and intercellular regions become harder to distinguish in SEM-based techniques [197]. Therefore, TEM or atom probe tomography based techniques must be used to properly assess the chemical segregation present in these alloys.

The TEM maps and chemical line profile presented in Fig. 7.4 and Fig. 7.5 confirm that the chemical segregation is reduced by the high thermal gradients and interfacial velocities present in SLM. Some of the chemical species appeared to have no discernible segregation to the intercellular regions, such as Cr and W. Depletion of Co and the enrichment of Ni, Al, and Ta within the intercellular regions was observed. The directionality of the segregation (i.e. whether solute enrichment, $k < 1$, or depletion, $k > 1$, occurs along the cell boundary) is consistent with previous experiments on this alloy class [197]. While an estimate of the distribution coefficient is difficult without a statistical measurement of the alloy concentration at various stages of the solidification process followed by fitting this data with an appropriate model (such as the Gulliver-Scheil equation for equilibrium solidification processes [51, 55]), it is still useful to compare these results to previous studies by taking the ratio of the alloy concentration in the intracelluar region, C_{intra}, and the intercellular region, C_{inter}. This was done by taking the average composition of the STEM-EDS linescan in a 50 nm region in the center of the cell boundary (from 175-225 nm in Fig. 7.5) and by taking the average composition of the regions outside of the cell boundary (0-175 and 225-400 nm in Fig. 7.5). This resulted in measurements of the approximate distribution coefficients of $k_i = C_{intra}/C_{inter}$ to be $k_{Co} = 1.03$, $k_{Ni} = 1.01$, $k_{Al} = 0.92$, $k_{Cr} = 0.99$, $k_{Ta} = 0.82$, and $k_W = 1.04$.

There is a growing body of evidence that the heat treatments for AM processed superalloys that optimize the mechanical properties will differ from those utilized in wrought, cast, and powder metallurgy processing routes. The modification of the heat treatment schedule such that all steps are performed below the γ' solvus (HIP, SHT, and

aging) is responsible for the retention of the textured grain structure that forms during the AM process. This has been shown previously to lead to improved high temperature tensile ductility in EBM processed SB-CoNi-10 compared to a fully recrystallized microstructure that developed from super-solvus heat treatments [198]. These changes to the heat treatment schedule were combined with an increased nominal carbon content from 0.08 % to 0.35 at.% and a modified scan strategy. Due to the fine-scale of the segregation in AM processed superalloys, the hold time for super-solvus homogenizing heat treatments can be reduced from several hours for Bridgman cast single crystals to only several minutes while achieving similar levels of homogenization [104, 105]. In the case of EBM processed CMSX-4®, it is even possible to apply a short time, super-solvus SHT (<5 m, 1310 °C) and not induce recrystallization, likely due to the reduced amount of internal stresses present in EBM processed materials printed with a high pre-heat temperature [97, 105]. Future studies on SLM processed alloys should consider the use of elevated preheat temperatures above the conventionally used 200 °C to further reduce the magnitude of thermal stresses in the as-built condition. This could allow future iterations of CoNi-base alloys to use short-time, super-solvus homogenization heat treatments while maintaining the textured grain structure acquired from the additive process. This would allow for greater control of the γ' distribution, which could result in enhanced high temperature mechanical properties.

The SB-CoNi-10C build contained bars that were highly dense and others that had increased amounts of alumina inclusions that debited the tensile ductility at elevated temperatures. The formation of alumina inclusions at varied locations within the build chamber will need to be minimized in order to improve mechanical reliability. The formation of oxides during fusion-based additive processes can be promoted by the atmosphere and/or by the concentration of retained gases in the powders used for printing [256, 297, 298]. These particles are often on the order of 25-150 nm in diameter, as shown

in Fig. 7.4a, and can be leveraged for increased dislocation pinning and increased alloy strength when intentionally added in a controlled manner to the alloy microstructure.

After HT3, the SB-CoNi-10C alloy has the highest recorded room temperature yield strengths and ultimate tensile strengths in both the XY- and Z-orientations compared to other iterations of the alloy. This increase in strength is thought to be due to the additional lower temperature age included in HT3 and due to the retained columnar grain structure achieved by preventing complete recrystallization with the sub-solvus heat treatment schedule. Co- and CoNi-base superalloys have been previously demonstrated to have lower yield strengths than their Ni-base counterparts, especially at temperatures near the peak of the yield strength anomaly which is less pronounced in Co- and CoNi-base alloys [24, 25, 192, 299]. These reduced yield strengths are likely due to the reduced {111} plane anti-phase boundary energies that have been computationally determined for Co-rich γ' compositions which make these precipitates less resistant to dislocation shear by $1/2\langle 110\rangle$ dislocations [176]. Since the compositional design space of multi-component CoNi-alloys with balanced properties is large, the design of future CoNi-alloy compositions with elevated room temperature and high temperature strength will benefit from high-throughput computational approaches. An increased understanding on the effect of composition on the planar fault energies in the (Co, Ni)$_3$(Al, W, Ta, etc.) $L1_2$ phase combined with thermodynamic phase stability calculations using the CALPHAD method could result in novel CoNi-alloys with improved strength and high temperature stability [32, 176]. However, improvements to currently available thermodynamic databases may be required as alloy compositions continue to be investigated between the Co-rich and Ni-rich regions of phase diagrams, as systematic inaccuracies in phase boundary locations and solidification behavior have been observed in CoNi-base systems [32, 198].

The tensile testing results at 760 °C show that SB-CoNi-10C can possess ductilities of 13% in the Z-orientation and in excess of 3% in the XY-orientation. This is in contrast to

high γ' volume fraction Ni-base superalloys such as CM 247 LC® which have excellent yield strength and ultimate tensile strength at 760 °C when processed through SLM yet have tensile ductilities of 3.5% in the Z-orientation [294] and 1.4% in the XY-orientation [290]. With respect to strength, the CoNi-alloy has higher yield and UTS at 760 °C compared to SLM Hastelloy®[§§] X and behaves similarly to SLM Inconel® 939, which is a Ni-base superalloy that is designed to have 30 to 50% volume percent of γ' after heat treatment.

The elevated temperature tensile tests on SB-CoNi-10C have demonstrated that this CoNi-base superalloy exhibits a ductility minimum similar to other wrought, powder metallurgy (PM), and AM processed Ni-base superalloys [284, 285, 286, 287, 288, 289]. The intermediate temperature ductility minimum in wrought superalloys can be improved through recrystallization with super-solvus heat treatment that typically results in a substantial increase in grain size and a corresponding reduction in grain boundary area [285]. A similar drastic increase in grain size has not been observed after super-solvus heat treatments applied to AM processed SB-CoNi-10 and SB-CoNi-10C [197]. Observations of oxidation in the intergranular regions of the fracture surfaces of SB-CoNi-10C after intermediate temperature testing suggests that a time-dependent process such as grain boundary oxidation contributes to the observed ductility minimum. High strain-rate tensile testing at 850 °C on an EBM processed version of SB-CoNi-10 revealed improved tensile strengths and ductilities compared to quasi-static tensile tests [198], which further supports the hypothesis that time-dependent processes at intermediate temperatures promote the occurrence of the ductility minimum in this alloy. Similar tensile tests at high strain-rates have demonstrated improved ductility in chromia-forming superalloys as well, suggesting that the specific mode of oxidation does not have a strong effect on the presence of a ductility minimum [285]. Therefore, the intermediate temperature

[§§]Hastelloy® is a registered trademark of Haynes International Inc. Corporation

ductility minimum in the investigated CoNi-base superalloy shows signatures similar to those observed in Ni-base alloys: a dependence on strain rate, occurrence at temperatures near the peak in the yield strength, and a transition from intragranular to intergranular failure at the ductility minimum.

7.5 Conclusions

The conclusions of this study are as follows:

- A CoNi-base superalloy (SB-CoNi-10) and a higher carbon containing variant (SB-CoNi-10C) were successfully fabricated by SLM.
- Chemical microsegregation in the as-printed condition is less pronounced in the SLM fabricated SB-CoNi-10 compared to EBM or Bridgman cast versions.
- Super-solvus heat treatments result in complete recrystallization of the grain-scale microstructure, whereas sub-solvus treatments do not undergo recrystallization and retain grain structures similar to the as-printed microstructure.
- After a sub-solvus HIP at 1177 °C / 4 h / 103 MPa and sub-solvus SHT at 1177 °C for 1 h, aging at 950 °C results in a peak hardness between 0 and 4 h of aging. This corresponds with the precipitation and coarsening of a finer population of γ' in the regions between primary γ' formed during sub-solvus heat treatment.
- Sub-solvus heat treatments and increased carbon content increased the tensile ductility at 760 °C compared to a recrystallized iteration of SB-CoNi-10 with a lower carbon content.
- Additional aging for 20 h at 800 °C increases both the yield strength and the ultimate tensile strength at room temperature and at 760 °C, but this benefit may

not persist at higher testing temperatures.

Chapter 8

Conclusions and recommendations for future work

The development of γ'-containing Co- and CoNi-base superalloys over the past 15 years has resulted in promising new classes of alloys for high temperature applications. These alloys may find applications in turbine hot sections, nuclear reactors and chemical processing. Depending on the desired properties in service, these alloys may be processed into a variety of forms including fine-grained forgings, cast single crystals, or through the burgeoning additive manufacturing processes. However, a transition between currently employed Ni-base alloys and γ'-containing Co- and CoNi-base alloys for single crystalline turbine blades is unlikely to occur with the current state-of-the-art. This is due to the lower γ' solvus still observed in Co- and CoNi-base alloys, higher mass density, less favorable oxidation resistance, and higher cost of Co compared to Ni. In spite of this, the CoNi-base superalloys provide a pathway for developing high γ' volume fraction superalloys for AM due to their better solidification behavior and wider processing window that results in reduced cracking susceptibility compared to Ni-base superalloys.

The work in this thesis has sought to describe the high temperature mechanical

properties and 3D printability of a novel class of CoNi-base superalloys. The key results are as follows:

- The high γ' volume fraction CoNi-base superalloy SB-CoNi-10 has a γ'-solvus near 1200 °C (~50 to 100 °C lower than many Ni-base blade alloys), the ability to form a thin α-Al_2O_3 scale with small amounts of overlaying oxides after brief exposure to air at 1100 °C, and a mass density similar to 1st-generation Ni-base superalloys.

- The compositional space that expresses these properties is characterized by a low W content to reduce density, elevated Al and Cr content to improve oxidation performance, and Ta additions that stabilize the γ' precipitates to higher temperatures.

- This alloy has improved low cycle fatigue response compared to previous single crystal Co-base superalloys, where single-crystal Co-base superalloys are more susceptible to oxidation-assisted surface cracking that promotes short fatigue lifetimes.

- These CoNi-alloys have been found to be resistant to crack formation when fabricated by fusion-based AM processing pathways such as SLM and EBM.

- The grain structure and γ' precipitate structure can be controlled through appropriate heat treatment schedules to tune the mechanical properties.

However, the SB-CoNi-10 alloy varients described in this work are likely not optimized and additional improvements to mechanical, thermophysical, and environmental properties could be realized. In this chapter, some suggested future work will be described that could further improve our understanding of Co- and CoNi-base superalloys with the overall focus of property improvement at elevated temperatures.

8.1 Low cycle fatigue of Co- and CoNi-base superalloys with P-type rafted microstructures

Microstructural degradation known as rafting can occur in Ni-base superalloys due to the high temperature tensile loading present in creep testing and thermo-mechanical fatigue testing. The local stress state within the γ channels is determined by both the externally applied load and the misfit stresses imposed by the small negative misfit of the Ni_3Al γ' and the matrix. The relaxation of this misfit by dislocations within the horizontal γ channels creates a driving force for directional coarsening of the γ' where the elimination of vertically aligned γ/γ' interfaces occurs through a diffusion controlled process. This produces the N-type (i.e. normal-type) rafted microstructure. Since Co- and CoNi-base superalloys typically have small positive misfit parameters, the directional coarsening eliminates the γ/γ' interfaces that are perpendicular to the loading direction, resulting in the P-type (i.e. parallel-type) rafted microstructure.

Several studies have investigated the impact of the rafted γ/γ' microstructure on the creep performance of Ni-base superalloys, but fewer studies have been performed on the impact of fatigue resistance. By pre-deforming the Ni-base blade alloy CMSX-4 in tension and compression (producing N-type and P-type rafted microstructures, respectively), elevated temperature strain-controlled LCF tests at R = 0 by Ott and Mughrabi revealed that the P-type rafted microstructure had better resistance to fatigue failure than the undisturbed microstructure and the N-type rafted microstructure [181, 182]. An example of their results is shown in Fig. 8.1. Fatigue cracks are frequently observed to propagate along the γ/γ' interfaces which are oriented normal to the loading direction in the unmodified and N-type microstructures. The vertical γ/γ' interfaces in the P-type rafted specimen results in significant amounts of crack deflection. Examples of fatigue cracks that form at 1050 °C for each of these microstructures is displayed in Fig. 8.2

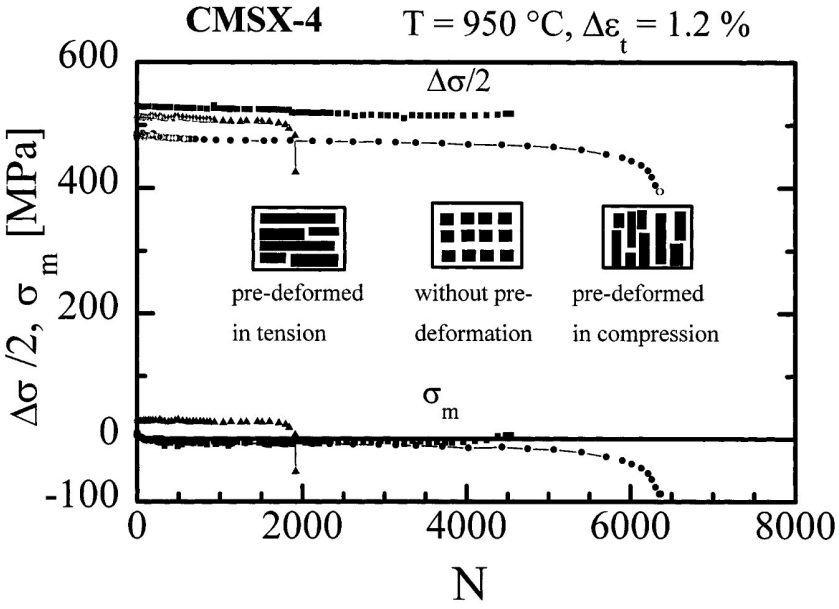

Figure 8.1: Cyclic deformation curves of CMSX-4 specimens with three different kinds of γ/γ'-morphology. The three initial γ/γ'-morphologies are indicated schematically. T = 950 °C, $\Delta\epsilon_t$ = 1.2%. Reproduced from "Dependence of the high-temperature low-cycle fatigue behaviour of the monocrystalline nickel-base superalloys CMSX-4 and CMSX-6 on the γ/γ'-morphology" by M. Ott & H. Mughrabi, 1999, *Mater. Sci. Eng. A* **272**, p. 24-30. Copyright 1999 by Elsevier Science S.A. Reproduced with permission [182].

However, since the Ni-base alloy CMSX-4 has a negative misfit parameter, the P-type rafted microstructure partially reverts to the N-type microstructure during testing in tension, resulting in an ambiguously rafted microstructure.

By performing similar high temperature strain-controlled fatigue tests on Co- and CoNi-base superalloys with R = 0 loading at T = 950 °C it is hypothesized that these alloys would have excellent fatigue crack growth resistance, due to the formation and retention of the P-type rafted microstructure. This study could be performed on pre-deformed microstructures and also on an unmodified microstructure that would directionally coarsen into the P-type rafted microstructure during fatigue testing. Interrupted testing could demonstrate that small cracks are blunted by the P-type rafted γ/γ' interfaces which may reduce the crack propagation rate and delay long crack growth. Ad-

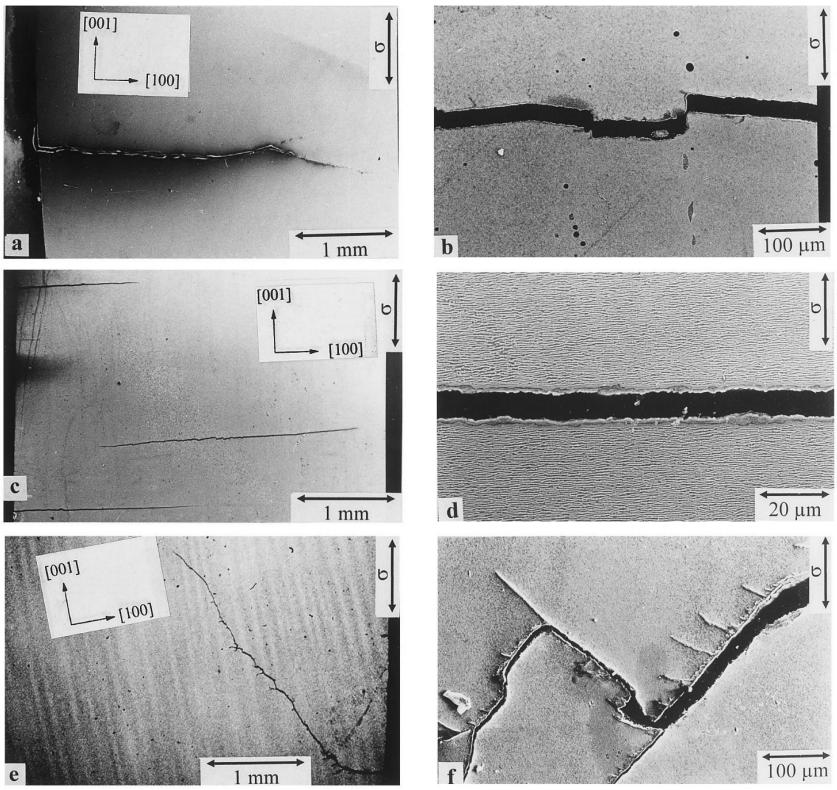

Figure 8.2: Fatigue crack propagation in the alloy CMSX-4 after fatigue at 1050 °C, $\Delta\epsilon_t = 0.9\%$. SEM-micrographs. Dependence on the γ/γ'-morphology, (010)-section parallel to [001]. (a, b) A specimen with cuboidal γ'-particles; (c, d) a specimen with γ/γ'-rafts perpendicular to the stress axis; (e, f) a specimen with γ/γ'-rafts parallel to the stress axis. Reproduced from "Dependence of the high-temperature low-cycle fatigue behaviour of the monocrystalline nickel-base superalloys CMSX-4 and CMSX-6 on the γ/γ'-morphology" by M. Ott & H. Mughrabi, 1999, *Mater. Sci. Eng. A* **272**, p. 24-30. Copyright 1999 by Elsevier Science S.A. Reproduced with permission [182].

ditional tests at a lower temperature (such as 750 °C) on pre-deformed microstructures could show that the fatigue properties improve across numerous temperature regimes due to the P-type rafting that is preferred by Co- and CoNi-base superalloys.

These types of fatigue tests at elevated temperatures would have been difficult to perform on previous low γ' solvus Co-base alloys (such as ternary Co-Al-W alloys) since significant γ' dissolution would occur at temperatures necessary for rafting. Additionally, it should be noted that significant directional coarsening did not occur in either of the low cycle fatigue studies presented in Ch. 2 and Ch. 4. In Ch. 2, testing was performed

with R = 0.1 (i.e. cyclic loading in tension) but at the intermediate temperature of T = 750 °C where rafting is sluggish. In Ch. 4, testing was performed at a higher temperature of T = 950 °C but with R = -1 (i.e. fully reversed loading). Therefore, new experiments would need to be carried out at T $\geq$ 950 °C and R $\geq$ 0 in order to investigate the effect of P-type rafting on CoNi-base superalloys. Strain-controlled testing would be preferred over load-control testing in order to prevent significant ratcheting strains that can develop in load-control testing with R $\geq$ 0.

8.2 Rapid experimental alloy modification

While the reduced number of major alloying additions (6 major constituents of Co-Ni-Al-Cr-Ta-W) has been essential to enable an efficient search of the compositional space through ion plasma deposition, it is likely that additional complexity would further benefit alloy properties. Using the SB-CoNi-10 alloy composition as a starting point, it would be interesting to explore the impact of Ti, Nb, Mo, and Re on phase stability, γ' volume fraction, yield strength, and creep performance of these alloys. However, exploring this compositional space would be prohibitively time-intensive through traditional arc-melting studies. Additionally, making decisions about how much of the novel alloying addition to add and which elements to replace would likely be arbitrarily determined by the researcher and have a low guarantee of success at accomplishing the various balanced properties desired.

One technique that has been recently demonstrated to rapidly explore phase stability in CoNi-base alloys has been through a combined CALPHAD and diffusion multiple approach [35, 36, 158]. In these studies, a base alloy of Co-20Ni-7Al-8W-1Ta-4Ti (at.%) was joined into a complex diffusion multiple with several modified versions of the base alloy with alloy modifications of interest (e.g. alloy 5Nb3W replaced W content with

Nb content, 40Ni explored additions of Ni, 0W explored reduction of W, and so on.) The diffusion multiple was then encapsulated in Ni, HIP'd at 1200 °C and 160 MPa for 5 h, and aged at 1000 °C for 1000 h to get close to equilibrium. A schematic of the diffusion multiple along with a photograph after heat treatment is shown in Fig. 8.3. Careful compositional measurements along the diffusion multiple interfaces can provide information about the alloy content necessary to exit the two-phase γ-γ' phase field and produce deleterious phases such as β, χ, and μ phases. This diffusion multiple could then be tested with Vickers hardness indentation to identify compositional regions of higher strength. While this may be difficult, it is also possible to oxidize the final diffusion multiple and employ PSLS to determine the formation of α-Al_2O_3 or thick overlaying oxides. Through this approach, a significant understanding of the compositional space around SB-CoNi-10 could be acquired rapidly and arc-melting studies could be performed on a select few number of candidate alloys.

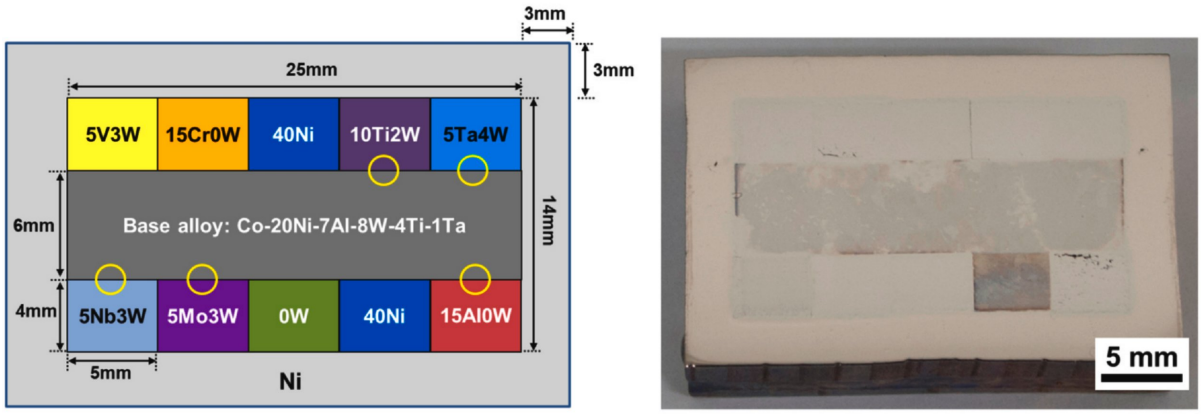

Figure 8.3: (a) Cross-sectional schematic of the diffusion multiple used to explore compostional space around Co-20Ni-7Al-8W-1Ta-4Ti at.% and (b) a photograph of the prepared diffusion multiple after heat treatment. Reproduced from "High-throughput exploration of alloying effects on the microstructural stability and properties of multi-component CoNi-base superalloys" by W. Li et al., 2021, *J. Alloy Compd.* **881**, p. 160618. Copyright 2021 by Elsevier B.V. Reproduced with permission [36].

Provided that compositional measurements from the diffusion multiple are collected

using a high-quality standards-based quantification technique such as EPMA, the composition and phase information could be used to further refine and develop cobalt containing thermodynamic databases produced by companies such as CompuTherm and Thermo-Calc. These databases can be used to make predictions about alloy behavior that are difficult or impossible to produce experimentally, such as Scheil solidification simulations and phase fraction vs. temperature diagrams. However, as demonstrated at several points throughout this dissertation, the currently existing thermodynamic databases struggle with complex compositions in the CoNi-base alloy space. Further enhancement of these databases will be essential for rapid assessment of numerous candidate alloys. These databases can provide powerful insights, such as those presented by Tang et al. in their "alloys-by-design" framework that developed the ABD-850AM and ABD-900AM Ni-base alloys for additive manufacturing [116, 300]. They were able to assess the Scheil freezing range and the γ' volume fraction at 900 °C for $>10^7$ trial alloy compositions with a resolution of 0.1 at.%. Pareto front approaches with pre-determined cut-off values (e.g. γ' volume fraction < 0.35, strain-age cracking merit index < 4 wt.%, Scheil freezing range < 275 °C, etc.) were then used to select several alloys with optimized properties for experimental validation.

8.3 Minor elements in CoNi-base AM alloys: grain-boundary engineering and carbide/oxide precipitation

While the development of single crystal Ni-base superalloys is marked by the reduction of grain-boundary strengtheners and precipitate formers such as C, B, and Zr [6], the fine-scale polycrystalline microstructures that often arise from the additive process re-

quire the reintroduction of these minor elements to improve grain boundary ductility. For example, Co-base superalloys with additions of 0.02 at.% B have significantly improved high temperature ductility compared to B-free alloys, as shown in Fig. 8.4. However, caution must be exercised when introducing these elements since excess amounts of these alloys can reduce solidus temperatures and promote the formation of liquid-rich films that increase the hot cracking susceptibility [99, 301]. The more favorable solute segregation exhibited by Co- and CoNi-base alloys may accommodate greater amounts of these elements than Ni-base alloys while retaining 3D printability, but this has yet to be rigorously investigated.

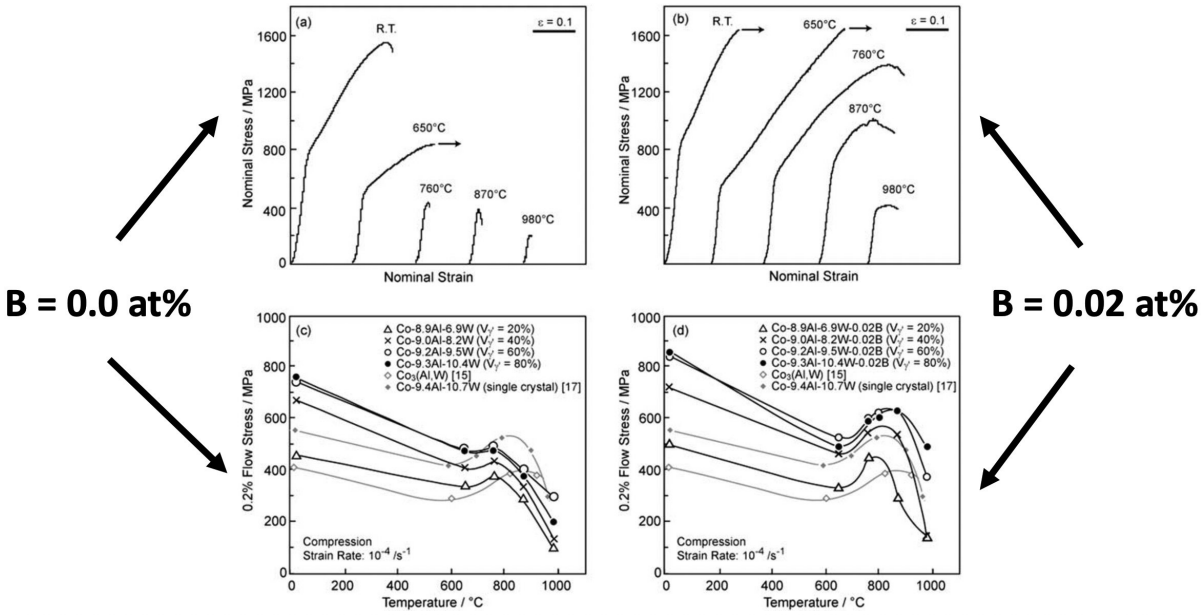

Figure 8.4: (a) Cross-sectional schematic of the diffusion multiple used to explore compostional space around Co-20Ni-7Al-8W-1Ta-4Ti at.% and (b) a photograph of the prepared diffusion multiple after heat treatment. Adapted from "Ductility enhancement by boron addition in Co–Al–W high-temperature alloys" by K. Shinagawa et al., 2009, *Scripta Mater.* **61**, p. 612-615. Copyright 2009 by Acta Materialia Inc. Adapted with permission [119].

Looking at the Ni-C binary phase diagram, the distribution coefficient of carbon is between 0.3 to 0.35, so carbon segregates strongly to the liquid promoting carbide forma-

tion within the mushy zone during soldification [53]. As carbon content increases, there is often a transition from blocky to either script or nodular morphology carbides, with the blocky carbides being promoted during solidification when high thermal gradients are present [53]. The AM versions of SB-CoNi-10 presented in this thesis contained greater carbon contents than the SX version presented in Ch. 3 to increase the TaC carbide precipitation along the grain boundaries after heat treatment. In all cases, the carbide morphology was of the blocky type and boride precipitation along grain boundaries was never observed. Novel versions of SB-CoNi-10 are currently being developed with both elevated carbon content and boron content, with roughly double the boron content as before. Processing these alloys through SLM and performing intermediate temperature tensile testing may reveal increased grain boundary ductility that wasn't present in previous iterations of the alloy. The specific precipitates that will form in the as-printed and heat-treated alloys are not yet clear, especially since the SB-CoNi-10 alloys currently have a low W content and W-rich borides are commonly observed in other alloys [302], but the presence of any borides may indicate that the grain boundaries are effectively saturated with boron compared to previous lower boron alloys [101]. A recent study by McAuliffe et al. was focused on classifying the precipitates that form in CoNi-base superalloys with varying amounts of B, C, Ti, and Zr. They used a combined EBSD and EDS approach combined with a unsupervised machine learning methods (principle component analysis, PCA) to make high fidelity estimations of the carbides and borides present in their CoNi-alloys. This process is significantly simpler than performing site-specific FIB lift-out and TEM investigations that would normally be necessary for precipitate classification, especially since light elements such as C, B, and O are difficult to quantify by EDS and STEM-EDS methods alone. Their work confirmed that carbide contents greater than 0.2 at.% were needed to produce M_6C carbides (M = metallic species) and boron contents greater than 0.08 at.% B were needed to produce M_2B borides in their

CoNi-alloys systems [302]. This suggests that the higher B content SB-CoNi-10 alloys in development for SLM studies will likely form borides and carbides.

(a)

Alloy	Co	Ni	Mo	Cr	Al	W	Ta	C	B	Zr	Ti
1	~ 36	~ 36	2	12	10	2.75	1.25	**0.300**	**0.085**	0.040	0
2	~ 36	~ 36	2	12	10	2.75	1.25	**0.296**	**0.043**	0.040	0
3	~ 36	~ 36	2	12	10	2.75	1.25	**0.224**	**0.041**	0.040	0
4	~ 36	~ 36	2	12	10	2.75	1.25	**0.100**	**0.042**	0.040	0
5	~ 36	~ 36	2	12	10	2.75	1.25	**0.100**	**0.020**	0.040	0
6	~ 36	~ 36	2	12	10	2.75	1.25	**0.180**	**0.085**	0.040	0
7	~ 36	~ 36	2	12	10	2.75	1.25	**0.250**	**0.125**	0.040	0
8	~ 36	~ 36	2	12	10	2.75	1.25	**0.250**	**0.200**	0.040	0
9	~ 36	~ 36	2	12	10	2.75	1.25	**0.300**	**0.110**	0.040	0
10	~ 36	~ 36	2	12	10	2.75	1.25	0.100	0.042	**0.020**	**0.1**
11	~ 36	~ 36	2	12	10	2.75	1.25	0.100	0.042	**0.020**	**0.2**
12	~ 36	~ 36	2	12	10	2.75	1.25	0.100	0.042	**0.020**	**0.3**
13	~ 36	~ 36	2	12	10	2.75	1.25	0.100	0.042	**0.040**	**0.3**
V208C [9]	~ 36	~ 34	0	**15**	**10.5**	3	1	0.150	0.200	0.040	0
L1	~ 34	~ 35	2	**13**	**12**	2.75	1.25	0.300	0.110	0.040	0
L2	~ 34	~ 35	2	**13**	**12**	2.75	1.25	0.300	0.440	0.040	0

The first nine alter C and B content. Alloys 10 to 13 adjust Zr and Ti composition.
Bold represents adjustment.

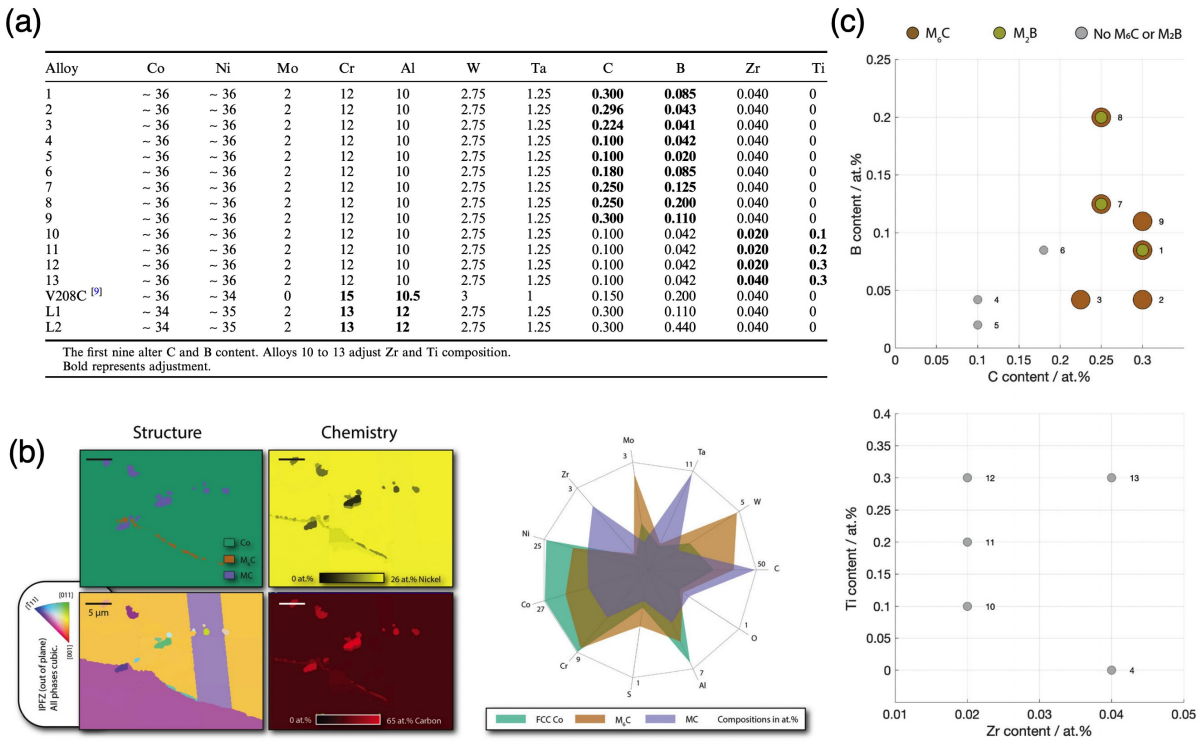

Figure 8.5: (a) nominal compositions (in at.%) for the alloys developed by McAuliffe et al., as well as V208C [303]. (b) The EBSD/EDS PCA approach. Chemical and structural information is combined and corresponding relationships are extracted using statistical methods from the dataset. (c) Phase diagram of precipitate observations across investigated composition space for alloys 1–13. Adapted from "Quantitative Precipitate Classification and Grain Boundary Property Control in Co/Ni-Base Superalloys" by T. McAuliffe et al., 2021, *Metall. Mater. Trans. A* **52**, p. 1649-1664. Copyright 2021 by the Authors through a Creative Commons CC BY license [302].

Additionally, the formation of oxides and nitrides can occur depending on the atmosphere of the build chamber during printing and the retained gases in the powders used for printing [256, 297, 298]. These particles are often on the order of 25-150 nm in diameter and can be leveraged for increased dislocation pinning and increased alloy strength similar to oxide-dispersion strengthened alloys. Interestingly, increased laser energy density during printing results in a reduced oxygen content in the alloy. This is likely due

to oxygen removal from the melt pool by the formation of strongly oxidized spatter that is ejected from the melt pool due to the dynamic fluid flow processes in the melt pool governed by Marangoni convection and evaporation recoil pressure [297, 304, 305]. However, excessive oxide formation can deleteriously affect the alloy ductility. The schematic in Fig. 8.6 shows how gases in the build chamber can be introduced into the melt pool during the build process. Careful control of the build chamber atmosphere during printing with intentional additions of O_2 or CO_2 could increase the room temperature yield strengths of CoNi-base superalloys, which are currently low compared to their Ni-base counterparts.

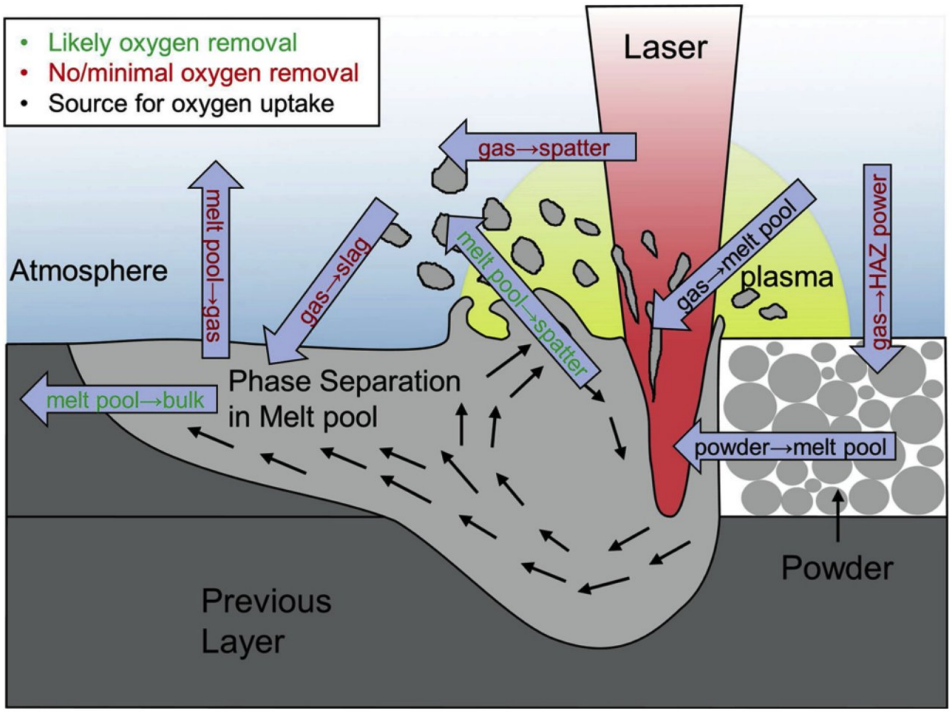

Figure 8.6: Schematic of the interactions between laser, gas and liquid melt pool which effect the sources of oxygen, oxygen pickup, and oxygen loss, showing potential sources of oxygen uptake, and paths for oxygen removal from the melt pool. Reproduced from "In-situ synthesis of oxides by reactive process atmospheres during L-PBF of stainless steel" by M. Haines et al., 2020, *Additive Manufacturing* **33**, p. 101178. Copyright 2020 by Elsevier B.V. Reproduced with permission [297].

Appendix A

Appendix

A.1 Chemical certifications of CoNi-alloy ingots, powders, and prints

This appendix contains chemical certifications of the various SB-CoNi-10 alloys explored in this dissertation. These alloys were frequently referred to internally as "DMREF" alloys before publication, and this prior naming scheme was used in many of these reports. "DMREF10" corresponds to "SB-CoNi-10", "DMREF10-C" corresponds to "SB-CoNi-10C", and so forth. These certificates measure the amounts of the major alloying additions as well as minor and tramp element concentrations. All results are presented in wt.% and can be converted into at.% by the reader. The figure captions indicate which chapters and figures contain the alloy described by the chemical certification.

Northern Analytical Laboratory, Inc. **TEST REPORT**

13 Delta Drive, Unit #4
Londonderry, NH 03053
Phone: 603-434-8400
Fax: 603-434-8500
EMAIL: nalabs@northernanalytical.com
Website: www.northernanalytical.com

Customer:	Mr. Colin Stewart	Received:	11/9/18	NAL #	OG65326
Company:	University Of California Santa Barbara	Identity:	See Below	Report Date:	12/6/18
		Material:	Various Alloys	Page No:	1 of 2
Address:	Materials Dept. Bldg 503, Rm 1355 Santa Barbara, CA 93016	Condition:	Solid	PO #	GW0000269600
		Test Per:	TP-ICP2	INST/MOD:	Spectro Arcos

METHOD: ICP-OES

Sample ID	Rene N5	DMREF-10	DMREF-10+PX
Al(wt%)	6.14	5.84	5.95
Co(wt%)	7.37	38.7	39.0
Cr(wt%)	6.65	4.73	4.84
Mo(wt%)	1.47	--	--
Ni(wt%)	Balance	35.9	36.0
Re(wt%)	2.87	--	--
Ta(wt%)	6.41	10.5	10.4
W(wt%)	4.89	3.10	3.09

Notes:

Analysis By: **Gregory Whissel / Analytical Chemist**
Approved By: **William A. Guidoboni / Sr. Analytical Chemist**

Figure A.1: The major alloying additions of an arc-melted button of SB-CoNi-10 and the polycrystalline ingot of SB-CoNi-10+ before single crystal casting. Results from the arc-melted button are in Ch. 3, specifically Fig. 3.4, 3.7, 3.8, and 3.9. Results from the single crystal castings of SB-CoNi-10+ are in Ch. 3, specifically Fig. 3.10, 3.11, 3.12, 3.13, 3.14, 3.15, 3.19, and 3.20.

Glow Discharge Mass Spectroscopy Test Report - VG9000

NORTHERN ANALYTICAL LABORATORY, INC.

13 Delta Dr. #4, Londonderry, NH 03053
Phone: (603) 434-8400
Fax: (603) 434-8500
www.northernanalytical.com

SAMPLE NO.	OG65326
FILE NO.	3UCSB2
DATE:	11/28/18
Date Received:	11/9/18

C. Stewart — Co + Ni Base / Solid — PO # GW0000269600

Univ.of California Santa Barbara
Materials Bldg 503 Rm 1355
Santa Barbara CA 93106 — DMREF-10

ANALYSIS	ppmw	ANALYSIS	ppmw	ANALYSIS	ppmw
~~H~~		Zn	0.10	Pr	<0.05
Li	<0.1	Ga	1.0	Nd	<0.05
Be	<0.1	Ge	<0.5	Sm	<0.05
B	1.3	As	0.58	Eu	<0.05
~~C~~		Se	<0.5	Gd	<0.05
~~N~~		Br	<0.5	Tb	<0.05
~~O~~		Rb	<10	Dy	<0.05
F	<0.1	Sr	<5	Ho	<0.05
Na	0.46	Y	<1	Er	<0.05
Mg	0.010	Zr	370	Tm	<0.05
Al	Major	Nb	35	Yb	4.4
Si	57	Mo	34	Lu	<0.05
P	4.7	Ru	<1	Hf	7.2
S	1.8	Rh	<0.1	Ta	Major
Cl	0.019	Pd	<0.5	W	Major
K	0.21	Ag	<0.5	Re	0.13
Ca	0.060	Cd	<0.2	Os	<0.1
Sc	<0.1	In	<0.1	Ir	<0.1
Ti	6.0	Sn	0.17	Pt	<0.1
V	0.49	Sb	0.12	Au	<0.5
Cr	Major	Te	<0.1	Hg	<0.5
Mn	1.2	I	<0.1	Tl	<0.05
Fe	620	Cs	<0.1	Pb	<0.01
Co	Major	Ba	<0.3	Bi	0.01
Ni	Major	La	<0.1	Th	0.090
Cu	17	Ce	<0.1	U	0.081

Accredited Nadcap™ Materials Testing Laboratory

ANALYSIS BY: Ed Taylor / Analytical Chemist
Name/Function

APPROVED BY: William A. Guidoboni / Sr. Analytical Chemist
Name/Function

Figure A.2: The tramp alloying additions of an arc-melted button of SB-CoNi-10. Results from the arc-melted button are in Ch. 3, specifically Fig. 3.4, 3.7, 3.8, and 3.9.

Glow Discharge Mass Spectroscopy Test Report - VG9000

NORTHERN ANALYTICAL LABORATORY, INC.

13 Delta Dr. #4, Londonderry, NH 03053	SAMPLE NO.	OG65326
Phone: (603) 434-8400	FILE NO.	3UCSB3
Fax: (603) 434-8500	DATE:	11/28/18
www.northernanalytical.com	Date Received:	11/9/18

C. Stewart — Co + Ni Base / Solid — PO # GW0000269600

Univ.of California Santa Barbara

Materials Bldg 503 Rm 1355

Santa Barbara CA 93106 — DMREF-10 + PX

ANALYSIS	ppmw	ANALYSIS	ppmw	ANALYSIS	ppmw
~~H~~		Zn	0.55	Pr	<0.05
Li	<0.1	Ga	3.4	Nd	<0.05
Be	<0.1	Ge	<0.5	Sm	<0.05
B	180	As	1.1	Eu	<0.05
~~C~~		Se	<0.5	Gd	<0.05
~~N~~		Br	<0.5	Tb	<0.05
~~O~~		Rb	<5	Dy	<0.05
F	<0.1	Sr	<1	Ho	<0.05
Na	0.20	Y	51	Er	<0.05
Mg	0.75	Zr	6.8	Tm	<0.05
Al	Major	Nb	20	Yb	<0.05
Si	100	Mo	30	Lu	<0.05
P	0.85	Ru	<1	Hf	590
S	0.67	Rh	<0.1	Ta	Major
Cl	0.10	Pd	<0.5	W	Major
K	0.077	Ag	≤1	Re	<0.1
Ca	0.17	Cd	<0.2	Os	<0.1
Sc	<0.1	In	<0.1	Ir	<0.1
Ti	0.80	Sn	1.7	Pt	<0.1
V	11	Sb	0.17	Au	<0.5
Cr	Major	Te	<0.1	Hg	<0.5
Mn	0.42	I	<0.1	Tl	<0.05
Fe	50	Cs	<0.1	Pb	0.29
Co	Major	Ba	<0.3	Bi	0.017
Ni	Major	La	0.36	Th	<0.01
Cu	17	Ce	0.17	U	0.011

Accredited Nadcap™ Materials Testing Laboratory

ANALYSIS BY: Ed Taylor / Analytical Chemist
Name/Function

APPROVED BY: William A. Guidoboni / Sr. Analytical Chemist
Name/Function

Figure A.3: The tramp alloying additions of the polycrystalline ingot of SB-CoNi-10+ before single crystal casting. Results from the single crystal castings of SB-CoNi-10+ are in Ch. 3, specifically Fig. 3.10, 3.11, 3.12, 3.13, 3.14, 3.15, 3.19, and 3.20, and all fatigue tests in Ch. 4 were on SX SB-CoNi-10+.

Northern Analytical Laboratory, Inc. **TEST REPORT**

13 Delta Drive, Unit #4
Londonderry, NH 03053
Phone: 603-434-8400
Fax: 603-434-8500
EMAIL: nalabs@northernanalytical.com
Website: www.northernanalytical.com

Customer:	Carolina Frey	Received:	1/27/20	NAL #	OGI67730
Company:	University Of California Santa Barbara	Identity:	See Below	Report Date:	1/29/20
		Material:	Cobalt-nickel superalloys	Page No:	1 of 2
Address:	Materials Dept. Bldg 503, Rm 1355 Santa Barbara, CA 93016	Condition:	Solid	PO #	GW0000337650
		Test Per:	TP-ICP2	INST/MOD:	Spectro Arcos

METHOD: ICP-OES

Sample ID	Sean 1	Sean 2
	Powder(EBM)	Solid (EBM)
Al(wt%)	5.93	5.96
Co(wt%)	38.9	39.1
Cr(wt%)	4.90	4.84
Ni(wt%)	35.8	36.1
Ta(wt%)	10.7	11.0
W(wt%)	3.03	3.09

Notes:

Analysis By: **Gregory Whissel / Analytical Chemist**
Approved By: **William A. Guidoboni / Sr. Analytical Chemist**

Figure A.4: The major alloying additions of the EBM powder cut of SB-CoNi-10 (Powder(EBM)) and an as-printed block of EBM SB-CoNi-10 (Solid (EBM)). Results on EBM SB-CoNi-10 are shown in Ch. 5, specifically 5.1, 5.2, 5.3, 5.4, 5.6, and 5.7, as well as Ch. 6 which focuses on EBM SB-CoNi-10 exclusively.

Northern Analytical Laboratory, Inc. **TEST REPORT**

13 Delta Drive, Unit #4
Londonderry, NH 03053
Phone: 603-434-8400
FAX: 603-434-8500
EMAIL: nalabs@northernanalytical.com
Website: www.northernanalytical.com

Customer:	Ms. Leah Mills	Received:	12/17/19	NAL #	L67570
Address:	University of California	Identity:	See Below	Report Date:	1/15/2020
	Santa Barbara	Material:	Ni base; Refractory alloys	Page No:	1 of 1
	Materials Bldg. 503 Rm 1335	Condition:	Solid	PO #	GW0000331598
	Santa Barbara, CA 93106-505	Test Per:	TP-LECO2,3	INST/MOD:	TCH600, CS744

METHOD: Combustion / Inert Gas Fusion

SAMPLE ID.	C(wt%)	N(wt%)	O(wt%)
S-SA-12-am	0.0017±0.0001	0.019±0.001	0.023±0.002
S-CML-60-am	0.0130±0.0053	0.095±0.001	0.058±0.002
S-CML80-am	0.0091±0.0011	0.126±0.001	0.068±0.001
S-CML-90-am	0.0099±0.0009	0.121±0.003	0.084±0.004
S-CML-71-am	0.0065±0.0011	0.110±0.003	0.065±0.001
S-CML-101-am	0.0075±0.0008	0.062±0.001	0.062±0.001
POWDER EBM	0.0317±0.0005	0.0006±0.0001	0.0115±0.0003
SOLID EBM	0.0283±0.0009	≤0.0005	0.0058±0.0009

Notes: Standard deviation values are 1-sigma (σ).

Analysis By: **Ed Taylor / Analytical Chemist**
Approved By: **William A. Guidoboni / Sr. Analytical Chemist**

Figure A.5: The minor alloying additions C, N, and O of the EBM powder cut of SB-CoNi-10 (POWDER EBM) and an as-printed block of EBM SB-CoNi-10 (SOLID EBM). Results on EBM SB-CoNi-10 are shown in Ch. 5, specifically 5.1, 5.2, 5.3, 5.4, 5.6, and 5.7, as well as Ch. 6 which focuses on EBM SB-CoNi-10 exclusively.

Glow Discharge Mass Spectroscopy Test Report - VG9000

NORTHERN ANALYTICAL LABORATORY, INC.

13 Delta Dr. #4, Londonderry, NH 03053		SAMPLE NO.	OGI67730
Phone: (603) 434-8400		FILE NO.	2USCB1
Fax: (603) 434-8500		DATE:	2/4/20
www.northernanalytical.com	Method: TP-GD1	Date Received:	1/27/20
Carolina Frey	Nickel Alloy / EBM Powder	PO # GW0000337650	
University of California			
Santa Barbara Materials Dept.			
Santa Barbara, CA 93016	#SEAN1		

ANALYSIS	ppmw	ANALYSIS	ppmw	ANALYSIS	ppmw
~~H~~		Zn	0.40	Pr	<0.1
Li	<0.1	Ga	4.0	Nd	<0.1
Be	<0.1	Ge	0.86	Sm	<0.1
B	187	As	0.30	Eu	<0.1
~~C~~		Se	<1	Gd	<0.1
~~N~~		Br	<0.5	Tb	<0.1
~~O~~		Rb	<10	Dy	<0.1
F	<1	Sr	<10	Ho	<0.1
Na	2.3	Y	90	Er	<0.1
Mg	1.6	Zr	110	Tm	<0.1
Al	Major	Nb	83	Yb	<0.1
Si	300	Mo	65	Lu	<0.1
P	2.6	Ru	<1	Hf	850
S	3.4	Rh	<0.1	Ta	Major
Cl	4.9	Pd	<0.5	W	Major
K	0.20	Ag	<1	Re	0.60
Ca	1.7	Cd	<0.5	Os	<0.1
Sc	<0.1	In	<0.1	Ir	<0.1
Ti	990	Sn	1.4	Pt	<1
V	34	Sb	3.2	Au	<1
Cr	Major	Te	<0.5	Hg	<1
Mn	6.3	I	<0.1	Tl	<0.5
Fe	2600	Cs	<0.1	Pb	0.11
Co	Major	Ba	<0.5	Bi	<0.1
Ni	Major	La	<0.5	Th	<0.1
Cu	240	Ce	<0.5	U	0.13

The Measurement Uncertainty is included in the Pass/Fail criteria. [values] within false accept/false reject range

Accredited Nadcap™ Materials Testing Laboratory

ANALYSIS BY: William A. Guidoboni / Sr. Analytical Chemist
Name/Function

APPROVED BY: Richard J. Guidoboni / Analytical Chemist III
Name/Function

Figure A.6: The tramp alloying additions of the EBM powder cut of SB-CoNi-10. Results on EBM SB-CoNi-10 are shown in Ch. 5, specifically 5.1, 5.2, 5.3, 5.4, 5.6, and 5.7, as well as Ch. 6 which focuses on EBM SB-CoNi-10 exclusively.

Glow Discharge Mass Spectroscopy Test Report - VG9000

NORTHERN ANALYTICAL LABORATORY, INC.

13 Delta Dr. #4, Londonderry, NH 03053		SAMPLE NO.	OGI67730
Phone: (603) 434-8400		FILE NO.	2USCB2
Fax: (603) 434-8500		DATE:	2/4/20
www.northernanalytical.com	Method: TP-GD1	Date Received:	1/27/20
Carolina Frey	Nickel Alloy / EBM Solid	PO #	GW0000337650
University of California			
Santa Barbara Materials Dept.			
Santa Barbara, CA 93016	#SEAN2		

ANALYSIS	ppmw	ANALYSIS	ppmw	ANALYSIS	ppmw
~~H~~		Zn	0.21	Pr	<0.1
Li	<0.1	Ga	7.5	Nd	<0.1
Be	<0.1	Ge	<0.5	Sm	<0.1
B	177	As	0.30	Eu	<0.1
~~C~~		Se	<1	Gd	<0.1
~~N~~		Br	<0.5	Tb	<0.1
~~O~~		Rb	<10	Dy	<0.1
F	<1	Sr	<10	Ho	<0.1
Na	0.48	Y	130	Er	<0.1
Mg	1.3	Zr	160	Tm	<0.1
Al	Major	Nb	110	Yb	<0.1
Si	245	Mo	48	Lu	<0.1
P	1.7	Ru	<1	Hf	1125
S	3.7	Rh	<0.1	Ta	Major
Cl	0.80	Pd	<0.5	W	Major
K	0.35	Ag	<1	Re	0.70
Ca	1.6	Cd	<0.5	Os	<0.1
Sc	<0.1	In	<0.1	Ir	<0.1
Ti	725	Sn	2.5	Pt	<1
V	48	Sb	1.7	Au	<1
Cr	Major	Te	<0.5	Hg	<1
Mn	10	I	<0.1	Tl	<0.5
Fe	2550	Cs	<0.1	Pb	0.059
Co	Major	Ba	<0.5	Bi	<0.1
Ni	Major	La	<0.5	Th	<0.1
Cu	290	Ce	<0.5	U	0.16

The Measurement Uncertainty is included in the Pass/Fail criteria. [values] within false accept/false reject range

Accredited Nadcap™ Materials Testing Laboratory

ANALYSIS BY: William A. Guidoboni / Sr. Analytical Chemist (Name/Function)

APPROVED BY: Richard J. Guidoboni / Analytical Chemist III (Name/Function)

Figure A.7: The tramp alloying additions of an as-printed block of EBM SB-CoNi-10. Results on EBM SB-CoNi-10 are shown in Ch. 5, specifically 5.1, 5.2, 5.3, 5.4, 5.6, and 5.7, as well as Ch. 6 which focuses on EBM SB-CoNi-10 exclusively.

CERTIFICATE OF TESTS

CARPENTER®

P.O. Box 14662
Reading, PA 19612-4662
U.S.A.

Address Reply To:

Carpenter Technology Corporation
P.O. Box 14662
Reading, PA 19612-4662

CUSTOMER ORDER NO.	CARPENTER NO.	DATE SHIPPED	WEIGHT
N/A	R&D Heat 131300	July 9th, 2019	1.15 lbs.

PRODUCT DESCRIPTION	SPECIFICATION
DMREF10 Powder (-177/+53 micron)	Revised 12/6/19 to correct typographical error. Cobalt is 39.30% not 39.90%. KMF. Chemistry certified in weight%, unless noted otherwise
Powder produced in R&D 300-lb. VIM Atomizer	

Heat No.	C	S	N	O	Co	Cr	Ni	Ta
131300	0.030	<0.0005	<0.001	0.006	39.30	5.18	36.20	10.50

W	Al	B	Hf
3.00	5.43	0.010	0.04

I certify this information to be true and correct as contained in the records of

Authorized Representative
Carpenter Technology Corporation

NOTE: The recording of false, fictitious or fraudulent statements or entries on this document may be punished as a felony under Federal Statutes including Federal Law, Title 18, Chapter 47.

Form 2-303-A

Figure A.8: Chemical certification of the SLM cut of the SB-CoNi-10 powder. Results and alloys printed from this powder are shown in Ch. 5 and Ch. 7, specifically 5.1, 5.2, 5.3, 5.5, 5.6, 7.2, 7.3, 7.4, 7.5, 7.6, 7.7, 7.8, 7.9, 7.11, and 7.12.

REPORT OF TEST RESULTS

CARPENTER®

P.O. Box 14662
Reading, PA 19612-4662
U.S.A.

Address Reply To:
Carpenter Technology Corporation
P.O. Box 14662
Reading, PA 19612-4662

CUSTOMER ORDER NO.	CARPENTER NO.	DATE SHIPPED	WEIGHT
N/A	R&D Heat 131349	TBD	lbs.

PRODUCT DESCRIPTION	SPECIFICATION
Alloy DMREF10-C Powder	Chemistry certified in weight%, unless noted otherwise
Powder produced in R&D 300-lb. VIM Atomizer	

Particle size	Weight
-177 / +53 micron	92 lbs.
-53 / +15 micron	132 lbs.

Chemical Composition

Heat No.	C	O	N	S	Ni	Co	Ta	Cr	Al
131349	0.069	0.015	<0.001	<0.001	35.93	39.69	10.40	5.24	5.98

Hf	W	Nb	Fe	Zr
0.057	3.06	<0.01	0.03	0.01

B*	Bi*	Ga*	Pb*	Y**
<.013	<0.3 ppm	<10 ppm	<3 ppm	0.006

Test Methods:
Carbon, Oxygen, Nitrogen, and Sulfur tested via Leco using the -53/+15 particle size
Major constituents tested via XRay using dip sample.
Tramp elements* tested via Mass Spectroscopy using dip sample.
Yttrium** tested via wet chem analysis using the as-atomized powder.

Results compiled by: Kurt Frantz

Powder Product Metallurgy
Carpenter Technology Corporation

Figure A.9: Chemical certification of SB-CoNi-10C powder. Results and alloys printed from this powder are shown in Ch. 7, specifically Figs. 7.1, 7.2, 7.10, 7.11, 7.12, 7.13, 7.14, and 7.15.

REPORT OF TEST RESULTS

CARPENTER®

P.O. Box 14662
Reading, PA 19612-4662
U.S.A.

Address Reply To:
Carpenter Technology Corporation
P.O. Box 14662
Reading, PA 19612-4662

CUSTOMER ORDER NO.	CARPENTER NO.	DATE SHIPPED	WEIGHT
N/A	R&D Heat 131348	TBD	lbs.

PRODUCT DESCRIPTION	SPECIFICATION
Alloy DMREF10-LC Powder	Chemistry certified in weight%, unless noted otherwise
Powder produced in R&D 300-lb. VIM Atomizer	

Particle size	Weight
-177 / +53 micron	92 lbs.
-53 / +15 micron	133 lbs.

Chemical Composition

Heat No.	C	O	N	S	Ni	Co	Ta	Cr	Al
131348	0.020	0.012	<0.001	<0.001	35.88	39.66	10.43	5.27	5.97

Hf	W	Nb	Fe	Zr
0.055	3.03	0.01	0.04	0.01

B*	Bi*	Ga*	Pb*	Y**
<.013	<0.3 ppm	<10 ppm	<3 ppm	0.007

Test Methods:
Carbon, Oxygen, Nitrogen, and Sulfur tested via Leco using the -53/+15 particle size
Major constituents tested via XRay using dip sample.
Tramp elements* tested via Mass Spectroscopy using dip sample.
Yttrium** tested via wet chem analysis using the as-atomized powder.

Results compiled by: Kurt Frantz

Powder Product Metallurgy
Carpenter Technology Corporation

Figure A.10: Chemical certification of SB-CoNi-10LC powder. As of the writing of this dissertation, this powder has not been processed by SLM and was recently processed by EBM.

Bibliography

[1] R. Darolia, Development of strong, oxidation and corrosion resistant nickel-based superalloys: critical review of challenges, progress and prospects, *Int. Mater. Rev.* **64** (2019) 355–380.

[2] M. Valenti, Reaching for 60 percent, *Mech. Eng.* **124** (2002) 35–39.

[3] T. M. Pollock, Alloy design for aircraft engines, *Nat. Mater.* **15** (2016) 809–815.

[4] T. M. Pollock and S. Tin, Nickel-based superalloys for advanced turbine engines: Chemistry, microstructure, and properties, *J. Propul. Power* **22** (2006) 361–374.

[5] R. Reed, *The Superalloys, Fundamentals and Applications*. Cambridge University Press, 2006.

[6] C. Sims, A History of Superalloy Metallurgy for Superalloy Metallurgists, in *Superalloys 1984 (Fifth International Symposium)* (M. Gell, ed.), (Warrendale, PA), pp. 399–419, AIME, 1984.

[7] L. M. Bortoluci Ormastroni, S. Utada, J. Rame, L. Mataveli Suave, K. Kawagishi, H. Harada, P. Villechaise, and J. Cormier, Tensile, Low Cycle Fatigue, and Very High Cycle Fatigue Characterizations of Advanced Single Crystal Nickel-Based Superalloys, in *Superalloys 2020* (S. Tin, M. Hardy, J. Clews, J. Cormier, Q. Feng, J. Marcin, C. O'Brien, and A. Suzuki, eds.), (Warrendale, PA), pp. 341–351, TMS, 2020.

[8] A. Volek, F. Pyczak, R. F. Singer, and H. Mughrabi, Partitioning of Re between γ and γ' phase in nickel-base superalloys, *Scripta Mater.* **52** (2005) 141–145.

[9] J. S. Van Sluytman, A. L. Fontaine, J. M. Cairney, and T. M. Pollock, Elemental partitioning of platinum group metal containing Ni-base superalloys using electron microprobe analysis and atom probe tomography, *Acta Mater.* **58** (2010) 1952–1962.

[10] H. Mughrabi, The importance of sign and magnitude of γ/γ' lattice misfit in superalloys - With special reference to the new γ'-hardened cobalt-base superalloys, *Acta Mater.* **81** (2014) 21–29.

[11] K. V. Vamsi and S. Karthikeyan, High-throughput estimation of planar fault energies in A_3B compounds with $L1_2$ structure, *Acta Mater.* **145** (2018) 532–542.

[12] T. M. Pollock and A. S. Argon, Creep resistance of CMSX-3 nickel base superalloy single crystals, *Acta Metall. Mater.* **40** (1992) 1–30.

[13] A. Mottura and R. C. Reed, What is the role of rhenium in single crystal superalloys?, *MATEC Web of Conferences* **14** (2014) 01001.

[14] K. Kawagishi, A.-C. Yeh, T. Yokokawa, T. Kobayashi, Y. Koizumi, and H. Harada, Development of an oxidation-resistant high-strength sixth-generation single-crystal superalloy TMS-238, in *Superalloys 2012* (E. Huron, R. Reed, M. Hardy, M. Mills, R. Montero, P. Portella, and J. Telesman, eds.), (Warrendale, PA), pp. 189–195, TMS, 2012.

[15] P. Hallensleben, H. Schaar, P. Thome, N. Jöns, A. Jafarizadeh, I. Steinbach, G. Eggeler, and J. Frenzel, On the evolution of cast microstructures during processing of single crystal Ni-base superalloys using a Bridgman seed technique, *Mater. Design* **128** (2017) 98–111.

[16] University Of Cambridge, "Creep mechanisms." url: https://www.doitpoms.ac.uk/tlplib/creep/mechanisms.php. Online. Accessed 15 July 2021.

[17] S. Tin and T. M. Pollock, Predicting freckle formation in single crystal Ni-base superalloys, *J. Mater. Sci.* **39** (2004) 7199–7205.

[18] M. Pröbstle, S. Neumeier, P. Feldner, R. Rettig, H. E. Helmer, R. F. Singer, and M. Göken, Improved creep strength of nickel-base superalloys by optimized γ/γ' partitioning behavior of solid solution strengthening elements, *Mat. Sci. Eng.: A* **676** (2016) 411–420.

[19] N. C. Ritter, R. Sowa, J. C. Schauer, D. Gruber, T. Goehler, R. Rettig, E. Povoden-Karadeniz, C. Koerner, and R. F. Singer, Effects of Solid Solution Strengthening Elements Mo, Re, Ru, and W on Transition Temperatures in Nickel-Based Superalloys with High γ'-Volume Fraction: Comparison of Experiment and CALPHAD Calculations, *Metall. Mater. Trans. A* **49** (2018) 3206–3216.

[20] K. V. Vamsi and S. Karthikeyan, Modeling APB energies in multicomponent Ni-base superalloys, *Intermetallics* **132** (2021) 107124.

[21] C. S. Lee, *Precipitation-Hardening Characteristics of Ternary Cobalt-Aluminum-X Alloys.* PhD thesis, University of Arizona, 1971.

[22] J. Sato, T. Omori, K. Oikawa, I. Ohnuma, R. Kainuma, and K. Ishida, Cobalt-Base High-Temperature Alloys, *Science* **312** (2006) 90–91.

[23] T. M. Pollock, J. Dibbern, M. Tsunekane, J. Zhu, and A. Suzuki, New Co-based γ-γ' high-temperature alloys, *JOM* **62** (2010) 58–63.

[24] A. Suzuki, G. C. Denolf, and T. M. Pollock, Flow stress anomalies in γ/γ' two-phase Co–Al–W-base alloys, *Scripta Mater.* **56** (2007) 385–388.

[25] A. Suzuki and T. M. Pollock, High-temperature strength and deformation of γ/γ' two-phase Co-Al-W-base alloys, *Acta Mater.* **56** (2008) 1288–1297.

[26] N. V. Kazantseva, S. L. Demakov, A. S. Yurovskikh, N. N. Stepanova, N. I. Vinogradova, D. I. Davydov, and S. V. Lepikhin, Phase diagram of the Co–Al–W system. structure and phase transformations near the Co_3(Al, W) intermetallic composition range, *Phys. Met. Metallogr.* **117** (2016) 701–709.

[27] K. Shinagawa, T. Omori, J. Sato, K. Oikawa, I. Ohnuma, R. Kainuma, and K. Ishida, Phase Equilibria and Microstructure on γ' Phase in Co-Ni-Al-W System, *Mater. Trans.* **49** (2008) 1474–1479.

[28] M. Knop, P. Mulvey, F. Ismail, A. Radecka, K. M. Rahman, T. C. Lindley, B. A. Shollock, M. C. Hardy, M. P. Moody, T. L. Martin, P. A. Bagot, and D. Dye, A New Polycrystalline Co-Ni Superalloy, *JOM* **66** (2014) 2495–2501.

[29] S. Neumeier, L. P. Freund, and M. Göken, Novel wrought γ/γ' cobalt base superalloys with high strength and improved oxidation resistance, *Scripta Mater.* **109** (2015) 104–107.

[30] C. H. Zenk, S. Neumeier, N. M. Engl, S. G. Fries, O. Dolotko, M. Weiser, S. Virtanen, and M. Göken, Intermediate Co/Ni-base model superalloys - Thermophysical properties, creep and oxidation, *Scripta Mater.* **112** (2016) 83–86.

[31] C. H. Zenk, S. Neumeier, M. Kolb, N. Volz, S. G. Fries, O. Dolotko, I. Povstugar, D. Raabe, and M. Göken, The Role of the Base Element in γ' Strengthened Cobalt / Nickel-Base, in *Superalloys 2016* (M. Hardy, E. Huron, U. Glatzel, B. Griffin, B. Lewis, C. Rae, V. Seetharaman, and S. Tin, eds.), (Warrendale, PA), pp. 971–980, TMS, 2016.

[32] E. A. Lass, Application of Computational Thermodynamics to the Design of a Co-Ni-Based γ'-Strengthened Superalloy, *Metall. Mater. Trans. A* **48** (2017) 2443–2459.

[33] E. A. Lass, D. J. Sauza, D. C. Dunand, and D. N. Seidman, Multicomponent γ'-strengthened Co-based superalloys with increased solvus temperatures and reduced mass densities, *Acta Mater.* **147** (2018) 284–295.

[34] C. A. Stewart, S. P. Murray, A. Suzuki, T. M. Pollock, and C. G. Levi, Accelerated discovery of oxidation resistant CoNi-base γ/γ' alloys with high $L1_2$ solvus and low density, *Mater. Design* **189** (2020) 108445.

[35] W. Li, L. Li, C. Wei, J. C. Zhao, and Q. Feng, Effects of Ni, Cr and W on the microstructural stability of multicomponent CoNi-base superalloys studied using CALPHAD and diffusion-multiple approaches, *J. Mater. Sci. Technol.* **80** (2021) 139–149.

[36] W. Li, L. Li, S. Antonov, C. Wei, J.-C. Zhao, and Q. Feng, High-throughput exploration of alloying effects on the microstructural stability and properties of multi-component CoNi-base superalloys, *J. Alloys Compd.* **881** (2021) 160618.

[37] T. Carter, Common failures in gas turbine blades, *Eng. Fail. Anal.* **12** (2005) 237–247.

[38] S. K. Makineni, B. Nithin, and K. Chattopadhyay, A new tungsten-free γ-γ' Co-Al-Mo-Nb-based superalloy, *Scripta Mater.* **98** (2015) 36–39.

[39] S. K. Makineni, A. Samanta, T. Rojhirunsakool, T. Alam, B. Nithin, A. K. Singh, R. Banerjee, and K. Chattopadhyay, A new class of high strength high temperature Cobalt based γ-γ' Co-Mo-Al alloys stabilized with Ta addition, *Acta Mater.* **97** (2015) 29–40.

[40] S. K. Makineni, B. Nithin, and K. Chattopadhyay, Synthesis of a new tungsten-free γ-γ' Cobalt-based superalloy by tuning alloying additions, *Acta Mater.* **85** (2015) 85–94.

[41] C. H. Zenk, I. Povstugar, R. Li, F. Rinaldi, S. Neumeier, D. Raabe, and M. Göken, A novel type of Co–Ti–Cr-base γ/γ' superalloys with low mass density, *Acta Mater.* **135** (2017) 244–251.

[42] C. H. Zenk, S. Neumeier, H. J. Stone, and M. Göken, Mechanical properties and lattice misfit of γ/γ' strengthened Co-base superalloys in the Co-W-Al-Ti quaternary system, *Intermetallics* **55** (2014) 28–39.

[43] L. Klein, A. Bauer, S. Neumeier, M. Göken, and S. Virtanen, High temperature oxidation of γ/γ'-strengthened Co-base superalloys, *Corros. Sci.* **53** (2011) 2027–2034.

[44] H.-Y. Yan, V. A. Vorontsov, and D. Dye, Effect of alloying on the oxidation behaviour of Co-Al-W superalloys, *Corros. Sci.* **83** (2014) 382–395.

[45] H.-Y. Yan, V. A. Vorontsov, and D. Dye, Alloying effects in polycrystalline γ' strengthened Co-Al-W base alloys, *Intermetallics* **48** (2014) 44–53.

[46] C. A. Stewart, R. K. Rhein, A. Suzuki, T. M. Pollock, and C. G. Levi, Oxide Scale Formation in Novel γ-γ' Cobalt-Based Alloys, in *Superalloys 2016* (M. Hardy, E. Huron, U. Glatzel, B. Griffin, B. Lewis, C. Rae, V. Seetharaman, and S. Tin, eds.), (Warrendale, PA), pp. 991–999, TMS, 2016.

[47] A. C. Yeh, K. Kawagishi, H. Harada, T. Yokokawa, Y. Koizumi, T. Kobayashi, D. H. Ping, J. Fujioka, and T. Suzuki, Development of Si-bearing 4th generation Ni-base single crystal superalloys, in *Superalloys 2008* (R. Reed, K. Green, P. Caron, T. Gabb, M. Farhmann, E. Huron, and S. Woodard, eds.), pp. 619–628, TMS, 2008.

[48] C. A. Stewart, A. Suzuki, T. M. Pollock, and C. G. Levi, Rapid Assessment of Oxidation Behavior in Co-Based γ/γ' Alloys, *Oxid. Met.* **90** (2018) 485–498.

[49] C. A. Stewart, A. Suzuki, R. K. Rhein, T. M. Pollock, and C. G. Levi, Oxidation Behavior Across Composition Space Relevant to Co-based γ/γ' Alloys, *Metall. Mater. Trans. A* **50** (2019) 5445–5458.

[50] C. A. Stewart, *Accelerated Design and Characterization of Oxidation Resistant Co-Based γ/γ' Superalloys*. PhD thesis, University of California, Santa Barbara, 2019.

[51] M. Tsunekane, A. Suzuki, and T. M. Pollock, Single-crystal solidification of new Co-Al-W-base alloys, *Intermetallics* **19** (2011) 636–643.

[52] J. Koßmann, C. H. Zenk, I. Lopez-Galilea, S. Neumeier, A. Kostka, S. Huth, W. Theisen, M. Göken, R. Drautz, and T. Hammerschmidt, Microsegregation and precipitates of an as-cast Co-based superalloy—microstructural characterization and phase stability modelling, *J. Mater. Sci.* **50** (2015) 6329–6338.

[53] S. Tin and T. M. Pollock, Stabilization of thermosolutal convective instabilities in Ni-based single-crystal superalloys: Carbide precipitation and Rayleigh numbers, *Metall. Mater. Trans. A* **34 A** (2003) 1953–1967.

[54] D. Ma, H. Lu, and A. Bührig-Polaczek, Experimental trials of the Thin Shell Casting (TSC) technology for directional solidification, *IOP Conf. Ser.-Mat. Sci.* **27** (2011) 012036.

[55] E. Scheil, Bemerkungen zur schichtkristallbildung, *Z. Metallkd.* **34** (1942) 70–72.

[56] Y. Mishima, S. Ochiai, M. Yodogawa, and T. Suzuki, Mechanical Properties of Ni3Al with Ternary Addition of Transition Metal Elements, *T. Jpn. I. Met.* **27** (1986) 41–50.

[57] P. Geng, W. Li, X. Zhang, Y. Deng, H. Kou, J. Ma, J. Shao, L. Chen, and X. Wu, A theoretical model for yield strength anomaly of Ni-base superalloys at elevated temperature, *J. Alloys Compd.* **706** (2017) 340–343.

[58] K. V. Vamsi and S. Karthikeyan, Deformation modes and yield strength anomaly in $L1_2$ compounds, *J. Alloys Compd.* **860** (2021) 158411.

[59] T. Murakumo, T. Kobayashi, Y. Koizumi, and H. Harada, Creep behaviour of Ni-base single-crystal superalloys with various γ' volume fraction, *Acta Mater.* **52** (2004) 3737–3744.

[60] A. Giamei, EAFOSR Annual Report FR-11009, tech. rep., 1978.

[61] M. Huang and J. Zhu, An overview of rhenium effect in single-crystal superalloys, *Rare Metals* **35** (2016) 127–139.

[62] M. S. Titus, A. Suzuki, and T. M. Pollock, Creep and directional coarsening in single crystals of new γ-γ' Cobalt-base alloys, *Scripta Mater.* **66** (2012) 574–577.

[63] M. S. Titus, A. Suzuki, and T. M. Pollock, High Temperature Creep of New $L1_2$-containing Cobalt-base Superalloys, in *Superalloys 2012* (E. Huron, R. Reed, M. Hardy, M. Mills, R. Montero, P. Portella, and J. Telesman, eds.), pp. 823–832, TMS, 2012.

[64] K. Tanaka, M. Ooshima, N. Tsuno, A. Sato, and H. Inui, Creep deformation of single crystals of new Co-Al-W-based alloys with fcc/$L1_2$ two-phase microstructures, *Philos. Mag.* **92** (2012) 4011–4027.

[65] A. Bezold, N. Volz, F. Xue, C. H. Zenk, S. Neumeier, and M. Göken, On the Precipitation-Strengthening Contribution of the Ta-Containing Co3(Al,W)-Phase to the Creep Properties of γ/γ' Cobalt-Base Superalloys, *Metall. Mater. Trans. A* **51** (2020) 1567–1574.

[66] M. Kolb, C. H. Zenk, A. Kirzinger, I. Povstugar, D. Raabe, S. Neumeier, and M. Göken, Influence of rhenium on γ'-strengthened cobalt-base superalloys, *J. Mater. Res.* **32** (2017) 2551–2559.

[67] Y. M. Eggeler, M. S. Titus, A. Suzuki, and T. M. Pollock, Creep deformation-induced antiphase boundaries in L12-containing single-crystal cobalt-base superalloys, *Acta Mater.* **77** (2014) 352–359.

[68] M. S. Titus, Y. M. Eggeler, A. Suzuki, and T. M. Pollock, Creep-induced planar defects in $L1_2$-containing Co- and CoNi-base single-crystal superalloys, *Acta Mater.* **82** (2015) 530–539.

[69] M. S. Titus, A. Mottura, G. Babu Viswanathan, A. Suzuki, M. J. Mills, and T. M. Pollock, High resolution energy dispersive spectroscopy mapping of planar defects in $L1_2$-containing Co-base superalloys, *Acta Mater.* **89** (2015) 423–437.

[70] Y. M. Eggeler, J. Müller, M. S. Titus, A. Suzuki, T. M. Pollock, and E. Spiecker, Planar defect formation in the γ' phase during high temperature creep in single crystal CoNi-base superalloys, *Acta Mater.* **113** (2016) 335–349.

[71] N. Volz, F. Xue, C. H. Zenk, A. Bezold, S. Gabel, A. P. A. Subramanyam, R. Drautz, T. Hammerschmidt, S. K. Makineni, B. Gault, M. Göken, and S. Neumeier, Understanding creep of a single-crystalline Co-Al-W-Ta superalloy by studying the deformation mechanism, segregation tendency and stacking fault energy, *Acta Mater.* **214** (2021) 117019.

[72] S. Lu, S. Antonov, L. Li, and Q. Feng, Two Steady-State Creep Stages in Co-Al-W-Base Single-Crystal Superalloys at 1273 K/137 MPa, *Metall. Mater. Trans. A* **49** (2018) 4079–4089.

[73] T. M. Smith, B. D. Esser, N. Antolin, A. Carlsson, R. E. Williams, A. Wessman, T. Hanlon, H. L. Fraser, W. Windl, D. W. McComb, and M. J. Mills, Phase transformation strengthening of high-temperature superalloys, *Nat. Commun.* **7** (2016) 13434.

[74] T. M. Smith, T. P. Gabb, K. N. Wertz, J. Stuckner, L. J. Evans, A. J. Egan, and M. J. Mills, Enhancing the Creep Strength of Next-Generation Disk Superalloys via Local Phase Transformation Strengthening, in *Superalloys 2020* (S. Tin, M. Hardy, J. Clews, J. Cormier, Q. Feng, J. Marcin, C. O'Brien, and A. Suzuki, eds.), (Warrendale, PA), pp. 726–736, TMS, 2020.

[75] B. A. Cowles, High cycle fatigue in aircraft gas turbines - an industry perspective, *Int. J. Fracture* **80** (1996) 147–163.

[76] A. Cervellon, S. Hémery, P. Kürnsteiner, B. Gault, P. Kontis, and J. Cormier, Crack initiation mechanisms during very high cycle fatigue of Ni-based single crystal superalloys at high temperature, *Acta Mater.* **188** (2020) 131–144.

[77] A. Pineau and S. Antolovich, High temperature fatigue of nickel-base superalloys - A review with special emphasis on deformation modes and oxidation, *Eng. Fail. Anal.* **16** (2009) 2668–2697.

[78] N. Pugno, M. Ciavarella, P. Cornetti, and A. Carpinteri, A generalized Paris' law for fatigue crack growth, *J. Mech. Phys. Solids* **54** (2006) 1333–1349.

[79] S. Steuer, P. Villechaise, T. M. Pollock, and J. Cormier, Benefits of high gradient solidification for creep and low cycle fatigue of AM1 single crystal superalloy, *Mat. Sci. Eng. A* **645** (2015) 109–115.

[80] H. Mughrabi, Cyclic slip irreversibilities and the evolution of fatigue damage, *Metall. Mater. Trans. B* **40** (2009) 431–453.

[81] D. W. MacLachlan and D. M. Knowles, Fatigue behaviour and lifing of two single crystal superalloys, *Fatigue Fract. Engng. Mater. Struct.* **24** (2001) 503–521.

[82] C. Yablinsky, *Characterization of Fatigue Mechanisms in Ni-based Superalloys.* PhD thesis, The Ohio State University, 2010.

[83] M. A. Lafata, L. H. Rettberg, C. Mercer, and T. M. Pollock, Sustained Peak Low-Cycle Fatigue in Single Crystals with Equilibrium γ-γ' Coatings, in *Superalloys 2016: Proceedings of the 13th International Symposium on Superalloys* (M. Hardy, E. Huron, U. Glatzel, B. Griffin, B. Lewis, C. Rae, V. Seetharaman, and S. Tin, eds.), (Warrendale, PA), pp. 405–413, TMS, 2016.

[84] M. A. Lafata, L. H. Rettberg, M. Y. He, and T. M. Pollock, Oxidation-Assisted Crack Growth in Single-Crystal Superalloys during Fatigue with Compressive Holds, *Metall. Mater. Trans. A* **49** (2018) 105–116.

[85] C. R. Deckard, Part generation by layer-wise selective laser sintering, Master's thesis, University of Texas at Austin, 1986.

[86] C. R. Deckard, *Selective laser sintering.* PhD thesis, University of Texas at Austin, 1988.

[87] J. A. Manriquez-Frayre and D. L. Bourell, Selective laser sintering of binary metallic powder, in *Solid freeform fabrication symposium*, pp. 99–106, 1990.

[88] T. DebRoy, T. Mukherjee, J. O. Milewski, J. W. Elmer, B. Ribic, J. J. Blecher, and W. Zhang, Scientific, technological and economic issues in metal printing and their solutions, *Nat. Mater.* **18** (2019) 1026–1032.

[89] R. Huang, M. Riddle, D. Graziano, J. Warren, S. Das, S. Nimbalkar, J. Cresko, and E. Masanet, Energy and emissions saving potential of additive manufacturing: the case of lightweight aircraft components, *J. Clean. Prod.* **135** (2016) 1559–1570.

[90] EOS, "Locking shaft for the aircraft door of an airbus a350." url: eos.info/en/3d-printing-examples-applications/aerospace-3d-printing/airbus-case-study. Online. Accessed 9 June 2021.

[91] H. P. Tang, M. Qian, N. Liu, X. Z. Zhang, G. Y. Yang, and J. Wang, Effect of Powder Reuse Times on Additive Manufacturing of Ti-6Al-4V by Selective Electron Beam Melting, *JOM* **67** (2015) 555–563.

[92] S. M. Yusuf, S. Cutler, and N. Gao, Review: The Impact of Metal Additive Manufacturing on the Aerospace Industry Shahir, *Metals* **9** (2019) 1286.

[93] R. Stamp, P. Fox, W. O'Neill, E. Jones, and C. Sutcliffe, The development of a scanning strategy for the manufacture of porous biomaterials by selective laser melting, *J. Mater. Sci.-Mater. M.* **20** (2009) 1839–1848.

[94] C. Y. Yap, C. K. Chua, Z. L. Dong, Z. H. Liu, D. Q. Zhang, L. E. Loh, and S. L. Sing, Review of selective laser melting: Materials and applications, *Appl. Phys. Rev.* **2** (2015) 041101.

[95] W. J. Sames, F. A. List, S. Pannala, R. R. Dehoff, and S. S. Babu, The metallurgy and processing science of metal additive manufacturing, *Int. Mater. Rev.* **61** (2016) 315–360.

[96] RP Photonics Consulting GmbH, "Yag lasers." url: rp-photonics.com/yag_lasers.html. Online. Accessed 9 June 2021.

[97] C. Körner, Additive manufacturing of metallic components by selective electron beam melting - A review, *Int. Mater. Rev.* **61** (2016) 361–377.

[98] S. S. Babu, N. Raghavan, J. Raplee, S. J. Foster, C. Frederick, M. Haines, R. Dinwiddie, M. K. Kirka, A. Plotkowski, Y. Lee, and R. R. Dehoff, Additive Manufacturing of Nickel Superalloys: Opportunities for Innovation and Challenges Related to Qualification, *Metall. Mater. Trans. A* **49** (2018) 3764–3780.

[99] E. Chauvet, P. Kontis, E. A. Jägle, B. Gault, D. Raabe, C. Tassin, J. J. Blandin, R. Dendievel, B. Vayre, S. Abed, and G. Martin, Hot cracking mechanism affecting a non-weldable Ni-based superalloy produced by selective electron Beam Melting, *Acta Mater.* **142** (2018) 82–94.

[100] J. H. Martin, B. D. Yahata, J. M. Hundley, J. A. Mayer, T. A. Schaedler, and T. M. Pollock, 3D printing of high-strength aluminium alloys, *Nature* **549** (2017) 365–369.

[101] P. Kontis, E. Chauvet, Z. Peng, J. He, A. K. da Silva, D. Raabe, C. Tassin, J. J. Blandin, S. Abed, R. Dendievel, B. Gault, and G. Martin, Atomic-scale grain boundary engineering to overcome hot-cracking in additively-manufactured superalloys, *Acta Mater.* **177** (2019) 209–221, [arXiv:1905.0953].

[102] G. Çam and M. Koçak, Progress in joining of advanced materials, *Int. Mater. Rev.* **43** (1998) 1–44.

[103] M. Ramsperger, R. F. Singer, and C. Körner, Microstructure of the Nickel-Base Superalloy CMSX-4 Fabricated by Selective Electron Beam Melting, *Metall. Mater. Trans. A* **47** (2016) 1469–1480.

[104] I. Lopez-Galilea, B. Ruttert, J. He, T. Hammerschmidt, R. Drautz, B. Gault, and W. Theisen, Additive manufacturing of CMSX-4 Ni-base superalloy by selective laser melting: Influence of processing parameters and heat treatment, *Addit. Manuf.* **30** (2019) 100874.

[105] M. Ramsperger, L. Mújica Roncery, I. Lopez-Galilea, R. F. Singer, W. Theisen, and C. Körner, Solution Heat Treatment of the Single Crystal Nickel-Base Superalloy CMSX-4 Fabricated by Selective Electron Beam Melting, *Adv. Eng. Mater.* **17** (2015) 1486–1493.

[106] M. Ramsperger and C. Körner, Selective electron beam melting of the single crystalline Nickel-base superalloy CMSX-4®: From columnar grains to a single crystal, in *Superalloys 2016: Proceedings of the 13th International Symposium on Superalloys* (M. Hardy, E. Huron, U. Glatzel, B. Griffin, B. Lewis, C. Rae, V. Seetharaman, and S. Tin, eds.), (Warrendale, PA), pp. 341–349, TMS, 2016.

[107] E. Chauvet, C. Tassin, J. J. Blandin, R. Dendievel, and G. Martin, Producing Ni-base superalloys single crystal by selective electron beam melting, *Scripta Mater.* **152** (2018) 15–19.

[108] C. Körner, M. Ramsperger, C. Meid, D. Bürger, P. Wollgramm, M. Bartsch, and G. Eggeler, Microstructure and Mechanical Properties of CMSX-4 Single Crystals Prepared by Additive Manufacturing, *Metall. Mater. Trans. A* **49** (2018) 3781–3792.

[109] P. Fernandez-Zelaiae, M. M. Kirka, A. M. Rossy, Y. Lee, and S. N. Dryepondt, Nickel-based superalloy single crystals fabricated via electron beam melting, *Acta Mater.* (2021) 117133.

[110] M. Rappaz, A. Jacot, and W. J. Boettinger, Last-stage solidification of alloys: Theoretical model of dendrite-arm and grain coalescence, *Metall. Mater. Trans. A* **34 A** (2003) 467–479.

[111] M. Rappaz, J. M. Drezet, and M. Gremaud, A new hot-tearing criterion, *Metall. Mater. Trans. A* **30** (1999) 449–455.

[112] S. Kou, A criterion for cracking during solidification, *Acta Mater.* **88** (2015) 366–374.

[113] R. Engeli, T. Etter, S. Hövel, and K. Wegener, Processability of different IN738LC powder batches by selective laser melting, *J. Mater. Process. Tech.* **229** (2016) 484–491.

[114] N. J. Harrison, I. Todd, and K. Mumtaz, Reduction of micro-cracking in nickel superalloys processed by Selective Laser Melting: A fundamental alloy design approach, *Acta Mater.* **94** (2015) 59–68.

[115] R. Engeli, T. Etter, and H. Meidani, "Gamma prime precipitation strengthened nickel-base superalloy for use in powder based additive manufacturing process." EP2886225 (A1). 2015.

[116] Y. T. Tang, C. Panwisawas, J. N. Ghoussoub, Y. Gong, J. W. G. Clark, A. A. N. Németh, D. G. Mccartney, and R. C. Reed, Acta Materialia Alloys-by-design : Application to new superalloys for additive manufacturing, *Acta Mater.* **202** (2021) 417–436.

[117] S. P. Murray, J.-C. Stinville, P. G. Callahan, R. K. Rhein, and T. M. Pollock, Low Cycle Fatigue of Single Crystal γ'-containing Co-based Superalloys at 750 °C, *Metall. Mater. Trans. A* **51** (2020) 200–213.

[118] C. L. Brundidge and T. M. Pollock, Processing to Fatigue Properties: Benefits of High Gradient Casting for Single Crystal Airfoils, in *Superalloys 2012* (E. Huron, R. Reed, M. Hardy, M. Mills, R. Montero, P. Portella, and J. Telesman, eds.), (Warrendale, PA), pp. 379–385, TMS, 2012.

[119] K. Shinagawa, T. Omori, K. Oikawa, R. Kainuma, and K. Ishida, Ductility enhancement by boron addition in Co-Al-W high-temperature alloys, *Scripta Mater.* **61** (2009) 612–615.

[120] F. Xue, H. J. Zhou, and Q. Feng, Improved High-Temperature Microstructural Stability and Creep Property of Novel Co-Base Single-Crystal Alloys Containing Ta and Ti, *JOM* **66** (2014) 2486–2494.

[121] B. R. Goodlet, L. Mills, B. Bales, M.-A. Charpagne, S. P. Murray, W. C. Lenthe, L. Petzold, and T. M. Pollock, Elastic Properties of Novel Co- and CoNi-Based Superalloys Determined through Bayesian Inference and Resonant Ultrasound Spectroscopy, *Metall. Mater. Trans. A* **49** (2018) 2324–2339.

[122] L. P. Freund, S. Giese, D. Schwimmer, H. W. Höppel, S. Neumeier, and M. Göken, High temperature properties and fatigue strength of novel wrought γ/γ' Co-base superalloys, *J. Mater. Res.* **32** (2017) 4475–4482.

[123] R. K. Rhein, P. G. Callahan, S. P. Murray, J.-C. Stinville, M. S. Titus, A. Van der Ven, and T. M. Pollock, Creep Behavior of Quinary γ'-Strengthened Co-Based Superalloys, *Metall. Mater. Trans. A* **49** (2018) 4090–4098.

[124] J. C. Yen, F. J. Chang, and S. Chang, A New Criterion for Automatic Multilevel Thresholding, *IEEE T. Image Process.* **4** (1995) 370–378.

[125] J. Schindelin, I. Arganda-Carreras, E. Frise, V. Kaynig, M. Longair, T. Pietzsch, S. Preibisch, C. Rueden, S. Saalfeld, B. Schmid, J.-Y. Tinevez, D. J. White, V. Hartenstein, K. Eliceiri, P. Tomancak, and A. Cardona, Fiji: an open-source platform for biological-image analysis., *Nat. Methods* **9** (2012) 676–82.

[126] H. U. Hong, B. G. Choi, I. S. Kim, Y. S. Yoo, and C. Y. Jo, Characterization of deformation mechanisms during low cycle fatigue of a single crystal nickel-based superalloy, *J. Mater. Sci.* **46** (2011) 5245–5251.

[127] X. Zhang, T. Jin, N. R. Zhao, Z. H. Wang, X. F. Sun, H. R. Guan, and Z. Q. Hu, Effect of strain rate on the tensile behavior of a single crystal nickel-base superalloy, *Mat. Sci. Eng. A* **492** (2008) 364–369.

[128] A. C. Yeh, S. C. Wang, C. F. Cheng, Y. J. Chang, and S. C. Chang, Oxidation behaviour of Si-bearing Co-based alloys, *Oxid. Met.* **86** (2016) 99–112.

[129] S. A. J. Forsik, A. O. Polar Rosas, T. Wang, G. A. Colombo, N. Zhou, S. J. Kernion, and M. E. Epler, High-Temperature Oxidation Behavior of a Novel Co-Base Superalloy, *Metall. Mater. Trans. A* **49** (2018) 4058–4069.

[130] F. Abe, H. Araki, H. Yoshida, and M. Okada, The role of aluminum and titanium on the oxidation process of a nickel-base superalloy in steam at 800 °C, *Oxid. Met.* **27** (1987) 21–36.

[131] C. A. Phalnikar, E. B. Evans, and W. M. Baldwin, High Temperature Scaling of Cobalt-Chromium Alloys, *J. Electrochem. Soc.* **103** (1956) 429–438.

[132] L. Klein, A. Zendegani, M. Palumbo, S. G. Fries, and S. Virtanen, First approach for thermodynamic modelling of the high temperature oxidation behaviour of ternary γ'-strengthened Co-Al-W superalloys, *Corros. Sci.* **89** (2014) 1–5.

[133] J. M. F. Colinas and C. O. Areán, Kinetics of solid-state spinel formation: Effect of cation coordination preference, *J. Solid State Chem.* **109** (1994) 43–46.

[134] J. Wu, C. Li, Y. Liu, X. Xia, Y. Wu, Z. Ma, and H. Wang, Influences of solution cooling rate on microstructural evolution of a multiphase Ni_3Al-based intermetallic alloy, *Intermetallics* **109** (2019) 48–59.

[135] R. Viswanathan, N. S. Cheruvu, and K. S. Chan, Coatings for advanced large frame combustion turbines for power generation, in *ASME Turbo Expo 2003 Power for Land, Sea, & Air*, (Atlanta, Georgia), pp. 1–14, ASME, 2003.

[136] M. I. Wood, Mechanical interactions between coatings and superalloys under conditions of fatigue, *Surf. Coat. Technol.* **39-40** (1989) 29–42.

[137] T. A. Taylor and P. N. Walsh, Thermal expansion of MCrAlY alloys, *Surf. Coat. Technol.* **177-178** (2004) 24–31.

[138] F. Cao, B. Tryon, C. J. Torbet, and T. M. Pollock, Microstructural evolution and failure characteristics of a NiCoCrAlY bond coat in "hot spot" cyclic oxidation, *Acta Mater.* **57** (2009) 3885–3894.

[139] J. M. Martínez-Esnaola, A. Martín-Meizoso, E. E. Affeldt, A. Bennett, and M. Fuentes, High Temperature Fatigue in Single Crystal Superalloys, *Fatigue Fract. Engng. Mater. Struct.* **20** (1997) 771–788.

[140] M. M. Nagl, S. R. J. Saunders, W. T. Evans, and D. J. Hall, The tensile failure of nickel oxide scales at ambient and at growth temperature, *Corros. Sci.* **35** (1993) 965–977.

[141] D. Tromans and J. A. Meech, Fracture toughness and surface energies of minerals: theoretical estimates for oxides, sulphides, silicates, and halides, *Miner. Eng.* **15** (2002) 1027–1041.

[142] E. Si, Stress Intensity Factors for Edge Cracks in Round Bars, *Eng. Fract. Mech.* **37** (1990) 805–812.

[143] N. B. Pilling and R. Bedworth, The oxidation of metals at high temperatures, *J. I. Met.* **29** (1923) 529–591.

[144] P. Kofstad, On the Formation of Porosity and Microchannels in Growing Scales, *Oxid. Met.* **24** (1985) 265–276.

[145] H. E. Evans, Stress effects in high temperature oxidation of metals, *Int. Mater. Rev.* **40** (1995) 1–40.

[146] P. Paris and F. Erdogan, A Critical Analysis of Crack Propagation Laws, *J. Basic Eng.-T. ASME* **85** (1963) 528.

[147] E. Fleury and L. Rémy, Low cycle fatigue damage in nickel-base superalloy single crystals at elevated temperature, *Mat. Sci. Eng. A* **167** (1993) 23–30.

[148] M. Weiser, Y. M. Eggeler, E. Spiecker, and S. Virtanen, Early stages of scale formation during oxidation of γ/γ' strengthened single crystal ternary Co-base superalloy at 900 °C, *Corros. Sci.* **135** (2018) 78–86.

[149] E. J. Opila, Volatility of Common Protective Oxides in High-Temperature Water Vapor: Current Understanding and Unanswered Questions, *Mater. Sci. Forum* **461-464** (2004) 765–774.

[150] P. Berthod, Kinetics of high temperature oxidation and chromia volatilization for a binary Ni-Cr alloy, *Oxid. Met.* **64** (2005) 235–252.

[151] T. Omori, K. Oikawa, J. Sato, I. Ohnuma, U. R. Kattner, R. Kainuma, and K. Ishida, Partition behavior of alloying elements and phase transformation temperatures in Co-Al-W-base quaternary systems, *Intermetallics* **32** (2013) 274–283.

[152] M. S. Titus, L. H. Rettberg, and T. M. Pollock, High Temperature Creep of γ'-Containing CoNi-base alloys, in *Superalloys 2016* (M. Hardy, E. Huron, U. Glatzel, B. Griffin, B. Lewis, C. Rae, V. Seetharaman, and S. Tin, eds.), (Warrendale, PA), pp. 141–148, TMS, 2016.

[153] N. Volz, C. H. Zenk, R. Cherukuri, T. Kalfhaus, M. Weiser, S. K. Makineni, C. Betzing, M. Lenz, B. Gault, S. G. Fries, J. Schreuer, R. Vaßen, S. Virtanen, D. Raabe, E. Spiecker, S. Neumeier, and M. Göken, Thermophysical and Mechanical Properties of Advanced Single Crystalline Co-base Superalloys, *Metall. Mater. Trans. A* **49** (2018) 4099–4109.

[154] A. Mouttura, N. Warnken, M. Miller, M. Finnis, and R. Reed, Atom probe tomography analysis of the distribution of rhenium in nickel alloys, *Acta Mater.* **58** (2010) 931–942.

[155] R. R. Adharapurapu, J. Zhu, V. S. Dheeradhada, D. M. Lipkin, and T. M. Pollock, A combinatorial investigation of palladium and platinum additions to β-NiAl overlay coatings, *Acta Mater.* **77** (2014) 379–393.

[156] J. Zhu, M. S. Titus, and T. M. Pollock, Experimental Investigation and Thermodynamic Modeling of the Co-Rich Region in the Co-Al-Ni-W Quaternary System, *Journal of Phase Equilibria and Diffusion* **35** (2014) 595–611.

[157] A. Mottura, A. Janotti, and T. M. Pollock, Alloying Effects in the γ' phase of Co-based superalloys, in *Superalloys 2012* (E. S. Huron, R. C. Reed, M. C. Hardy, M. J. Mills, R. E. Montero, P. D. Portella, and J. Telesman, eds.), pp. 685–693, TMS (The Minerals, Metals & Materials Society), 2012.

[158] W. Li, L. Li, S. Antonov, and Q. Feng, Effective design of a Co-Ni-Al-W-Ta-Ti alloy with high γ' solvus temperature and microstructural stability using combined CALPHAD and experimental approaches, *Mater. Design* **180** (2019) 107912.

[159] F. H. Stott, G. C. Wood, and J. Stringer, The influence of alloying elements on the development and maintenance of protective scales, *Oxid. Met.* **44** (1995) 113–145.

[160] A. Suzuki, H. Inui, and T. M. Pollock, $L1_2$-Strengthened Cobalt-Base Superalloys, *Ann. Rev. Mater. Res.* **45** (2015) 345–368.

[161] Y. Xu, L. Zhang, J. Li, X. Xiao, X. Cao, G. Jia, and Z. Shen, Relationship between Ti/Al ratio and stress-rupture properties in nickel-based superalloy, *Mat. Sci. Eng.: A* **544** (2012) 48–53.

[162] M. Simonetti and P. Caron, Role and behaviour of μ phase during deformation of a nickel-based single crystal superalloy, *Mat. Sci. Eng.: A* **254** (1998) 1–12.

[163] L. P. Freund, A. Stark, F. Pyczak, N. Schell, M. Göken, and S. Neumeier, The grain boundary pinning effect of the μ phase in an advanced polycrystalline γ/γ' Co-base superalloy, *J. Alloys Compd.* **753** (2018) 333–342.

[164] L. P. Freund, A. Stark, A. Kirchmayer, N. Schell, F. Pyczak, M. Göken, and S. Neumeier, The Effect of a Grain Boundary Pinning B2 Phase on Polycrystalline Co-Based Superalloys with Reduced Density, *Metall. Mater. Trans. A* **49** (2018) 4070–4078.

[165] P. Y. Hou, Segregation phenomena at thermally grown Al_2O_3/alloy interfaces, *Ann. Rev. Mater. Res.* **38** (2008) 275–298.

[166] D. R. Clarke, V. K. Tolpygo, and M. Gentleman, Luminescence-based characterization of protective oxides: From failure mechanisms to non-destructive evaluation, *Mater. Sci. Forum* **461-464** (2004) 621–630.

[167] Y. Minamino, Y. Koizumi, N. Tsuji, T. Yamada, and T. Takahashi, Interdiffusion in Co solid solutions of Co-Al-Cr-Ni system at 1423 K, *Mater. Trans.* **44** (2003) 63–71.

[168] T. M. Pollock, W. H. Murphy, E. H. Goldman, D. L. Uram, and J. S. Tu, Grain Defect Formation During Directional Solidification of Nickel Base Single Crystals, in *Superalloys 1992* (S. Antolovch, R. Stusrud, R. MacKay, D. Anton, T. Khan, R. Kissinger, and D. Klarstrom, eds.), pp. 125–134, TMS, 1992.

[169] R. W. Jackson, M. S. Titus, M. R. Begley, and T. M. Pollock, Thermal expansion behavior of new Co-based alloys and implications for coatings, *Surf. Coat. Technol.* **289** (2016) 61–68.

[170] M. H. Yoo, On the theory of anomalous yield behavior of Ni_3Al - Effect of elastic anisotropy, *Scripta Metall.* **20** (1986) 915–920.

[171] K. V. Vamsi and S. Karthikeyan, Yield anomaly in $L1_2$ $Co_3Al_xW_{1-x}$ vis-à-vis Ni_3Al, *Scripta Mater.* **130** (2017) 269–273.

[172] K. Harris, G. L. Erickson, and R. E. Schwer, Development of the Single Crystal Alloys CM SX-2 and CM SX-3 for Advanced Technology Turbine Engines, vol. 5: Ceramics; Structures and Dynamics; Controls, Diagnostics and Instrumentation; Education; Process Industries of *Turbo Expo: Power for Land, Sea, and Air*, 1983.

[173] M. G. Hebsur and R. V. Miner, Elevated Temperature Tension, Compression, and Creep-Rupture Behavior of [001]-Oriented Single Crystal Superalloy PWA 1480, tech. rep., Lewis Research Center, NASA, Cleveland, OH, 1987.

[174] H. Peng, Y. Shi, S. Gong, H. Guo, and B. Chen, Microstructure, mechanical properties and cracking behaviour in a γ'-precipitation strengthened nickel-base superalloy fabricated by electron beam melting, *Mater. Design* **159** (2018) 155–169.

[175] A. Sengupta, S. K. Putatunda, L. Bartosiewicz, J. Hangas, M. Peputapeck, and E. E. Alberts, Tensile Behavior of a New Single-Crystal Nickel-Based Superalloy (CMSX-4) at Room and Elevated Temperatures, *J. Mater. Eng. Perform.* **3** (1994) 73–81.

[176] K. V. Vamsi, S. P. Murray, and T. M. Pollock, The Yield Strength Anomaly in Co-Ni Design Space, in *Superalloys 2020* (S. Tin, M. Hardy, J. Clews, J. Cormier, Q. Feng, J. Marcin, C. O'Brien, and A. Suzuki, eds.), pp. 948–958, Springer International Publishing, 2020.

[177] A. Ardell, Precipitation hardening, *Metall. Trans. A* **16** (1985) 2131–2165.

[178] B. R. Goodlet, S. P. Murray, B. Bales, J. Rossin, C. J. Torbet, and T. M. Pollock, Temperature dependence of single crystal elastic constants in a CoNi-Base alloy: A new methodology, *Mat. Sci. Eng.: A* **803** (2021) 140507.

[179] S. P. Murray, A. Cervellon, J. Cormier, and T. M. Pollock, Low cycle fatigue of a single crystal CoNi-base superalloy, *Mat. Sci. Eng.: A* **827** (2021) 142007.

[180] M. Maldini, M. Marchionni, M. Nazmy, M. Staubli, and G. Osinkolu, Creep and Fatigue Properties of a Directionally Solidified Nickel Base Superalloy at Elevated Temperature, in *Superalloys 1996* (R. D. Kissinger, D. J. Dye, D. L. Anton, A. D. Cetel, M. V. Nathal, T. M. Pollock, and D. A. Woodford, eds.), pp. 327–334, TMS, 1996.

[181] M. Ott and H. Mughrabi, Dependence of the Isothermal Fatigue Behaviour of a Monocrystalline Nickel-Base Superalloy on the γ/γ' Morphology, in *Fatigue '96* (G. Lütjering and H. Nowack, eds.), (Berlin), pp. 789–794, Elseview Science Ltd., 1996.

[182] M. Ott and H. Mughrabi, Dependence of the high-temperature low-cycle fatigue behaviour of the monocrystalline nickel-base superalloys CMSX-4 and CMSX-6 on the γ/γ'-morphology, *Mater. Sci. Eng.: A* **272** (1999) 24–30.

[183] L. Bortoluci Ormastroni, L. Mataveli Suave, A. Cervellon, P. Villechaise, and J. Cormier, LCF, HCF and VHCF life sensitivity to solution heat treatment of a third-generation Ni-based single crystal superalloy, *Int. J. Fatigue* **130** (2020) 105247.

[184] M. Lamm and R. Singer, The effect of casting conditions on the high-cycle fatigue properties of the single-crystal nickel-base superalloy PWA 1483, *Metall. Mater. Trans. A* **38** (2007) 1177–1183.

[185] P. Liu, H. Huang, S. Antonov, C. Wen, D. Xue, H. Chen, L. Li, Q. Feng, T. Omori, and Y. Su, Machine learning assisted design of γ'-strengthened Co-base superalloys with multi-performance optimization, *npj Comput. Mater.* **6** (2020) 1–9.

[186] M. Zou, W. Li, L. Li, J.-C. Zhao, and Q. Feng, Machine Learning Assisted Design Approach for Developing γ'-Strengthened Co-Ni-Base Superalloys, in *Superalloys 2020* (S. Tin, M. Hardy, J. Clews, J. Cormier, Q. Feng, J. Marcin, C. O'Brien, and A. Suzuki, eds.), (Warrendale, PA), pp. 937–947, TMS, 2020. 1011.1669.

[187] P. Mazot and J. de Fouquet, Détermination par la méthode de résonance des constantes d'élasticité de monocristaux de superalliage base nickel am1 entre l'ambiante et 1100 °c, *Mém. Étud. Sci. Rev. Mét.* **89** (1992) 165–170.

[188] J. Cormier, P. Gadaud, M. Czaplicki, R. Y. Zhang, H. B. Dong, T. M. Smith, F. Zhang, J. S. Tiley, and S. L. Semiatin, In-Situ Determination of Precipitation Kinetics During Heat Treatment of Superalloy 718, *Metall. Mater. Trans. A* **52** (2021) 500–511.

[189] P. Gadaud. Personal communication.

[190] P. Perruchaut, *Etude des interactions fatigue-fluage-oxydation sur l'endommagement du superalliage monocristallin AM1.* PhD thesis, Université de Poitiers, ENSMA, Poitiers, France, 1997.

[191] W. Lenthe, S. Singh, and M. D. Graef, A spherical harmonic transform approach to the indexing of electron back-scattered diffraction patterns, *Ultramicroscopy* **207** (2019) 112841.

[192] Z. Fan, C. Wang, C. Zhang, Y. Yu, H. Chen, and Z. Yang, The temperature dependence of high-temperature strength and deformation mechanism in a single crystal CoNi-base superalloy, *Mat. Sci. Eng.: A* **735** (2018) 114–120.

[193] P. Caron, F. Diologent, and S. Drawin, Influence of chemistry on the tensile yield strength of nickel-based single crystal superalloys, *Adv. Mater. Res.* **278** (2011) 345–350.

[194] J. Cormier. Personal communication.

[195] M. Aursand and B. Skallerud, Mode I stress intensity factors for semi-elliptical fatigue cracks in curved round bars, *Theor. Appl. Fract. Mec.* **112** (2021) 102904.

[196] G. Fuchs, Solution heat treatment response of a third generation single crystal Ni-base superalloy, *Mater. Sci. Eng.: A* **300** (2001) 52–60.

[197] S. P. Murray, K. M. Pusch, A. T. Polonsky, C. J. Torbet, G. G. Seward, N. Zhou, S. A. Forsik, P. Nandwana, M. M. Kirka, R. R. Dehoff, W. E. Slye, and T. M. Pollock, A defect-resistant Co–Ni superalloy for 3D printing, *Nat. Commun.* **11** (2020) 4975.

[198] S. P. Murray, K. M. Pusch, A. T. Polonsky, C. J. Torbet, G. G. E. Seward, P. Nandwana, M. M. Kirka, R. R. Dehoff, N. Zhou, S. A. J. Forsik, W. Slye, and T. M. Pollock, Microstructure and Tensile Properties of a CoNi-Based Superalloy Fabricated by Selective Electron Beam Melting, in *Superalloys 2020* (S. Tin, M. Hardy, J. Clews, J. Cormier, Q. Feng, J. Marcin, C. O'Brien, and A. Suzuki, eds.), (Warrendale, PA), pp. 880–890, TMS, 2020.

[199] A. Cervellon, J. Z. Yi, F. Corpace, Z. Hervier, J. Rigney, P. K. Wright, C. J. Torbet, J. Cormier, J. W. Jones, and T. M. Pollock, Creep, Fatigue, and Oxidation Interactions During High and Very High Cycle Fatigue at Elevated Temperature of Nickel-Based Single Crystal Superalloys, in *Superalloys 2020* (S. Tin, M. Hardy, J. Clews, J. Cormier, Q. Feng, J. Marcin, C. O'Brien, and A. Suzuki, eds.), (Warrendale, PA), pp. 185–195, TMS, 2020.

[200] P. Caron and O. Lavigne, Recent Studies at Onera on Superalloys for Single Crystal Turbine Blades, *J. Aerospace Lab* (2011) 1–14.

[201] P. Caron, High γ' Solvus New Generation Nickel-Based Superalloys for Single Crystal Turbine Blade Applications, in *Superalloys 2000* (T. M. Pollock, R. D. Kissinger, R. R. Bowman, K. A. Green, M. Mclean, S. Olson, and J. J. Schirra, eds.), (Warrendale, PA), pp. 737–746, TMS, 2000.

[202] E. Fedorova, D. Monceau, and D. Oquab, Quantification of growth kinetics and adherence of oxide scales formed on Ni-based superalloys at high temperature, *Corros. Sci.* **52** (2010) 3932–3942.

[203] P. Audigié, A. Rouaix-Vande Put, A. Malié, and D. Monceau, High-temperature cyclic oxidation behaviour of Pt-rich γ-γ' coatings. Part I: Oxidation kinetics of coated AM1 systems after very long-term exposure at 1100 °C, *Corros. Sci.* **144** (2018) 127–135.

[204] P. Berthod, L. Aranda, S. Mathieu, and M. Vilasi, Influence of water vapour on the rate of oxidation of a Ni-25wt.%Cr alloy at high temperature, *Oxid. Met.* **79** (2013) 517–527.

[205] A. Bauer, S. Neumeier, F. Pyczak, and M. Göken, Microstructure and creep strength of different γ/γ'- strengthened Co-base superalloy variants, *Scripta Mater.* **63** (2010) 1197–1200.

[206] A. Royer, P. Bastie, and M. Veron, In situ determination of γ' phase volume fraction and of relations between lattice parameters and precipitate morphology in ni-based single crystal superalloy, *Acta Mater.* **46** (1998) 5357–5368.

[207] T. Grosdidier, A. Hazotte, and A. Simon, Precipitation and dissolution processes in γ/γ' single crystal nickel-based superalloys, *Mater. Sci. Eng.: A* **256** (1998) 183–196.

[208] M. Geuffrard, *Amorçage et micro-propagation de fissure en fatigue à haute température à partir de défauts dans un superalliage monocristallin.* PhD thesis, Ecole Nationale Supérieure des Mines de Paris, Paris, France, 2010.

[209] J. Moverare, S. Johansson, and R. Reed, Deformation and damage mechanisms during thermal-mechanical fatigue of a single-crystal superalloy, *Acta Mater.* **57** (2009) 2266–2276.

[210] L. H. Rettberg and T. M. Pollock, Localized recrystallization during creep in nickel-based superalloys GTD444 and René N5, *Acta Mater.* **73** (2014) 287–297.

[211] S. Hamadi, F. Hamon, J. Delautre, J. Cormier, P. Villechaise, S. Utada, P. Kontis, and N. Bozzolo, Consequences of a Room-Temperature Plastic Deformation During Processing on Creep Durability of a Ni-Based SX Superalloy, *Metall. Mater. Trans. A* **49** (2018) 4246–4261.

[212] S. Utada, J. Rame, S. Hamadi, J. Delautre, P. Villechaise, and J. Cormier, Kinetics of creep damage accumulation induced by a room-temperature plastic deformation introduced during processing of AM1 Ni-based single crystal superalloy, *Mater. Sci. Eng.: A* **789** (2020) 139571.

[213] P. Lehto, Adaptive domain misorientation approach for the EBSD measurement of deformation induced dislocation sub-structures, *Ultramicroscopy* **222** (2021) 113203.

[214] N. Bozzolo and M. Bernacki, Viewpoint on the Formation and Evolution of Annealing Twins During Thermomechanical Processing of FCC Metals and Alloys, *Metall. Mater. Trans. A* **51** (2020) 2665–2684.

[215] A. Cervellon, J. Cormier, F. Mauget, Z. Hervier, and Y. Nadot, Very High Cycle Fatigue of Ni-Based Single-Crystal Superalloys at High Temperature, *Metall. Mater. Trans. A* **49** (2018) 3938–3950.

[216] B. Beeston, I. Dillamore, and R. Smallman, The Stacking-Fault Energy of Some Nickel-Cobalt Alloys, *Met. Sci. J.* **2** (1968) 12–14.

[217] K. V. Vamsi, M.-A. Charpagne, and T. M. Pollock, High-throughput approach for estimation of intrinsic barriers in FCC structures for alloy design, *Scripta Mater.* **204** (2021) 114126.

[218] N. Volz, C. H. Zenk, T. Halvaci, K. Matuszewska, S. Neumeier, and M. Göken, Castability and Recrystallization Behavior of γ'-Strengthened Co-Base Superalloys, in *Superalloys 2020* (S. Tin, M. Hardy, J. Clews, J. Cormier, Q. Feng, J. Marcin, C. O'Brien, and A. Suzuki, eds.), (Warrendale, PA), pp. 901–908, TMS, 2020.

[219] L. Feng, D. Lv, R. K. Rhein, J. G. Goiri, M. S. Titus, A. Van der Ven, T. M. Pollock, and Y. Wang, Shearing of γ' particles in Co-base and Co-Ni-base superalloys, *Acta Mater.* **161** (2018) 99–109.

[220] C. L. Brundidge, D. Van Drasek, B. Wang, and T. M. Pollock, Structure refinement by a liquid metal cooling solidification process for single-crystal nickel-base superalloys, *Metall. Mater. Trans. A* **43** (2012) 965–976.

[221] J. B. Roca, P. Vaishnav, E. R. H. Fuchs, and M. G. Morgan, Policy needed for additive manufacturing, *Nat. Mater.* **15** (2016) 815–818.

[222] P. Heinl, L. Müller, C. Körner, R. F. Singer, and F. A. Müller, Cellular Ti-6Al-4V structures with interconnected macro porosity for bone implants fabricated by selective electron beam melting, *Acta Biomater.* **4** (2008) 1536–1544.

[223] Y. Zhang, L. Wu, X. Guo, S. Kane, Y. Deng, Y. G. Jung, J. H. Lee, and J. Zhang, Additive Manufacturing of Metallic Materials: A Review, *J. Mater. Eng. Perform.* **27** (2018) 1–13.

[224] R. Thamburaj, W. Wallace, and J. A. Goldak, Post-weld heat-treatment cracking in superalloys, *Int. Met. Rev.* **28** (1983) 1–22.

[225] M. Prager and C. S. Shira, Welding of precipitation-hardening nickel-base alloys, *Weld. Res. Counc. Bull.* **128** (1968) 1–64.

[226] N. D'Souza and H. B. Dong, Solidification path in third-generation Ni-based superalloys, with an emphasis on last stage solidification, *Scripta Mater.* **56** (2007) 41–44.

[227] S. Kou, A criterion for cracking during solidification, *Acta Mater.* **88** (2015) 366–374.

[228] S. Kou, A Simple Index for Predicting the Susceptibility to Solidification Cracking, *Weld. J.* **94** (2015) 374–388.

[229] H. Dobbelstein, M. Thiele, E. L. Gurevich, E. P. George, and A. Ostendorf, Direct metal deposition of refractory high entropy alloy MoNbTaW, *Phys. Procedia* **83** (2016) 624–633.

[230] N. Kaufmann, M. Imran, T. M. Wischeropp, C. Emmelmann, S. Siddique, and F. Walther, Influence of process parameters on the quality of aluminium alloy en AW 7075 using Selective Laser Melting (SLM), *Phys. Procedia* **83** (2016) 918–926.

[231] Y. S. Lee, M. M. Kirka, S. Kim, N. Sridharan, A. Okello, R. R. Dehoff, and S. S. Babu, Asymmetric Cracking in Mar-M247 Alloy Builds During Electron Beam Powder Bed Fusion Additive Manufacturing, *Metall. Mater. Trans. A* **49** (2018) 5065–5079.

[232] C. Panwisawas, Y. T. Tang, and R. C. Reed, Metal 3D printing as a disruptive technology for superalloys, *Nat. Commun.* **11** (2020) 1–4.

[233] N. Li, S. Huang, G. Zhang, R. Qin, W. Liu, H. Xiong, G. Shi, and J. Blackburn, Progress in additive manufacturing on new materials: A review, *J. Mater. Sci. Technol.* **35** (2019) 242–269.

[234] M. Haines, A. Plotkowski, C. L. Frederick, E. J. Schwalbach, and S. S. Babu, A sensitivity analysis of the columnar-to-equiaxed transition for Ni-based superalloys in electron beam additive manufacturing, *Comp. Mater. Sci.* **155** (2018) 340–349.

[235] B. Vrancken, L. Thijs, J. P. Kruth, and J. Van Humbeeck, Microstructure and mechanical properties of a novel β titanium metallic composite by selective laser melting, *Acta Mater.* **68** (2014) 150–158.

[236] National Research Council, *Integrated Computational Materials Engineering: A Transformational Discipline for Improved Competitiveness and National Security.* National Academies Press, 2008.

[237] A. Mottura, A. Janotti, and T. M. Pollock, A first-principles study of the effect of Ta on the superlattice intrinsic stacking fault energy of L1 2-Co 3(Al,W), *Intermetallics* **28** (2012) 138–143.

[238] K. V. Vamsi and T. M. Pollock, A new proximate structure for the APB (111) in $L1_2$ compounds, *Scripta Mater.* **182** (2020) 38–42.

[239] Y. Wang and J. Li, Phase field modeling of defects and deformation, *Acta Mater.* **58** (2010) 1212–1235.

[240] T. M. Pollock, C. A. Stewart, S. P. Murray, and C. G. Levi, High temperature oxidation resistant co-based gamma/gamma prime alloys dmref-co, *US Patent Application* (2020) 16/375,687.

[241] R. Hobbs, S. Tin, C. Rae, R. Broomfield, and C. Humphreys, Solidification characteristics of advanced nickel-base single crystal superalloys, in *Superalloys 2004* (T. M. Pollock, H. Harada, T. E. Howson, R. C. Reed, J. J. Schirra, and S. Walston, eds.), pp. 819–825, The Minerals, Metals & Materials Society, 2004.

[242] M. M. Kirka, K. A. Unocic, N. Raghavan, F. Medina, R. R. Dehoff, and S. S. Babu, Microstructure Development in Electron Beam-Melted Inconel 718 and Associated Tensile Properties, *JOM* **68** (2016) 1012–1020.

[243] H. Wang, X. Zhang, G. B. Wang, J. Shen, G. Q. Zhang, Y. P. Li, and M. Yan, Selective laser melting of the hard-to-weld IN738LC superalloy: Efforts to mitigate defects and the resultant microstructural and mechanical properties, *J. Alloys Compd.* **807** (2019) 151662.

[244] N. Matan, D. C. Cox, P. Carter, M. A. Rist, C. Rae, and R. Reed, Creep of CMSX-4 superalloy single crystals: effects of rafting at high temperature, *Acta Mater.* **47** (1999) 3367–3381.

[245] J. C. Stinville, K. Gallup, and T. M. Pollock, Transverse Creep of Nickel-Base Superalloy Bicrystals, *Metall. Mater. Trans. A* **46** (2015) 2516–2529.

[246] A. Van der Ven, J. C. Thomas, Q. Xu, and J. Bhattacharya, Linking the electronic structure of solids to their thermodynamic and kinetic properties, *Math. Comput. Simulat.* **80** (2010) 1393–1410.

[247] A. Van Der Ven, J. C. Thomas, B. Puchala, and A. R. Natarajan, First-Principles Statistical Mechanics of Multicomponent Crystals, *Ann. Rev. Mater. Res.* **48** (2018) 27–55.

[248] N. Raghavan, R. Dehoff, S. Pannala, S. Simunovic, M. Kirka, J. Turner, N. Carlson, and S. S. Babu, Numerical modeling of heat-transfer and the influence of process parameters on tailoring the grain morphology of IN718 in electron beam additive manufacturing, *Acta Mater.* **112** (2016) 303–314.

[249] D. Zhang, Z. Feng, C. Wang, W. Wang, Z. Liu, and W. Niu, Comparison of microstructures and mechanical properties of Inconel 718 alloy processed by selective laser melting and casting, *Mat. Sci. Eng.: A* **724** (2018) 357–367.

[250] B. Ruttert, M. Ramsperger, L. Mujica Roncery, I. Lopez-Galilea, C. Körner, and W. Theisen, Impact of hot isostatic pressing on microstructures of CMSX-4 Ni-base superalloy fabricated by selective electron beam melting, *Mater. Design* **110** (2016) 720–727.

[251] D. Woodford and J. Frawley, The Effect of Grain Boundary Orientation on Creep and Rupture of IN-738 and Nichrome, *Metall. Trans.* **5** (1974) 2005–2013.

[252] J. T. Guo, C. Yuan, H. C. Yang, V. Lupinc, and M. Maldini, Creep-rupture behavior of a directionally solidified nickel-base superalloy, *Metall. Mater. Trans. A* **32** (2001) 1103–1110.

[253] A. Basak, Additive manufacturing of high-gamma prime nickel-based superalloys through selective laser melting (SLM), in *Solid Freeform Fabrication 2019: Proceedings of the 30th Annual International Solid Freeform Fabrication Symposium—An Additive Manufacturing Conference* (D. Bourell, J. Beaman, R. Crawford, S. Fish, D. Kovar, and C. Seepersad, eds.), pp. 554–575, University of Texas at Austin, 2019.

[254] A. V. Sotov, A. V. Agapovichev, V. G. Smelov, V. V. Kokareva, M. O. Dmitrieva, A. A. Melnikov, S. P. Golanov, and Y. M. Anurov, Investigation of the IN-738 superalloy microstructure and mechanical properties for the manufacturing of gas turbine engine nozzle guide vane by selective laser melting, *I. J. Adv. Manuf. Tech.* **107** (2020) 2525–2535.

[255] S. Tin, Intelligent alloy design: Engineering single crystals superalloys amenable for manufacture, *Materials Science and Technology* **25** (2009) 136–146.

[256] A. T. Polonsky, M. P. Echlin, W. C. Lenthe, R. R. Dehoff, M. M. Kirka, and T. M. Pollock, Defects and 3D structural inhomogeneity in electron beam additively manufactured Inconel 718, *Mater. Charact.* **143** (2018) 171–181.

[257] Y. Q. Chen, E. Francis, J. Robson, M. Preuss, and S. J. Haigh, Compositional variations for small-scale gamma prime (γ') precipitates formed at different cooling rates in an advanced Ni-based superalloy, *Acta Mater.* **85** (2015) 199–206.

[258] S. Asavavisithchai, W. Homkrajai, and P. Wangyao, Strain-age cracking after postweld heat treatments in inconel 738 superalloy, *High Temp. Mater. Proc.* **29** (2010) 61–67.

[259] A. Szczotok and R. Przeliorz, Phase transformations in CMSX-4 nickel-base superalloy, *IOP Conf. Ser.-Mat. Sci.* **35** (2012) 012005.

[260] J. W. Park, J. M. Vitek, S. S. Babu, and S. A. David, Stray grain formation, thermomechanical stress and solidification cracking in single crystal nickel base superalloy welds, *Sci. Technol. Weld. Joi.* **9** (2004) 472–482.

[261] B. Song, X. Zhao, S. Li, C. Han, Q. Wei, S. Wen, J. Liu, and Y. Shi, Differences in microstructure and properties between selective laser melting and traditional manufacturing for fabrication of metal parts: A review, *Front. Mech. Eng.* **10** (2015) 111–125.

[262] X. Zhang, C. J. Yocom, B. Mao, and Y. Liao, Microstructure evolution during selective laser melting of metallic materials: A review, *J. Laser Appl.* **31** (2019) 031201.

[263] H. Jia, H. Sun, H. Wang, Y. Wu, and H. Wang, Scanning strategy in selective laser melting (SLM): a review, *I. J. Adv. Manuf. Tech.* **113** (2021) 2413–2435.

[264] E. Liverani, S. Toschi, L. Ceschini, and A. Fortunato, Effect of selective laser melting (SLM) process parameters on microstructure and mechanical properties of 316L austenitic stainless steel, *J. Mater. Process. Tech.* **249** (2017) 255–263.

[265] Y. M. Wang, T. Voisin, J. T. McKeown, J. Ye, N. P. Calta, Z. Li, Z. Zeng, Y. Zhang, W. Chen, T. T. Roehling, R. T. Ott, M. K. Santala, P. J. Depond, M. J. Matthews, A. V. Hamza, and T. Zhu, Additively manufactured hierarchical stainless steels with high strength and ductility, *Nat. Mater.* **17** (2018) 63–70.

[266] A. Röttger, J. Boes, W. Theisen, M. Thiele, C. Esen, A. Edelmann, and R. Hellmann, Microstructure and mechanical properties of 316L austenitic stainless steel processed by different SLM devices, *I. J. Adv. Manuf. Tech.* **108** (2020) 769–783.

[267] M. Simonelli, Y. Y. Tse, and C. Tuck, Microstructure of Ti-6Al-4V produced by selective laser melting, *J. Phys.: Conf. Ser.* **371** (2012) 012084.

[268] H. K. Rafi, N. V. Karthik, H. Gong, T. L. Starr, and B. E. Stucker, Microstructures and mechanical properties of Ti6Al4V parts fabricated by selective laser melting and electron beam melting, *J. Mater. Eng. Perform.* **22** (2013) 3872–3883.

[269] P. Kumar, O. Prakash, and U. Ramamurty, Micro-and meso-structures and their influence on mechanical properties of selectively laser melted Ti-6Al-4V, *Acta Mater.* **154** (2018) 246–260.

[270] E. Brandl, U. Heckenberger, V. Holzinger, and D. Buchbinder, Additive manufactured AlSi10Mg samples using Selective Laser Melting (SLM): Microstructure, high cycle fatigue, and fracture behavior, *Mater. Design* **34** (2012) 159–169.

[271] W. Li, S. Li, J. Liu, A. Zhang, Y. Zhou, Q. Wei, C. Yan, and Y. Shi, Effect of heat treatment on AlSi10Mg alloy fabricated by selective laser melting: Microstructure evolution, mechanical properties and fracture mechanism, *Mat. Sci. Eng.: A* **663** (2016) 116–125.

[272] F. Trevisan, F. Calignano, M. Lorusso, J. Pakkanen, A. Aversa, E. P. Ambrosio, M. Lombardi, P. Fino, and D. Manfredi, On the selective laser melting (SLM) of the AlSi10Mg alloy: Process, microstructure, and mechanical properties, *Materials* **10** (2017) 76.

[273] J. Zhang, B. Song, Q. Wei, D. Bourell, and Y. Shi, A review of selective laser melting of aluminum alloys: Processing, microstructure, property and developing trends, *J. Mater. Sci. Technol.* **35** (2019) 270–284.

[274] S. Li, Q. Wei, Y. Shi, C. K. Chua, Z. Zhu, and D. Zhang, Microstructure Characteristics of Inconel 625 Superalloy Manufactured by Selective Laser Melting, *J. Mater. Sci. Technol.* **31** (2015) 946–952.

[275] M. Leary, M. Mazur, H. Williams, E. Yang, A. Alghamdi, B. Lozanovski, X. Zhang, D. Shidid, L. Farahbod-Sternahl, G. Witt, I. Kelbassa, P. Choong, M. Qian, and M. Brandt, Inconel 625 lattice structures manufactured by selective laser melting (SLM): Mechanical properties, deformation and failure modes, *Mater. Design* **157** (2018) 179–199.

[276] I. Koutiri, E. Pessard, P. Peyre, O. Amlou, and T. De Terris, Influence of SLM process parameters on the surface finish, porosity rate and fatigue behavior of as-built Inconel 625 parts, *J. Mater. Process. Tech.* **255** (2018) 536–546.

[277] Z. Wang, K. Guan, M. Gao, X. Li, X. Chen, and X. Zeng, The microstructure and mechanical properties of deposited-IN718 by selective laser melting, *J. Alloys Compd.* **513** (2012) 518–523.

[278] J. Strößner, M. Terock, and U. Glatzel, Mechanical and Microstructural Investigation of Nickel-Based Superalloy IN718 Manufactured by Selective Laser Melting (SLM), *Adv. Eng. Mater.* **17** (2015) 1099–1105.

[279] T. Trosch, J. Strößner, R. Völkl, and U. Glatzel, Microstructure and mechanical properties of selective laser melted Inconel 718 compared to forging and casting, *Mater. Lett.* **164** (2016) 428–431.

[280] M. D. Sangid, T. A. Book, D. Naragani, J. Rotella, P. Ravi, A. Finch, P. Kenesei, J. S. Park, H. Sharma, J. Almer, and X. Xiao, Role of heat treatment and build orientation in the microstructure sensitive deformation characteristics of IN718 produced via SLM additive manufacturing, *Addit. Manuf.* **22** (2018) 479–496.

[281] L. N. Carter, M. M. Attallah, and R. C. Reed, Laser Powder Bed Fabrication of Nickel-Base Superalloys: Influence of Parameters; Characterisation, Quantification and Mitigation of Cracking, in *Superalloys 2012* (E. S. Huron, R. C. Reed, M. C. Hardy, M. J. Mills, R. E. Montero, P. D. Portella, and J. Telesman, eds.), (Warrendale, PA), pp. 577–586, TMS, 2012.

[282] L. N. Carter, C. Martin, P. J. Withers, and M. M. Attallah, The influence of the laser scan strategy on grain structure and cracking behaviour in SLM powder-bed fabricated nickel superalloy, *J. Alloys Compd.* **615** (2014) 338–347.

[283] S. Catchpole-Smith, N. Aboulkhair, L. Parry, C. Tuck, I. A. Ashcroft, and A. Clare, Fractal scan strategies for selective laser melting of 'unweldable' nickel superalloys, *Addit. Manuf.* **15** (2017) 113–122.

[284] A. A. N. Németh, D. J. Crudden, D. M. Collins, D. E. J. Armstrong, and R. C. Reed, Novel techniques to assess environmentally-assisted cracking in a Nickel-based superalloy, in *Superalloys 2016: Proceedings of the 13th International Symposium on Superalloys* (M. Hardy, E. Huron, U. Glatzel, B. Griffin, B. Lewis, C. Rae, V. Seetharaman, and S. Tin, eds.), (Warrendale, PA), pp. 801–810, TMS, 2016.

[285] A. A. Németh, D. J. Crudden, D. E. Armstrong, D. M. Collins, K. Li, A. J. Wilkinson, C. R. Grovenor, and R. C. Reed, Environmentally-assisted grain boundary attack as a mechanism of embrittlement in a nickel-based superalloy, *Acta Mater.* **126** (2017) 361–371.

[286] L. Z. He, Q. Zheng, X. F. Sun, G. C. Hou, H. R. Guan, and Z. Q. Hu, Low ductility at intermediate temperature of Ni-base superalloy M963, *Mat. Sci. Eng.: A* **380** (2004) 340–348.

[287] L. Zheng, G. Schmitz, Y. Meng, R. Chellali, and R. Schlesiger, Mechanism of intermediate temperature embrittlement of Ni and Ni-based superalloys, *Crit. Rev. Solid State* **37** (2012) 181–214.

[288] H. J. Chung, J. Y. Huh, and W. S. Jung, Intermediate temperature brittleness of Ni based superalloy Nimonic263, *Mater. Charact.* **140** (2018) 9–14.

[289] J. Kangazian, M. Shamanian, A. Kermanpur, E. Foroozmehr, and M. Badrossamay, Investigation of microstructure-tensile behavior relationship in Hastelloy X Ni-based superalloy processed by laser powder-bed fusion: Insights into the elevated temperature ductility loss, *Mat. Sci. Eng.: A* **823** (2021) 141742.

[290] S. Griffiths, H. Ghasemi-Tabasi, A. De Luca, J. Pado, S. S. Joglekar, J. Jhabvala, R. E. Logé, and C. Leinenbach, Influence of Hf on the heat treatment response of additively manufactured Ni-base superalloy CM247LC, *Mater. Charact.* **171** (2021) 110815.

[291] EDAX, "Oim analysis v8." url: https://www.edax.com/products/ebsd/oim-analysis/oim-analysis-v8. Online. Accessed 6 July 2021.

[292] O. Sanchez-Mata, J. A. Muñiz-Lerma, X. Wang, S. E. Atabay, M. Attarian Shandiz, and M. Brochu, Microstructure and mechanical properties at room and elevated temperature of crack-free Hastelloy X fabricated by laser powder bed fusion, *Mat. Sci. Eng.: A* **780** (2020) 139177.

[293] EOS GmbH, EOS NickelAlloy IN939 Material Data Sheet, tech. rep., 2021.

[294] L. N. Carter, *Selective laser melting of nickel superalloys for high temperature applications*. PhD thesis, University of Birmingham, 2013.

[295] M. J. Aziz, Model for solute redistribution during rapid solidification, *J. Appl. Phys.* **53** (1982) 1158–1168.

[296] R. A. Michi, A. Plotkowski, A. Shyam, R. R. Dehoff, and S. S. Babu, Towards high-temperature applications of aluminium alloys enabled by additive manufacturing, *Int. Mater. Rev.* (2021) 1–48.

[297] M. P. Haines, N. J. Peter, S. S. Babu, and E. A. Jägle, In-situ synthesis of oxides by reactive process atmospheres during L-PBF of stainless steel, *Addit. Manuf.* **33** (2020) 101178.

[298] A. Després, C. Mayer, M. Veron, E. F. Rauch, M. Bugnet, J. J. Blandin, G. Renou, C. Tassin, P. Donnadieu, and G. Martin, On the variety and formation sequence of second-phase particles in nickel-based superalloys fabricated by laser powder bed fusion, *Materialia* **15** (2021) 101037.

[299] Z. M. T. Chen, N. L. Okamoto, M. Demura, and H. Inui, Micropillar compression deformation of single crystals of Co3(Al,W) with the L12 structure, *Scripta Mater.* **121** (2016) 28–31.

[300] Y. T. Tang, J. N. Ghoussoub, C. Panwisawas, D. M. Collins, S. Amirkhanlou, J. W. Clark, A. A. Németh, D. Graham McCartney, and R. C. Reed, The Effect of Heat Treatment on Tensile Yielding Response of the New Superalloy ABD-900AM for Additive Manufacturing, in *Superalloys 2020* (S. Tin, M. Hardy, J. Clews, J. Cormier, Q. Feng, J. Marcin, C. O'Brien, and A. Suzuki, eds.), (Warrendale, PA), pp. 1055–1065, TMS, 2020.

[301] A. Després, S. Antonov, C. Mayer, C. Tassin, J.-j. Blandin, P. Kontis, and G. Martin, On the role of boron, carbon and zirconium on hot cracking and creep resistance of additively manufactured polycrystalline superalloys, *arXiv* (2021) 2105.08307.

[302] T. P. McAuliffe, I. Bantounas, L. R. Reynolds, A. Foden, M. C. Hardy, T. B. Britton, and D. Dye, Quantitative Precipitate Classification and Grain Boundary Property Control in Co/Ni-Base Superalloys, *Metall. Mater. Trans. A* **52** (2021) 1649–1664, [arXiv:2009.0094].

[303] D. Dye, M. Hardy, H. Yan, M. Knop, and H. Stone. EP2821519B1. 2017.

[304] R. Fabbro, S. Slimani, I. Doudet, F. Coste, and F. Briand, Experimental study of the dynamical coupling between the induced vapour plume and the melt pool for Nd-Yag CW laser welding, *J. Phys. D: Appl. Phys.* **39** (2006) 394–400.

[305] S. A. Khairallah, A. T. Anderson, A. Rubenchik, and W. E. King, Laser powder-bed fusion additive manufacturing: Physics of complex melt flow and

formation mechanisms of pores, spatter, and denudation zones, *Acta Mater.* **108** (2016) 36–45.